The potential of observations of radiocarbon in atmospheric CO2 for the atmospheric inversion of fossil fuel CO2 emission at regional scale

Yilong Wang

NNT : 2016SACLV113

THESE DE DOCTORAT
DE
L'UNIVERSITE PARIS-SACLAY
PREPAREE A L'UNIVERSITE VERSAILLES SAINT-QUENTIN EN YVELINES

ÉCOLE DOCTORALE N °129
Sciences de l'environnement d'Ile-de-France

Spécialité de doctorat : Météorologie, océanographie, physique de l'environnement

Par

M. Yilong WANG

The potential of observations of radiocarbon in atmospheric CO_2 for the atmospheric inversion of fossil fuel CO_2 emission at regional scale

Thèse présentée et soutenue à LSCE, le 30 novembre 2016 :

Composition du Jury :

Philippe BOUSQUET, UVSQ, président du Jury
John MILLER, NOAA, rapporteur
Heather GRAVEN, Imperial College London, rapporteur
Ingeborg LEVIN, University of Heidelberg, examinateur
Philippe CIAIS, LSCE, directeur de thèse
Grégoire BROQUET, LSCE, co-directeur de thèse

université PARIS-SACLAY
ÉCOLE DOCTORALE
Sciences chimiques : molécules, matériaux, instrumentation et biosystèmes

Titre : Le potentiel des mesures du radiocarbone du CO_2 atmospherique pour l'inversion des émissions fossiles de CO_2 à l'échelle régionale

Mots clés : l'inversion atmospherique, émissions fossiles, radiocarbone, l'échelle régionale, réseaux continentaux d'observation

Résumé : Dans le contexte du réchauffement climatique, des états et des villes s'engagent à réduire leurs émissions de gaz à effet de serre et en particulier celles de CO_2. Une quantification précise des émissions est nécessaire aux scientifiques et aux décideurs politiques. La qualité des inventaires des émissions dues à la consommation des combustibles fossiles, qui reposent sur des données statistiques compilées et rapportées par les émetteurs, reste très variable selon les pays. Les mesures atmosphériques et la modélisation inverse pourraient fournir une information indépendante pour la vérification de ces émissions. Il est cependant difficile de séparer le signal de CO_2 fossile (CO_2CF) du signal des flux naturels dans les mesures atmosphériques fournies par les réseaux continentaux de mesure au sol. L'objectif de ma thèse est d'améliorer la compréhension du potentiel des données de $^{14}CO_2$, un des traceurs permettant de séparer le signal de CO_2CF des autres sources de CO_2, pour l'estimation objective des émissions fossiles aux échelles nationales par inversion atmosphérique.

J'ai développé des systèmes d'inversions mondiaux basés sur le modèle de transport atmospherique LMDz à basse résolution (2.5 ° ×3.75 °), et reposant sur des réseaux de mesure du CO_2 et du $^{14}CO_2$, résolvant les émissions fossiles à l'échelle subcontinentale / mensuelle en Europe et en Chine.

Dans le Chapitre 2, j'ai défini et quantifié les sources d'erreurs de modélisationprincipales, puis analysé leur impact pour l'estimation des bilans d'émissions fossiles à grande échelle avec un système d'inversion mondial en faisant l'hypothèse que les données de CO_2CF peuvent être directement déduites des données de $^{14}CO_2$. Les analyses soulignent l'impact de la méconnaissance de la distribution spatiale des émissions de CO_2 et du CO_2CF aux résolutions spatiales plus fines que celle du modèle de transport.

Dans le Chapitre 3, j'ai utilisé le système, les hypothèses et les diagnostics d'erreurs de modélisation du Chapitre 2 dans une série d'expériences avec des données synthétiques pour évaluer le potentiel d'un tel système d'inversion et de différents réseaux d'observation virtuels pour l'estimation les bilans régionaux d' émission fossile en Europe. Les résultats indiquent qu'en assimilant des moyennes sur 2 semaines de mesures CO_2CF issues du réseau actuel de 17 sites $^{14}CO_2$ en Europe, l'inversion réduirait l'incertitude sur les émissions mensuelles pour l'Ouest de l'Allemagne de 30% par rapport à l'incertitude supposée sur les inventaires utilisés comme connaissance a priori dans le cadre du formalisme Bayésien de l'inversion. En utilisant un réseau plus dense en Europe, constitué de 43 futurs sites, des réductions d'incertitude de 47% pourraient être réalisées pour les bilans annuels des émissions pour les régions où le réseau serait le plus dense.

Dans le Chapitre 4, j'ai implémenté un système d'inversion global isotopique permettant d'assimiler conjointement des données atmosphériques de CO_2 et de $^{14}CO_2$ pour résoudre simultanément les émissions fossiles et les flux naturels de CO_2 en Europe et en Chine. L'objectif est de dépasser l'hypothèse que les variations de $^{14}CO_2$ ne sont liées qu'au CO_2CF, en tenant compte ses flux de $^{14}CO_2$ non fossiles. Les résultats confirment que les données de $^{14}CO_2$ sont utiles pour séparer le CO_2CF du signal des flux naturels près des régions fortement émettrices, rendant les données de $^{14}CO_2$ moyennes sur 2 semaines plus efficaces que les données journalières de CO_2 pour l'estimation des émissions.

Université Paris-Saclay
Espace Technologique / Immeuble Discovery
Route de l'Orme aux Merisiers RD 128 / 91190 Saint-Aubin, France

Title : The potential of observations of radiocarbon in atmospheric CO_2 for the inversion of fossil fuel CO_2 emission at regional scale

Keywords : atmospheric inversion, fossil fuel emissions, radiocarbon, regional scale, continental observation networks

Abstract : Climate change has prompted nations, provinces, and cities to take actions to reduce anthropogenic sources of CO_2 and other greenhouse gases. Accurate and consistent quantification of the emissions is required for both scientists and policymakers. Inventories of the CO_2 emissions due to fossil fuel combustion are based on statistical data collected and reported by the emitters themselves and their quality is highly variable between countries. In principle, atmospheric measurements and inverse modeling could provide independent information to verify and evaluate these emissions. However, there are difficulties to separate the fossil fuel CO_2 signal ($FFCO_2$) from the signal of natural CO_2 fluxes, in the atmospheric CO_2 measurements from ground based continental networks. In this thesis, I aimed to improve the understanding of the potential of atmospheric $^{14}CO_2$ measurements, one of the few tracers helping to separate $FFCO_2$ from the signal of other CO_2 sources, for the objective estimate of the fossil fuel emissions at national or provincial scales based on atmospheric inversion.

I developed global inversion systems based on the global coarse-resolution (2.5 °×3.75 °) LMDZ atmospheric transport model, and on continental networks of atmospheric observations of CO_2 and $^{14}CO_2$, solving for the fossil fuel emissions at sub-continental / monthly scales in Europe and in China.

In Chapter 2, I defined and quantified critical sources of modeling errors and their impact on the inversion of large-scale budget of the fossil fuel emissions when using a global inversion system and assuming $FFCO_2$ data can be directly derived from $^{14}CO_2$ measurements. The analysis highlighted the impact of ignoring the spatial distribution of the emissions and $FFCO_2$ at a resolution higher than that of the transport model.

In Chapter 3, I applied inversions with the system, assumptions and diagnostics of the modeling error from Chapter 2 in a series of Observing System Simulation Experiments to evaluate the skill of such an inversion system and of different virtual observation networks for estimating regional budgets of fossil fuel emissions in Europe. Results indicate that if assimilating continuous 2-week mean $FFCO_2$ data from 17 existing $^{14}CO_2$ European sites, the inversion would reduce the uncertainties in monthly fossil fuel emissions of western Germany by 30% compared to the assumed uncertainty in the inventories used as a prior knowledge in the Bayesian framework of the inversion. Using a larger network of 43 European sites that may be available in the future, up to 47% uncertainty reduction could be achieved for annual budgets of fossil fuel emissions for regions where the network would be the densest.

In Chapter 4, I implemented a global isotopic inversion system that jointly assimilates atmospheric observations of CO_2 and $^{14}CO_2$ to simultaneously solve for fossil fuel emissions and natural CO_2 fluxes over Europe and China. The purpose is to move beyond the assumption that variations in $^{14}CO_2$ relate only to $FFCO_2$ by accounting for non-fossil $^{14}CO_2$ fluxes. The results confirm that $^{14}CO_2$ data are useful to separate $FFCO_2$ from the signal of natural fluxes at sites close to large emission regions, making 2-week mean $^{14}CO_2$ data more efficient than daily CO_2 data for estimating the emissions.

Université Paris-Saclay
Espace Technologique / Immeuble Discovery
Route de l'Orme aux Merisiers RD 128 / 91190 Saint-Aubin, France

Acknowledgement

The three-year PhD study is like an adventure. This adventure is not a relaxing trip with flowers and applause, but a road filled with difficulties and struggles. After obstacle and obstacle, the limits of the patience and motivation are always being challenged. Ultimately, perseverance brings its own reward when one became strong enough. Fortunately, in this great adventure I did not have to face this test alone. I would like to express my sincere gratitude to many people.

The first people to mention are my supervisor, Dr. Philippe Ciais. Philippe, thank you very much for your trust in my potential and giving me the opportunity to study at LSCE. I am really grateful for the inspiring discussions with you. Your curiosity and creativity enlighten me a lot. I always felt lucky to have you as my supervisor in the scientific research. I would also give my special appreciation to Dr. Grégoire Broquet. You are very supportive and encouraging. Some of the most challenging and stressful moments of my PhD were connected with conversations between the two of us. You have strict requirements and your guide and comments are invaluable for any young scientist.

I would also like to thank the rest of my thesis committee: John B. Miller, Heather Graven, Ingeborg Levin, Edouard Bard, Philippe Heinrich and Philippe Bousquet, for your insightful comments and all the questions that stimulate me to widen my sight from various perspectives.

Thanks to Shu Tao and Shilong Piao for their recommendations which gave me the opportunity to pursue my PhD at LSCE. Thanks to my Chinese friends in France, Xuhui Wang, Wei Li, Yi Yin, Shushi Peng, Tao Wang, Lin Wu, Ye Huang, Xin Lin, Jinfeng Chang, Chao Yue and Chunjing Qiu, for your help in my daily life and all the fun we have had in the past three years.

My sincere thanks also goes to Felix Vogel, Diego Santaren, Johannes Staufer, Victoria Naipal, Ana Bastos, Vladislav Bastrikov, Matthieu Guimberteau, Emilie Joetzjer and all the colleagues at LSCE. Working with you is full of hilarity and joys.

Last but not the least, I'd like to thank my family. My parents are always supportive whatever decision I have made. And thanks to my wife, Dan Zhu, for your company. We have the similar interests not only on science but also on life, making even the debate between us heartwarming.

Table of contents

Chapter 1 Introduction

1.1 The role of fossil fuel emissions in climate change

Global air and ocean temperature has increased substantially over the last 100 years (Intergovernmental Panel on Climate Change, IPCC, 2013). Anthropogenic greenhouse gas (GHGs) emissions of carbon dioxide (CO_2), methane (CH_4) and nitrous oxide (N_2O) are the dominant causes of the observed warming since the pre-industrial era. Among the well-mixed GHGs, CO_2 is the largest single contributor that perturbs the Earth's energy budget and drives the climate change (IPCC, 2013). Cumulative emissions of anthropogenic CO_2 to the atmosphere amounts to 580 ±70 Pg C (1 Pg C = 10^{15} g C) (Le Quéré et al., 2015) between 1750 and 2013. Less than half of the amount (250 ±5 Pg C) has accumulated in the atmosphere, leading to a rise of atmospheric concentrations from about 278 parts per million (ppm) (Etheridge et al., 1996) to approximately 400 ppm nowadays (Dlugokencky and Tans, 2016). The relationship between anthropogenic emissions and atmospheric concentrations is supported by: 1) a close correlation between the north-south gradient of atmospheric CO_2 and the difference in the consumption of fossil fuel between the hemispheres (Tans et al., 1989; Fan et al., 1998) and 2) the analogy between the changing rate of CO_2 emissions from fossil fuel burning and the rate of CO_2 increase in the atmosphere (IPCC, 2013), 3) a decreasing temporal trend in the atmospheric $^{13}C/^{12}C$ ratio of atmospheric CO_2 (Keeling et al., 2005; Ciais et al., 1995), 4) observed decrease of $^{14}C/^{12}C$ isotopic ratio of atmospheric CO_2 (Levin et al., 2010; Graven et al., 2012), 5) The observed changes in atmospheric O_2 content (Keeling, 1996).

Of the total anthropogenic carbon emitted to the atmosphere, the combustion of fossil fuel and the cement production have released 392 ± 30 Pg C from 1751 to 2013 (Boden et al., 2016). Emissions from fossil fuel burning and cement production have become the dominant source of anthropogenic emissions since 1920s and their relative share has increased progressively until present, contributing about 91% of the total anthropogenic emissions from 2004 to 2013 (Le Quéré et al., 2015). In 2013, the CO_2 emitted from fossil fuel combustion and cement production reached 9.9 ±0.5 Pg C (Le Quéré et al., 2015), and more than 50% of these emissions were from the world top three contributors: China (2.8 Pg

C), the US (1.4 Pg C) and the European Union (0.99 Pg C). The unambiguous and large contribution of the emission from fossil fuel and cement production to global climate change has prompted nations, provinces, states and cities to take actions to reduce fossil fuel emissions of CO_2 and other GHGs. In this study, for simplicity, I use the term "fossil fuel emissions" to refer to the anthropogenic CO_2 emissions from the combustion of fossil fuels (coal, gas, oil and gas flaring) and from the cement production.

1.2 Current inventories of fossil fuel emissions and uncertainties

Datasets of fossil fuel CO_2 emissions with comprehensive global coverage are available at two different scales: national annual total and spatially/temporally distributed maps at high resolution. The United Nations Framework Convention on Climate Change (UNFCCC) maintains a database of national GHG emissions for the negotiations of international treaties, based on self-reports from its signatory countries. Its member states are classified as Annex I countries (43 in total in October 2016) or non-Annex I countries (154 in total in October 2016), which have different requirements for the report of national inventories. The group of Annex I countries, which include most industrial countries, are required to submit detailed inventories every year. The non-Annex I countries submit their national inventories as part of their National Communications with less frequency. For example, the latest national communication of China is for 2005 (NDRC, 2012). There are other four institutions that compile and publish national annual fossil fuel emissions across the world on a regular basis: 1) the International Energy Agency (IEA) provides the estimates of fossil fuel emissions across different sectors using the energy databases compiled by IEA and the United Nations Statistics Office (UNSO), and using the default methods and emission factors from the 2006 IPCC Guidelines for National Greenhouse Gas Inventories (IEA, 2015; IPCC, 2006); 2) the United States Energy Information Administration (EIA) relies primarily on EIA-collected national statistical reports and emission factors related to the energy content of different fuel types (coal petroleum, natural gas) (EIA, 2016); 3) The Carbon Dioxide Analysis Information Center (CDIAC) derives fossil fuel emission estimates (Boden et al., 2016) primarily from energy statistics published by UNSO (UN, 2016) and mass-dependent emission factors (Marland and Rotty, 1984); 4) A joint project of the European Commission Joint Research Centre (JRC) and the Netherlands Environmental Assessment Agency (PBL) publishes sectoral emissions of many species including CO_2 from fossil fuel based on the

IEA energy statistics and default IPCC emission factors (Olivier et al., 2015). An additional energy consumption dataset from the British Petroleum, which produces data much more rapidly than the other organizations, has also been used to estimate more recent global fossil fuel emissions (Le Quéré et al., 2015).

These compilations are all based on estimations of the amount of fuel consumption, the average carbon content of each fuel type, and the fraction of the fuel that ends up in actual oxidation. However, despite the apparent similarities in the data used by the reporting organizations, significant discrepancies exist between products. Sources of discrepancies include different data inputs, distinct system boundaries (i.e. emission activities that are included), different accounting method (e.g. top-down determined apparent consumption method by CDIAC (Andres et al., 2012) and sectoral approach by other institutions), categorizing fuels or emission sources differently, and utilizing different emission factors. Table 1 summarizes some of the main aspects that are different among the six inventories.

Table 1 Comparisons of six fossil fuel emission inventories

	UNFCCC[a]	IEA (2015)	EIA (2016)	CDIAC (Boden et al., 2016)	EDGAR (Olivier et al., 2015)	BP (BP, 2016)
Primary source of energy data	national statistics	IEA and UNSO	EIA	UNSO	IEA and UNSO	BP
Emission factors	IPCC and country-specific	IPCC	EIA	US-based	IPCC	Unknown
Countries included[b]	191	137+3 other	224	224	214	67+5 other
Bunker fuels	Yes	Yes	Yes	Yes	Yes	Yes
Gas flaring	Yes	No	Yes	Yes	Yes	No
cement production	Yes	No	No	Yes	Yes	No
Non-fuel uses	Yes	No	Yes	Yes	Yes	No

[a] available at http://unfccc.int/di/DetailedByParty.do

[b] IEA: 68 countries have been summed in 3 groups of ‘other countries’

The second representation of global fossil fuel emission datasets is in a geographically and temporally distributed manner, is motivated mainly by the scientific communities.

Details of fossil fuel emissions are required to understand their socio-economic and climatic drivers. Studies on carbon cycle also requires more finely resolved fossil fuel emissions to improve the diagnostic of regional carbon budgets. The policymaking community is also increasingly recognizing the need for accurate and highly resolved fossil fuel emissions in the context of emerging requirements for carbon trading systems and the implementation of emission reduction commitments (Pacala et al., 2010).

The Vulcan inventory (Gurney et al., 2009), which is built from highly detailed bottom-up data on fuel consumptions, contains fossil fuel emission estimates for both point and nonpoint sources in the US at a spatial scale of less than 100 km^2. But the activity data are often not available at local scale for all the countries, alternative proxies like population density or traffic intensity are used to downscale the national emission to smaller scales. The CDIAC product distributes its national annual fossil fuel emission into 1 °×1 ° grid cells according to population density in 1984 (Andres et al., 2016). The Open source Data Inventory of Anthropogenic CO_2 emission (ODIAC, Oda and Maksyutov, 2011) disaggregates national emissions by combing satellite observations of the global nightlight distribution and the locations of the world's power plants (Carbon Monitoring and Action, http://carma.org) on a 1 km ×1km grid. Wang et al. (2013) established a global 0.1 °×0.1 °map of fuel combustion and corresponding CO_2 emissions (PKU-CO_2) based on disaggregation of available national and sub-national data, the latter in some countries like China and India. EDGAR (Olivier et al., 2015) provides sectoral annual fossil fuel emission maps on a 0.1 °×0.1 ° grid, based on more than 40 different geographic datasets including urban and rural population density, sectoral energy consumption map, power plant locations, road density etc. In addition, Rayner et al. (2010) developed a data assimilation approach (called FFDAS) based on the distributions of nightlights, populations and economic indexes and established a global emission map at 0.25 ° resolution. Efforts on the temporal profile of fossil fuel emissions are less common than those for spatial allocation of fossil fuel emissions. Andres et al. (2011) constructed fossil fuel emissions at monthly time scale using monthly energy data (available for 21 countries) and proxy assignments (for remaining countries). EDGARv3.2 provided sectoral time profiles (EDGAR/PBL, 2010), which was tuned and used to derive the CO_2 release and Oxygen uptake from Fossil Fuel Emission Estimate (COFFEE) dataset (Steinbach et al., 2011). Gurney et al. (2009) and Pregger et al. (2007) incorporate data streams of varying temporal profiles for different sectors and provide down

to hourly products of fossil fuel emissions for the US and Europe, respectively.

Table 2 summarize the main products of global/regional gridded fossil fuel emissions. Apart from these products, other datasets, such as HTAP_V2 dataset (http://edgar.jrc.ec.europa.eu/htap_v2/index.php), TNO-MACC-II dataset (Kuenen et al., 2014), EMEP dataset (Vestreng et al., 2007) etc., though mainly focus on the air pollutants, also give useful insights on the spatial/temporal distribution of the energy use. But little effort has been done to combine the spatial/temporal distribution of the air pollutant to indicate the CO_2 emissions from fossil fuel.

Table 2 Comparison of products of gridded fossil fuel CO_2 emission maps

Products	**Spatial resolution**	**Spatial allocation method**	**Temporal resolution**	**Species**	**References**
Global products					
EDGAR(V4.2)	0.1 °	based on sectoral proxy data	annual mean	CO_2, CO, NOx…	Olivier et al., 2015
PKU-CO_2	0.1 °	based on national/sub-national fuel data and point sources	annual mean	CO_2	Wang et al. ACP 2013
ODIAC	1 km	based on nightlight distribution and point sources	annual mean	CO_2	Oda and Maksyutov, 2011
FFDAS	0.25 °and 0.1 °	data assimilation	annual mean	CO_2	Rayner et al., 2010 Asefi-Najafabady et al., 2014
CDIAC	0.1 °	based on population density	monthly mean	CO_2	Boden et al., 2016;
COFFEE	1 °	EDGARv3.2	hourly	CO_2, and oxidative ratio (O_2)	Steinbach et al., 2011
IER-CARBONES	1 °	EDGARv4.2	hourly	CO_2	
regional products					
MEIC (China)	0.25 °	based on sectoral proxy data	monthly mean	CO_2, CO, NOx …	http://www.meicmodel.org/
Vulcan (US)	10 km	bottom up accounting	hourly	CO_2	Gurney et al., 2009
IER-CarboEurope (Europe)	5 km	based on sectoral proxy data	hourly	CO_2	Pregger et al. 2007

The uncertainty associated with the estimate of fossil fuel emissions are subject to 1) the national inventories and 2) the spatial/temporal distribution of the emissions. It is estimated that uncertainties in the emissions of developed countries are on the order ±5%

(Andres et al., 1996; Marland, 2008; Rypdal and Winiwarter, 2001). In contrast, uncertainties in the emissions of developing countries with "less well-developed energy data system" (IPCC, 2006) are considered to be significantly higher. For example, Gregg et al. (2008) found that the energy data of China could vary by 23% between revisions. And a recent analysis of Chinese annual emissions found the coal carbon content in Chinese coal are on average 40% lower than the default values of IPCC (Liu et al., 2015), reducing the Chinese annual emissions by 14% compared to EDGAR estimates. The uncertainties in spatial/temporal distribution of the fossil fuel emissions are mainly associated with the spatial/temporal allocation methods. For example, the population density is a first-order approximation to downscale national fossil fuel emissions, but does not capture high-spatial resolution patterns and large point sources (Rayner et al., 2010; Wang et al. 2013). Usually, uncertainties are not reported on the distribution of fossil fuel emissions. In this context, comparison between different emission products can give useful insights, even though the underlying data are usually not fully independent. Ciais et al. (2010) found that at 50km resolution, for example, the difference between two emission maps is estimated to be about 50% of the mean. A comparison (Andres et al., 2012) between the spatial distributions of EDGARv4 and the IER-CarbonEurope (aggregated at annual scale) emission maps shows that relative differences are largest for the highest fossil fuel emissions at fine resolution (1/12 degree), while the relative differences of small fossil fuel emissions are insensitive to spatial resolution.

1.3 Need for independent quantifications of fossil fuel emissions

1.3.1 Verifying national commitments of emission reductions

In line with the Conference of the Parties at Paris, 162 countries and regions have submitted their Intended Nationally Determined Contributions (INDC, available at http://www4.unfccc.int/submissions/indc/Submission%20Pages/submissions.aspx) to the UNFCCC. For example, China committed to achieving the peaking of CO_2 emissions around or before 2030. The European Council also claimed their objective of reducing greenhouse gas emissions by at least 40% by 2030 compared to 1990. However, national inventory reporting has a number of limitations. These include but are not limited to: 1) various inventory methods adopted by different countries, 2) the poor accounting of emissions in

developing countries, 3) uncertainties in reported data, 4) the time lag between the occurrence of the emissions and the report of the inventories. These limitations make the international review of national reports hard to fully harmonize all the inventories and to assess them on an equal basis. For example, Elzen et al. (2013) showed that the accounting method of self-reported fossil fuel emissions would influence the final inventories and lead to distinct conclusions regarding the national responsibilities. In this context, an independent way of quantifying emission changes for all countries based on internationally accepted data (e.g., surface monitoring network, satellite data, etc.) would create a basis for verifying the national commitments of emission reductions.

1.3.2 Improving the understanding of carbon exchanges between atmosphere and terrestrial and ocean surface

The emission of fossil fuel CO_2 is a key component of carbon cycle. An important effort in carbon cycle research is to quantify the spatial and temporal characteristics of sources and sinks of CO_2 to the Earth's atmosphere, and how they will respond to climate change and evolve in the future. Because CO_2 sources and sinks can hardly be directly observed all over the world, a powerful approach is to infer these fluxes from measurements of atmospheric CO_2 mole fractions, using inverse modeling techniques (or atmospheric inversion). The atmospheric inversion makes use of the fact that the variations of the fluxes are reflected in the variations atmosphere concentrations. The atmospheric inversion is based on Bayesian theorem, incorporating: i) a prior knowledge about the fluxes, ii) a set of atmospheric observations, iii) physical understanding to relate these observations to the prior knowledge (include but is not limited to atmospheric transport models), and iv and v) the uncertainties in the prior knowledge and in the observations.

In the conventional inversion framework, it is commonly assumed that the uncertainty of fossil fuel emissions is negligible compared to the uncertainty of the oceanic and biospheric fluxes, and the intra-annual variations of fossil fuel emissions are neglected in view of the large climatically-driven variations of the biosphere exchanges so that the natural fluxes are adjusted to match the observed atmospheric CO_2 gradients, while the fossil fuel fluxes are prescribed as a fixed boundary condition of the inversion. These assumptions, however, are not valid given the large uncertainties in the fossil fuel emissions mentioned

above. In a global inverse modelling framework with coarse regions, Gurney et al. (2005) showed that the neglect of temporal variations in fossil fuel emissions resulted in monthly biases of regional land fluxes up to 50% during certain times of the year. Peylin et al. (2011) showed that when using different fossil fuel emissions in the inversion system, the differences in the inverted annual biospheric fluxes over Europe are comparable to the differences in annual fossil fuel emissions and are around 30% of the annual mean European ecosystem carbon sink. These biases could be even larger at finer scales (Peylin et al., 2011; Wang et al., 2013). All these results pointed out a high demand to improve the estimate of spatially and temporally resolved fossil fuel emissions at the scale of grid cells of transport models, which goes from several degrees in global studies to a few kilometers in regional studies.

1.4 Current attempts in estimating of fossil fuel emissions from atmospheric measurements

Despite the important role of fossil fuel emissions in the international climate negotiations and in diagnostics of the carbon cycle, current efforts have had little success constraining CO_2 emissions from fossil fuel emissions by using atmospheric measurements and inversion models at annual and national scales (Pacala et al., 2010; Miller and Michalak, 2016). The potential of existing and upcoming surface or space-based observations for constraining anthropogenic emissions is not yet fully quantified.

Some studies have reported detectable total column CO_2 enhancements at the level of several ppms over highly industrialized regions (Schneising et al., 2013; Kort et al., 2012). However, the utility of current satellite-based CO_2 observations is limited by measurement noise, measurement biases, the spatial and temporal sparsity of observations, and the limited sensitivity of observations to CO_2 changes in the near-surface atmosphere related to surface fluxes. In addition, the signals of $FFCO_2$ in total column CO_2 could be obscured by the variations in the signals of natural fluxes during growing seasons (Keppel-Aleks et al. 2013). Remote sensing observations may therefore have limitations in their ability to constrain fossil fuel emissions budgets at national / regional scale and at temporal scales useful for informing policy decisions (e.g. annual budgets). The surface observation networks could identify anthropogenic emissions in some areas of the North America during a few months of the year (Shiga et al., 2014). But similar to the space-based observations, this

identification is hampered by biospheric CO_2 fluxes, by atmospheric transport errors, and by the sparsity or quality of the CO_2 observations.

In the case of distinguishing $FFCO_2$ from the signal of biogenic CO_2, radiocarbon (^{14}C) measurements provide additional information because, contrary to biogenic/oceanic CO_2, CO_2 emitted from fossil fuel combustion contain no ^{14}C due to the age of these carbon deposits being many orders of magnitude larger than the decay lifetime of ^{14}C (~5730 y). Measurements of radiocarbon in CO_2 together with measurements of total CO_2 have been used to interpret the fossil fuel emissions over local scales (Levin et al., 2003; Levin et al., 2011; Turnbull et al., 2014). However, these measurements have not been incorporated in any inversion system to constrain fossil fuel emissions over larger domain, due to the high cost and paucity of the $^{14}CO_2$ measurements. In 2010, the National Research Council (Pacala et al., 2010) has recommended that the US invest $5–10 million annually for 10,000 radiocarbon measurements. And as part of the Integrated Carbon Observing System (ICOS) project, a continental scale network of standardized, long-term and high precision atmospheric measurements of total CO2 and $^{14}CO_2$ is also being set up in Europe. The ICOS network is expected to sample 2-week integrated $^{14}CO_2$ at about 40 ICOS stations (in total 1,000 analyses per year; ICOS Stakeholder handbook 2013 at http://www.icos-uk.org/uk-icos/sites/uk-icos/files/documents/Stakeholders%20Handbook%202013.pdf), with the aim of determining the signal of $FFCO_2$ and detecting fossil fuel emissions changes. With these expectations of the expanding networks, some recent theoretical studies (Pacala et al., 2010; Basu et al., 2016) have showed optimistic perspectives to use the atmospheric $^{14}CO_2$ observations to improve our knowledge of fossil fuel emissions.

1.5 Objectives and structure of this thesis

This PhD thesis will explore the possibilities of using atmospheric observations to infer the monthly fossil fuel emissions at scales of regions. A region here is defined as the typical area of a medium-sized country in Europe. The following questions are addressed in this PhD thesis: What is the spatiotemporal distribution of atmospheric CO_2 emitted from fossil fuel combustion? How can we use those signals to constrain fossil fuel emissions from the atmospheric concentrations? Is it possible to separate $FFCO_2$ from the signal of the natural fluxes using atmospheric $^{14}CO_2$ measurements?

In Chapter 2, I set up a global atmospheric inversion system based on the coarse-resolution LMDZv4 atmospheric transport model, and on ground-based network of continental stations, solving for the monthly fossil fuel emissions at regional scales. In this chapter, the simplification is made that ^{14}C in CO_2 measures only pure $FFCO_2$. I characterize the critical sources of errors in such a global inversion system. These errors arise from the mismatch between the resolution of the transport model and the spatial variability of the actual fluxes and concentrations, and from the mismatch between the resolution of the inverse modelling and that of the transport model. These errors are quantified and compared to the atmospheric signature of the uncertainties in the monthly budgets of the emissions, highlighting their impacts on the inversion results.

In Chapter 3, I test the potential of the inversion system from Chapter 2 and of 2-week mean $FFCO_2$ observations from the network of existing 17 radiocarbon stations of to quantify the fossil fuel emissions over Europe at annual and regional scales. The potential of expanding networks of $FFCO_2$ atmospheric measurement sites are also explored.

In Chapter 4, a global isotopic inversion system is set up to jointly assimilate atmospheric CO_2 and $^{14}CO_2$ observations to move beyond the approximation made in Chapter 3 that variations in atmospheric $^{14}CO_2$ are only related to fossil fuel emissions. The potential of radiocarbon measurements in separating the signal of biogenic CO_2 and $FFCO_2$, in quantifying fossil fuel emissions and in improving estimates of biogenic fluxes are investigated over Europe and China.

References

Andres, R. J., Boden, T. A., Bréon, F. M., Ciais, P., Davis, S., Erickson, D., Gregg, J. S., Jacobson, A., Marland, G., Miller, J., Oda, T., Olivier, J. G. J., Raupach, M. R., Rayner, P. and Treanton, K.: A synthesis of carbon dioxide emissions from fossil-fuel combustion, Biogeosciences, 9(5), 1845–1871, 2012.

Andres, R. J., Gregg, J. S., Losey, L., Marland, G. and Boden, T. A.: Monthly, global emissions of carbon dioxide from fossil fuel consumption, Tellus B, 63(3), 309–327, 2011.

Andres, R. J., Marland, G., Fung, I. and Matthews, E.: A 1 °×1 °distribution of carbon dioxide emissions from fossil fuel consumption and cement manufacture, 1950–1990, Global Biogeochemical Cycles, 10(3), 419–429, 1996.

Asefi-Najafabady, S., Rayner, P. J., Gurney, K. R., McRobert, A., Song, Y., Coltin, K., Huang, J., Elvidge, C. and Baugh, K.: A multiyear, global gridded fossil fuel CO_2 emission data product: Evaluation and analysis of results, Journal of Geophysical Research, 2014.

Basu, S., Miller, J. B. and Lehman, S.: Separation of biospheric and fossil fuel fluxes of CO_2 by atmospheric inversion of CO_2 and $^{14}CO_2$ measurements: Observation System Simulations, Atmospheric Chemistry and Physics, 16(9), 5665–5683, 2016.

Boden, T. A., Marland, G. and Andres, R. J.: Global, Regional, and National Fossil-Fuel CO_2 Emissions, [online] Available from: https://doi.org/10.3334/CDIAC/00001_V2016 (Accessed 2 October 2016), 2016.

BP: BP statistical review of world energy, London: British Petroleum., 2016.

Ciais, P., Paris, J. D., Marland, G., Peylin, P., Piao, S. L., Levin, I., Pregger, T., Scholz, Y., Friedrich, R., Rivier, L., Houwelling, S. and Schulze, E. D.: The European carbon balance. Part 1: fossil fuel emissions, Global Change Biology, 16(5), 1395–1408, 2010.

Ciais, P., Tans, P., Trolier, M., White, J. W. and Francey, R.: A large Northern Hemisphere terrestrial CO2 sink indicated by the $^{13}C/^{12}C$ ratio of atmospheric CO_2, Science, (269), 1098–102, 1995.

Dlugokencky, E. and Tans, P.: ESRL Global Monitoring Division - Global Greenhouse Gas Reference Network, [online] Available from: http://www.esrl.noaa.gov/gmd/ccgg/trends/global.html#global (Accessed 2 August 2016), 2016.

EDGAR/PBL: Temporal variation of anthropogenic sources, http://themasites.pbl.nl/en/themasites/edgar/documentation/ content/Temporal-variation.html, European Commission, Joint Research Centre (JRC)/Netherlands Environmental Assessment Agency (PBL), (Accessed 2 August 2016), 2010.

EIA, U.: Annual energy outlook 2016, US Energy Information Administration, Washington, DC [online] Available from: http://petrofed.winwinhosting.net/newsletter/WR-305_18Apr13/w305_01.pdf (Accessed 3 October 2016), 2016.

Elzen, M. G. J. den, Olivier, J. G. J., Höhne, N. and Janssens-Maenhout, G.: Countries' contributions to climate change: effect of accounting for all greenhouse gases, recent trends, basic needs and technological progress, Climatic Change, 121(2), 397–412, 2013.

Etheridge, D. M., Steele, L. P., Langenfelds, R. L., Francey, R. J., Barnola, J.-M. and Morgan, V. I.: Natural and anthropogenic changes in atmospheric CO_2 over the last 1000 years from air in Antarctic ice and firn, Journal of Geophysical Research, 101(D2), 4115–4128, 1996.

Fan, S., Gloor, M., Mahlman, J., Pacala, S., Sarmiento, J., Takahashi, T. and Tans, P.: A large terrestrial carbon sink in North America implied by atmospheric and oceanic carbon dioxide data and models, Science, 282(5388), 442–446, 1998.

Graven, H. D., Guilderson, T. P. and Keeling, R. F.: Observations of radiocarbon in CO_2 at seven global sampling sites in the Scripps flask network: Analysis of spatial gradients and seasonal cycles, Journal of Geophysical Research, 117(D2), 2012.

Gregg, J. S., Andres, R. J. and Marland, G.: China: Emissions pattern of the world leader in CO_2 emissions from fossil fuel consumption and cement production, Geophysical Research Letters, 35(8), 2008.

Gurney, K. R., Chen, Y.-H., Maki, T., Kawa, S. R., Andrews, A. and Zhu, Z.: Sensitivity of atmospheric CO_2 inversions to seasonal and interannual variations in fossil fuel emissions, Journal of Geophysical Research, 110(D10), 2005.

Gurney, K. R., Mendoza, D. L., Zhou, Y., Fischer, M. L., Miller, C. C., Geethakumar, S. and Can, S. de la R. du: High Resolution Fossil Fuel Combustion CO_2 Emission Fluxes for the United States,

Environmental Science & Technology, 43(14), 5535–5541, 2009.
IEA: CO2 emissions from fuel combustion-highlights, 2015ed, IEA, Paris. [online] Available from: http://www. iea. org/(Accessed 10 September 2016), 2015.
IPCC: 2006 IPCC Guidelines for National Greenhouse Gas Inventories, Intergovernmental Panel on Climate Change., 2006.
IPCC: IPCC, 2013: climate change 2013: the physical science basis. Contribution of working group I to the fifth assessment report of the intergovernmental panel on climate change, 2013.
Keeling, C. D., Piper, S. C., Bacastow, R. B., Wahlen, M., Whorf, T. P., Heimann, M. and Meijer, H. A.: Atmospheric CO2 and $^{13}CO_2$ exchange with the terrestrial biosphere and oceans from 1978 to 2000: observations and carbon cycle implications, in A history of atmospheric CO_2 and its effects on plants, animals, and ecosystems, pp. 83–113, Springer., 2005.
Keeling, R. F., Piper, S. C. and Heimann, M.: Global and hemispheric CO_2 sinks deduced from changes in atmospheric O_2 concentration, Nature, 381(6579), 218–221, 1996.
Keppel-Aleks, G., Wennberg, P. O., O'Dell, C. W. and Wunch, D.: Towards constraints on fossil fuel emissions from total column carbon dioxide, Atmospheric Chemistry and Physics, 13(8), 4349–4357, 2013.
Kort, E. A., Frankenberg, C., Miller, C. E. and Oda, T.: Space-based observations of megacity carbon dioxide, Geophysical Research Letters, 39(17), 2012.
Kuenen, J. J. P., Visschedijk, A. J. H., Jozwicka, M. and Denier van der Gon, H. A. C.: TNO-MACC_II emission inventory; a multi-year (2003–2009) consistent high-resolution European emission inventory for air quality modelling, Atmospheric Chemistry and Physics, 14(20), 10963–10976, 2014.
Le Quéré, C., Moriarty, R., Andrew, R. M., Peters, G. P., Ciais, P., Friedlingstein, P., Jones, S. D., Sitch, S., Tans, P., Arneth, A. and others: Global carbon budget 2014, Earth System Science Data, 7(1), 47–85, 2015.
Levin, I., Hammer, S., Eichelmann, E. and Vogel, F. R.: Verification of greenhouse gas emission reductions: the prospect of atmospheric monitoring in polluted areas, Philosophical transactions. Series A, Mathematical, physical, and engineering sciences, 369(1943), 1906–24, 2011.
Levin, I., Kromer, B., Schmidt, M. and Sartorius, H.: A novel approach for independent budgeting of fossil fuel CO2 over Europe by 14CO2 observations, Geophysical Research Letters, 30(23), 2003.
Levin, I., Naegler, T., Kromer, B., Diehl, M., Francey, R. J., Gomez-Pelaez, A. J., Steele, L. P., Wagenbach, D., Weller, R. and Worthy, D. E.: Observations and modelling of the global distribution and long-term trend of atmospheric $^{14}CO_2$, Tellus B, 62(1), 26–46, 2010.
Liu, Z., Guan, D., Wei, W., Davis, S. J., Ciais, P., Bai, J., Peng, S., Zhang, Q., Hubacek, K., Marland, G., Andres, R. J., Crawford-Brown, D., Lin, J., Zhao, H., Hong, C., Boden, T. A., Feng, K., Peters, G. P., Xi, F., Liu, J., Li, Y., Zhao, Y., Zeng, N. and He, K.: Reduced carbon emission estimates from fossil fuel combustion and cement production in China, Nature, 524(7565), 335–338, 2015.
Marland, G.: Uncertainties in Accounting for CO2From Fossil Fuels, Journal of Industrial Ecology, 12(2), 136–139, 2008.
Miller, S. M. and Michalak, A. M.: Constraining sector-specific CO_2 and CH_4 emissions in the United States, Atmospheric Chemistry and Physics Discussions, 1–33, 2016.
National Development and Reform Commission: Second National Communication on Climate Change of the People's Republic of China, Beijing., 2012.
Oda, T. and Maksyutov, S.: A very high-resolution (1 km ×1 km) global fossil fuel CO_2 emission inventory derived using a point source database and satellite observations of nighttime lights, Atmospheric Chemistry and Physics, 11(2), 543–556, 2011.
Olivier, J. G., Janssens-Maenhout, G., Muntean, M. and Peters, J. A. H. W.: Trends in global CO_2 emissions: 2015 Report, PBL Netherlands Environmental Assessment Agency Hague., 2015.
Pacala, S. W., Breidenich, C., Brewer, P. G., Fung, I. Y., Gunson, M. R., Heddle, G., Law, B. E., Marland, G., Paustian, K., Prather, M. and others: Verifying greenhouse gas emissions: methods to support international climate agreements., 2010.
Peylin, P., Houweling, S., Krol, M. C., Karstens, U., Rödenbeck, C., Geels, C., Vermeulen, A., Badawy, B., Aulagnier, C., Pregger, T., Delage, F., Pieterse, G., Ciais, P. and Heimann, M.: Importance of fossil fuel emission uncertainties over Europe for CO_2 modeling: model intercomparison, Atmospheric Chemistry and Physics, 11(13), 6607–6622, 2011.
Pregger, T., Scholz, Y. and Friedrich, R.: Documentation of the anthropogenic GHG emission data for

Europe provided in the Frame of CarboEurope GHG and CarboEurope IP, Institut für Energiewirtschaft und Rationelle Energieanwendung, Universität Stuttgart, Stuttgart, Germany, 2007.

Rayner, P. J., Raupach, M. R., Paget, M., Peylin, P. and Koffi, E.: A new global gridded data set of CO_2 emissions from fossil fuel combustion: Methodology and evaluation, Journal of Geophysical Research, 115, 2010.

Rypdal, K. and Winiwarter, W.: Uncertainties in greenhouse gas emission inventories—evaluation, comparability and implications, Environmental Science & Policy, 4(2), 107–116, 2001.

Schneising, O., Heymann, J., Buchwitz, M., Reuter, M., Bovensmann, H. and Burrows, J. P.: Anthropogenic carbon dioxide source areas observed from space: assessment of regional enhancements and trends, Atmospheric Chemistry and Physics, 13(5), 2445–2454, 2013.

Shiga, Y. P., Michalak, A. M., Gourdji, S. M., Mueller, K. L. and Yadav, V.: Detecting fossil fuel emissions patterns from subcontinental regions using North American in situ CO2measurements, Geophysical Research Letters, 41(12), 4381–4388, 2014.

Steinbach, J., Gerbig, C., Rödenbeck, C., Karstens, U., Minejima, C. and Mukai, H.: The CO_2 release and Oxygen uptake from Fossil Fuel Emission Estimate (COFFEE) dataset: effects from varying oxidative ratios, Atmospheric Chemistry and Physics, 11(14), 6855–6870, 2011.

Turnbull, J. C., Keller, E. D., Baisden, T., Brailsford, G., Bromley, T., Norris, M. and Zondervan, A.: Atmospheric measurement of point source fossil CO_2 emissions, Atmospheric Chemistry and Physics, 14(10), 5001–5014, 2014.

United Nations: 2013 Energy Statistics Yearbook, United Nations Department for Economic and Social Information and Policy Analysis, Statistics Division, New York., 2016.

Vestreng, V., Myhre, G., Fagerli, H., Reis, S. and Tarrasón, L.: Twenty-five years of continuous sulphur dioxide emission reduction in Europe, Atmospheric Chemistry and Physics, 7(13), 3663–3681, 2007.

Wang, R., Tao, S., Ciais, P., Shen, H. Z., Huang, Y., Chen, H., Shen, G. F., Wang, B., Li, W., Zhang, Y. Y., Lu, Y., Zhu, D., Chen, Y. C., Liu, X. P., Wang, W. T., Wang, X. L., Liu, W. X., Li, B. G. and Piao, S. L.: High-resolution mapping of combustion processes and implications for CO_2 emissions, Atmospheric Chemistry and Physics, 13(10), 5189–5203, 2013.

Chapter 2 Estimation of observation errors for large scale atmospheric inversion of CO_2 emissions from fossil fuel combustion

Summary

Continental ^{14}C measurements networks together with atmospheric CO2 measurements have been proposed as a future tool to provide an independent verification of fossil fuel emission budgets aggregated over large spatial scales by using atmospheric inversion approach. In a large-scale inversion system which is built on a global transport model of relatively coarse grid, the distribution of the actual emissions and concentrations have much finer patterns than the grid size of the transport model, raising so-called *representation errors*. When the inversion system solves for regional and monthly budgets of the emissions but not for the spatio-temporal distributions within the region-months, the mismatch between the relatively coarse resolution of the regions where emissions are optimized by the inversion and that of the transport model raise an issue of the so-called *aggregation errors*. These errors have specific features that are different from those in conventional inversions targeting at natural fluxes. These critical sources of errors could largely limit the skill of an inversion system but are rarely properly accounted for in previous inversion studies targeted at fossil fuel emissions.

This chapter first describes an atmospheric inversion framework dedicated to the inference of regional monthly emissions over Europe based on the LMDZv4 (2.5 °× 3.75 °) transport model and continental scale networks of measurement stations. Special attention is paid to address the derivation and analysis of the statistics of *representation* and *aggregation* errors in this inversion framework, along with the typical precision of $^{14}CO_2$-derived $FFCO_2$ signatures (i.e. the *measurement error*) and the errors in the modelling of atmospheric transport (i.e. the *transport error*). In an inversion system, all these errors are grouped under the generic term *observation errors*. In this chapter, observation errors are compared to the typical signals of $FFCO_2$ reflecting large-scale atmospheric gradients, and to the errors in

simulated $FFCO_2$ due to the uncertainties in emission maps used as the prior knowledge in the inversion. It is shown that the observation errors can reach up to about 50% of the typical signals, and that the representation and measurement errors are the dominant sources of the observation errors. The analysis highlights the fact that the representation and aggregation errors have large temporal auto-correlation scales, making it difficult to separate these errors from the signature of the prior uncertainty in the emissions at large scale when assimilating 1-day to 1-month integrated atmospheric $FFCO_2$ observations. Accounting for these temporal auto-correlations is important to make a realistic assessment of the skill of such inversion systems, but this was seldom done in previous studies of the potential of ^{14}C networks to constrain fossil emissions. On the other hand, the representation and aggregation errors have small spatial correlation scales, highlighting the need for dense networks to improve the estimate of $FFCO_2$ emissions at large scale.

The statistics of the representation and aggregation errors derived in this chapter is primarily related to the specific atmospheric inversion framework we use through this thesis. But this study brings new insights regarding these errors to the inversion of the $FFCO_2$ emissions. The structure and typical amplitude of the representation error derived for the transport of uncertainties in the fossil fuel emissions in Europe at ~3 ° resolution should be similar for other transport models with similar spatial resolution. The practical derivation of their statistics can also be easily generalized and used for other studies.

This chapter has been submitted to the peer-reviewed journal *Tellus B*.

Estimation of observation errors for large scale atmospheric inversion of CO_2 emissions from fossil fuel combustion

By Yilong Wang[1*], Grégoire Broquet[1], Philippe Ciais[1], Frédéric Chevallier[1], Felix Vogel[1], Nikolay Kadygrov[1], Lin Wu[1], Yi Yin[1], Rong Wang[1], Shu Tao[2]

[1]Laboratoire des Sciences du Climat et de l'Environnement, CEA-CNRS-UVSQ- Université Paris Saclay, 91191, Gif-sur-Yvette CEDEX, France

[2]Laboratory for Earth Surface Processes, College of Urban and Environmental Sciences, Peking University, Beijing 100871, China

Running head: observation errors for $FFCO_2$ atmospheric inversion

Submitted to Tellus B

April 19, 2016

*Corresponding author.
e-mail: yilong.wang@lsce.ipsl.fr

ABSTRACT

National annual inventories of CO_2 emitted during fossil fuel consumption ($FFCO_2$) bear 5%-10% uncertainties for developed countries, and are likely higher at intra annual scales or for developing countries. Given the current international efforts of mitigating actions, there is a need for independent verifications of these inventories. Atmospheric inversion assimilating atmospheric gradients of CO_2 and radiocarbon measurements could provide an independent way of monitoring $FFCO_2$ emissions. A strategy would be to deploy such measurements over continental scale networks and to conduct continental to global scale atmospheric inversions targeting the national and 1-month scale budgets of the emissions. Uncertainties in the high resolution distribution of the emissions could limit the skill for such a large scale inversion framework. This study is dedicated to the derivation, typical quantification and analysis of critical sources of errors that affect the inversion of $FFCO_2$ emissions when solving for them at a relatively coarse resolution with a coarse grid transport model. These errors include those due to the mismatch between the resolution of the transport model and the spatial variability of the actual fluxes and concentrations (i.e. the *representation errors*) and those due to the mismatch between the resolution of the inverse modelling and that of the transport model (i.e. the *aggregation errors*). We propose a practical method to quantify these sources of errors, and compare them with the precision of $FFCO_2$ measurements (i.e. the *measurement errors*) and the errors in the modelling of atmospheric transport (i.e. the *transport errors*). The results show that both the representation and measurement errors can be much larger than the aggregation errors. The magnitude of representation and aggregation errors is sensitive to sampling heights and temporal sampling integration time. The combination of these errors can reach up to about 50% of the typical signals, i.e. the atmospheric large-scale mean afternoon $FFCO_2$ gradients between sites being assimilated by the inversion system. These errors have large temporal auto-correlation scales, but short spatial correlation scales. This indicates the need for accounting for these temporal auto-correlations in the atmospheric inversions and the need for dense networks to limit the impact of these errors on the inversion of $FFCO_2$ emissions at large scale. More generally, comparisons of the representation and aggregation errors to the errors in simulated $FFCO_2$ gradients due to uncertainties in current inventories suggest that the potential of inversions using global coarse-resolution models (with typical horizontal resolution of a

couple of degrees) to retrieve $FFCO_2$ emissions at sub-continental scale could be limited, and that meso-scale models with smaller representation errors would effectively increase the potential of inversions to constrain $FFCO_2$ emission estimates.

Key words: fossil fuel, radiocarbon, global atmospheric inversion, observation error, Europe

1. Introduction

Emissions from combustion of fossil fuels is the primary driver of increasing atmospheric CO_2 (Ballantyne et al., 2015). Improved knowledge of $FFCO_2$ emissions and their trends is necessary to understand the drivers of their variations, as well as to measure the effectiveness of mitigation actions (Pacala et al., 2010). Accurate estimates of emissions for the baselines years and the years after help verifying agreed-upon emission reduction targets. Implicitly, this requires that the uncertainties in the estimates of the emissions are much smaller than the amount of emissions to be reduced over a certain period of time.

Currently, fossil fuel CO_2 emissions are established by inventories mainly at the scale of countries, based on energy or fuel use statistics. In these inventories, sectorial data concerning each activity that produces emissions are multiplied by combustion efficiencies and emission factors. Such inventories thus have uncertainties related to imperfect data of energy or fuel use statistics, combustion efficiencies and emission factors (Macknick, 2009; Andres et al., 2012; Liu et al., 2015). Emission inventories are self-reported by countries using non-comparable methodologies and different datasets (Ciais et al., 2010), although the IPCC has published guidelines of good practice for emission reporting (IPCC, 2006). It is estimated that national annual $FFCO_2$ emissions have 2-sigma uncertainties ranging from 5% in OECD countries (Marland, 2008), 15-20% for China (Gregg et al., 2008) to 50% or more for less-developed countries (Andres et al., 2014). Global $FFCO_2$ emission maps (e.g. EDGAR, http://edgar.jrc.ec.europa.eu (Olivier et al., 2005); PKU-CO2, Wang et al., 2013 (Wang et al., 2013); CDIAC, (Andres et al., 1996); ODIAC, (Oda and Maksyutov, 2011)) are compiled based on these national inventories and on the disaggregation of national (regional) emissions, or by bottom-up modeling of emissions based on local to regional activity data (Gurney et al., 2009). These products are available at a relatively high spatial resolution, typically down to

0.1 °, but often without considering detailed spatial variations of emission processes. Also different downscaling assumptions result in disagreements between emission maps (Oda and Maksyutov, 2011; Wang et al., 2013). These products usually provide annual values without temporal profiles associated with emissions at the intra annual scale. Thus these emission maps often have larger uncertainties at sub-national and monthly scale (Ciais et al., 2010; Gregg et al., 2008).

An appealing method to independently assess $FFCO_2$ emissions is to use an atmospheric inversion approach (Ray et al., 2014). The atmospheric inversion approach consists in adjusting the estimates of emissions to minimize the distance between modelled and observed mixing ratios, yielding an optimized posterior estimate. It uses a statistical method, which relies on statistics of the uncertainty in the prior estimate of the emissions and of the other sources of model-measurement misfits (transport errors, measurement errors, model-measurement mismatch due to different spatial representativeness, etc., which are grouped under the generic term *observation errors*). Atmospheric inversions have been used so far for estimating natural CO_2 fluxes, with most studies being at the scale of large regions (Bousquet et al., 2000; Gurney et al., 2002), and few studies at the scale of small regions (Lauvaux et al., 2008; Broquet et al., 2011). These inversions have mainly used ground based *in-situ* atmospheric measurements while exploiting satellite measurements is presently challenging (Chevallier and O'Dell, 2013).

A first strategy to sample the atmosphere with *in-situ* stations for the inversion of $FFCO_2$ emissions would be to place stations very close to the largest fossil fuel CO_2 sources (cities, power plants, etc.). This allows the detection of a clear signature of $FFCO_2$ emissions in the measured CO_2 gradients (Bréon et al., 2015). Very high-resolution inversion systems are required to exploit such data (Brioude et al., 2012; McKain et al., 2012; Newman et al., 2013; Bréon et al., 2015). A limitation of this sampling strategy is that it would necessitate dense networks and very high-resolution inversions around every large CO_2 emitting area, while smaller sources will not be captured.

The second strategy is to sample the atmosphere away from local $FFCO_2$ sources to monitor an atmospheric signal integrating their signature at the sub-continental scale. With this strategy, one may expect inversions to solve for fossil fuel emissions at the scale of sub-continental regions (e.g. middle sized countries in EU, groups of States in the US, provinces in

China) using a network of stations distributed across a large sub-continental domain (Pacala et al., 2010). This sampling strategy could benefit from the existing infrastructure of in-situ networks already set-up for the monitoring of natural fluxes (e.g. the European Integrated Carbon Observing System, ICOS, https://www.icos-ri.eu/; NOAA-ESRL, http://www.esrl.noaa.gov/research/themes/carbon/).

A difficulty for inversions to solve for $FFCO_2$ emissions based on atmospheric observations on a continental scale network is to separate the signal from fossil fuels from that of natural (biogenic and oceanic) fluxes in the atmospheric measurements. The effect of natural fluxes on atmospheric CO_2 gradients is indeed comparable to that of fossil fuel emissions, as long as the stations are not immediately close to anthropogenic sources. A filtering of the $FFCO_2$ signature based on knowledge on the spatial distribution and temporal profiles of $FFCO_2$ emissions is presently challenging because of uncertainties in the spatial and temporal distribution of emissions and because large scale transport models can hardly account for the potential of this information, which is concentrated at relatively high resolution. This explains why there has not been any attempt at conducting inversions that separate fossil fuel emissions from natural fluxes using real CO_2 measurements alone from existing continental networks.

To circumvent the problem of separating natural fluxes and fossil fuel emissions in the atmospheric signals, it is possible to use proxies of the CO_2 mole fraction from fossil fuel emissions in large-scale inversions. Several proxies have been proposed for $FFCO_2$ (Gamnitzer et al., 2006; Rivier et al., 2006), but none of them is as close to a pure fossil fuel CO_2 tracer as radiocarbon in CO_2. Measurements of radiocarbon in CO_2 together with measurements of total CO_2 can be used to separate $FFCO_2$ (Levin et al., 2003) based on the principle that fossil fuel emitted CO_2 comes from geological deposits, and is radiocarbon-free. In this context, our study gives insights on the potential of the inversion of fossil fuel emissions in Europe based on hypothetical networks of collocated measurements of radiocarbon in CO_2 and total CO_2 measurements.

Note that radiocarbon in CO_2 is only a proxy of $FFCO_2$ and that its atmospheric gradients are also partly influenced by the transport of fluxes from stratosphere, ocean, biosphere and nuclear facilities as well as by that of fossil fuel emissions (Randerson et al., 2002; Naegler and Levin, 2006; Graven and Gruber, 2011). Within industrialized continents, radiocarbon gradients

are however dominated by the signal of $FFCO_2$ emissions (Graven and Gruber, 2011; Levin et al., 2011). In our studies, we postulate that atmospheric radiocarbon-CO_2 observations are exact measurements of the $FFCO_2$ component in atmospheric CO_2. We also postulate that numerous measurements of radiocarbon-CO_2 could be made at many sites of a continental atmospheric network. In practice, radiocarbon is expensive to measure (e.g. can only be performed in discrete air samples, not *in-situ*), so that the implementation costs of dense radiocarbon sampling networks could be a limitation as well.

Nevertheless, these two assumptions are not a limitation to the scope of this study focusing on evaluating whether the signal of $FFCO_2$ gradients between continental sites that are not in the vicinity of high emission areas are large enough compared to modelling errors and radiocarbon measurement errors, and whether these gradients are representative enough of the emissions averaged at sub-national scales so that the use of a coarse-grid transport model remains valid for constraining sub-national $FFCO_2$ emissions.

The recent OSSE study of Ray et al. (2014) demonstrated that using a network of 35 towers sampling atmospheric $FFCO_2$ mixing ratios every 3 h across the U.S. with an uncertainty arbitrarily set to 0.1 ppm (which is very optimistic given the current precision of radiocarbon-CO_2 measurements), an atmospheric inversion at 1 °×1 °resolution could reduce errors on 8 day-averaged country-level fossil-fuel emissions by a factor of two. In the context of the US Inter-academy report on emission verification, Pacala et al. (2010) presented another OSSE experiment suggesting that, based on a hypothetical massive set of 10,000 atmospheric $^{14}CO_2$ measurements in one year and a perfect transport model of 5 ° horizontal resolution, an atmospheric inversion could reduce the uncertainty of the monthly mean fossil-fuel flux in the US from 100% to less than 10%. Moreover, Basu et al. (2016) developed a dual-tracer inversion framework assimilating both CO_2 and $^{14}CO_2$. They showed that given the actual coverage of $^{14}CO_2$ measurements available in 2010 over US, the dual-tracer inversion can recover the US national annual total $FFCO_2$ emission to better than 1%.

In this study, we attempt at analysing in details the weight of potentially critical limitations of the large scale inversion of fossil fuel emissions. In particular, we characterize how much such an approach relies on the knowledge of the spatial distribution of the emissions at high resolution while continental scale observation networks and inversion systems can hardly solve

for it. When dealing with a large scale inversion system, one also needs to carefully account for the fact that the grid size of transport models (typically 100-300 km for global models, down to 5-10 km for regional models; Law et al., 2008) is larger than the scale of emissions, which have very fine scale patterns. This ensemble of misfits between the scales controlled or modelled within the inversion system and that of actual emissions and patterns in the mixing ratios generates so-called aggregation and representation errors in the inversion (Gerbig et al., 2003; Lin et al., 2006) to which this paper gives a special attention.

This study specifically addresses the derivation and analysis of the statistics of representation and aggregation errors in comparison to the typical $FFCO_2$ signals at measurement sites. This work focuses on the derivation and analysis of these errors for an atmospheric inversion framework dedicated to the inference of national scale monthly emissions over European countries using continental scale networks of measurement stations. This inversion framework uses a global atmospheric transport model and global maps of the emissions with spatial and temporal distributions within countries and one month. Having a global configuration ensures that uncertainties in fossil fuel CO_2 emitted over other regions of the globe outside a target continent are properly accounted for. This study assumes that daily to monthly mean $FFCO_2$ gradients can be estimated between numerous sites and a "reference" site sampling the free tropospheric air over a continent by $^{14}CO_2$ measurements, with a precision of 1 ppm due to the typical measurement errors and to uncertainties in the conversion of $^{14}CO_2$ and CO_2 measurements into $FFCO_2$ (Levin et al., 2003).

The detailed objectives of this paper are:

- To develop a theoretical derivation of the different sources of observation errors arising from the estimation of fossil fuel emissions at regional scale by an atmospheric inversion using a coarse-grid transport model. We provide a theoretical definition of the aggregation and representation errors and to separate them from two other types of observation errors: the measurement errors and the model transport errors. This synthetic derivation of critical sources of errors, which have been analysed for inversion of natural fluxes in various studies (Kaminski et al., 2001; Engelen, 2002; Gerbig et al., 2003; Wu et al., 2011), is adapted to the inversion of $FFCO_2$ emissions.
- To derive practical estimates of the representation and aggregation errors based on the

above theoretical definitions.

- To compare the representation and aggregation errors to simpler estimates of the model transport and measurements errors, to the signal of $FFCO_2$ simulated at the sites of continental scale networks, and to the corresponding statistics of errors due to the uncertainties in the prior estimates of the emissions (i.e., the errors that the inversion aims at filtering with the model – data comparisons). While the specific error values are function of the inversion configuration and while we compute them for $FFCO_2$ observations in Europe only, our analysis gives useful insights into typical observation errors and signal intrinsically related to the large scale inversion of fossil fuel emissions.

Due to the link between the representation and aggregation errors with the configuration of the inversion, section 2 first describes the large-scale fossil fuel emission inversion framework, and then develops the derivation for each term of the observation errors mentioned above. Special attention is given to the representation and aggregation errors when using a coarse-grid transport model and optimizing emissions at the scale of sub-continental regions. Practical ways to estimate these two errors are given in section 3. Results for representation errors, aggregation errors and the errors due to the prior uncertainties in the simulation of observations in Europe are discussed in section 4 and section 5. In section 6, we compare these errors with the measurement error, model transport error, and typical signals of $FFCO_2$. We also discuss the effects of the spatial (temporal) resolution of the modelling (respectively observation) framework for the atmospheric inversion of $FFCO_2$ emissions. Conclusions are drawn in section 7.

2. Methodology

The inversion framework considered here follows the Bayesian linear update (Enting et al., 1993; Tarantola, 2005) of a prior statistical knowledge $p(\mathbf{x}^t \mid \mathbf{x}^b)$ on the actual value $\mathbf{x}^t$ for a set of control variables $\mathbf{x}$ (among which some variables underlie the target quantities i.e. budgets of $FFCO_2$ emissions at large scale), where $\mathbf{x}^b$ is a prior estimate of these variables. The update relies on some observations $\mathbf{y}^o$ (here $FFCO_2$ atmospheric measurements), on an affine observation operator $\mathbf{x} \mapsto \mathbf{H}\mathbf{x}+\mathbf{y}_{fixed}$ (including the global coarse-grid transport model and the

distribution of the emissions at high resolution, and the signature of the influence of sources of $FFCO_2$ that is not controlled by the inversion) linking the control space $\mathbf{x}$ to the observation space $\mathbf{y}$ and on statistics $p(\mathbf{y}^o\text{-}\mathbf{H}\mathbf{x}^t\text{-}\mathbf{y}_{fixed} \mid \mathbf{x}^t)$ of the sources of observation errors (i.e. errors that are not due to the uncertainties in the estimate of $\mathbf{x}^t$ in the comparison between $\mathbf{H}\mathbf{x}^t+\mathbf{y}_{fixed}$ and the observations $\mathbf{y}^0$). It also follows the traditional assumption that the statistics of the prior and observation uncertainties are unbiased, Gaussian and independent of each other (Tarantola, 2005) so that $p(\mathbf{x}^t - \mathbf{x}^b \mid \mathbf{x}^b) \sim N(\mathbf{0},\mathbf{B})$ and $p(\mathbf{y}^o\text{-}\mathbf{H}\mathbf{x}^t\text{-}\mathbf{y}_{fixed} \mid \mathbf{x}^t) \sim N(\mathbf{0},\mathbf{R})$ where $\mathbf{B}$ and $\mathbf{R}$ are the prior error and observation error covariance matrices, and so that the posterior statistical estimate of $\mathbf{x}^t$ from the optimal update given $\mathbf{x}^b$ and $\mathbf{y}^o$, is a Gaussian distribution that can be written $p(\mathbf{x}^t \mid \mathbf{x}^b, \mathbf{y}^o) \sim N(\mathbf{x}^a,\mathbf{A})$, where

$$\mathbf{A} = (\mathbf{B}^{-1}+\mathbf{H}^T\mathbf{R}^{-1}\mathbf{H})^{-1} \quad (1)$$

$$\mathbf{x}^a = \mathbf{x}^b + \mathbf{A}\mathbf{H}^T\mathbf{R}^{-1}(\mathbf{y}^o\text{-}\mathbf{H}\mathbf{x}^b\text{-}\mathbf{y}_{fixed}) \quad (2)$$

We focus on the characterization of several critical terms of the observation error $p(\mathbf{y}^o\text{-}\mathbf{H}\mathbf{x}^t\text{-}\mathbf{y}_{fixed} \mid \mathbf{x}^t)$, on the relevance of the assumption that the observation error can be represented by a Gaussian and unbiased distribution $N(\mathbf{0},\mathbf{R})$, and on the derivation of a relevant $\mathbf{R}$ matrix for our configuration of a large scale fossil fuel emission inversion. The observation error plays a critical role in the estimate of the posterior uncertainty characterized by its covariance matrix $\mathbf{A}$. If its projection back to the flux space (i.e. the term $\mathbf{H}^T\mathbf{R}^{-1}\mathbf{H}$ in Equation (1)) is far larger than the uncertainty in the fluxes that the inversion is expected to control (the $\mathbf{B}$ matrix), the assimilation of atmospheric observations will bring little and/or highly uncertain information about the fluxes and the potential of the inversion will be low. The observation error $p(\mathbf{y}^o\text{-}\mathbf{H}\mathbf{x}^t\text{-}\mathbf{y}_{fixed} \mid \mathbf{x}^t)$ will be compared to an estimate of the projection of the prior uncertainty in the observation space $p(\mathbf{H}(\mathbf{x}^t - \mathbf{x}^b) \mid \mathbf{x}^b)$ to give insights on this (indicating whether the signature of the prior uncertainty should be easy to filter in the prior model – data misfits $\mathbf{y}^o\text{-}\mathbf{H}\mathbf{x}^b\text{-}\mathbf{y}_{fixed}$) even though the full computation of Equation (1) is required to define whether the assimilation of atmospheric observation strongly decreases the uncertainty in the flux estimates.

The nature of the observation error strongly depends on the nature of the $\mathbf{x}$ and $\mathbf{y}$ space, and on the trueness and precision of the observation operator $\mathbf{x}\mapsto\mathbf{H}\mathbf{x}+\mathbf{y}_{fixed}$. In the following we first present the practical configuration of these elements given our practical inversion framework. Then, we propose a theoretical decomposition of the observation errors with an

emphasis on the terms that should be critical for our practical inversion framework and with a specific care at defining the representation and aggregation errors.

In practice the simulations, inversions and analysis are conducted for a 1-year period arbitrarily chosen to be a typical year 2007. This choice has consequences regarding the meteorological conditions and the level of emissions that are taken into account in our modeling framework but we expect that the conclusions from the analysis should not be strongly sensitive to this choice.

2.1 Configuration of the control and observation space of the inversion and of the observation operator

2.1.1 Control vector

We divide the globe, according to administrative boundaries, into a set of emitting regions whose monthly mean fossil fuel emission budgets are solved for during a whole year (Figure 1a). The corresponding space discretization is higher in continents that have the largest emission densities (Europe, US and China, Figure 1b-d). The spatial resolution in Europe is in agreement with the typical size of European countries. It is finer in western Europe where emissions can be high in specific regions such as northern Italy, southern England, eastern and western Germany. In the US and China, the spatial discretization is also increased in the most populated and industrialized areas (i.e., the east and west coasts in the US, and the south-eastern coast in China). In a given emitting region, the inversion controls the budget of $FFCO_2$ emissions (in Mg C/hour) for each of the 12 months during one year, but does not solve for the space and time distribution within each region or at sub-monthly intervals.

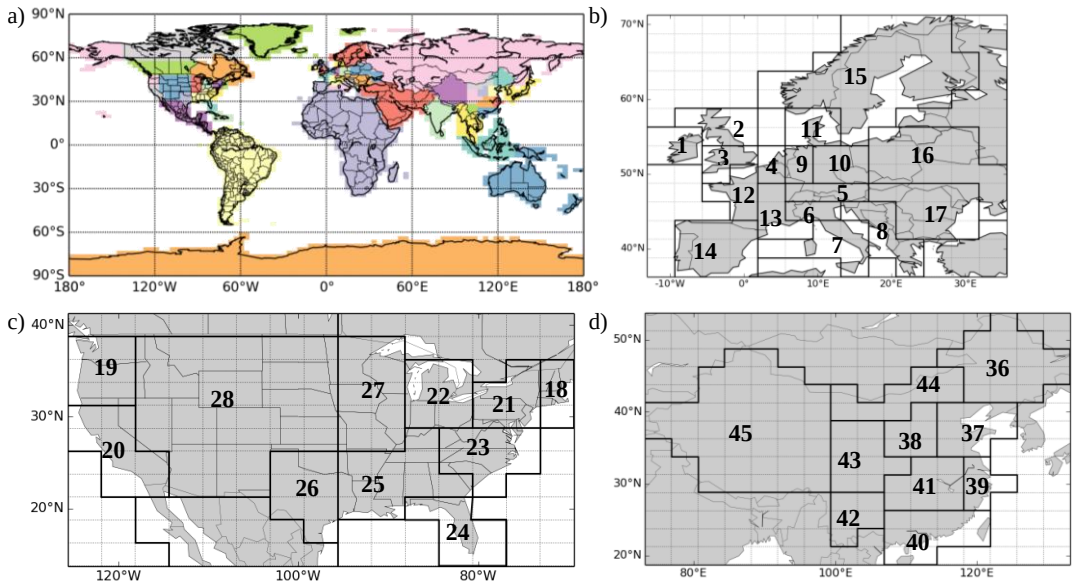

Figure 1 a) Map of the 56 regions whose monthly emission budgets are controlled by the inversion; b) zoom on the 17 control regions in Europe; c) zoom on the 11 control regions in the United States; d) zoom on the 10 control regions in China

2.1.2 Observation vector

The observation vector consists in $FFCO_2$ gradients between sites of hypothetical ground-based European networks of atmospheric total CO_2 and $^{14}CO_2$ measurements (that are used together to compute $FFCO_2$) throughout one year, at a typical height of 100 m above ground level (magl). More precisely, we consider gradients between simultaneous $FFCO_2$ observations at any site of these networks and a reference site sampling the free tropospheric air over Europe, as is traditionally done when analyzing $^{14}CO_2$ measurements (Levin et al., 2008). Here, we select the High Alpine Research Station Jungfraujoch (JFJ, located at 3450 m a.s.l. in Switzerland) as the reference site for European stations. Continuous measurement of total CO_2 has been made for years in Europe (within the CarboEurope-IP, GHG-Europe and ICOS programs) and US (within the NOAA-ESRL framework) at tens of sites. A given radiocarbon measurement can be applied to a sample with any temporal integration time from 1 hour to 1 month since air samples could be filled at constant rates over long periods. However, the cost of the $^{14}CO_2$ analysis of one sample is presently high so that monitoring of $^{14}CO_2$ during a whole year favors the choice of integrated samples at the daily to monthly scale (Levin, 1980; Turnbull et al., 2009; Vogel et al., 2013). We have also accounted for the technical ability to have an intermittent filling (Levin et al., 2008). Indeed, state-of-art inversion systems generally make use of data during afternoon

only due to limitations in modeling the vertical mixing during other periods of the day. We thus assume that mean afternoon $FFCO_2$ observations are sampled during 12:00-18:00 local time at the sites.

The locations of the stations where $^{14}CO_2$ measurements are made are assumed to be inland and distant from urban areas and other large sources, and aim to monitor the signature of the emissions at sub-continental scale. However, some sites will necessarily be closer to emitting areas than others, with consequences regarding the representativeness and amplitude of the measured $FFCO_2$ signal. We thus define two types of sites, both corresponding to land model grid cells: "urban" and "rural" sites, based on a threshold on the population density (ORNL, 2008) within the grid cells where the stations are located. This threshold is country-dependent and matches the World Bank urbanization data (available at http://data.worldbank.org/indicator/SP.URB.TOTL.IN.ZS?page=1&order=wbapi_data_value_2011%20wbapi_data_value%20wbapi_data_value-first&sort=asc) for each country as done by Wang et al. (2013).

2.1.3 Observation operator

The observations are only influenced by the initial condition and the emissions during the year. As indicated above, the emissions are controlled by the inversion. Through diffusion by atmospheric transport, the spatial patterns of $FFCO_2$ from a pulse of emissions at a given time appear to become negligible (with an amplitude smaller than 0.1 ppm) within about 2 weeks, so that the influence of the global $FFCO_2$ distribution on January 1st, 2007 (i.e. the initial condition of the inversion experiments in our studies) is quite negligible for our simulations of gradients of $FFCO_2$ in Europe in 2007, even for the results in January 2007 (not shown here). In our modelling framework and corresponding simulations, initial conditions for the $FFCO_2$ field in the atmosphere by the 1st day of the inversion year are thus ignored.

Consequently, the observation operator considered in this study is linear and does not bear an affine term $\mathbf{y}_{fixed}$ reflecting, in the observation gradients, the influence of a source or sink of $FFCO_2$ that is not rescaled by our control vector. Therefore, it can be denoted $\mathbf{H}$. We decompose it into:

$$\mathbf{H}=\mathbf{H}_{samp}\,\mathbf{H}_{transp}\,\mathbf{H}_{distr} \quad (3)$$

In this formulation, **H** is a chain of three operators denoting the distribution of emissions within each region-month corresponding to the control variables ($\mathbf{H}_{distr}$), the atmospheric transport ($\mathbf{H}_{transp}$), and the sampling of atmospheric gradients corresponding to the observation vector from the transport model outputs ($\mathbf{H}_{samp}$) respectively. The spatial and temporal (sub-monthly) distribution operator $\mathbf{x} \rightarrow \mathbf{f} = \mathbf{H}_{distr}\ \mathbf{x}$ distributes the emission budgets for each region and month **x** into gridded emissions **f** at the spatial and temporal resolution expected as input of the atmospheric transport model. The atmospheric transport operator $\mathbf{f} \rightarrow \mathbf{c} = \mathbf{H}_{transp}\ \mathbf{f}$ simulates the $FFCO_2$ field **c** using an atmospheric transport model with prescribed emissions **f**. The sampling operator $\mathbf{c} \rightarrow \mathbf{y} = \mathbf{H}_{samp}\ \mathbf{c}$ applies the atmospheric sampling procedure described above.

Each column of **H** represents the signature (the so-called response function) in the observation space of a unitary increment of the budget of the emissions in a given control region-month. Figure 2 gives the frame of the observation operator and its link to control and observation vectors.

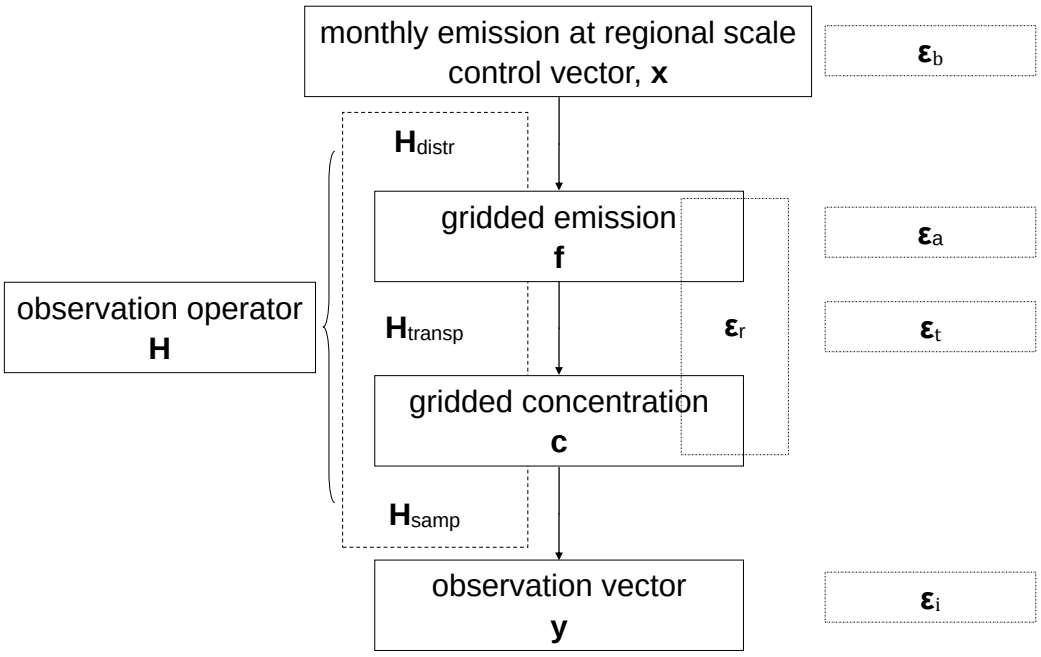

Figure 2 Components of observation operator and its link with the control and observation vectors

For the observation operator used in practice, we use a coarse-grid transport model and emission inventories which catch the typical spatial and temporal large-scale variations in the $FFCO_2$ emissions and concentrations and thus ensure the realism of the typical estimates of uncertainties in our study. The corresponding products bear the typical precision/trueness of the products that are used by state-of-the-art inversion systems when assimilating real data to quantify CO_2 natural fluxes at large scale.

1) Inventory used for the mapping of the emissions at high resolution

We use the PKU-CO_2-2007 global emission inventory for 2007 (Wang et al., 2013) to model, by the $\mathbf{H}_{distr}$ operator, the spatial distribution of emissions within the regions of control. PKU-CO_2-2007 is a high-resolution (0.1 °) annual emission map based on the disaggregation of national emission budgets using sub-national statistics. Regarding the sub-monthly temporal distribution of emissions within each month, we assume a flat temporal profile, as in many large scale natural flux inversion systems (Peylin et al., 2013). We denote by $\mathbf{H}_{distr}^{PKU}$ the practical implementation of the distribution operator $\mathbf{H}_{distr}$.

2) Global transport model configuration

An off-line version of the atmospheric general circulation model of Laboratoire de Météorologie Dynamique (LMDZ) (version 4) (Hourdin et al., 2006) is used as our atmospheric transport operator. The corresponding LMDZ simulation was nudged to the re-analyzed wind fields from the European Centre for Medium-Range Weather Forecasts (ECMWF) Interim Reanalysis (ERA-Interim, (Berrisford et al., 2009)). LMDZ has participated to a series of intercomparison exercises for the simulation of CO_2 concentrations (Law et al., 2008) and is able to reproduce most of the daily variations of the large scale transport of $FFCO_2$ (Peylin et al., 2011). The model configuration used here has a horizontal resolution of 3.75 °×2.5 ° (longitude×latitude) and 19 hybrid sigma-pressure layers to discretize the vertical profile between the surface and the top of the atmosphere. We denote by $\mathbf{H}_{transp}^{LMDZ}$ the resulting practical implementation of $\mathbf{H}_{transp}$.

3) Observation sampling of the transport model outputs

In the observation operator, the practical simulation of $FFCO_2$ gradients corresponding to the observation vector relies on the simple extraction of individual concentration data at the measurement locations and then on the computation of differences between these concentration

at different sites. We extract a concentration for a given location by taking the value in the transport model grid cell within which the site locates rather than interpolating values from several transport model grid cells. Usually, the height of the first level of LMDZ is about 150 magl. All the observations being assumed at 100 magl, they are all extracted from the first level of this version of LMDZ, except that of the reference site, Jungfraujoch (JFJ). JFJ is located at 3450 m above sea level (masl) but close to the ground level, at the top of a mountain. Since the LMDZ model poorly solves the topography in mountain areas, its ground level in the grid cell corresponding to JFJ is located far lower than this height. In order to ensure that the modelled concentrations are representative of the free tropospheric air, JFJ observations are extracted from the 6th level of LMDZ, which is usually located between 2700 and 3800 masl. 1-day to 1-month mean afternoon $FFCO_2$ data are sampled in time. We denote by $\mathbf{H}_{samp}^{coloc}$ the resulting practical implementation of $\mathbf{H}_{samp}$.

To sum up, the observation operator that will be used in practice for inversions in the following can be written $\mathbf{H}^{prac} = \mathbf{H}_{samp}^{coloc}\,\mathbf{H}_{transp}^{LMDZ}\,\mathbf{H}_{distr}^{PKU}$.

2.2 Theoretical derivation of the critical observation errors

In this section, we are interested in decomposing the observation error $p(\mathbf{y}^o - \mathbf{H}\mathbf{x}^t | \mathbf{x}^t)$ for a typical $\mathbf{H}$ in order to isolate some critical sources of errors in practice. The observation operator $\mathbf{H} = \mathbf{H}_{samp}\,\mathbf{H}_{transp}\,\mathbf{H}_{distr}$ maps low-resolution budgets of the emissions into a coarse spatial grid. But each term of this operator is likely not perfectly represented in the following ways: 1) the products for the distribution of emissions within countries such as the one used to build $\mathbf{H}_{distr}^{PKU}$ are necessarily imperfect; 2) the-state-of-the-art transport model such as the one used in $\mathbf{H}_{transp}^{LMDZ}$ are necessarily imperfect; 3) the spatial representativeness of the measurements close to the ground can be low with coarse-resolution transport models and it can be difficult to represent the measurements in the vertical grid of the coarse-resolution models (Broquet et al., 2011; Pillai et al., 2011) which impacts the precision/trueness of practical models for $\mathbf{H}_{samp}$ $\mathbf{H}_{transp}$. These add to the high measurement errors that have to be accounted for when monitoring $FFCO_2$.

Focusing on these sources of errors, the term $\mathbf{y}^o - \mathbf{H}\mathbf{x}^t$ can be decomposed as follows:

$$\mathbf{y}^o - \mathbf{H}\mathbf{x}^t = \underbrace{\left(\mathbf{y}^o - \mathbf{H}_{\text{transpHR}}{}^t\mathbf{f}_{\text{HR}}{}^t\right)}_{\boldsymbol{\varepsilon_i}} + \underbrace{\left(\mathbf{H}_{\text{samp}}\mathbf{H}_{\text{transpHR}}{}^t\mathbf{f}_{\text{HR}}{}^t - \mathbf{H}_{\text{samp}}\mathbf{H}_{\text{transp}}{}^t\mathbf{H}_{\text{distr}}{}^t\mathbf{x}^t\right)}_{\boldsymbol{\varepsilon_r}}$$
$$+ \underbrace{\left(\mathbf{H}_{\text{samp}}\mathbf{H}_{\text{transp}}{}^t\mathbf{H}_{\text{distr}}{}^t\mathbf{x}^t - \mathbf{H}_{\text{samp}}\mathbf{H}_{\text{transp}}\mathbf{H}_{\text{distr}}{}^t\mathbf{x}^t\right)}_{\boldsymbol{\varepsilon_t}} \quad (4)$$
$$+ \underbrace{\left(\mathbf{H}_{\text{samp}}\mathbf{H}_{\text{transp}}\mathbf{H}_{\text{distr}}{}^t\mathbf{x}^t - \mathbf{H}_{\text{samp}}\mathbf{H}_{\text{transp}}\mathbf{H}_{\text{distr}}\mathbf{x}^t\right)}_{\boldsymbol{\varepsilon_a}}$$

where $\mathbf{H}_{\text{transpHR}}$ is a theoretical operator corresponding to the linear transport from emissions $\mathbf{f}_{\text{HR}}$ to $\mathbf{y}$, $\mathbf{f}_{\text{HR}}$ and this transport being represented using the "infinitely high" resolution (i.e. continuously instead of using a discrete form) needed for catching all the patterns in the emissions and concentrations; Superscripts ^{t} denotes the true value of the emissions or observation operators at their corresponding space and time resolution (a "true observation operator" meaning here a perfect operator without any model error).

We define the different terms of the observation error $\mathbf{y}^o - \mathbf{H}\mathbf{x}^t$ based on this decomposition:

1) $\mathbf{y}^o - \mathbf{H}_{\text{transpHR}}{}^t\mathbf{f}_{\text{HR}}{}^t$ corresponds to the "measurement error" $\boldsymbol{\varepsilon}_i$, which is associated with the precision of $FFCO_2$ gradients derived from measurements of ^{14}C and CO_2. The assumption given in section 1 that this precision is 1 ppm is discussed in section 2.3.

2) $\mathbf{H}_{\text{transpHR}}{}^t\mathbf{f}_{\text{HR}}{}^t - \mathbf{H}_{\text{samp}}\mathbf{H}_{\text{transp}}{}^t\mathbf{H}_{\text{distr}}{}^t\mathbf{x}^t$ corresponds to the representation error $\boldsymbol{\varepsilon}_r$ which arises from the modelling of concentrations and emissions at the coarse resolution of the transport model in the observation operator. This error could be further split into errors due to missing high resolution variations of the emissions at the model sub-grid scales, and errors due to comparing concentrations averaged at the model resolution to measurements with a far lower spatial representativeness. Appendix A1 discuss such a decomposition, which, in practice, artificially attributes most of the representation errors to the former or to the latter depending on the mathematical formulation. Therefore, even though this decomposition would have a physical meaning, it will be ignored hereafter.

3) $\mathbf{H}_{\text{samp}}\mathbf{H}_{\text{transp}}{}^t\mathbf{H}_{\text{distr}}{}^t\mathbf{x}^t$ - $\mathbf{H}_{\text{samp}}\mathbf{H}_{\text{transp}}\mathbf{H}_{\text{distr}}{}^t\mathbf{x}^t$ corresponds to the transport errors $\boldsymbol{\varepsilon}_t$ due to the use of discretized and simplified equation for modelling the transport.

4) $\mathbf{H}_{\text{samp}}\mathbf{H}_{\text{transp}}\mathbf{H}_{\text{distr}}{}^t\mathbf{x}^t - \mathbf{H}_{\text{samp}}\mathbf{H}_{\text{transp}}\mathbf{H}_{\text{distr}}\mathbf{x}^t$ corresponds to the aggregation error $\boldsymbol{\varepsilon}_a$ due to the imperfect representation of the distribution of the monthly emissions within the region-months controlled by the inversion when using $\mathbf{H}_{\text{distr.}}$

The total observation error $\boldsymbol{\varepsilon}_o$ defined by $p(\mathbf{y}^o - \mathbf{H}\mathbf{x}^t - \mathbf{y}_{fixed} | \mathbf{x}^t)$ can be expressed as:

$$\boldsymbol{\varepsilon}_o = \boldsymbol{\varepsilon}_i + \boldsymbol{\varepsilon}_r + \boldsymbol{\varepsilon}_t + \boldsymbol{\varepsilon}_a \quad (5)$$

Several of these terms are proportional to the value of $\mathbf{x}^t$ while $\mathbf{x}^t$ can take any value in the statistical framework of our inversion problem. This prevents, theoretically, from computing a fixed covariance $\mathbf{R}$ of the observation error assuming that this error can be represented by a distribution $N(\mathbf{0},\mathbf{R})$. The configuration of such an error in the inversion systems generally ignore such a dependence of the model errors (transport, representation and aggregation errors) on the possible values for the actual fluxes which is a strong limitation for the application of the traditional data assimilation framework to flux inversion problems. In practice, we will derive $\mathbf{R}$ based on assumptions regarding the typical value for $\mathbf{x}^t$ in our inversion cases.

Assuming that all the errors in Equation (4) are independent from each other ignoring dependency of these errors upon possible values for $\mathbf{x}^t$, and that they are all Gaussian and unbiased, one can write that $\boldsymbol{\varepsilon}_i \sim N(\mathbf{0}, \mathbf{R}_i)$, $\boldsymbol{\varepsilon}_r \sim N(\mathbf{0}, \mathbf{R}_r)$, $\boldsymbol{\varepsilon}_t \sim N(\mathbf{0}, \mathbf{R}_t)$, $\boldsymbol{\varepsilon}_a \sim N(\mathbf{0}, \mathbf{R}_a)$, and compute $\mathbf{R}$ as the sum of the covariances of the different errors:

$$\mathbf{R} = \mathbf{R}_i + \mathbf{R}_r + \mathbf{R}_t + \mathbf{R}_a \quad (6)$$

Of note is that our formulations of the representation error and of the aggregation error are similar to the derivations of representation error by Gerbig et al. (2003) and of aggregation error by Engelen (2002), respectively. However, our formulation of the aggregation error slightly differs from that of Kaminski et al. (2001) and Bocquet et al. (2011). We use a sort of "bottom-up" approach to derive it, starting from the decomposition of the observation errors once having defined it as the sum of all sources of model data misfits other than the prior uncertainties and that are independent from these prior uncertainties. Kaminski et al. (2001) and Bocquet et al. (2011) rather followed what we consider as a "top-down" approach to derive this aggregation error. Indeed, their introduction of the covariance of the aggregation error in the observation error covariance matrix ensures that the computation of the statistics for $p(\mathbf{x}^t | \mathbf{y}^o, \mathbf{x}^b)$ is the same regardless of the control resolution. Due to the use of the usual assumption of the atmospheric inversion that the observation error is independent of the prior uncertainty, our "bottom-up" method ignores potential correlations between the aggregation errors and the prior uncertainties, which is not the case of the "top-down" approaches. Therefore, the formulations of the covariance of the aggregation error in Kaminski et al. (2001) and Bocquet et al. (2011) include

a component related to this correlation, which is ignored in our formulation. As discussed in Appendix A2, we have nevertheless computed the corresponding component and concluded that its weight is relatively small and negligible for our study. The mathematical details and a discussion regarding the potential correlations between the aggregation errors and the prior uncertainties are given in Appendix A2.

2.3 Insights on the specificity or generality of the observation errors investigated in this study

In theory, results for control regions do not vary with the resolution of the control vector if the aggregation error $\boldsymbol{\varepsilon}_a$ is perfectly accounted for by $\mathbf{R}$ in the inversion configuration (see the demonstration in the Appendix based on the notations given above in section 2.2). In other words, an inversion at coarse resolution that accounts for aggregation errors $\boldsymbol{\varepsilon}_a$ should give the same results for monthly fluxes over large regions as the same inversion applied to solve for hourly fluxes at the highest resolution (transport model grid). This is due to the equivalence between accounting for the uncertainties of fluxes within regions/month through their projection in the observation error or through their assigned prior uncertainty (given the assumptions underlying the inversion framework). In this sense, even though they are formally a function of the control vector, the aggregation errors at a scale larger than the transport model resolution are not specific to a given inverse modelling set-up. Considering that the choice of the control resolution reflects a targeted resolution for the fluxes, aggregation errors rather reflect the impact for the monitoring of the fluxes at this targeted resolution of the uncertainties in the distribution of the fluxes at higher spatial or temporal resolutions. Increasing the control resolution would thus not, in theory, help solving for fluxes at the targeted resolution.

On the opposite, representation error is strongly linked to a specific inversion configuration. Increasing the resolution of the transport model used for the inversion necessarily decreases them without a full compensation of this decrease by the rise of prior uncertainties. The transport errors should also depend on the transport modelling configuration. For example, synoptic patterns and the influence of the surface topography on the transport are better simulated at higher resolution. However, different transport models are also based on different parameterizations and computational approach, etc., which makes the quantification and

evaluation of the transport errors as a function of the model complicated and efforts have rather focused on the derivation of typical transport errors based on the spread of different transport models (Law et al., 2008; Peylin et al., 2011).

Finally, the errors in the measurements in our study should be fully independent of the inverse modelling framework. The 1 ppm measurement error for $FFCO_2$ gradients between sites corresponds to typical values based on the analysis of air samples by accelerator mass spectrometry (AMS) for $^{14}CO_2$ (2‰-3‰, (Vogel et al., 2010; Turnbull et al., 2014)) and by typical analyzers for continuous CO_2 samples (Chen et al., 2010; Turnbull et al., 2011). Apart from these errors, various fluxes that influence the atmospheric $^{14}CO_2$, such as those from cosmogenic production, ocean, biosphere and nuclear facilities,make the direct conversion into $FFCO_2$ gradients bear complex uncertainties whose typical values may exceed 1 ppm for some locations and periods of times (Hsueh et al., 2007; Bozhinova et al., 2013; Vogel et al., 2013). These additional sources of uncertainties are not included in this study.

3. Practical calculation of observation errors

In the inversion system, we use $\mathbf{H}^{prac}=\mathbf{H}_{samp}{}^{coloc}\mathbf{H}_{transp}{}^{LMDZ}\mathbf{H}_{distr}{}^{PKU}$ as the observation operator. But here, we use a relatively independent representation of the "actual" and higher resolution operators involved in the theoretical formulation of the observation errors in sect. 2.2 in order to derive an estimate of these errors. These actual and higher resolution operators should bear patterns of the emissions, transport and concentration variability which should be realistic enough so that this estimate of the observation errors can provide a realistic characterization of the representation and aggregation errors when using real measurements.

A European configuration of the meso-scale transport model CHIMERE (Schmidt et al., 2001) run with a 0.5° horizontal resolution, with twenty-five hybrid sigma-pressure vertical layers from the surface to the pressure altitude of 450 hPa, and with hourly concentration outputs (to be aggregated into 1-day to 1-month mean afternoon data) is used to simulate $\mathbf{H}_{transpHR}{}^{t}$ and $\mathbf{H}_{transp}{}^{t}$. However, the LMDZ model is still used to model the practical $\mathbf{H}_{transp}$ when calculating the aggregation error. The CHIMERE simulations are initialized at 50 ppm on January 1st, 2007.

We model $\mathbf{H}_{transpHR}{}^{t}$ by feeding CHIMERE with 0.5 ° resolution maps of the emissions and using the 1-day to 1-month mean afternoon 0.5 °-resolution and 25-vertical-level concentration fields to extract simulated gradients of $FFCO_2$. Since the resolution of this CHIMERE configuration is not infinitely high, in practice, a sampling operator is still needed to model $\mathbf{H}_{transpHR}{}^{t}$. The vertical resolution of CHIMERE being about 35 to 45 m for the first three levels, the 100 magl observations involved in the computation of the $FFCO_2$ gradients at high resolution are extracted in the third level of this model (and in the 0.5 ° horizontal model grid cell containing the horizontal position of the stations, using a sampling option similar to that used in $\mathbf{H}_{samp}{}^{coloc}$).The $FFCO_2$ concentrations at the reference site are extracted from the 23rd vertical level of CHIMERE corresponding to the altitude of 3450 masl in the 0.5 ° grid cell where the reference site located. This transport (and sampling) configuration that is used to model $\mathbf{H}_{transpHR}{}^{t}$ is denoted $\mathbf{H}_{transpHR}{}^{CHIM}$.

By degrading the horizontal and temporal resolution of the emissions in input of the CHIMERE model and by averaging (horizontally and vertically) the mole fractions in output of the CHIMERE simulations we model $\mathbf{H}_{transp}{}^{t}$. The spatial aggregation of the CHIMERE outputs consists first in a vertical aggregation, and then on a horizontal aggregation. The horizontal aggregation does not fully correspond to an aggregation within the LMDZ grid cells (i.e. to the interpolation of the 0.5 ° resolution fields for CHIMERE into the 3.75 °×2.5 ° resolution grid of LMDZ). For simplicity, the 0.5 ° CHIMERE grid cells are rather aggregated from blocks of 6×6 grid cells to yield coarse grid at the 3 ° resolution which is close to that of the LMDZ grid. $\mathbf{H}_{transp}{}^{CHIM}$ denotes the configuration where CHIMERE is fed with emissions maps aggregated at 3 ° resolution (close to that of the LMDZ model) and over 3-hour time windows, and where CHIMERE 1-day to 1-month mean afternoon output concentrations are, again, aggregated at 3 ° resolution. For the modelling of $\mathbf{H}_{samp}$ in the computation of the error due to aggregation at the transport model resolution and in the computation of the representation error we apply an operator which follows the principle of $\mathbf{H}_{samp}{}^{coloc}$ (and which we will thus also denote $\mathbf{H}_{samp}{}^{coloc}$) i.e. $FFCO_2$ observations are extracted in the first aggregated vertical levels for all the sites but the reference site, which is extracted in the 6th aggregated vertical level, and in the co-located aggregated 3 ° horizontal grid cells of the $\mathbf{H}_{transp}{}^{CHIM}$ outputs. When calculating the error due to the aggregation at region-month scale, we use $\mathbf{H}_{samp}{}^{coloc}$ to model $\mathbf{H}_{samp}$ and

apply it to $\mathbf{H}_{transp}^{LMDZ}$.

Associating CHIMERE at 0.5 °resolution with $\mathbf{H}_{transpHR}^{t}$ (and consequently 0.5 °resolution maps of the emissions with $\mathbf{f}_{HR}^{t}$) assumes that the main variations (i.e. those which have the largest impact for data at 100 magl) of emissions or concentrations within 3 °resolution grid cells occur at scales larger than 0.5 °. Furthermore, simulating $\mathbf{H}_{transpHR}^{t}$ and $\mathbf{H}_{transp}^{t}$ with CHIMERE which is a regional model (over Europe) assumes that the aggregation and representation errors in Europe due to the coarse representation of these emissions or of their signature outside Europe is negligible.

$\mathbf{H}_{distr}^{t}$ (with outputs at 3 °and 3-hour resolution), the distribution of $\mathbf{f}_{HR}^{t}$ at 0.5 °and 1-hour resolution and $\mathbf{x}^{t}$ are modelled using the 0.1 °×0.1 ° EDGARv4.2 2007 emission map (http://edgar.jrc.ec.europa.eu) convoluted with temporal profiles (at 1-hour resolution) from IER (available at http://carbones.ier.uni-stuttgart.de/wms/index.html). We denote this emission inventory EDG-IER afterwards. Aggregating this inventory at 1-hour / 0.5 °resolution or at the scale of the inversion control region/month provides respectively $\mathbf{f}_{HR}^{EDG\text{-}IER}$ and $\mathbf{x}^{EDG\text{-}IER}$ that are used to model $\mathbf{f}_{HR}^{t}$ and $\mathbf{x}^{t}$. Aggregating this inventory at 3-hour / 3 °resolution (when computing representation errors at the coarse transport resolution using CHIMERE) or 3-hour / 3.75 °×2.5 ° (when computing aggregation errors using LMDZ) and then rescaling it homogeneously within each region/month of control for the inversions to get unitary budget of emissions provides $\mathbf{H}_{distr}^{EDG\text{-}IER}$ (using the same notation for the operator when the output "emission" space is at 3° or 3.75 °×2.5 °resolution) which is used to model $\mathbf{H}_{distr}^{t}$.

With these practical choices for modeling the operators involved in the different types of observation errors defined in section 2.2, the representation error writes:

$$\mathbf{H}_{transpHR}^{CHIM}\mathbf{f}_{HR}^{EDG\text{-}IER} - \mathbf{H}_{samp}^{coloc}\mathbf{H}_{transp}^{CHIM}\mathbf{H}_{distr}^{EDG\text{-}IER}\mathbf{x}^{EDG\text{-}IER} \quad (7)$$

, and the aggregation error writes:

$$\mathbf{H}_{samp}^{coloc}\mathbf{H}_{transp}^{LMDZ}\mathbf{H}_{distr}^{EDG\text{-}IER}\mathbf{x}^{EDG\text{-}IER} - \mathbf{H}_{samp}^{coloc}\mathbf{H}_{transp}^{LMDZ}\mathbf{H}_{distr}^{PKU}\mathbf{x}^{EDG\text{-}IER} \quad (8)$$

We only have one practical realization for each of these terms and thus of the corresponding errors, therefore, in order to derive their standard deviation and to investigate whether they bear potential temporal or spatial correlation, we make the strong assumption that the errors at different time and locations have relatively similar statistical distributions. However, this assumption of spatial and temporal homogeneity will be applied for adequate

subset of observation time, locations and type, which will require a categorization of the observations.

Based on this assumption, we analyze the typical statistics of the representation and aggregation errors by using distributions of occurrences of these errors for different subsets (categories) of observations. Since observation sites of continental networks could locate in any grid cell, all the spatial grid cells and all 1-day to 1-month afternoon time windows are used and categorized among different subsets for this analysis. The different spatial and temporal categories will be defined based on the analysis of the spatial and temporal variations of the errors. The potential temporal auto-correlations and spatial correlations within/across categories are also analyzed.

Using a similar approach, transport errors could have been evaluated using $\mathbf{H}_{samp}{}^{coloc}\mathbf{H}_{transp}{}^{CHIM}\mathbf{H}_{distr}{}^{EDG\text{-}IER}\mathbf{x}^{EDG\text{-}IER}$ and $\mathbf{H}_{samp}{}^{coloc}\mathbf{H}_{transp}{}^{LMDZ}\mathbf{H}_{distr}{}^{EDG\text{-}IER}\mathbf{x}^{EDG\text{-}IER}$. However, the spatial resolution and orography of $\mathbf{H}_{transp}{}^{CHIM}$ and $\mathbf{H}_{transp}{}^{LMDZ}$ are not exactly the same and this could have artificially increased the transport error with representation error. Therefore, we make a simpler estimation of the transport errors for simulated $FFCO_2$ gradients based on that of transport errors for simulated $FFCO_2$ at individual sites.

For this estimation, we make several assumptions. First, we assume that there is no temporal auto-correlation of the transport error in simulated daily mean afternoon concentrations between different days at a given location. Second, we assume that the standard deviation of the transport error in simulated daily mean afternoon concentrations is constant in time at a given location. Finally, we assume that the ratio between this standard deviation and the temporal standard deviations of the 1-year long time series of the simulated daily mean afternoon concentrations in the corresponding grid cell of the transport model is constant in space (i.e. that this ratio is identical for all grid cells of the transport model). The underlying assumption is that the transport models should be less reliable at sites where the concentrations have a larger variability (Peylin et al., 2005; Geels et al., 2007). These assumptions allow us to use the station of (SAC) near Paris for deriving a generalized estimate of the ratio between the transport errors and the simulated $FFCO_2$ temporal variability. According to Peylin et al. (2011), the annual average of the standard deviations between simulated hourly mean $FFCO_2$ concentrations at this site from a set of state-of-the-art transport models is 2.34 ppm. We use

this value to define the standard deviation of the transport errors associated with the simulated daily afternoon mean concentrations. The standard deviation of the 1-year long time series of the daily afternoon mean concentrations simulated within one year with our practical implementation of the simulation of 3-hourly concentrations $\mathbf{H}_{\text{transp}}^{\text{LMDZ}}\mathbf{H}_{\text{distr}}^{\text{EDG-IER}}\mathbf{x}^{\text{EDG-IER}}$ at SAC is 2.93 ppm. So the ratio between the standard deviation of the transport error for daily afternoon mean concentrations and the standard deviation of simulated time series for the daily afternoon mean concentrations within one year for any site is assumed to be 2.34/2.93=0.8. For any potential sites (in any grid cells in LMDZ), we thus multiply this ratio by the standard deviation of the simulated daily afternoon mean concentrations within one year to get an estimate of the transport error statistics for the daily afternoon mean $FFCO_2$. Transport errors for daily to monthly mean afternoon $FFCO_2$ are then derived based on the value obtained for daily afternoon mean $FFCO_2$ and on the above mentioned assumption that there is no temporal auto-correlation of the transport errors between afternoon mean concentrations in different days. For example, our estimate of the transport error for 2-week mean afternoon concentrations (mean of 14 days) is equal to $2.93\times0.8/\sqrt{14}=0.63$ ppm at SAC site.

Following this estimation, the transport error in the 2-week mean afternoon $FFCO_2$ concentration at JFJ site is 0.37 ppm. The transport error in the 1-day to 1-month mean afternoon $FFCO_2$ gradients between any site and JFJ is calculated assuming no spatial correlation of the transport errors between sites, i.e. as $\sqrt{(\boldsymbol{\varepsilon}_{t,i}^2+\boldsymbol{\varepsilon}_{t,JFJ}^2)}$ where $\boldsymbol{\varepsilon}_{t,i}$ is the transport error for concentrations at site *i* and $\boldsymbol{\varepsilon}_{t,JFJ}$ is the transport error in concentrations at site JFJ at the corresponding 1-day to 1-month scale. As a result, the transport errors in the 2-week mean afternoon $FFCO_2$ gradients from 100 magl sites to the JFJ reference site range from 0.52 ppm to 1.11 ppm. The transport errors in the 1-day mean afternoon $FFCO_2$ gradients range from 1.94 to 4.15 ppm (from 0.36 to 0.77 ppm in the case of errors on 1-month mean afternoon $FFCO_2$ gradients, respectively).

As indicated in section 2, we also want to compare the observation errors to the projection of the prior uncertainty in the observation space $p(\mathbf{H}(\mathbf{x}^t - \mathbf{x}^b) \mid \mathbf{x}^b)$ denoted $\mathbf{H}\boldsymbol{\varepsilon}_b$ (and called "prior $FFCO_2$ errors" hereafter, $\boldsymbol{\varepsilon}_b$ corresponding to the prior uncertainties). Following the same approach as for the estimation of the representation and aggregation errors, and setting $\mathbf{x}^b$, as in

the companion inversion studies, with emission budgets from PKU-CO_2-2007 (hereafter $\mathbf{x}^{PKU}$), we derive estimates of $\mathbf{H}\boldsymbol{\varepsilon}_b$ based on statistics on $\mathbf{H}^{prac}(\mathbf{x}^{EDG\text{-}IER}-\mathbf{x}^{PKU})$.

4. Results: estimates of the representation and aggregation errors

This section characterizes the representation, aggregation and prior $FFCO_2$ errors, derived from the method described in section 3. This characterization consists in providing their typical values (estimates of their standard deviations), investigating whether they bear temporal or spatial correlations while such correlations of the observation errors are traditionally ignored by atmospheric inversions (Rödenbeck et al., 2003; Chevallier et al., 2005; Peylin et al., 2013), and in investigating the validity of the assumptions that these observation errors have Gaussian and unbiased distributions. Section 4 focuses on the errors for a standard sampling strategy i.e. 2-week mean afternoon sampling at 100 magl. Section 5 will explore the sensitivity of the results to the temporal sampling strategy (from 1-day to 1-month mean afternoon sampling) and give insights on the errors that would have been obtained if considering measurements sites with a different measurement height.

Finally (in section 6), we compare the typical values of the representation, aggregation and prior $FFCO_2$ errors to the model transport errors (derived in section 3), to the measurements errors (given in the introduction), and to the typical signal of $FFCO_2$ modelled at the sites considered in this study.

4.1 Spatial distribution of the errors and spatial categorization

The root mean square (RMS) of the representation, aggregation and prior $FFCO_2$ errors for the 1-year long time-series of 2-week mean $FFCO_2$ gradients at each of the 0.5° to 3.5°×2.75° horizontal grid cells (depending on the error and thus on the scale at which it can be computed) are given in Figure 3b, c and d. In general, the RMS of the representation error for land grid cells ranges between 0.4 and 4.0 ppm across Europe, while the RMS of the aggregation and prior $FFCO_2$ errors are much smaller.

From Figure 3b, the representation error at 100 magl shows higher values in the grid-cells

classified as urbanized and large cities such as London, Paris, industrialized areas in Germany, etc. More generally, the spatial distribution of representation error shows a good consistency with the mask of the urban grid cells defined based on the population density (Figure 3a, see its definition in section 2.1.2), indicating higher representation error in urban grid cells. We conclude that different statistics of the representation error need to be derived for the "urban" 0.5 ° resolution land grid cells of the mask in Figure 3a in one hand, and "rural" 0.5° land grid cells of this mask on the other hand.

On the opposite, the aggregation error (Figure 3c) being sampled at the coarse (~3° horizontally) grid resolution while urban area have generally smaller horizontal scales, their subsampling and thus the derivation of statistics for "urban" and "rural" grid cells (defined in Section 2.1.2) does not seem to be adapted.

The prior $FFCO_2$ errors (Figure 3d) have a magnitude similar to the aggregation error. Their spatial distribution is strongly linked with that of the differences between the emission budgets for the control regions / months from the two inventories EDG-IER and PKU-CO_2-2007. As a consequence, it is not systematically consistent with that of the most urbanized areas in Europe. As an example, mean prior $FFCO_2$ errors reach 0.5 ppm in the Balkans but do not exceed 0.3 ppm in Northern Italy or in England. As for the aggregation error, the derivation of statistics of the prior $FFCO_2$ error for "urban" and "rural" grid cells is not adapted.

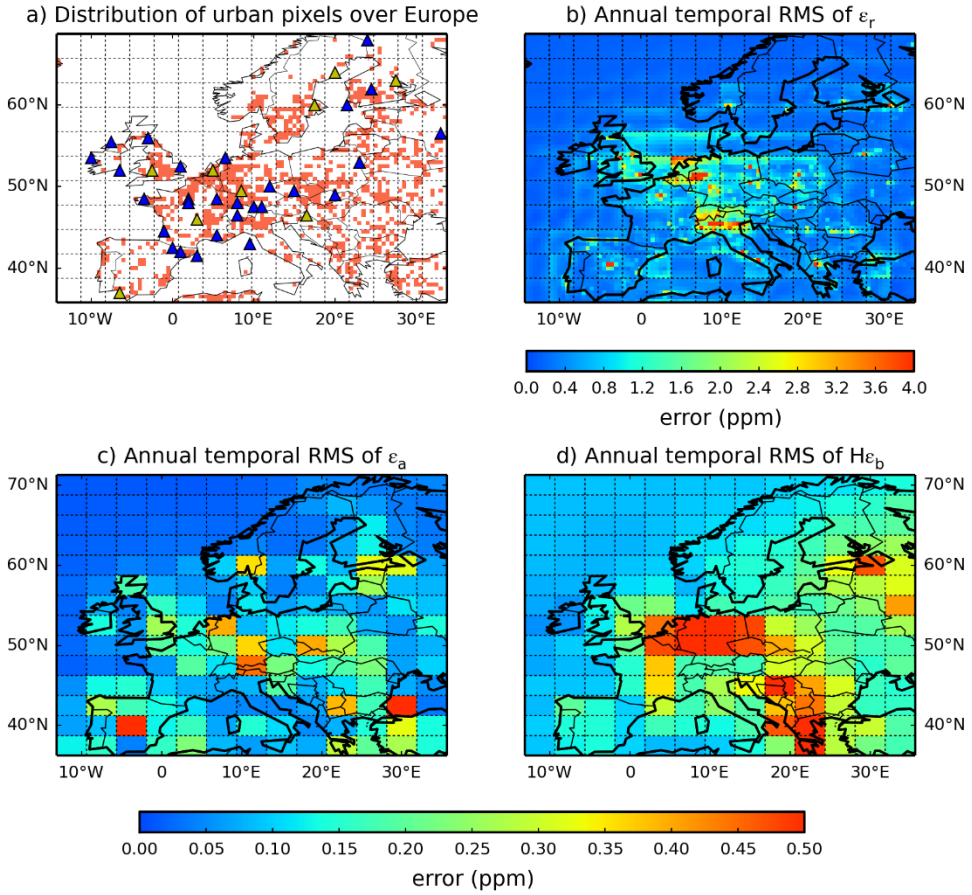

Figure 3 Distribution of urban pixels (defined by population density, section 2.1.2) over Europe at 0.5 ° resolution (a) and maps of the root mean square (RMS) of the 1-year long time series of the representation errors ε_r (at 0.5° resolution) (b),ε_a (at 3.75 °×2.5 ° resolution) (c) and the prior $FFCO_2$ errors $\mathbf{H}\varepsilon_b$ (at 3.75 °×2.5 ° resolution) (d) for 2-week mean afternoon $FFCO_2$ gradients (from 100 magl sites to the JFJ reference site) (unit: ppm). In (a), the triangles give the location of the sites of a typical continental observation network similar to ICOS (ICOS, 2008; 2013); blue triangles means that the stations are in "rural" pixels, while yellow triangles means the stations fall in "urban" pixels.

4.2 Temporal evolution of the errors and temporal categorization

Assuming that the statistics of the observation errors are independent of the location within the spatial categories defined above, we analyze the temporal variations of these statistics through that of the spatial RMS (over all corresponding 0.5 ° to 3.5 °×2.75 ° horizontal land grid cells) of the urban and rural representation errors, of the aggregation errors and of the prior $FFCO_2$ errors for the 2-week mean afternoon $FFCO_2$ gradients to JFJ. The corresponding time series are given in Figure 4.

There is a clear seasonal variation of the urban and rural representation errors (Figure 4a). In spring and summer, when the vertical mixing of the lower atmosphere is stronger, the representation error drops to about 0.7 ppm for urban areas and 0.5 ppm for rural areas, while

in winter, it can peak at about 2.3 ppm over urban grid cells and 1.1 ppm over rural grid cells, which is about twice the values in summer. Levene's test shows that the variances of the representation errors are distinct between the four seasons, except when comparing values for urban representation errors in spring vs. summer (p<0.05 between rural values of all other pairs of seasons, or between urban values of any pair of season). Therefore, different statistics of the representation errors need to be derived for the different seasons i.e. spring (March to May), summer (June to August.), autumn (September to November) and winter (December, January and February). The prior $FFCO_2$ errors also show significant differences between the different seasons (p<0.05 between all pairs of seasons). So the same seasonal categorization will also applied to them.

By contrast, there is only small seasonal variations of the aggregation error (Figure 4b). ε_a has lower values in spring and summer than in autumn and winter (Levene's test, p<0.05). Consequently, we use different statistics for ε_a in spring/summer and in autumn/winter.

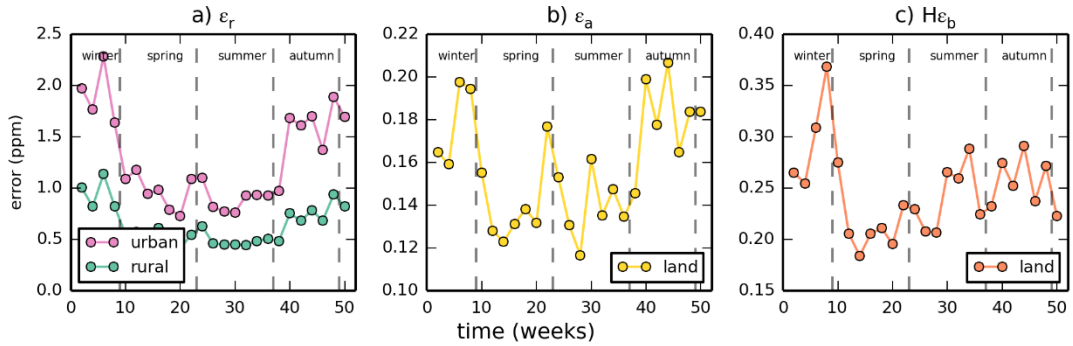

Figure 4 Time series of the spatial RMS of the urban and rural representation errors (a), of the aggregation errors (b) and of the prior $FFCO_2$ errors (c) for 2-week mean afternoon $FFCO_2$ gradients (from 100 magl sites to the JFJ reference site) (unit: ppm).

4.3 Statistics of the errors

The distributions of most of the different categories of representation, aggregation and prior $FFCO_2$ errors defined by the sections 4.1 and 4.2 are shown in Figure 5. These categories used to build these distributions have a high number of values (at least 715 samples within one category, this minimum number applying to $\mathbf{H\varepsilon_b}$ in winter) so that the statistics from these distributions should be robust.

Two theoretical distributions are superimposed to each of the practical sampling of the

errors in Figure 5: a Gaussian distribution whose mean and standard deviation correspond to that of the practical sampling, and a Cauchy distribution whose location and scale parameters correspond to that of the practical sampling. For all categories of representation, aggregation and prior $FFCO_2$ errors, the Gaussian distribution is a poor approximation of the practical distribution, whereas the Cauchy distribution, with a relatively narrow peak, generally fits better with the practical distribution.

All these distributions have near-zero means, which supports the assumption that observation errors are unbiased. The standard deviations of these distributions are indicated in Table 1. The representation errors are much larger than the aggregation errors, and reach as high as 1.89 ppm for "urban" grid cells in winter (Figure 5c). The aggregation errors(Figure 5e and 5f) are about one order of magnitude smaller than representation errors. The prior $FFCO_2$ errors (Figure 5g and 5h) are slightly larger than the aggregation errors but are still lower than the representation error by a factor of 3 to 6.

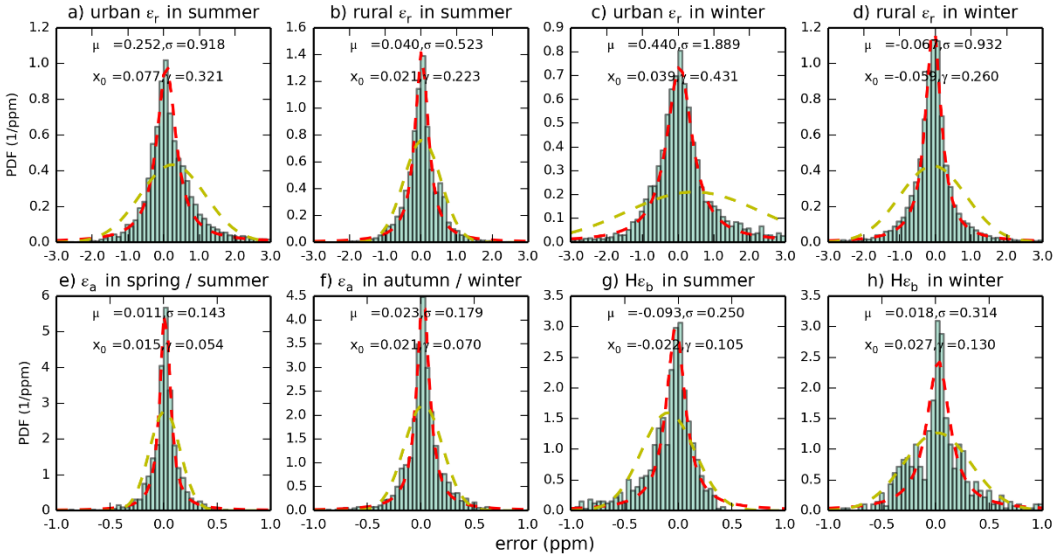

Figure 5 Probability density functions (PDFs) of the representation, aggregation and prior $FFCO_2$ errors for 2-week mean afternoon gradients (from 100 magl sites to the JFJ reference site) for nearly all of the categories defined by sections 4.1 and 4.2 (only PDFs in spring and fall for urban and rural representation errors and for the prior $FFCO_2$ errors are not shown). The theoretical fit of these PDFs with Gaussian distributions (yellow dash lines) in terms of mean (μ) and standard deviations (σ), and the theoretical fit of these PDFs with Cauchy distributions (red dash lines) in terms of location parameter (x0) and scale factor (γ) are also reported on the graphs.

Table 1 Standard deviations (in ppm) of the different categories of representation, aggregation and prior $FFCO_2$ errors for the 2-week mean afternoon $FFCO_2$ gradients and seasonal RMS (in ppm) of the $FFCO_2$ gradients between all potential rural or urban locations of 100 magl continental sites and JFJ and over all time periods during each season as simulated at 0.5 °resolution when using CHIMERE and the EDG-IER inventory (i.e. our practical representation of the true gradients $\mathbf{H}_{transpHR}{}^t\mathbf{f}_{HR}{}^t$)

	Spring		Summer		Autumn		Winter	
	Urban	Rural	Urban	Rural	Urban	Rural	Urban	Rural
ε_r	0.99	0.52	0.92	0.52	1.50	0.71	1.89	0.93
ε_a	0.17				0.21			
$\mathbf{H}\varepsilon_b$	0.22		0.25		0.27		0.31	
"True" gradient	3.1	2.4	2.9	2.2	4.1	3.0	5.0	3.7

The temporal correlations of the different spatial categories of representation, aggregation and prior $FFCO_2$ errors for 2-week mean afternoon gradients are illustrated in Figure 6a using the temporal auto-correlations for errors of all the occurrences of the gradients from all the potential 100 magl sites to the JFJ reference site. The autocorrelation for a given time-lag is derived from the ensemble across all times and sites of all couples of errors which both apply to the same site and to two times separated by the given time-lag. Initial estimates accounting for the temporal categories (not shown) indicated that the temporal auto-correlations for different seasons are quite close to each other, so the temporal categorization is ignored here.

There are strong temporal auto-correlations in all types of errors for 2-week mean afternoon gradients. The temporal auto-correlations of the representation errors, of the aggregation errors and of the prior $FFCO_2$ errors are above 0.4 even when the timelag exceeds 3 months. The estimates of the autocorrelations of the errors computed separately for each potential site used in the gradient $FFCO_2$ computations (not shown), are nearly null for timelag larger than 1 month for most of the potential sites. This indicates that the errors combine a sort of long term error component that is specific to each site (acting as a bias it does not show up in the site correlation), and a short term error component whose typical correlation timescale is smaller than 1 month. A sum of two exponentially decaying functions $r(\Delta t)=a\times e^{-}$

$^{\Delta t/b}+(1-a)\times e^{-\Delta t/c}$ is thus fitted to the estimate of the temporal auto-correlations (when using a sampling of the errors across all the times and sites) of each type of error, where Δt is the timelag (in days) and a, b, c are the parameters that are optimized by the regressions (Table 2). The short timescale of correlation b arising from these regressions ranges from 10 days for the prior $FFCO_2$ error to 19 days for the urban representation error. These values are close to the sampling integration time of 2 weeks. The long timescale of correlation c is larger than 1 year except for the prior $FFCO_2$ errors. The relative weight of the short term component of the errors (a) for the 2-week mean afternoon $FFCO_2$ gradients is systematically below 40%. It is more important for the representation errors than for the aggregation and prior $FFCO_2$ errors.

Table 2 The parameters optimized by the regressions of the temporal auto-correlations of the representation, aggregation and prior $FFCO_2$ errors for 2-week and 1-day mean afternoon $FFCO_2$ gradients (from all the potential 100 magl sites to JFJ), using e-folding functions $r(\Delta t)=a\times e^{-\Delta t/b}+(1-a)\times e^{-\Delta t/c}$ and ignoring the different temporal categories.

	a	*b*	*c*
2-week mean afternoon $FFCO_2$ gradients			
urban ε_r	0.29	18.9	>365
rural ε_r	0.36	11.6	>365
ε_a	0.16	11.2	>365
$H\varepsilon_b$	0.21	10.5	332
1-day mean afternoon $FFCO_2$ gradients			
urban ε_r	0.66	0.90	>365
rural ε_r	0.78	0.78	>365
ε_a	0.54	1.1	>365
$H\varepsilon_b$	0.49	2.1	325

The spatial correlations within the different categories of error on 2-week mean afternoon gradients or between the urban and rural representation errors on 2-week mean afternoon gradients are shown in Figure 6b. Their estimates for a given distance are based on the ensemble across all times and sites of all couples of errors which both apply to the same time and to two sites separated by the given distance (using intervals for this distance of $\pm$20 km for the

representation errors at the 0.5 horizontal resolution, and of ±150 km for the aggregation errors and the prior $FFCO_2$ errors at the 3.75°×2.5° resolution). Again, initial estimates accounting for the temporal categories (not shown) indicated that the spatial correlations for the different seasons are quite close, so the temporal categorization is also ignored here.

The spatial correlations of the representation and aggregation errors drop very fast with increasing distance which is not the case for the prior $FFCO_2$ errors. The urban and rural representation errors even have negative spatial correlations when the distance is within the range of 100-300 km. This is driven by the fact that the representation and aggregation errors when using the average concentration and emissions (respectively) within a given area (a grid cell or a region) are necessarily balanced and have thus opposite signs over areas smaller than that of this area. An exponentially decaying function $r(\Delta d)=e^{-\Delta d/a}$ is fitted to these estimates of spatial correlations, where Δd is the distance (in kilometers) and where a is the parameter that the regressions derive. The e-folding correlation lengths a are 75 and 86 km for the urban and rural representation errors respectively. The spatial correlations between urban and rural representation error has a similar e-folding correlation length of 55 km. In general, even though those correlations between rural and urban representation errors are smaller than that within a given category of representation error, they are very close to them, and the spatial correlations of the representation errors are weakly impacted by the categories which we have defined for these errors. The e-folding correlation length a is 171 km for the aggregation error. All of the correlation lengths derived for the representation and aggregation errors are thus smaller than the length of the LMDZ transport model grid cells. The spatial correlations of the representation and aggregation errors are thus negligible at this transport model resolution. However, the correlation length scale of the prior $FFCO_2$ errors is approximately 700 km, which is larger than transport model resolution.

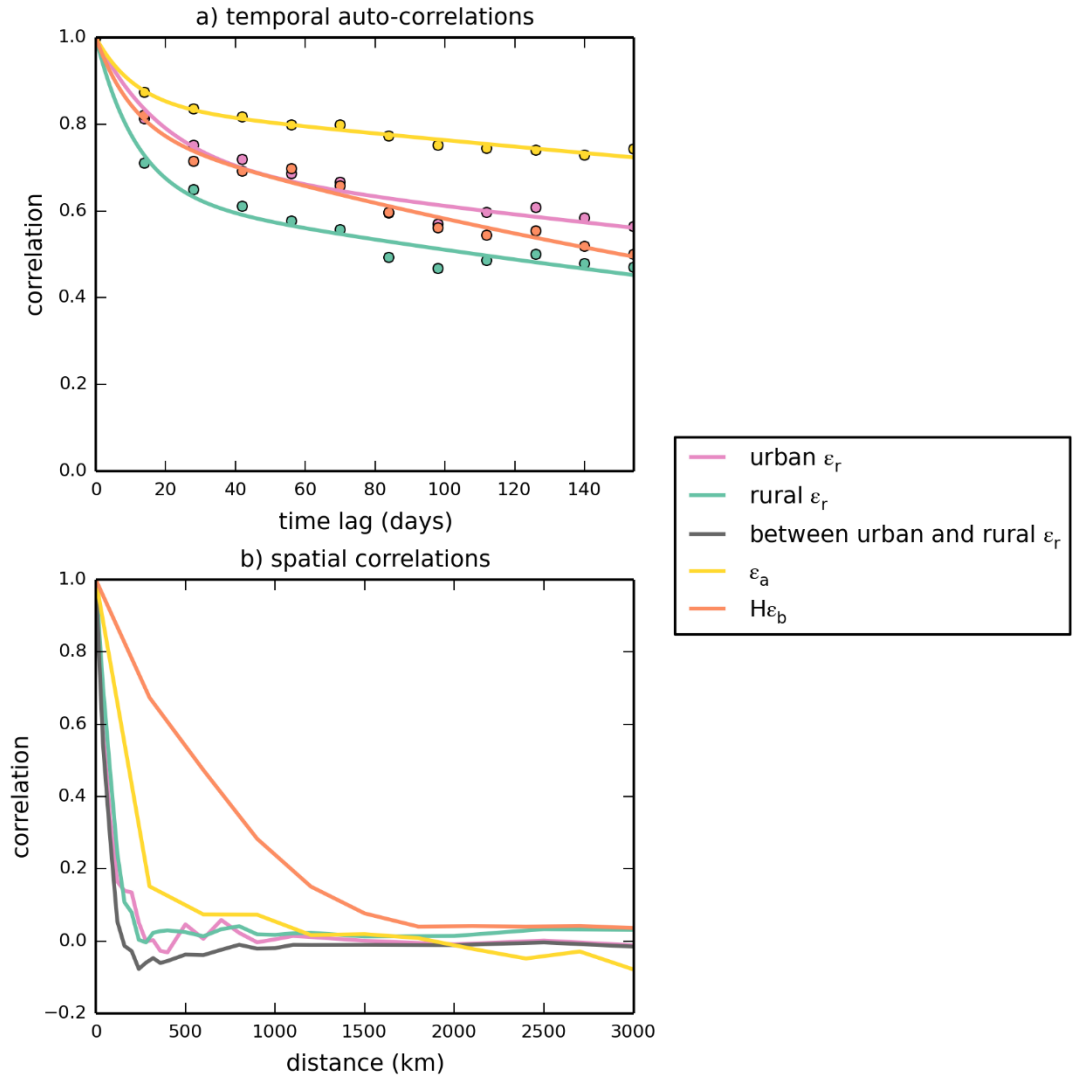

Figure 6 Estimates of the correlations for the different spatial categories of representation errors (urban ε_r in purple and rural ε_r in green), aggregation errors (in yellow) and prior $FFCO_2$ errors (in red) for 2-week mean afternoon $FFCO_2$ gradients (from all the potential 100 magl sites to JFJ), ignoring the different temporal categories (i.e. mixing errors from all seasons and thus computing temporal auto-correlations between errors across different seasons or using a temporal sampling across different seasons to compute spatial correlations). a) Temporal auto-correlations. Dots correspond to the estimates of the temporal auto-correlations. Lines correspond to regression curves with e-folding functions $r(\Delta t)=a\times e^{-\Delta t/b}+(1-a)\times e^{-\Delta t/c}$, where Δt is the timelag (in days), and where a, b and c are the parameters optimized by the regression. b) Spatial correlations. The spatial correlations between urban and rural representation errors (in brown) are given along with the correlations within the different categories of errors.

5. Sensitivity of the results to the sampling heights and to the temporal sampling

5.1 Sensitivity to the sampling heights

All the results above are derived for 2-week mean afternoon gradients between sites at 100

magl and JFJ. However, actual sampling heights for continuous measurement sites can range from less than 50 magl to more than 300 magl (Kadygrov et al., 2015). We thus investigate the variations of the different categories of representation, aggregation and prior $FFCO_2$ errors for 2-week mean afternoon gradients as a function of the sampling heights for all sites whose difference to JFJ correspond to these gradients, from near ground (20 magl) to top of planetary boundary layer (1000 magl, roughly). The height of the measurements at the JFJ reference site is not modified hereafter. The $\mathbf{H}_{samp}^{coloc}$ and $\mathbf{H}_{transpHR}^{CHIM}$ operators (their selection of the LMDZ and CHIMERE vertical levels corresponding to the measurement locations; see section 2.1.3 and section 3) are adapted for such a derivation of the vertical profiles of the errors. The sampling heights tested are 20, 50, 100, 200, 300, 500 and 1000 magl. These heights correspond to seven different vertical levels in CHIMERE (the bottom sampling height corresponds to the 1st CHIMERE level while the top sampling height corresponds to the 12nd to 15th CHIMERE level depending on the horizontal grid cells). The representation errors being computed at the spatial resolution of CHIMERE, we thus obtain different value of the different categories of representation errors per sampling height. However, due to its coarse vertical discretization, these sampling heights correspond to only the first five levels of the LMDZ model. This explains why only five values of the different type of categories of aggregation and prior $FFCO_2$ errors (that are computed at the spatial resolution of LMDZ) are derived for these seven sampling heights.

Figure 7 shows the corresponding vertical variations of the standard deviations of all the occurrences of each category of representation, aggregation and prior $FFCO_2$ errors for 2-week mean afternoon gradients. All categories of the errors decrease significantly with increasing sampling height. However, the different categories of errors have different vertical profiles. The standard deviation of the representation error for gradients between 300 magl sites in “urban” grid cells and JFJ is equal to ~70% (in summer) or to ~50% (in winter) of the values for gradients between 20 magl sites in urban grid cells and JFJ. This seasonal variation of the decrease with height is likely due to the higher emissions but shallower depth of the vertical mixing in fall-winter than in spring-summer. The representation errors of $FFCO_2$ gradients between rural grid cells and JFJ have relatively smaller vertical variations. This is likely due to the fact that the atmospheric signature of the emitting urban grid cells and thus the

corresponding representation errors have been highly diffused in the vertical during the transport from such urban grid cells to the rural grid cells. The standard deviations of the aggregation errors for gradients between 300 magl sites in "urban" grid cells and JFJ are equal to about 75% of those for gradients between 20 magl sites and JFJ. Of note is also that the aggregation errors drop significantly as the heights exceed 400 magl unlike the representation errors. The vertical distribution of the prior $FFCO_2$ errors is similar to that of the aggregation errors. As a consequence, from the surface to 100-300 magl, the ratio of the prior $FFCO_2$ errors over the sum of all observation errors increases. However, mainly due to the fact that measurement errors do not decrease with altitude, this ratio decreases with increasing heights above 300 magl.

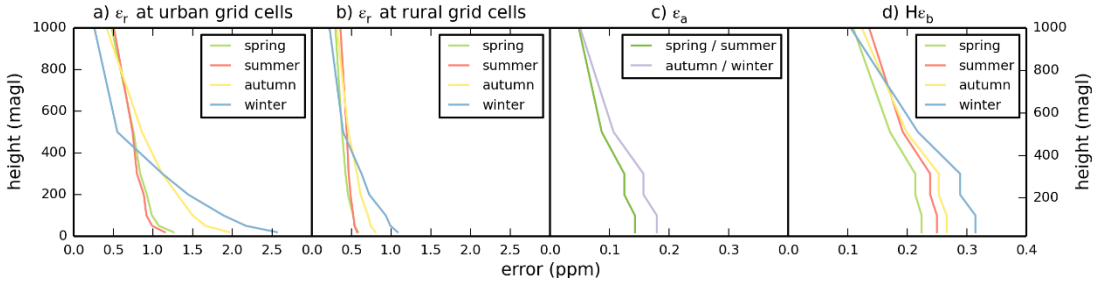

Figure 7 Standard deviations of all the occurrences of the representation, aggregation and prior $FFCO_2$ errors for specific categories of 2-week mean afternoon $FFCO_2$ gradients, as a function of the sampling height above ground (unit: ppm)

5.2 Sensitivity to the temporal sampling

All the results above about the representation and aggregation errors are derived for 2-week mean $FFCO_2$ afternoon gradients. Here, we investigate the representation and aggregation errors for 1-day, 1-week, 2-week and 1-month mean afternoon gradients between 100 magl sites and the JFJ reference site. The $\mathbf{H}_{samp}^{coloc}$ and $\mathbf{H}_{transp}^{CHIM}$ operators (their temporal averaging of the afternoon $FFCO_2$ gradients; see section 2.1.3 and section 3) are adapted accordingly.

The standard deviations of all the occurrences of $FFCO_2$ gradients within each category of the representation, aggregation and prior $FFCO_2$ errors, and of the gradients generated using our practical simulation of the actual gradients $\mathbf{H}_{transpHR}{}^{t}\mathbf{f}_{HR}{}^{t}$ are shown in Figure 8 as a function of the sampling integration time. All the errors and simulated gradients decrease significantly from 1-day mean afternoon samplings to 2-week mean afternoon samplings, while the decrease of the values from 2-week to 1-month mean afternoon samplings is relatively small. As

analyzed earlier when studying the temporal auto-correlations of the errors, this highlights the fact that these errors combine a long-term component specific to each site and a short term component. Figure 8e and 8f show that this also applies to the simulation of the $FFCO_2$ gradients. As for the analysis of the temporal autocorrelations of the errors, a sum of two exponentially decaying functions $\varepsilon(l)= \varepsilon(1)\times[a\times e^{-(l-1)/b}+(1-a)\times e^{-(l-1)/c}]$ is thus fitted to the values of the errors and simulated gradients as functions of the sampling integration time, where l is the integration time (in days) of the mean afternoon sampling, $\varepsilon(1)$ is the standard deviations of the errors (or simulated gradients) with 1-day sampling, and where a, b and c are the parameters that are optimized by the regressions. The values obtained for the b range between 3 and 5 days, and those of c often exceed 1 year (Table 3), reflecting, as when fitting the temporal auto correlations, the synoptic timescales and a long-term site specific error respectively. While for the representation and aggregation errors, a (the weight of the short term component, Table 3) ranges between 24% and 44%, it is lower for the prior $FFCO_2$ errors (17% to 22% depending on the season) and for the simulated gradients (9% to 20% depending on the season).

Further analysis of the results when using different sampling integration time for the observations indicates that the spatial correlations of the errors do not evolve significantly as a function of this integration time. However, Figure 9 shows that the temporal correlations of the representation errors associated with 1-day mean afternoon gradients decrease a lot with increasing timelag until the timelag reaches 1 week, which could not be characterized when analyzing errors for 2-week mean gradients in section 4.3. Fitting the temporal correlations of the errors for 1-day mean samplings with the sum of two exponentially decaying functions (as when analyzing the temporal correlations of the errors for 2-week mean gradients, Table 2) indicate that the timescale of correlation for the short term components of the representation and aggregation errors is about 1 day and that for the prior $FFCO_2$ error is 2.1 days. On the other hand, the timescale of the long-term component of the errors for 1-day mean gradients still exceed 1 year except for the prior $FFCO_2$ error, as when analyzing errors for 2-week mean gradients. However, the relative weight of the short-term component (a) are one to two times higher than that for 2-week mean afternoon gradients when analyzing the 1-day mean gradients.

Of note is the fact that the aggregation error for 1-day gradients due to the coarse resolution of the control vector has a component (in addition to the short term and long term components

already characterized) that has a weekly cycle which is shown by the cycle of the temporal autocorrelations of the error at this frequency, and which reflects the quite artificial differences between the flat temporal profiles of the emissions in the PKU-CO_2-2007 inventory and the hourly variations of the emissions in the EDG-IER inventory. The existence, for all types of errors, of a third component at the daily scale in addition to a short term component at the synoptic scale and to the long term component, which could not be detected by the analysis of the autocorrelations at the 2-week mean scale, could explain the differences between the results obtained when analysing the results at the 1-day vs. 2-week scale.

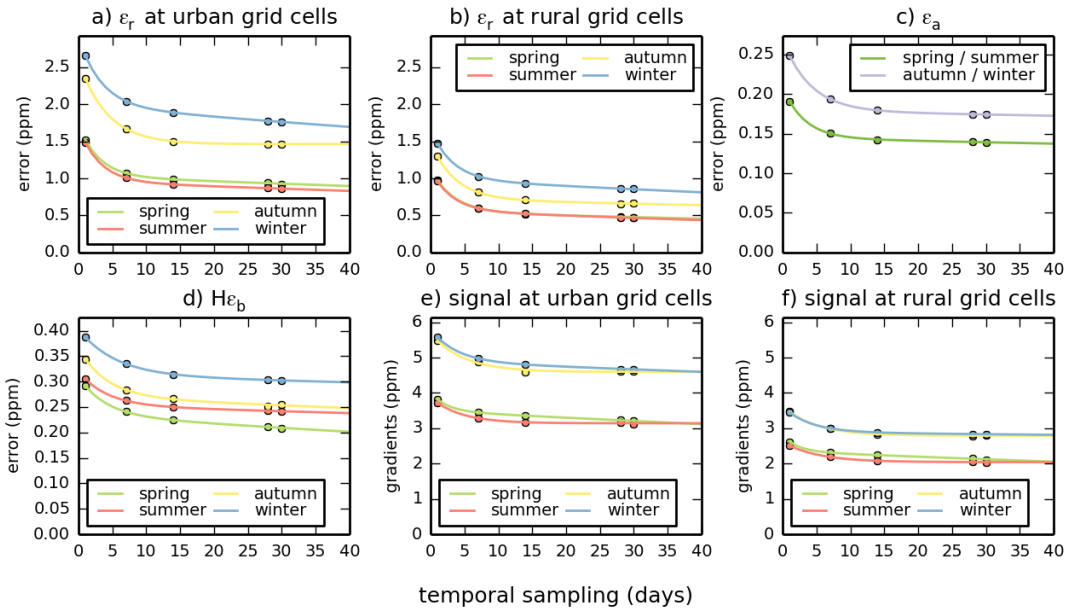

Figure 8 Standard deviations of all the occurrences of the representation, aggregation and prior $FFCO_2$ errors for 1-day to 1-month mean afternoon $FFCO_2$ gradients between 100 magl sites and the JFJ reference site (unit: ppm), and RMS of the simulated gradients at 0.5 ° resolution when using CHIMERE and the EDG-IER inventory (i.e. our practical representation of $\mathbf{H}_{HR \rightarrow HR}{}^{t}\mathbf{f}_{HR}{}^{t}$). The sampling durations are expressed in days. Dots correspond to the estimates of the standard deviations of the errors and of the quadratic mean of the simulated gradients. Lines correspond to regression curves with e-folding functions $\varepsilon(l)= \varepsilon(1)\times[a \times e^{-(l-1)/b}+(1-a) \times e^{-(l-1)/c}]$, where l is the duration (in days) of the mean afternoon sampling, $\varepsilon(1)$ is the standard deviations of the errors (or simulated gradients) for 1-day sampling, and where a, b and c are the parameters optimized by the regressions. Results for a) urban ε_r; b) rural ε_r;c) ε_a; d) $\mathbf{H}\varepsilon_b$; e) simulated gradients for urban grid cells; f) simulated gradients for rural grid cells.

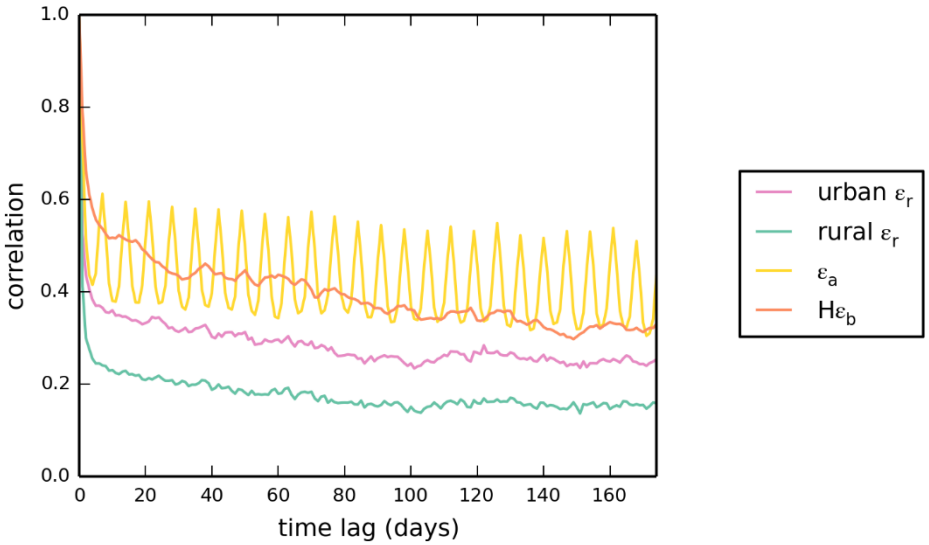

Figure 9 Temporal auto-correlations of the representation (urban ε_r in purple and rural ε_r in green), aggregation (in yellow) and prior $FFCO_2$ errors (in red) for 1-day mean afternoon $FFCO_2$ gradients (from all the potential 100 magl sites to JFJ), ignoring the different temporal categories (i.e. mixing errors from all seasons and thus computing temporal auto-correlations between errors across different seasons).

Table 3 The parameters optimized by the regressions of the standard deviations of the representation, aggregation and prior $FFCO_2$ errors as functions of the temporal sampling of the observations, for 1-day to 1-month mean afternoon $FFCO_2$ gradients between 100 magl sites and the JFJ reference site (unit: ppm), and RMS of the simulated gradients at 0.5 °resolution when using CHIMERE and the EDG-IER inventory (i.e. our practical representation of $\mathbf{H}_{transpHR}{}^t\mathbf{f}_{HR}{}^t$).

	Spring			summer			autumn			winter		
	a	*b*	*c*	*a*	*b*	*c*	*a*	*b*	*c*	*a*	*b*	*c*
urban ε_r	0.33	2.9	288	0.36	3.0	280	0.38	4.1	>365	0.26	3.4	258
rural ε_r	0.44	3.3	220	0.41	3.0	154	0.44	3.5	316	0.33	3.2	202
ε_a	0.24	3.2	>365	0.24	3.2	>365	0.28	4.1	>365	0.28	4.1	>365
$\mathbf{H}\varepsilon_b$	0.20	3.9	263	0.17	4.1	>365	0.22	4.1	>365	0.19	5.4	>365
simulated gradients (urban)	0.09	2.3	353	0.16	4.4	>365	0.16	4.8	>365	0.13	3.8	>365
simulated gradients (rural)	0.11	2.2	300	0.19	5.1	>365	0.20	4.8	>365	0.16	4.0	>365

6. Discussion

6.1 Validity of the assumption that the observation errors of $FFCO_2$ gradients have an unbiased and Gaussian distribution

In section 2.2, we justified our estimation of the representation, aggregation and prior $FFCO_2$ errors based on the assumption that the distributions of these errors are Gaussian and unbiased (as required for the application of the atmospheric inversion framework; (Lorenc, 1986)). Figure 5 shows that the means of the representation, aggregation and prior $FFCO_2$ errors are much smaller than the standard deviations of these errors, indicating that the assumption that their distribution is unbiased is relevant. A Cauchy distribution generally shows a better fit with the practical sampling of the errors than the Gaussian distribution, but the Gaussian distribution is still a good approximation of the former. However, the dependence of the long term component of the errors to the sites used for the computation of the gradients could be interpreted as a sort of local bias in the representation and aggregation errors. While such a behavior of the prior errors is generally well anticipated by inversion systems assuming long temporal autocorrelations of the prior uncertainties, these representation and aggregation errors can hardly be considered as a random noise for the observations as is done traditionally. However, accounting for both the short term and the long term error temporal correlations in the configuration of the inversion systems is feasible if using the type of regressions used in this study, and, if done, should enable a good characterization of these errors. And these analysis strengthen the posterior justification for our practical derivation of the representation and aggregation errors.

6.2 The different temporal components of the errors and simulated gradients

The analysis of the temporal autocorrelations of the errors for 2-week to 1-day mean errors and of the decrease in the standard deviation of the errors as a function of the temporal sampling integration time reveals three rather than two dominating component of the representation, aggregation and prior $FFCO_2$ errors. The first component, at the daily scale, may be driven by the day to day variations of the emissions which are high compared to the long term variations of these emissions and which are highly uncertain in present inventories. This component can be highlighted when analyzing errors for 1-day mean gradients only. The second component, at the synoptic scale, is likely related to the transport of the error from the emission areas to the sites through synoptic events which are a critical component of the transport in Europe (Parazoo et al., 2008; Garc á et al., 2010). The third component is related to the slowly varying (at the

"long-term" seasonal to inter-annual scales), continuous and direct influence of the emission in the vicinity (in the same transport model grid cell) of the different sites, which thus significantly varies from site to site and depending whether it applies to urban or rural sites. The urban sites receive a strong signature of the emissions in their vicinity while the rural sites are affected by these emissions in their corresponding grid cells through a more indirect process of aggregation, and with a weaker signal. This explains why the relative weight of the synoptic component compared to the long term one is generally smaller for gradients between urban sites and JFJ than for gradients between rural sites and JFJ.

The analysis of these different components reveals that the daily components dominate in the errors and simulated signal. This component is cancelled when sampling the observations at the 1-week to the 1-month scale, in which case the long-term component dominates the errors and simulated signal. The differences between the numbers (Table 2) characterizing the temporal scales of these components and their relative weight depending on the specific analysis lead in this study can be explained by the uncertainties associated with these statistical analyses, by the difficulty to make a regression with a sum of three exponentially decaying functions when analyzing the errors and signal for 1-day mean gradients (which could, in principle, help reconcile it with the results when analyzing the errors and the signal for 2-week mean gradients), and by the difference between the analysis of the temporal correlations of errors for a given temporal sampling of the observations and that of the amplitude of the error for different temporal sampling of the observations. However, their general consistency gives insights into the typical correlation length scales to be used for accounting for such correlations when conducting atmospheric inversions, which will be critical given the amplitude of these correlations.

6.3 Comparison of the different errors: potential for filtering the signature of the uncertainties in the average emissions over large region?

The analysis of the standard deviation and of the temporal scales of autocorrelations of the errors indicate that the representation error and the transport errors are the largest observation errors for 100 magl afternoon observations for any temporal scale of sampling when using the modeling framework of our study. They are larger than the measurement errors (about 1 ppm)

which is the third dominant type of observation errors in our modeling framework. The aggregation errors have a relatively small standard deviation compared to these errors (see their smaller standard deviation in Table 1 and their shorter temporal scale of auto-correlation in Table 2).

In total, the weight of the observation errors can reach up to 50% of the typical amplitude of the simulated 1 week to 2 week mean afternoon $FFCO_2$ gradients, either for urban or rural sites, or for any season and temporal sampling. It can even reach up to 90% of this signal for 1-day mean afternoon $FFCO_2$ gradients. This questions the precision of the signature of the large scale budget of $FFCO_2$ emissions that could be filtered from the observations. Furthermore, the actual signal assimilated in inversions in order to correct for the prior knowledge on the emissions at the control / 1-month scale is that of the prior $FFCO_2$ errors whose amplitude is generally smaller than that of the representation, transport and measurements errors. From our analysis, the signals at a given site from uncertainties in the distribution of the local emissions (characterized by the representation error) exceed those of the uncertainties in the emissions at the regional scale and the signal from the uncertainties in the distribution of the emissions at the sub-regional scale (characterized by the aggregation error) at any temporal scale.

The temporal autocorrelations of the prior $FFCO_2$ error have a structure that is similar to that of the representation errors. Its long-term component has a shorter temporal scale than that of the representation error but this can hardly be viewed as a basis for a practical separation of the prior $FFCO_2$ and representation errors given that both these temporal scales exceed 300 days. The temporal length scale of the short term components for the prior $FFCO_2$ and representation errors are different. However, the combination of representation, aggregation, measurement and transport errors which all have their own temporal scale of correlations will likely make it difficult to exploit the structures of the short term variations to filter the prior $FFCO_2$ errors.

The most promising result for the potential filtering of the prior $FFCO_2$ errors lie in the analysis of the spatial correlations of the errors. The prior $FFCO_2$ errors are connected to uncertainties in emissions at large spatial scales which are not necessarily compensated between neighboring control regions, while representation and aggregation errors should be compensated at the resolutions of the transport model to the control vector (and thus cancelled through atmospheric mixing faster than the prior $FFCO_2$ errors). At the same time, transport

errors and measurement errors should not be correlated in space. In consequence, the spatial correlations of the prior $FFCO_2$ errors are larger than that of the observation errors. This could be exploited by the inversion to filter it if it can rely on a spatially dense network of measurement sites.

An analysis of the correlations between different types of errors and the transport conditions (e.g., wind direction and speed) could bring additional insights on the capability for isolating the prior $FFCO_2$ errors from the observations. However, such an analysis could hardly be based on the framework of this study for which the different types of error (in particular the representation and prior $FFCO_2$ errors) are derived using different modelling frameworks. A full assessment of this capability requires atmospheric inversions using the characterization of the errors from this study. However, this study already give insights into the challenges underlying the monitoring the emissions at large scale.

Of note is that the quite simple analysis of the sensitivity of the ratio between the prior $FFCO_2$ errors and the observation errors supports the monitoring of $FFCO_2$ at heights ranging between 100 magl and 300 magl when targeting the large scale budgets of emissions. It is also the traditional heights for ICOS network (Kadygrov et al., 2015).

The results from this study do not strongly encourage to sample $FFCO_2$ observations at high temporal resolution when targeting the regional / 1-month scale budgets of emissions with atmospheric inversion built on a coarse-grid transport model. We have shown the relative weight of the short term components of the observation errors are larger than that of the prior $FFCO_2$ errors and, as said previously, making it difficult to exploit the difference between the temporal correlation of these short term components to filter the prior $FFCO_2$ errors. However, again, atmospheric inversion experiments would be required to check how much the correlations of the errors with the transport could be exploited, even at high temporal resolution. Still, having 1-day mean sampling would dramatically decrease the weight of the measurement errors on longer time scales that can be considered as a random noise on each individual measurement of $FFCO_2$.

6.4 Increasing the spatial resolution of the atmospheric transport model and of the control variables to increase the potential of the atmospheric inversion?

As explained in section 2.3 and in the Appendix, in theory, controlling the emissions at high resolution or controlling emissions at large scale but perfectly accounting for the aggregation error would yield similar estimates of the emissions at large scale. In practice, as illustrated by Figure 6, the complex structure of the correlations in the aggregation error may prevent such a perfect account for this error in the inversion set-up. Therefore, in principle, it is better to solve for the emissions at the highest resolution as possible.

On the other hand, the representation and transport errors are also highly dependent on the transport model resolution. Since the representation errors are the largest component of the observation error for our modeling framework, increasing the transport model resolution should be viewed as the most critical mean for improving (if needed) the results from atmospheric inversion for the large scale monitoring of the emissions. Cancelling the representation errors would dramatically increase the ratio between the prior $FFCO_2$ errors and the observation errors. However, this would require using a regional inverse modeling framework focusing on a specific area (such as Europe, the US or China) since the horizontal resolution of the atmospheric transport model used for global inversion hardly exceed 3 °resolution.

7. Conclusion

This paper analyzes the critical sources of errors that influence atmospheric inversion of $FFCO_2$ emissions at sub-continental / monthly scale based on continental networks of daily to monthly mean afternoon atmospheric $FFCO_2$ observations. We provide a theoretical derivation of the representation and aggregation errors affecting daily to monthly mean afternoon $FFCO_2$ gradients between possible measurement sites and a background station. This theoretical derivation is adapted to the practical estimation of these errors in Europe for our specific inverse modelling framework that is based on a global coarse-resolution transport model. Our analysis focuses on the derivation of the standard deviations, temporal and spatial correlations of the representation and aggregation errors, the standard deviation of the transport model and measurement errors, along with the standard deviation of the atmospheric signature of the prior uncertainty in the regional / 1-month budgets of the emissions. These statistical parameters will be primarily used to set up a realistic configuration of the observation errors in inversion

experiments described in future papers. In particular, the modelling of the spatial and temporal correlations using one or two exponentially decaying functions and the optimized parameters from the regressions in this study will be used to model the observation error correlations in these experiments.

Our comparison between these statistical parameters for the different types of errors also aims at assessing the ability to filter the signature of the prior uncertainty in the large scale budgets of the emissions from the total observation errors when assimilating 1-day to 1-month mean afternoon $FFCO_2$ gradients (which underlies the potential for the large scale inversion of the emissions). It highlights that the representation, transport and measurement errors dominate the observations errors, while the weight of aggregation error is relatively small. In total, observation errors can reach up to 50% (90%) of the typical 2-week (1-day) mean $FFCO_2$ gradients, and are larger than the signature of the prior uncertainty in the large scale budgets of the emissions. Moderating the representation and transport errors by using a regional transport models at higher resolution could thus be a requirement for the monitoring of $FFCO_2$, even when targeting their large scale budgets. The analysis also highlight the fact the critical weight of the temporal correlation of the representation and aggregation errors, and in particular that they have a long-term component, make it difficult to separate these errors from the signature of the prior uncertainty in the emissions at large scale when assimilating the 1-day to 1-month mean afternoon $FFCO_2$ gradients. Filtering of the signature of the prior uncertainties could potentially rely on its spatial correlations scales which are significantly longer than that of the observation errors. This would require a network dense enough to capture the spatial coherence of this signature (at scales shorter than ~700 km), which could represent a larger number of sites than that of the present ICOS network. Finally, from this study, we do not recommend sampling $FFCO_2$ data at high (1-day to 1-week) rather than low (2-week to 1-month) temporal resolution for the global atmospheric inversion based on coarse-grid transport model, since it demonstrates the difficulties associated with filtering the signal from prior uncertainties at such temporal scales.

More generally, while the statistics of representation and aggregation errors derived in this study primarily relate to the specific atmospheric inversion framework we use in this study, this study brings insights regarding these errors for a wide range of atmospheric applications, and

more specifically to that dedicated to the inversion of the $FFCO_2$ emissions. The practical derivation of their statistics can be easily generalized based on our theoretical framework and used for other studies. The structure and typical amplitude of the representation error derived for the transport of uncertainties in the fossil fuel emissions in Europe at ~3 ° resolution with LMDZ should be similar for other transport models with similar spatial resolution. And the general conclusions raised above regarding the potential for filtering the signature of the uncertainty in the large scale budget of the emissions using "remote" measurement stations should be a general outreach of this study. While the correlations of the observation errors are generally ignored in atmospheric inversion, this study demonstrates how critical it should be to account for them. By conducting inversion experiments accounting for these correlations, the companion papers of this study should now indicate how much the potential for filtering the signature of the uncertainty in the large scale budget of the emissions based on its specific spatial structure can be effectively exploited by atmospheric inversion to control the regional / monthly scale budgets of the emissions.

Appendix

A1 Further decomposition of the representation error

In Equation (4), we derived the representation error as $\mathbf{H}_{transpHR}{}^{t}\mathbf{f}_{HR}{}^{t} - \mathbf{H}_{samp}\mathbf{H}_{transp}{}^{t}\mathbf{H}_{\mathbf{dist}}{}^{t}\mathbf{x}^{t}$. As indicated in section 2.2, it can be further decomposed to 1) errors arises from the modelling of concentrations at coarse resolution in the observation operator while it is compared to local measurements; 2) errors due to representing (averaging) the emissions at the coarse resolution of the transport model (into $\mathbf{f}^{t}=\mathbf{H}_{distr}{}^{t}\mathbf{x}^{t}$) and thus missing the true very-high resolution patterns in the emissions:

$$\mathbf{H}_{transpHR}{}^{t}\mathbf{f}_{HR}{}^{t} - \mathbf{H}_{samp}\mathbf{H}_{transp}{}^{t}\mathbf{H}_{\mathbf{dist}}{}^{t}\mathbf{x}^{t} = (\mathbf{H}_{transpHR}{}^{t}\mathbf{f}_{HR}{}^{t} - \mathbf{H}_{samp}\mathbf{H}_{transpHR\rightarrow LR}{}^{t}\mathbf{f}_{HR}{}^{t}) +$$
$$(\mathbf{H}_{samp}\mathbf{H}_{transpHR\rightarrow LR}{}^{t}\mathbf{f}_{HR}{}^{t} - \mathbf{H}_{samp}\mathbf{H}_{transp}{}^{t}\mathbf{H}_{\mathbf{dist}}{}^{t}\mathbf{x}^{t}) \quad \text{(A1-1)}$$

or in the other way round, accounting for the variability in the fluxes first:

$$\mathbf{H}_{transpHR}{}^{t}\mathbf{f}_{HR}{}^{t} - \mathbf{H}_{samp}\mathbf{H}_{transp}{}^{t}\mathbf{H}_{\mathbf{dist}}{}^{t}\mathbf{x}^{t} = (\mathbf{H}_{transpHR}{}^{t}\mathbf{f}_{HR}{}^{t} - \mathbf{H}_{samp}\mathbf{H}_{transpLR\rightarrow HR}{}^{t}\mathbf{H}_{\mathbf{dist}}{}^{t}\mathbf{x}^{t}) +$$
$$(\mathbf{H}_{samp}\mathbf{H}_{transpLR\rightarrow HR}{}^{t}\mathbf{H}_{\mathbf{dist}}{}^{t}\mathbf{x}^{t} - \mathbf{H}_{samp}\mathbf{H}_{transp}{}^{t}\mathbf{H}_{\mathbf{dist}}{}^{t}\mathbf{x}^{t}) \quad \text{(A1-2)}$$

where $\mathbf{H}_{transpHR\rightarrow LR}$ is a theoretical operator corresponding to the transport from emissions $\mathbf{f}_{HR}$

but whose output concentrations are projected into the coarse resolution space of the outputs of $\mathbf{H}_{transp}$, while $\mathbf{H}_{transpLR\rightarrow HR}$ is a theoretical operator corresponding to the transport from emissions at low resolution but whose output concentrations are at high resolution.

Following the notations as in section 3, we can derive a practical estimate corresponding to Equation (A1-1):

$$\mathbf{H}_{samp}{}^{coloc}\mathbf{H}_{transp}{}^{CHIM}\mathbf{f}_{HR}{}^{EDG\text{-}IER} - \mathbf{H}_{samp}{}^{coloc}\mathbf{H}_{transpHR\rightarrow LR}{}^{CHIM}\mathbf{f}_{HR}{}^{EDG\text{-}IER} \quad \text{(A1-3)}$$

and

$$\mathbf{H}_{samp}{}^{coloc}\mathbf{H}_{transpHR\rightarrow LR}{}^{CHIM}\mathbf{f}_{HR}{}^{EDG\text{-}IER} - \mathbf{H}_{samp}{}^{coloc}\mathbf{H}_{transp}{}^{CHIM}\mathbf{H}_{distr}{}^{EDG\text{-}IER}\mathbf{x}^{EDG\text{-}IER} \quad \text{(A1-4)}$$

or the practical estimate corresponding to Equation (A1-2):

$$\mathbf{H}_{samp}{}^{coloc}\mathbf{H}_{transp}{}^{CHIM}\mathbf{f}_{HR}{}^{EDG\text{-}IER} - \mathbf{H}_{samp}{}^{coloc}\mathbf{H}_{transpLR\rightarrow HR}{}^{CHIM}\mathbf{H}_{distr}{}^{EDG\text{-}IER}\mathbf{x}^{EDG\text{-}IER} \quad \text{(A1-5)}$$

and

$$\mathbf{H}_{samp}{}^{coloc}\mathbf{H}_{transpLR\rightarrow HR}{}^{CHIM}\mathbf{H}_{distr}{}^{EDG\text{-}IER}\mathbf{x}^{EDG\text{-}IER} - \mathbf{H}_{samp}{}^{coloc}\mathbf{H}_{transp}{}^{CHIM}\mathbf{H}_{distr}{}^{EDG\text{-}IER}\mathbf{x}^{EDG\text{-}IER} \quad \text{(A1-6)}$$

We have made those two practical computations for these two decomposition (not shown here). The dominant component is dependent on the order of the decomposition (A1-1 vs. A1-2), the first term being larger than the second term for each decomposition. Therefore, there is no robust characterization of each sub-component of the representation error, even though they correspond to different physical processes. We thus avoid further analysis of these decomposition of the representation error

A2 Equivalence of the results for large region-months from an inversion at transport model resolution and from an inversion at large region-months resolution

In this section, we demonstrate that using the same atmospheric transport model but solving for emissions at the transport model resolution (called hereafter "pixel level") or for large regions / time windows (accounting for aggregation error) should lead to the same results for large regions/time windows. The relationship between the control vectors at pixel level and at large region level is $\mathbf{x}_{PIX}=\mathbf{H}_{distr}\mathbf{x}$. We define the aggregation operator $\boldsymbol{\Gamma}$ which aggregates the emissions at pixel level into large regions and time windows. The product between $\boldsymbol{\Gamma}$ and $\mathbf{H}_{distr}$ yields the identity matrix ($\boldsymbol{\Gamma}\mathbf{H}_{distr} = \mathbf{I}$) and $\boldsymbol{\Gamma}\mathbf{x}_{PIX}=\mathbf{x}$. The observation operator when using a pixel level control vector writes $\mathbf{H}_{PIX}=\mathbf{H}_{samp}\,\mathbf{H}_{transp}$ and $\mathbf{H}=\mathbf{H}_{PIX}\,\mathbf{H}_{distr}$.

Assuming that errors have a Gaussian and unbiased distribution, at the pixel level, the prior

uncertainty covariance is denoted $\mathbf{B}_{PIX}$. The pixel level uncertainty $\boldsymbol{\varepsilon}_{PIX}$ is composed by an uncertainty at a resolution higher than that of the large region $\boldsymbol{\varepsilon}_{SUBR}$ ($\boldsymbol{\Gamma}\boldsymbol{\varepsilon}_{SUBR}=0$) whose covariance is denoted $\mathbf{B}_{SUBR}$ and verifies $\boldsymbol{\Gamma}\ \mathbf{B}_{SUBR}=0$ (see below), and by the projection $\mathbf{H}_{distr}\boldsymbol{\varepsilon}$ of the uncertainty at the level of the large region $\boldsymbol{\varepsilon}$, whose covariance can be written $\mathbf{H}_{distr}\mathbf{B}\mathbf{H}_{distr}^{T}$. These 2 components are not necessarily independent, so that $\mathbf{B}_{PIX}= \mathbf{B}_{SUBR}+ \mathbf{H}_{distr}\mathbf{B}\mathbf{H}_{distr}^{T}+2\mathbf{B}_{cov}$ where $\mathbf{B}_{cov}$ is the matrix of covariance between $\mathbf{H}_{distr}\boldsymbol{\varepsilon}$ and $\boldsymbol{\varepsilon}_{SUBR}$ which verifies $\boldsymbol{\Gamma}\ \mathbf{B}_{cov}=0$ (see below). Our bottom-up definition of the aggregation error is based on the assumption that $\mathbf{B}_{cov}=0$ and corresponds to $\mathbf{R}_a=\mathbf{H}_{PIX}\mathbf{B}_{SUBR}\mathbf{H}_{PIX}^{T}$ (i.e. on the projection of $\boldsymbol{\varepsilon}_{SUBR}$). On the other hand, the top down approach of (Kaminski et al. (2001)) fully account for $\mathbf{B}_{cov}$ by defining $\mathbf{R}_a=\mathbf{H}_{PIX}(\mathbf{B}_{PIX}-\mathbf{H}_{distr}\mathbf{B}\mathbf{H}_{distr}^{T})\ \mathbf{H}_{PIX}^{T}$ i.e. $\mathbf{R}_a=\mathbf{H}_{PIX}(\mathbf{B}_{SUBR}+2\ \mathbf{B}_{cov})\mathbf{H}_{PIX}^{T}$. A common formulation of the covariance of the aggregation error is thus $\mathbf{R}_a=\mathbf{H}_{PIX}(\mathbf{B}_{SUBR}+2\ \mathbf{B}_{cov})\mathbf{H}_{PIX}^{T}$ with the assumption that $\mathbf{B}_{cov}=0$ in our bottom-up framework (see the discussion regarding this assumption at end of this section).

The observation error covariance when using a pixel level control vector is denoted $\mathbf{R}_{PIX}$. Applying the alternative formulation of Equation (2) (ignoring $\mathbf{y}_{fixed}$ which is null in our framework):

$$\mathbf{x}^a=\mathbf{x}^b+\mathbf{B}\mathbf{H}^T(\mathbf{H}\mathbf{B}\mathbf{H}^T+\mathbf{R})^{-1}(\mathbf{y}^o-\mathbf{H}\mathbf{x}^b) \quad \text{(A2-1)}$$

at the pixel level and at the large region levels isolating aggregation error yields:

$$\mathbf{x}_{PIX}^a=\mathbf{x}_{PIX}^b+\mathbf{B}_{PIX}\mathbf{H}_{PIX}^T(\mathbf{H}_{PIX}\mathbf{B}_{PIX}\mathbf{H}_{PIX}^T+\mathbf{R}_{PIX})^{-1}(\mathbf{y}^o-\mathbf{H}_{PIX}\mathbf{x}_{PIX}^b) \quad \text{(A2-2)}$$

$$\mathbf{x}^a=\mathbf{x}^b+\mathbf{B}\mathbf{H}^T(\mathbf{H}\mathbf{B}\mathbf{H}^T+\mathbf{R}_a+\mathbf{R}_{PIX})^{-1}(\mathbf{y}^o-\mathbf{H}\mathbf{x}^b) \quad \text{(A2-3)}$$

Aggregating the results from Equation (A2-2) to large regions, we get

$$\boldsymbol{\Gamma}\mathbf{x}_{PIX}^a=\boldsymbol{\Gamma}\mathbf{x}_{PIX}^b+\boldsymbol{\Gamma}\mathbf{B}_{PIX}\mathbf{H}_{PIX}^T(\mathbf{H}_{PIX}\mathbf{B}_{PIX}\mathbf{H}_{PIX}^T+\mathbf{R}_{PIX})^{-1}(\mathbf{y}^o-\mathbf{H}_{PIX}\mathbf{x}_{PIX}^b) \quad \text{(A2-4)}$$

i.e. $\mathbf{x}^a=\mathbf{x}^b+(\boldsymbol{\Gamma}\mathbf{B}_{SUBR}+2\boldsymbol{\Gamma}\mathbf{B}_{cov}+\boldsymbol{\Gamma}\mathbf{H}_{distr}\mathbf{B}\mathbf{H}_{distr}^{T})\mathbf{H}_{PIX}^{T}(\mathbf{H}_{PIX}\mathbf{H}_{distr}\mathbf{B}\mathbf{H}_{distr}^{T}\mathbf{H}_{PIX}^{T}+$

$$\mathbf{H}_{PIX}(\mathbf{B}_{SUBR}+2\mathbf{B}_{cov})\mathbf{H}_{PIX}^{T}+\mathbf{R}_{PIX})^{-1}(\mathbf{y}^o-\mathbf{H}_{PIX}\mathbf{H}_{distr}\mathbf{x}^b) \quad \text{(A2-5)}$$

, which simplifies into Equation (A2-3) and thus it means that the inverted emissions at large scale are the same when using the two types of control vectors.

Regarding the demonstration that $\boldsymbol{\Gamma}\ \mathbf{B}_{SUBR}=0$ and $\boldsymbol{\Gamma}\ \mathbf{B}_{cov}=0$: detailing $\mathbf{B}_{SUBR}$ (and $\mathbf{B}_{cov}$) as the covariance of errors $\boldsymbol{\varepsilon}_{SUBR}$ (between $\mathbf{H}_{distr}\boldsymbol{\varepsilon}$ and $\boldsymbol{\varepsilon}_{SUBR}$) with $\boldsymbol{\Gamma}\boldsymbol{\varepsilon}_{SUBR}=0$, we get $\mathbf{B}_{SUBR}=$ $E[\boldsymbol{\varepsilon}_{SUBR}\bullet\boldsymbol{\varepsilon}_{SUBR}^{T}]$ and $\mathbf{B}_{cov}= E[\boldsymbol{\varepsilon}_{SUBR}\bullet(\mathbf{H}_{distr}\boldsymbol{\varepsilon})^{T}]$so that $\boldsymbol{\Gamma}\ \mathbf{B}_{SUBR}=\boldsymbol{\Gamma}E[\boldsymbol{\varepsilon}_{SUBR}\bullet\boldsymbol{\varepsilon}_{SUBR}^{T}] =$ $E[\boldsymbol{\Gamma}\boldsymbol{\varepsilon}_{SUBR}\bullet\boldsymbol{\varepsilon}_{SUBR}^{T}] = 0$ and $\boldsymbol{\Gamma}\ \mathbf{B}_{cov}=\boldsymbol{\Gamma}E[\boldsymbol{\varepsilon}_{SUBR}\bullet(\mathbf{H}_{distr}\boldsymbol{\varepsilon})^{T}] = E[\boldsymbol{\Gamma}\boldsymbol{\varepsilon}_{SUBR}\bullet(\mathbf{H}_{distr}\boldsymbol{\varepsilon})^{T}] = 0$.

The assumption that $\mathbf{B}_{cov}$=0 i.e. of the independence between the prior uncertainty and the uncertainty in the distribution of the emissions in the control regions $\boldsymbol{\varepsilon}_{SUBR}$ (and consequently between the prior uncertainty and the aggregation error) is likely strong.

The typical inventories used to produce both the prior estimate of the emissions and $\mathbf{H}_{distr}$ are built on a mix of "top-down" computations relying on a disaggregation of large scale budgets of the emissions from statistics on the fossil fuel consumption, and on "bottom-up" computations relying on emissions factors and local activity data. In the first type of computations, the data used for the disaggregation can be highly independent of the large scale statistics which would qualitatively support the assumption that $\mathbf{B}_{cov}$=0. However, the statistics on the consumption of different fossil fuels can be used to derive the separation of the emissions between different types of anthropogenic activities (e.g. liquid fuel can be mainly related to traffic, gas and coal mainly to power generation…) and thus to derive information on the spatial and temporal distribution of the emissions. Through such a process, uncertainties at large scale can thus be downscaled into uncertainties at higher resolution. Furthermore, errors in the different emission factors used for the bottom-up computations generates uncertainties that are highly correlated between the high and low resolution.

The assumption that the prior uncertainty and the aggregation error (that $\mathbf{B}_{cov}$=0) is thus unlikely, and we have tried to analyse the relative weight of the term $2\mathbf{H}_{PIX}\mathbf{B}_{cov}\mathbf{H}_{PIX}^{T}$ that we have implicitly ignored in the derivation of the aggregation error $\mathbf{R}_a=\mathbf{H}_{PIX}\mathbf{B}_{SUBR}\mathbf{H}_{PIX}^{T}$ instead of $\mathbf{R}_a=\mathbf{H}_{PIX}(\mathbf{B}_{SUBR}+2\ \mathbf{B}_{cov})\mathbf{H}_{PIX}^{T}$. Following a similar method and using the same notation as in section 3, we can derive an estimate of the diagonal of $\mathbf{H}_{PIX}(\mathbf{B}_{SUBR}+2\ \mathbf{B}_{cov})\mathbf{H}_{PIX}^{T}$ $=\mathbf{H}_{PIX}E[\boldsymbol{\varepsilon}_{SUBR}.(\boldsymbol{\varepsilon}_{SUBR}+2\mathbf{H}_{distr}\boldsymbol{\varepsilon})^{T}]\mathbf{H}_{PIX}^{T}$ from statistics on the diagonal elements of $[\mathbf{H}_{samp}{}^{coloc}\mathbf{H}_{transp}{}^{LMDZ}(\mathbf{H}_{dist}{}^{EDG\text{-}IER}-\mathbf{H}_{dist}{}^{PKU})\mathbf{x}^{EDG\text{-}IER}].[\mathbf{H}_{samp}{}^{coloc}\mathbf{H}_{transp}{}^{LMDZ}((\mathbf{H}_{dist}{}^{EDG\text{-}IER}-\mathbf{H}_{dist}{}^{PKU})\mathbf{x}^{EDG\text{-}IER}+2\mathbf{H}_{dist}{}^{PKU}(\mathbf{x}^{EDG\text{-}IER}-\mathbf{x}^{PKU}))]^{T}$. Following the categorization discussed in section 4.2, the difference between the corresponding estimate of the aggregation error and the one we have described in this study is about -0.03 ppm for both spring/summer and fall/winter. This would decrease the aggregation error by less than 20%. Considering the comparison with other sources of observation error (see Table 1), especially the representation error and the measurement error, such a modification would not impact the conclusions of this study.

Acknowledgement. The authors acknowledge the support of the French Commissariat à l'énergie atomique et aux énergies alternatives (CEA). This study is co-funded by the European Commission under the EU Seventh Research Framework Programme (grant agreement no. 283080, geocarbon project). G. Broquet and F. Vogel acknowledge funding from the industrial chair BridGES (supported by the Université de Versailles Saint-Quentin-en-Yvelines, the Commissariat à l'Energie Atomique et aux Energies Renouvelables, the Centre National de la Recherche Scientifique, Thales Alenia Space and Veolia). We are also grateful to Ingeborg Levin for the useful discussions on this topic. We also would like to thank the partners of the ICOS infrastructure for details of radiocarbon samplings and $FFCO_2$ monitoring.

References

Andres, R. J., Marland, G., Fung, I. and Matthews, E. 1996. A 1°×1° distribution of carbon dioxide emissions from fossil fuel consumption and cement manufacture, 1950–1990. *Global Biogeochemical Cycles* **10**, 419-429.

Andres, R. J., Boden, T. A., Bréon, F. M., Ciais, P., Davis, S. and co-authors 2012. A synthesis of carbon dioxide emissions from fossil-fuel combustion. *Biogeosciences* **9**, 1845-1871.

Andres, R. J., Boden, T. A. and Higdon, D. 2014. A new evaluation of the uncertainty associated with CDIAC estimates of fossil fuel carbon dioxide emission. *Tellus B* **66**.

Ballantyne, A. P., Andres, R., Houghton, R., Stocker, B. D., Wanninkhof, R. and co-authors 2015. Audit of the global carbon budget: estimate errors and their impact on uptake uncertainty. *Biogeosciences* **12**, 2565-2584.

Basu, S., Miller, J. B. and Lehman, S. 2016. Separation of biospheric and fossil fuel fluxes of CO_2 by atmospheric inversion of CO_2 and $^{14}CO_2$ measurements: Observation System Simulations, *Atmospheric Chemistry and Physics* **16**, 5665–5683.

Berrisford, P., Dee, D., Fielding, K., Fuentes, M., Kallberg, P. and co-authors 2009. The ERA-Interim Archive. *ERA report series*, 1-16.

Bocquet, M., Wu, L. and Chevallier, F. 2011. Bayesian design of control space for optimal assimilation of observations. Part I: Consistent multiscale formalism. *Quarterly Journal of the Royal Meteorological Society* **137**, 1340-1356.

Bousquet, P., Peylin, P., Ciais, P., Le Quéré, C., Friedlingstein, P. and co-authors 2000. Regional changes in carbon dioxide fluxes of land and oceans since 1980. *Science* **290**, 1342-1346.

Bozhinova, D., van der Molen, M. K., van der Velde, I. R., Krol, M. C., van der Laan, S., and co-authors 2014. Simulating the integrated summertime $\Delta^{14}CO_2$ signature from anthropogenic emissions over Western Europe, *Atmospheric Chemistry and Physics* **14**, 7273–7290, 2014.

Bréon, F. M., Broquet, G., Puygrenier, V., Chevallier, F., Xueref-Remy, I. and co-authors 2015. An attempt at estimating Paris area CO_2 emissions from atmospheric concentration measurements. *Atmospheric Chemistry and Physics* **15**, 1707-1724.

Brioude, J., Petron, G., Frost, G. J., Ahmadov, R., Angevine, W. M. and co-authors 2012. A new inversion method to calculate emission inventories without a prior at mesoscale: Application to the

anthropogenic CO_2 emission from Houston, Texas. *Journal of Geophysical Research* **117**.

Broquet, G., Chevallier, F., Rayner, P., Aulagnier, C., Pison, I. and co-authors 2011. A European summertime CO_2 biogenic flux inversion at mesoscale from continuous in situ mixing ratio measurements. *Journal of Geophysical Research* **116**.

Chen, H., Winderlich, J., Gerbig, C., Hoefer, A., Rella, C. W. and co-authors 2010. High-accuracy continuous airborne measurements of greenhouse gases (CO_2 and CH_4) using the cavity ring-down spectroscopy (CRDS) technique. *Atmospheric Measurement Techniques* **3**, 375-386.

Chevallier, F., Fisher, M., Peylin, P., Serrar, S., Bousquet, P. and co-authors 2005. Inferring CO_2 sources and sinks from satellite observations: Method and application to TOVS data. *Journal of Geophysical Research* **110**.

Chevallier, F. and O'Dell, C. W. 2013. Error statistics of Bayesian CO_2 flux inversion schemes as seen from GOSAT. *Geophysical Research Letters* **40**, 1252-1256.

Ciais, P., Paris, J. D., Marland, G., Peylin, P., Piao, S. L. and co-authors 2010. The European carbon balance. Part 1: fossil fuel emissions. *Global Change Biology* **16**, 1395-1408.

Engelen, R. J. 2002. On error estimation in atmospheric CO_2 inversions. *Journal of Geophysical Research* **107**.

Enting, I. G., Trudinger, C. M., Francey, R. J. and Granek, H. 1993. Synthesis inversion of atmospheric CO_2 using the GISS tracer transport model.

Gamnitzer, U., Karstens, U., Kromer, B., Neubert, R. E. M., Meijer, H. A. J. and co-authors 2006. Carbon monoxide: A quantitative tracer for fossil fuel CO_2? *Journal of Geophysical Research* **111**.

Garc á, M. Á., S ánchez, M. L. and P érez, I. A. 2010. Synoptic weather patterns associated with carbon dioxide levels in Northern Spain. *Science of The Total Environment* **408**, 3411-3417.

Geels, C., Gloor, M., Ciais, P., Bousquet, P., Peylin, P. and co-authors 2007. Comparing atmospheric transport models for future regional inversions over Europe – Part 1: mapping the atmospheric CO2 signals. *Atmospheric Chemistry and Physics* **7**, 3461-3479.

Gerbig, C., Lin, J. C., Wofsy, S. C., Daube, B. C., Andrews, A. E. and co-authors 2003. Toward constraining regional-scale fluxes of CO_2 with atmospheric observations over a continent: 1. Observed spatial variability from airborne platforms. *Journal of Geophysical Research: Atmospheres* **108**, n/a-n/a.

Graven, H. D. and Gruber, N. 2011. Continental-scale enrichment of atmospheric $^{14}CO_2$ from the nuclear power industry: potential impact on the estimation of fossil fuel-derived CO_2. *Atmospheric Chemistry and Physics* **11**, 12339-12349.

Gregg, J. S., Andres, R. J. and Marland, G. 2008. China: Emissions pattern of the world leader in CO_2 emissions from fossil fuel consumption and cement production. *Geophysical Research Letters* **35**.

Gurney, K. R., Law, R. M., Denning, A. S., Rayner, P. J., Baker, D. and co-authors 2002. Towards robust regional estimates of CO_2 sources and sinks using atmospheric transport models. *Nature* **415**, 626-630.

Hourdin, F., Musat, I., Bony, S., Braconnot, P., Codron, F. and co-authors 2006. The LMDZ4 general circulation model: climate performance and sensitivity to parametrized physics with emphasis on tropical convection. *Geophysical Research Letters* **27**, 787-813.

Hsueh, D. Y., Krakauer, N. Y., Randerson, J. T., Xu, X., Trumbore, S. E. and co-authors 2007. Regional patterns of radiocarbon and fossil fuel-derived CO_2 in surface air across North America. *Geophysical Research Letters* **34**.

IPCC 2006. 2006 IPCC Guidelines for National Greenhouse Gas Inventories. *Institutefor Global Environmental Strategies, Hayama, Kanagawa, Japan*.

Kadygrov, N., Broquet, G., Chevallier, F., Rivier, L., Gerbig, C. and co-authors 2015. On the potential of the ICOS atmospheric CO_2 measurement network for estimating the biogenic CO_2 budget of Europe, *Atmospheric Chemistry and Physics* **15**, 12765-12787.

Kaminski, T., Rayner, P. J., Heimann, M. and Enting, I. G. 2001. On aggregation errors in atmospheric transport inversion. *Journal of Geophysical Research* **106**, 4703-4715.

Lauvaux, T., Uliasz, M., Sarrat, C., Chevallier, F., Bousquet, P. and co-authors 2008. Mesoscale inversion: first results from the CERES campaign with synthetic data. *Atmospheric Chemistry and Physics* **8**, 3459-3471.

Law, R. M., Peters, W., Rödenbeck, C., Aulagnier, C., Baker, I. and co-authors 2008. TransCom model simulations of hourly atmospheric CO_2: Experimental overview and diurnal cycle results for 2002. *Global Biogeochemical Cycles* **22**.

Levin, I., Kromer, B., Schmidt, M. and Sartorius, H. 2003. A novel approach for independent budgeting of fossil fuel CO_2 over Europe by $^{14}CO_2$ observations. *Geophysical Research Letters* **30**.

Levin, I., Hammer, S., Kromer, B. and Meinhardt, F. 2008. Radiocarbon observations in atmospheric CO_2: determining fossil fuel CO_2 over Europe using Jungfraujoch observations as background. *Science of The Total Environment* **391**, 211-216.

Levin, I., Hammer, S., Eichelmann, E. and Vogel, F. R. 2011. Verification of greenhouse gas emission reductions: the prospect of atmospheric monitoring in polluted areas. *Philosophical transactions. Series A, Mathematical, physical, and engineering sciences* **369**, 1906-1924.

Levin, I. M. K. O. W. W. 1980. The effect of anthropogenic CO2 and 14C sources on the distribution of ^{14}C in the atmosphere. *Radiocarbon* **22**, 379-391.

Lin, J. C., Gerbig, C., Wofsy, S. C., Daube, B. C., Matross, D. M. and co-authors 2006. What have we learned from intensive atmospheric sampling field programmes of CO_2? *Tellus B* **58**, 331-343.

Liu, Y. Y., van Dijk, A. I. J. M., de Jeu, R. A. M., Canadell, J. G., McCabe, M. F. and co-authors 2015. Recent reversal in loss of global terrestrial biomass. *Nature Climate Change*.

Lorenc, A. C. 1986. Analysis methods for numerical weather prediction. *Quarterly Journal of the Royal Meteorological Society* **112**, 1177-1194.

Macknick, J. 2009. Energy and carbon dioxide emission data uncertainties. *IIASA Interim Report IR-09-32. Laxenburg: International Institute for Applied Systems Analysis*.

Marland, G. 2008. Uncertainties in Accounting for CO2From Fossil Fuels. *J Ind Ecol* **12**, 136-139.

McKain, K., Wofsy, S. C., Nehrkorn, T., Eluszkiewicz, J., Ehleringer, J. R. and co-authors 2012. Assessment of ground-based atmospheric observations for verification of greenhouse gas emissions from an urban region. *Proceedings of the National Academy of Sciences of the United States of America* **109**, 8423–8428.

Naegler, T. and Levin, I. 2006. Closing the global radiocarbon budget 1945–2005. *Journal of Geophysical Research* **111**.

Newman, S., Jeong, S., Fischer, M. L., Xu, X., Haman, C. L. and co-authors 2013. Diurnal tracking of anthropogenic CO_2 emissions in the Los Angeles basin megacity during spring 2010. *Atmospheric Chemistry and Physics* **13**, 4359-4372.

Oak Ridge National Laboratory (ORNL): LandScan Global Population 2007 Database, available at: http://www.ornl.gov/sci/landscan/, 2015.

Oda, T. and Maksyutov, S. 2011. A very high-resolution (1 km×1 km) global fossil fuel CO2 emission

inventory derived using a point source database and satellite observations of nighttime lights. *Atmospheric Chemistry and Physics* **11**, 543-556.

Olivier, J. G. J., Van Aardenne, J. A., Dentener, F. J., Pagliari, V., Ganzeveld, L. N. and co-authors 2005. Recent trends in global greenhouse gas emissions:regional trends 1970–2000 and spatial distributionof key sources in 2000. *Environmental Sciences* **2**, 81-99.

Pacala, S. W., Breidenich, C., Brewer, P. G., Fung, I. Y., Gunson, M. R. and co-authors 2010. Verifying greenhouse gas emissions: methods to support international climate agreements. *Committee on Methods for Estimating Greenhouse Gas Emissions*.

Parazoo, N. C., Denning, A. S., Kawa, S. R., Corbin, K. D., Lokupitiya, R. S. and co-authors 2008. Mechanisms for synoptic variations of atmospheric CO_2 in North America, South America and Europe. *Atmospheric Chemistry and Physics* **8**, 7239-7254.

Peylin, P., Rayner, P. J., Bousquet, P., Carouge, C., Hourdin, F. and co-authors 2005. Daily CO_2 flux estimates over Europe from continuous atmospheric measurements: 1, inverse methodology. *Atmospheric Chemistry and Physics* **5**, 3173-3186.

Peylin, P., Houweling, S., Krol, M. C., Karstens, U., Rödenbeck, C. and co-authors 2011. Importance of fossil fuel emission uncertainties over Europe for CO_2 modeling: model intercomparison. *Atmospheric Chemistry and Physics* **11**, 6607-6622.

Peylin, P., Law, R. M., Gurney, K. R., Chevallier, F., Jacobson, A. R. and co-authors 2013. Global atmospheric carbon budget: results from an ensemble of atmospheric CO_2 inversions. *Biogeosciences Discussions* **10**, 5301-5360.

Pillai, D., Gerbig, C., Ahmadov, R., Rödenbeck, C., Kretschmer, R. and co-authors 2011. High-resolution simulations of atmospheric CO_2 over complex terrain – representing the Ochsenkopf mountain tall tower. *Atmospheric Chemistry and Physics* **11**, 7445-7464.

Rödenbeck, C., Houweling, S., Gloor, M. and Heimann, M. 2003. CO_2 flux history 1982–2001 inferred from atmospheric data using a global inversion of atmospheric transport. *Atmospheric Chemistry and Physics* **3**, 1919-1964.

Randerson, J. T., Enting, I. G., Schuur, E. A. G., Caldeira, K. and Fung, I. Y. 2002. Seasonal and latitudinal variability of troposphere $\Delta^{14}CO_2$: Post bomb contributions from fossil fuels, oceans, the stratosphere, and the terrestrial biosphere. *Global Biogeochemical Cycles* **16**, 59-51-59-19.

Ray, J., Yadav, V., Michalak, A. M., van Bloemen Waanders, B. and McKenna, S. A. 2014. A multiresolution spatial parameterization for the estimation of fossil-fuel carbon dioxide emissions via atmospheric inversions. *Geoscientific Model Development* **7**, 1901-1918.

Rivier, L., Ciais, P., Hauglustaine, D. A., Bakwin, P., Bousquet, P. and co-authors 2006. Evaluation of SF_6, C_2Cl_4, and CO to approximate fossil fuel CO_2 in the Northern Hemisphere using a chemistry transport model. *Journal of Geophysical Research* **111**.

Schmidt, H., Derognat, C., Vautard, R. and Beekmann, M. 2001. A comparison of simulated and observed ozone mixing ratios for the summer of 1998 in Western Europe. *Atmospheric Environment* **35**, 6277-6297.

Tarantola, A. 2005. *Inverse problem theory and methods for model parameter estimation*, siam.

Turnbull, J., Miller, J., Lehman, S., Hurst, D., Peters, W. and co-authors 2009. Spatial distribution of $\Delta^{14}CO_2$ across Eurasia: measurements from the TROICA-8 expedition. *Atmospheric Chemistry and Physics* **9**, 175-187.

Turnbull, J. C., Tans, P. P., Lehman, S. J., Baker, D., Conway, T. J. and co-authors 2011. Atmospheric observations of carbon monoxide and fossil fuel CO_2 emissions from East Asia. *Journal of*

Geophysical Research **116**, D24306.

Turnbull, J. C., Keller, E. D., Baisden, T., Brailsford, G., Bromley, T. and co-authors 2014. Atmospheric measurement of point source fossil CO_2 emissions. *Atmospheric Chemistry and Physics* **14**, 5001-5014.

Vogel, F. R., Hammer, S., Steinhof, A., Kromer, B. and Levin, I. 2010. Implication of weekly and diurnal ^{14}C calibration on hourly estimates of CO-based fossil fuel CO_2 at a moderately polluted site in southwestern Germany. *Tellus B* **62**, 512-520.

Vogel, F. R., Levin, I. and Worthy, D. 2013. Implications for deriving regional fossil fuel CO_2 estimates from atmospheric observations in a hot spot of nuclear power plant $^{14}CO_2$ emissions. *Radiocarbon* **55**, 1556-1572.

Wang, R., Tao, S., Ciais, P., Shen, H. Z., Huang, Y. and co-authors 2013. High-resolution mapping of combustion processes and implications for CO_2 emissions. *Atmospheric Chemistry and Physics* **13**, 5189-5203.

Wu, L., Bocquet, M., Lauvaux, T., Chevallier, F., Rayner, P. and co-authors 2011. Optimal representation of source-sink fluxes for mesoscale carbon dioxide inversion with synthetic data. *Journal of Geophysical Research* **116**.

Chapter 3 Potential of European $^{14}CO_2$ observation network to estimate the fossil fuel CO_2 emissions via atmospheric inversions

Summary

Following the characterization of the observation errors in the previous chapter, this chapter presents a performance assessment of the same inversion system for constraining monthly to annual fossil fuel emissions in Europe regions.

The performance of the inversion is assessed in terms of uncertainties in the inverted emissions (i.e. the *posterior uncertainties*) and of uncertainty reductions compared to the uncertainty in the inventories which are used as a prior knowledge by the inversion (i.e. the *prior uncertainty*). These computations are based on 1-year long observing system simulation experiment (OSSE) frameworks. Several network configurations, going from 17 to 233 sites, and different sampling frequencies are tested in order to assess and compare the improvements that can be expected in the future from the extension of the network. Given the coverage of $^{14}CO_2$ stations that are available over Europe in 2016, the uncertainty reduction of monthly $FFCO_2$ emissions in Germany are larger than 30% when assimilating 2-week integrated radiocarbon-derived $FFCO_2$ data from these sites. Using 2-week integrated observations from a plausible Integrated Carbon Observing System (ICOS) atmospheric larger network of 43 sites that can be expected on the long-term, I found that the uncertainties in the annual budgets of fossil fuel emissions could be reduced by up to 47% for countries like Germany.

Increasing the number of stations or increasing sampling frequencies for the radiocarbon measurements would further improve the potential of the inversion of $FFCO_2$ emissions. However, the OSSEs show very limited potential for improving the estimate of the fossil fuel emissions over some low emitting regions, even when using large observations networks covering the whole Europe.

Given the posterior uncertainty in the annual budgets of fossil fuel emissions using the ICOS-like network and 2-week sampling, the uncertainty in the derived trend from a series estimate of emissions of 20 years is 0.43%, which could support the independent verification of fossil fuel emission reduction objectives.

This chapter is the integral text of the manuscript to be submitted to the peer-reviewed journal Atmospheric Chemistry and Physics (ACP).

Potential of European $^{14}CO_2$ observation network to estimate the fossil fuel CO_2 emissions via atmospheric inversions

Yilong Wang, Grégoire Broquet, Philippe Ciais, Frédéric Chevallier, Felix Vogel, Lin Wu, Yi Yin, Ingeborg Levin, Rong Wang, Shu Tao

Abstract

Estimates of country-scale annual CO_2 emissions from fossil fuel combustions derived from energy/fuel use statistics bear relative uncertainties on the order of 5% for developed countries, while different datasets reveal a range of up to 15% in a country like China. Relative uncertainties are larger for emissions at sub-national and sub-annual scales. By using precise atmospheric measurements of CO_2 and of its radiocarbon fraction, atmospheric inversions offer a promising way for improving the estimation of fossil fuel emissions and reducing these uncertainties. In this study, we develop a global inversion system solving for monthly fossil fuel emission budgets at regional scale (here a region being of the typical size of a middle-sized country in Europe) using virtual radiocarbon-based atmospheric CO_2 signal of fossil fuel emission ($FFCO_2$) data from a continental network of stations. The analytical Bayesian inversion system is built on the LMDZv4 coarse resolution transport model (with a 3.75 °×2.5 ° longitude ×latitude horizontal resolution; 19 layers in the vertical between the surface and the top of the atmosphere) in which sources of observation errors related to the resolution of the transport model and of the inversion are accounted for according to Wang et al. (2016). We assess the performance of this inversion system for constraining monthly to annual fossil fuel emissions in European regions in terms of uncertainties in the inverted emissions ("posterior uncertainties") and of uncertainty reductions compared to the uncertainty in the inventories of these emissions, which are used as a prior knowledge by the inversion ("prior uncertainty"). The assessment is based on two types of 1-year long Observing System Simulation Experiments (OSSE) frameworks: one relying on the statistical uncertainty assessment of the Bayesian inversion framework, and the other, more empirical, relying on the generation of synthetic truth and data and on the assimilation of these data with a biased prior emission field. With the coverage of $^{14}CO_2$ stations available in Europe in 2016 and with 2-week mean sampling, the uncertainty reduction of monthly fossil fuel emissions of a region where the network is rather dense (western Germany) are larger than 30%. An uncertainty reduction of up to 47% could be

achieved for the annual budgets of fossil fuel emissions in highly emitting countries, such as Germany, based on the assimilation of 2-week integrated data at 43 atmospheric measurement stations. Increasing number of stations or increasing sampling frequency for radiocarbon measurements would further improve the potential of the inversion of fossil fuel emissions. However, the OSSEs show very limited potential for improving the estimate of fossil fuel emissions over low emitting regions, even when using large observations network covering the whole European continent. Given the posterior uncertainty in annual emissions from OSSEs, we also show that monitoring the trend of fossil fuel emissions using our atmospheric inversion could be possible over a period longer than 20 years. The too coarse spatial resolution of the atmospheric transport model used in this study (despite being state of the art in global inversions of natural fluxes) and the corresponding representation errors is a key limiting factor to improve the capability of monitoring monthly emissions over Europe regions. Using regional inversion systems with high-resolution transport models should, in principle, increase the potential of the inversion of fossil fuel emissions, and this needs to be investigated.

3.1 Introduction

CO_2 emitted from combustion of fossil fuels is the major contributor to the increasing atmospheric CO_2 (Ballantyne et al., 2015). Knowledge of fossil fuel CO_2 emissions and their trends is essential to understand the drivers of their variations and to assess the effectiveness of climate and energy policies over time (Pacala et al., 2010).

Current fossil fuel emission are derived from inventories based on national or international energy/fuel use statistics, combustion efficiencies and emission factors. These inventories have low uncertainties in developed countries, and large uncertainties in developing countries, due to uncertain energy/fuel use data and fuel-specific emission factors (Liu et al., 2015; Ballantyne et al., 2015; Andres et al., 2014; Ciais et al., 2010). When emission inventories is distributed at sub-national and intra-annual scales or at high temporal/spatial resolution, either based on the disaggregation of national inventories according to socio-economic proxies (Wang et al., 2013; Pregger et al., 2007; Oda and Maksyutov, 2011) or based bottom-up modeling using regional activity data and sector-specific emission factors (Olivier et al., 2015; Gurney et al., 2009), there are larger relative

uncertainties at regional scale compared to national scale (Ciais et al., 2010; Wang et al., 2013). When comparing emission maps derived from different publications, uncertainties also arise from the treatment or land/water borders and the proxies used to map emissions (Andres et al., 2012).

Atmospheric inversions exploit the observed variability in atmospheric concentrations of CO_2 and provide an objective approach to assess CO_2 fluxes and their trends. Atmospheric inversions have been widely used to quantify natural carbon sources and sinks at global/regional scales (Broquet et al., 2011; Chevallier et al., 2010; Gurney et al., 2002). In order to monitor fossil fuel emissions with atmospheric measurements, a sampling strategy is to measure atmospheric CO_2 gradients around a large source such a city (Staufer et al., 2016; Cambaliza et al., 2014; Lindenmaier et al., 2014) or a power plant, in the vicinity of which the signal of $FFCO_2$ are easy to be separated from natural fluxes, either by CO_2 observations or co-emitted tracers. Attempts to monitor fossil fuel emissions at national to continental scales, using continental observation networks are still in infancy (Miller et al., 2016). A few pilot inversions have been recently conducted to test the concept of estimating national fossil fuel emissions of the US, based on the assimilation of (virtual) measurements of radiocarbon in atmospheric CO_2. The Observing System Simulation Experiments (OSSEs) described by Pacala et al. (2010) suggest that their atmospheric inversion could reduce the uncertainty in the monthly mean fossil fuel emissions of the US from 100% (assumed for a prior knowledge in their OSSEs) to less than 10%, given a hypothetical massive set of 10,000 atmospheric $^{14}CO_2$ observations sampled at 84 sites in one year and a perfect transport model with a 5 ° horizontal resolution. According to the OSSEs of Ray et al. (2014), using (virtual) observations of $FFCO_2$ mixing ratios every 3 h from a network of 35 measurement towers across the U.S. and an atmospheric inversion at 1 °×1 ° resolution could reduce errors on 8 day-averaged country-level fossil-fuel emissions from about 15% (for prior knowledge) down to 7%. Basu et al., 2016 developed a more advanced inversion system at 1 °×1 ° resolution to account for the fact that the CO_2 and $^{14}CO_2$ measurements do not directly provide accurate estimates of the $FFCO_2$ mixing ratios due to uncertainties in the impact of natural fluxes in the radiocarbon content of atmospheric CO_2. Using this inversion technique in a set of OSSEs, they showed that given the coverage of $^{14}CO_2$ measurements available in 2010 over North America (969 measurements per year) $FFCO_2$ can be separated from the natural fluxes well enough to constrain fossil fuel emissions estimate. The inverted US

national fossil fuel emission would bear less than 1% uncertainty for the year and less than 5% for most months. However, the actual scale of fossil fuel emissions is always smaller than the grid size of the transport models used in these studies (100-500 km). The misfits between the scales controlled or modelled within the inversion system and those of actual emissions and patterns in the mixing ratios generate so-called aggregation and representation errors. These are the critical sources of errors that affect the inversion of fossil fuel emissions (Wang et al., 2016), but they were not formally accounted for in previous studies.

In this study, we make a new assessment on the potential of an atmospheric inversion to quantify fossil fuel emissions at regional scale (a region being of the typical size of a middle-sized country in Europe) over the European continent. A special attention is paid to both representation and aggregation errors when using a coarse grid transport model and solving for regional budgets of fossil fuel emissions in the inversion system. Our transport model used for the inversion is LMDZv4 (Hourdin et al., 2006). Wang et al. (2016) evaluated the statistics of the errors of an inversion with this transport model when unknown fossil fuel emissions are optimized each month over different regions. Their results highlighted that the representation and aggregation errors have a prominent influence on the accuracy of the retrieval of fossil fuel emissions. Furthermore, the analysis of the temporal correlations in the representation and aggregation errors stressed the fact that they have a long-term component which makes the errors very large even at the monthly to annual scales which are targeted by the atmospheric inversion. On the other hand, the spatial correlations in the representation and aggregation errors were found to be rather short, implying the potential of dense networks to filter the errors caused by the uncertainties in an emission map used as the prior knowledge the inversion system (Wang et al. 2016). In sum, in this study we make a specific account for the representation and aggregation errors and check whether using dense networks could overcome the limitations brought by the coarse resolution transport model and corresponding representation and aggregation errors.

In the inversion system, we assume atmospheric $FFCO_2$ observations can be derived from CO_2 and $^{14}CO_2$ measurements across a set of continental sites. In recent years, as part of the ICOS project, a rather dense network of standardized, long-term and high precision atmospheric measurements of atmospheric CO_2 has been set up in Europe. Some of the ICOS sites also measure $^{14}CO_2$ and this type of measurement will be extended in the near term with the aim of determining the signal of $FFCO_2$. The ICOS network is expected to sample

2-week integrated $^{14}CO_2$ at about 40 stations in the future (in total 1,000 analyses per year; ICOS Stakeholder handbook 2013 at http://www.icos-uk.org/uk-icos/sites/uk-icos/files/documents/Stakeholders%20Handbook%202013.pdf). In this context, network assessment studies is encouraged to understand how much the network can increase our knowledge on the fossil fuel emissions.

We thus develop a global inversion system to solve for the monthly fossil fuel emission in different European regions by assimilating $FFCO_2$ gradients from CO_2 and $^{14}CO_2$ measurements at ICOS-like stations. We assess the potential of this inversion to improve regional fossil fuel emissions based either on the statistics of the theoretical posterior uncertainties diagnosed through the Bayesian statistical framework of the inversions, or on the misfits to a known truth in an OSSE framework (see section 3.2).

In this study, we focus on quantification of regional budgets of fossil fuel emission in one year. The monitoring of the long-term trends of fossil fuel emissions, usually defined as changes compared against emissions in a baseline year, is also important since climate mitigation actions are applied and verified on the long term. When the trend of fossil fuel emissions is calculated from a series of estimates for multiple years, either from inventories or from atmospheric inversions, uncertainties tend to be lower in emission trends than for the emission budgets for a given year (Pacala et al., 2010), implying that multi-year trends could be verified if the uncertainties in the estimate of emissions for each year is small enough. In this study, we thus make an attempt to assess the potential for emission trend detection with simple extrapolations from the posterior estimates from the 1-year inversions.

Section 3.2 gives a full description of the inversion and OSSE frameworks. Section 3.3 analyzes the statistics of the posterior emissions for different observation networks. Section 3.4 evaluate the potential on atmospheric inversion for trend detection and discuss the relevance of using a global inversion framework to quantify fossil fuel emissions. Conclusions are drawn in section 3.5.

3.2 Methodology

3.2.1 The configurations of the observation network

We consider three different observation networks, in which the number of the stations

goes from 17 to 233. The minimum network includes 17 sites, based on existing $^{14}CO_2$ stations in 2016. Using the location of these sites and of possible future stations discussed during the ICOS preparatory phase, we consider an intermediate ICOS network with 43 sites (NET43) based on the 2013 ICOS Stakeholder handbook. As shown in Fig. 1, the NET43 observation network has a large density in France, Germany, UK and Switzerland, but remains sparse in Eastern Europe. The site locations of the two networks are summarized in Table S1. Lastly, we also study a very dense network of with 233 sites (NET233) in which two $FFCO_2$ observational sites are placed in each European land pixel of the LMDZ transport model. The OSSEs with NET233 will reveal how much the skill of the inversion system varies in space with the availability of local stations. OSSEs with NET233 also make it possible to test the skill of the inversion system to constrain fossil fuel emissions in regions that are not extensively covered by the near-term ICOS network.

In each configuration of the network, the high-latitude station Jungfraujoch (JFJ), at 3450 meter above sea level (masl) in Switzerland which samples free-tropospheric air over Europe is defined as the reference station. The (virtual) atmospheric measurements of $^{14}CO_2$ and total CO_2 made at other sites are assumed to be at 100 meter above ground level (magl), the typical height of tall towers in continental scale networks (Kadygrov et al., 2015; Marquis and Tans, 2008). In this study, we will assimilate in the inversion gradients of $FFCO_2$ between each tall tower site and JFJ.

Wang et al. (2016) analyzed the structure and distributions of representation errors at different tall tower sites across Europe and characterized two types of stations based on the population density of the grid cells (at the resolution of 0.5 °×0.5 °) within which a station is located. Following their categorization, all the sites in the different networks are grouped as “urban” or “rural” sites. In the NET233, the two sites in each land pixel of the transport model are assumed to include one “urban” site and one “rural” site.

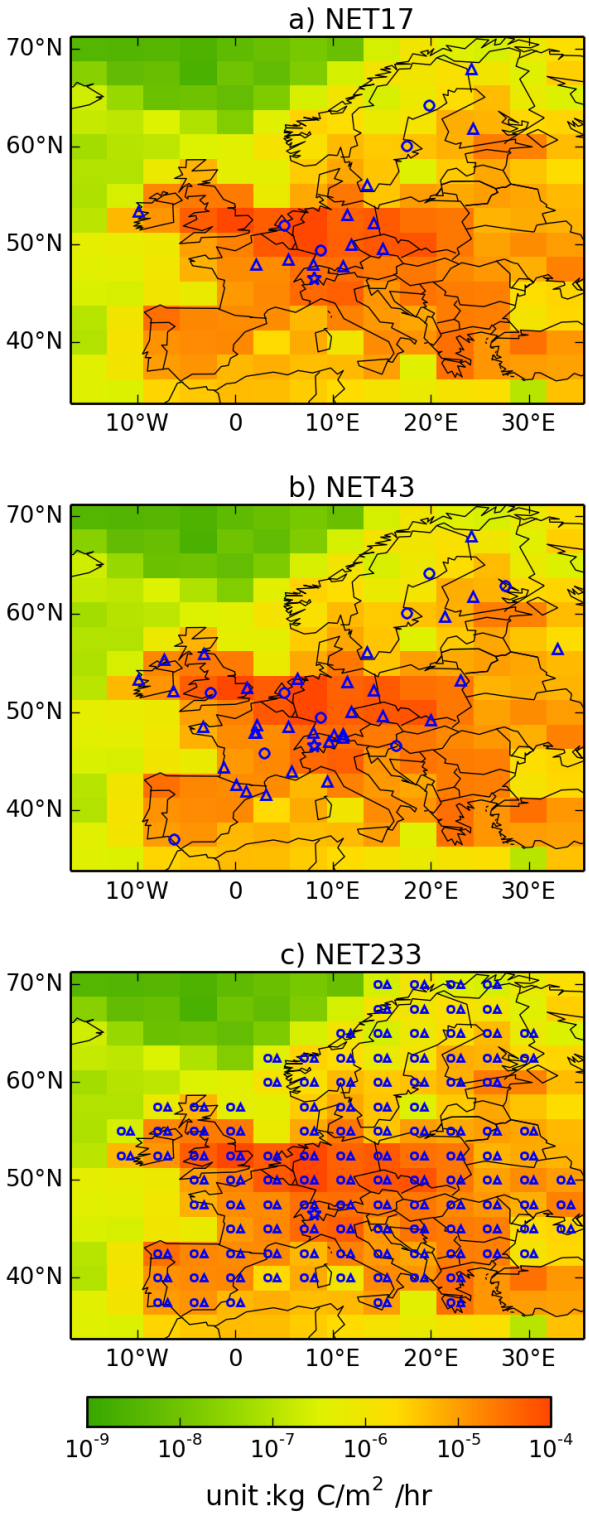

Figure 1 Site location for the three continental network configurations used in this study: a) NET17, b) NET38, c) and NET232. Circles correspond to "urban" sites and upper triangles are "rural" sites. Urban and rural sites are categorized according to the population density of the grid cells within which the stations are located. Of note is that in c) the stations plotted over ocean mean that they are on the land part within that pixel, but without explicit locations (see the text). The map of annual emissions in 2007 at the resolution of LMDZv4 from the PKU-CO_2 emission inventory is given in these figures.

3.2.2 Configuration of the inversion system

3.2.2.1. Method

The assessment of inversions related to the different ICOS networks to improve the estimates of fossil fuel emissions is based on the inversion system of Wang et al. (2016). In this section we only summarize the main elements of this inversion system, while the detailed description can be found in Wang et al. (2016).

The inversion relies on a Bayesian statistical framework: the estimate of the fossil fuel emission budgets at the monthly and regional to national scales, called hereafter the "control variables" $\mathbf{x}$, is corrected from a prior knowledge of these variables $\mathbf{x}^b$ (that from an inventory or a set of inventories covering the globe). This corrections is based on (i) a set of gradients of $FFCO_2$ mixing ratios during the afternoon (see section 3.2.2.2) across Europe, called hereafter the "observations" $\mathbf{y}_o$, (ii) the observation operator H linking the control variables to the observations (which includes the modeling of the CO_2 atmospheric transport) and (iii and iv) uncertainties in the prior estimate and observation errors . Assuming that the prior uncertainties and observation errors have an unbiased and Gaussian statistical distribution, characterized by the prior and observation uncertainty covariance matrices $\mathbf{B}$ and $\mathbf{R}$ respectively, the statistical distribution of the estimate of $\mathbf{x}$, given $\mathbf{x}^b$ and $\mathbf{y}_o$, is also unbiased and Gaussian, and its corresponding mean $\mathbf{x}^a$ and covariance matrix $\mathbf{A}$ are given by:

$$\mathbf{A} = (\mathbf{B}^{-1}+\mathbf{H}^T\mathbf{R}^{-1}\mathbf{H})^{-1} \quad (1)$$

$$\mathbf{x}^a = \mathbf{x}^b + \mathbf{A}\mathbf{H}^T\mathbf{R}^{-1}(\mathbf{y}_o-\mathbf{H}\mathbf{x}^b) \quad (2)$$

where ^{T} denotes the transpose, where $\mathbf{H}$ characterize the linear component of the observation operator H: $\mathbf{x}\mapsto\mathbf{H}\mathbf{x}+\mathbf{y}_{fixed}$, where $\mathbf{y}_{fixed}$ is the signature, through atmospheric transport, of the sources of $FFCO_2$ that is not controlled by the inversion, and where $\mathbf{H}$ maps the fossil fuel emission budgets at the monthly and regional to national scales to the observational space based on the spatial and temporal distribution of the emissions within a control region and within a month, and on the linear CO_2 atmospheric transport model (see section 3.2.2.2). Of note is that the observation error is a combination of the measurement errors, the model transport, model-measurement mismatch due to different spatial

representativeness, and errors from the model input that are not controlled by the inversion.

Eq. (1) demonstrates that **A** does not depend on the value for the observations $\mathbf{y}_o$ or on the prior emission budgets $\mathbf{x}^b$ themselves but only on the prior and observation error covariance matrices, on the observation times and locations (through the definition of the **y**-space and **H**), and on the observation operator. Eq. (2) shows that $\mathbf{x}^a$ also depend on the observations $\mathbf{y}_o$ and the prior emission budgets $\mathbf{x}^b$.

In this framework, a common performance indicator is the theoretical uncertainty reduction (UR) for specific budgets of the fossil fuel emissions (at control or larger space and time scales), defined by:

$$\mathrm{UR} = 1 - \frac{\sigma^a}{\sigma^b} \quad (3)$$

where σ^a and σ^b are the posterior and prior uncertainties in the corresponding budget of emissions. Such an indicator can directly be derived from the definition of **B** and from the theoretical computation of **A**. Of note is that the scores of uncertainty and of UR given in this study refer to the standard deviation of the theoretical uncertainty in a specific emission budget.

However, if the set-up of **B** and **R** do not perfectly match the actual statistics of the prior and observation uncertainties, or if the theoretical framework of the inversion (assuming that all sources of uncertainty have unbiased and Gaussian distributions and that the observation operator is linear) is not fully satisfied, such a theoretical computation of the UR may not perfectly reflect the actual performances of the inversions. Wang et al. (2016) derived statistics of the observation error covariances. They also highlighted that the distribution of their practical sample of such errors could depart from purely Gaussian distributions with the relatively simple kind of model for correlations in time and space traditionally used for atmospheric inversions. In this study, we thus challenge the inversion system using synthetic truth and errors that better reflects the type of observation errors sampled in practice by Wang et al. (2016) and use Eq. (2) to derive practical estimates of $\mathbf{x}^a$ and their misfits to the "true" emissions. This alternative indicator of the inversion performance, called hereafter misfit reduction (MR), allows testing the accuracy of the theoretical computation of the UR which relies on Eq. (1). We write it, for specific budgets of the fossil fuel emissions (at control or larger space and time scales):

$$\mathrm{MR} = 1 - \frac{\varepsilon^a}{\varepsilon^b} \quad (4)$$

where ε^a and ε^b are the posterior and prior misfits between the inverted and true values for the corresponding emission budgets. In this study, we discuss the uncertainties and misfits at the monthly and annual scales. Here, the "monthly" scores of uncertainty (or misfit) are calculated from the quadratic mean of the uncertainty (or misfit) of the 12 monthly budgets for that region. In addition, the scores of the relative uncertainty and misfit are defined as the ratios of the absolute uncertainties and misfits to the absolute prior emission budgets.

3.2.2.2. Practical setup

Control vector

The inversion system controls monthly budgets of fossil fuel emissions for a set of regions during the year 2007. The map of these regions is given in Fig. 2a. The space discretization of regions is higher where the emissions are the largest, in particular in Europe (area of interest), but also in US and China (no OSSE results shown in this study) (Fig. 2b, c and 3). In other areas (Fig. 2a and Table S2), the size of control regions is far larger, and can reach that of the continents. The spatial resolution of the control vector in Europe corresponds to the typical size of a middle-sized European country (e.g. France) but in Western Europe, where the emissions are the highest, the control vector has sub-national regions (e.g. southern and northern UK, southern and northern Italy, western and eastern Germany, western and eastern France in Fig. 2a). In US and China, smaller regions are also used where emissions are the largest (Fig. S1). Monthly emissions from ships over the ocean are also included in the control vector, so that the ocean is considered as one large region. In total, the world is divided into 54 land regions and 1 ocean region. Our inversion solves for the 12 monthly budgets of emissions for these regions, but not for the spatio-temporal distributions within each region and month. We do not control the emissions before 2007 nor the initial concentration of $FFCO_2$ on the initial date of the inversion, by January 1st of 2007.

Choosing year 2007 for the period of the inversion only impact the meteorological conditions and the level of emissions that are taken into account in our inversion framework. We assume that these conditions will not impact the conclusions from the analysis strongly so that they can be expected to be representative of average conditions for recent years.

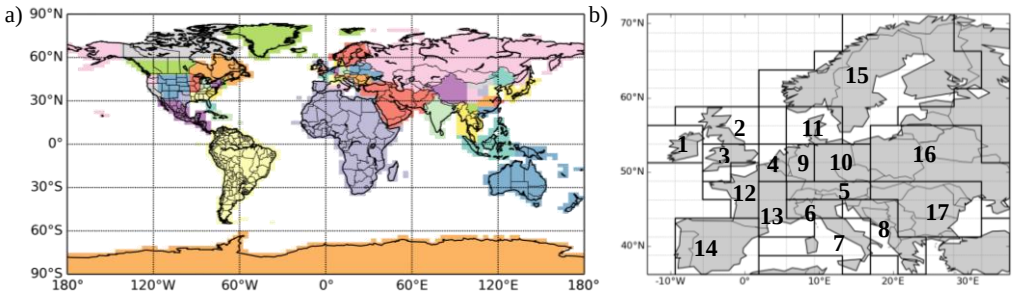

Figure 2 a) Map of the 56 regions whose monthly emission budgets are controlled by the inversion; b) zoom over the 17 control regions in Europe.

Time selection of data to be assimilated

State-of-art inversion systems generally make use of data during afternoon only, due to limitations of transport models for simulating near-surface mixing ratios during night-time. Given the assumed ability in this OSSE to have an intermittent filling of air samples, we thus define the observations to be selectively sampled only during the afternoon (12:00-18:00 local time). Since the cost of the $^{14}CO_2$ analysis of one sample is presently high, monitoring of $^{14}CO_2$ (and thus $FFCO_2$) during a whole year favors the choice of such time-integrated samples at the weekly to 2-week scale (Vogel et al., 2013). Thus we will first consider using 2-week integrated afternoon $FFCO_2$ data in the inversions. In addition, we present tests with a high-frequency temporal sampling, namely daily afternoon mean data, keeping in mind that such a sampling scheme would be costly (Levin et al., 2011; Vogel et al., 2013; Turnbull et al., 2016). Sampling $FFCO_2$ observations at high temporal resolution when targeting regional / 1-month scale budgets of emissions is not encouraged by our previous theoretical analysis of temporal auto-correlations of the observation errors (Wang et al., 2016). But having daily sampling would dramatically decrease the weight of the measurement errors on longer time scales that could be a base for improvements of the inversions, which deserves a specific test. While tests will be conducted with 2-week samplings for the three networks, daily sampling will only be tested for NET43 which is sufficient to draw conclusions regarding the usefulness of such a high frequency sampling scheme.

Observation operator

As indicated above, the initial conditions on January 1st, 2007 are not controlled by the inversion. This follows Wang et al. (2016) who checked that spatial patterns in $FFCO_2$ from the emissions at a given time appear to become negligible (with an amplitude smaller than 0.1 ppm at a tall tower near the surface) within about 2 weeks through diffusion during

atmospheric transport. The influence of the global $FFCO_2$ distribution on January 1st, 2007 (i.e. the initial condition of the inversion experiments in our studies) is negligible for the gradients of $FFCO_2$ in Europe even in January 2007, and thus for the estimates of monthly emissions in 2007.

In consequence, the observation operator is linear and does not have an affine term $\mathbf{y}_{fixed}$. The linear observation operator $\mathbf{H}$ consists of a chain of three sub-operators, $\mathbf{H}=\mathbf{H}_{samp}\mathbf{H}_{transp}\mathbf{H}_{distr}$, where $\mathbf{H}_{distr}$ maps the regional monthly fossil fuel emission budgets to an gridded emission map at the resolution of the transport model, where $\mathbf{H}_{transp}$ is the atmospheric transport, and where $\mathbf{H}_{samp}$ is the sampling of $FFCO_2$ gradients corresponding to the observation vector from the transport model outputs (Wang et al. 2016).

We used the high-resolution (0.1 °) annual fossil fuel emission map from PKU-CO_2 for 2007 (Wang et al., 2013) to model the spatial and temporal distribution of emissions within each region of control. PKU-CO_2 is an annual emission map with no temporal profile. We denote this implementation of $\mathbf{H}_{distr}$ by $\mathbf{H}_{distr}^{PKU}$.

The off-line version of the general circulation model of Laboratoire de Météorologie Dynamique LMDZv4 (Hourdin et al., 2006) forms the atmospheric transport operator $\mathbf{H}_{transp}$. Atmospheric transport simulations was nudged to analyzed wind fields from European Centre for Medium-Range Weather Forecasts (ECMWF) Interim Reanalysis (ERA-Interim, Berrisford et al., 2009) for the year 2007. We denote this realization of $\mathbf{H}_{transp}$ by $\mathbf{H}_{transp}^{LMDZ}$.

The sampling of $FFCO_2$ gradients relies on the extraction of individual mole fraction data at the measurement locations and then on the computation of differences between time series at each site and those at the reference site of JFJ. The mole fraction data for a given site is sampled as the value in the transport model grid cell containing this site. All measurements, except at the reference site JFJ, are sampled at 100 magl, the first level of LMDZ. The JFJ data is sampled at its actual height of 3450 masl (sixth level of LMDZ). The resulting practical implementation of $\mathbf{H}_{samp}$ is denoted by $\mathbf{H}_{samp}^{coloc}$. For different observation network and sampling integration time, this operator is adapted according to the temporal averaging of the afternoon $FFCO_2$ gradients.

To sum up, the observation operator that is used in practice for inversions is defined by $\mathbf{H}= \mathbf{H}_{samp}^{coloc}\ \mathbf{H}_{transp}^{LMDZ}\ \mathbf{H}_{distr}^{PKU}$.

Prior error covariance matrix

Usually, prior uncertainties in the estimate of the emissions from an inventory are only

reported at national and annual scales. Although there have been efforts to compare various fossil fuel emission estimates (Macknick et al., 2009; Ciais et al., 2010; Andres et al., 2012), the ability to characterize prior emission uncertainties is limited for sub-national and sub-annual scales. In this study, we use different streams of information to build the corresponding prior error covariance matrix **B** and it raises two quantifications of the prior uncertainties.

The first derivation of the **B** matrix is based on reported uncertainties for national emissions. Prior uncertainties are assumed to have Gaussian and unbiased distributions that are perfectly characterized by the set-up of a prior uncertainty covariance matrix, $\mathbf{B}^{theo}$. Usually, 1-sigma uncertainties in the self-reported annual national fossil fuel emissions are claimed to range from 1-2.5% for US (US EPA, 2015), 2%-7% for European countries (Andres et al., 2014; Ballantyne et al., 2015), to 7.5-10% for countries like China (Gregg et al., 2008; Liu et al., 2015). However, geographically distributed emission maps, even aggregated at national scale, may have larger uncertainties than national inventories, as indicated by the differences between two emission maps (see below), which could be larger than 10% at national and annual scale for European regions/countries. Based on this, prior uncertainties in monthly emissions are set–up based on three constraints: 1) uncertainties in annual emissions are 10% for US, European countries and China at national scale, and assumed to be 10% for other regions; 2) uncertainties in monthly emissions have a 2-month temporal auto-correlation and 3) spatial correlations between uncertainties in monthly emissions across adjacent regions within the same country are fixed to a negative value: -0.2 to account for the fact that emission estimates at sub-national scales are usually disaggregated from national inventories. This set-up of $\mathbf{B}^{theo}$ has the property that uncertainties in monthly emissions could surpass 10% and be as large as 30% in some regions.

The second estimation of the **B** matrix is based on the actual differences between two spatially gridded emission maps, used as the prior and true estimate of the large-scale fluxes in the second type of OSSEs (see section 3.2.3). The two emission maps considered are from PKU-CO_2 (Wang et al., 2013) and EDG-IER in 2007. The EDG-IER inventory is a gridded emission product that convolves the EDGAR annual emission map with (sector, country, month and year specific) monthly profiles and (country, sector and day specific) daily profiles and also with (country, day, hour and time zone specific) hourly profiles (available

at http://carbones.ier.uni-stuttgart.de/wms/index.html). The set-up of prior uncertainties covariance matrix based on the difference between PKU-CO_2 and EDG-IER maps is called $\mathbf{B}^{prac}$. In general, the differences of annual emissions from the control regions in Europe between these two emission maps range from 3% to 20%, but larger (44%) in the Balkans. Statistics of the difference between the two maps are fitted by a covariance model with different time-scales, namely monthly, 3-monthly, 6-monthly and annual. The correlations between the components of the uncertainties at different sub-annual time scales are modeled with exponential decay functions, in which the correlation lengths are 1 month, 3 months, 6 months, while uncertainties at annual scale are fully correlated. The mathematical formula for this computation is detailed in the Appendix A. In addition, we assume that there is no spatial correlation of the prior uncertainty between different regions.

While $\mathbf{B}^{prac}$ is built using an error covariance model which cannot perfectly characterize the covariance of the "actual prior errors", it is based on parameters that makes it better fit them than the $\mathbf{B}^{theo}$ matrix. One could debate whether our proposed derivation of $\mathbf{B}^{prac}$ is more or less adapted than that of $\mathbf{B}^{theo}$ to reflect uncertainties in inventories. The differences between the theoretical estimates of UR on regional budgets based on Eq (1) using $\mathbf{B}^{prac}$ or $\mathbf{B}^{theo}$ can be used to have an assessment of the range of the inversion skills given strongly different assumptions regarding the prior uncertainty in the emission budgets from inventories.

Observation error covariance matrix

Wang et al. (2016) characterized and proposed estimates for observation errors in the $FFCO_2$ gradients across Europe when using the modeling framework of our study. They decomposed the observation errors into four main components:

1) The measurement error $\boldsymbol{\varepsilon}_i$. This error is simply assumed to be 1 ppm with no temporal and spatial correlations. This 1 ppm measurement error for $FFCO_2$ gradients between sites corresponds to a combination of the typical precision of the analysis of air samples by accelerator mass spectrometry (AMS) for $^{14}CO_2$ (2‰-3‰) and by typical analyzers for continuous CO_2 samples (Vogel et al., 2010; Turnbull et al., 2014), and of uncertainties in the conversion of $^{14}CO_2$ and CO_2 measurements into $FFCO_2$ (Levin et al., 2003).

2) The representation error $\boldsymbol{\varepsilon}_r$. This error arises from the mismatch between the resolution of the transport model and the spatial variability of the actual fluxes and concentrations, due to

the modelling of concentrations and emissions at the coarse resolution of the transport model in the observation operator.

3) The transport errors $\boldsymbol{\varepsilon}_t$ due to the use of discretized and simplified equation for modeling the transport in practice.

4) The aggregation error $\boldsymbol{\varepsilon}_a$ due to the imperfect representation of the distribution of the emissions within each region/month controlled by the inversion when using $\mathbf{H}_{distr}$.

Assuming that all these components are independent from each other and have Gaussian and unbiased distributions: i.e. $\boldsymbol{\varepsilon}_i \sim N(\mathbf{0}, \mathbf{R}_i)$, $\boldsymbol{\varepsilon}_r \sim N(\mathbf{0}, \mathbf{R}_r)$, $\boldsymbol{\varepsilon}_t \sim N(\mathbf{0}, \mathbf{R}_t)$, $\boldsymbol{\varepsilon}_a \sim N(\mathbf{0}, \mathbf{R}_{adistr})$, $\mathbf{R}$ is given by the sum of the covariance matrices corresponding to different errors: $\mathbf{R} = \mathbf{R}_i + \mathbf{R}_r + \mathbf{R}_t + \mathbf{R}_a$.

Wang et al. (2016) sampled representation and aggregation errors in the same inversion system as used here, by using simulations with a mesoscale regional transport model and by degrading the spatial and temporal resolution of the emission maps in the input of this model and of the output mole fraction field. Based on these samples, Wang et al. (2016) defined values for the standard deviation of $\boldsymbol{\varepsilon}_r$ as a function of the season and on whether the corresponding measurement stations is urban or rural. For $\boldsymbol{\varepsilon}_a$, they derived a standard deviation that is a function of the semester only: spring/summer or autumn/winter. The temporal autocorrelations in the representation and aggregation errors, were characterized as the sum of a long-term component and a short-term component, both modeled using an exponentially decaying function: $r(\Delta t)=a \times e^{-\Delta t/b}+(1-a) \times e^{-\Delta t/c}$ where Δt is the timelag (in days) and a, b, c are parameters optimized by regressions against the samples of the errors. In this study, we use these estimate of the standard deviations and the parameters of the correlation functions for the different observation errors derived by Wang et al. (2016) to set-up the $\mathbf{R}$ matrix. The corresponding values for 2-week/daily mean afternoon $FFCO_2$ gradients are listed in Table 1 and Table 2.

Table 1 Standard deviations of the different observation errors (in ppm) for the 2-week/daily mean afternoon $FFCO_2$ gradients. (For the description of each error, see main text).

	Spring		Summer		Autumn		Winter	
	Urban	Rural	Urban	Rural	Urban	Rural	Urban	Rural
ε_i	1.0							
2-week mean afternoon $FFCO_2$ gradients								
ε_r	0.99	0.52	0.92	0.52	1.50	0.71	1.89	0.93
ε_a	0.17				0.21			
ε_t	0.52–1.11, site dependent							
daily mean afternoon $FFCO_2$ gradients								
ε_r	1.48	0.92	1.45	0.91	2.25	1.25	2.56	1.42
ε_a	0.24				0.30			
ε_t	1.94–4.15, site dependent							

Table 2 The parameters of the temporal autocorrelations in the representation and aggregation errors for 2-week/daily mean afternoon $FFCO_2$ gradients. The temporal correlations have a form of e-folding function $r(\Delta t)=a\times e^{-\Delta t/b}+(1-a)\times e^{-\Delta t/c}$.

	a	*b*	*c*
2-week mean afternoon $FFCO_2$ gradients			
urban ε_r	0.29	18.9	365
rural ε_r	0.36	11.6	365
ε_a	0.16	11.2	365
daily mean afternoon $FFCO_2$ gradients			
urban ε_r	0.66	0.90	365
rural ε_r	0.78	0.78	365
ε_a	0.54	1.1	365

3.2.3 Configurations of the two types of OSSEs

In this study, we consider two types of OSSEs associated with our two definitions of the

B matrix. In the first type of OSSE, the prior uncertainty and the observation errors are assumed to have Gaussian and unbiased distributions that are perfectly characterized by the set-up of the prior uncertainty covariance matrix $\mathbf{B}^{theo}$ and observation error **R** in the inversion system. With this assumption, the posterior uncertainty and UR are perfectly characterized by the theoretical application of Eq. (1). This first type of OSSEs is referred to as "theoretical inversion".

In the second type of OSSEs, we generate a synthetic prior estimate of the emissions, a synthetic truth (true emissions and true observation operator) and a set of synthetic observations. Here, the "actual" prior uncertainties and observation errors have a complex statistical distribution which is not perfectly adapted to the unbiased and Gaussian assumptions and are not perfectly reflected by the set-up of the prior uncertainty covariance matrix $\mathbf{B}^{prac}$ and observation error covariance matrix **R** in the inversion system. In such a context, the posterior uncertainty and UR cannot be perfectly characterized by the theoretical application of Eq. (1). Eq. (2) is thus applied using the synthetic data generated for this OSSE to derive scores of MR. This second type of OSSE is referred to as "practical inversion".

In practical inversions, the synthetic prior estimate of the regional/monthly emissions $\mathbf{x}^{b}$ are built based on the emissions from PKU-CO_2 ($\mathbf{x}^{PKU}$ hereafter). The synthetic truth and synthetic observations are modelled using a relatively independent representation of the "actual" emissions and the "actual" operators. These actual operators should bear patterns of the emissions and variability in the mole fractions which should be realistic enough so that such OSSEs can provide realistic characterizations of the potential of the inversions when using real measurements. Firstly, the synthetic true regional/monthly emissions are built based on the emission map from EDG-IER, referred to as $\mathbf{x}^{EDG\text{-}IER}$ hereafter. Secondly, the synthetic true observation operator is modelled by $\mathbf{H}^{true}=\mathbf{H}_{samp}{}^{coloc}\mathbf{H}_{transp}{}^{LMDZ}\mathbf{H}_{distr}{}^{EDG\text{-}IER}$. The differences between the synthetic true observation operator and the observation operator used in the inversion systems reflect the typical uncertainties associated with the imperfect distribution represented by the operator $\mathbf{H}_{distr}{}^{PKU}$. Thirdly, the synthetic true observation operator is applied to the synthetic true emissions to generate the time series of the "true" $FFCO_2$ mole fractions, called $\mathbf{y}^{t}$ hereafter. At last, the "true" mole fractions are perturbed in order to mimic the variability that cannot be modelled by the synthetic true emissions and synthetic true observation operator. Specifically, the variability that is not modelled by the synthetic truth include measurement error, the representation error which is connected to the

variations at scales smaller than the resolution of LMDZv4 (e.g. $\mathbf{H}_{transp}^{LMDZ}$), and the transport error. The perturbation follows the statistics of the corresponding errors quantified by Wang et al. (2016), as discussed in section 3.2.2.2. The configurations of the two types of OSSEs and of the corresponding inversion parameters are summarized in Table 3 and Fig. 3.

Table 3 Set-up and performance indicators of the theoretical and practical OSSEs (details see text)

input of the inversion	**theoretical inversions**	**practical inversions**
B	$\mathbf{B}^{theo}$	$\mathbf{B}^{prac}$
R	$\mathbf{R}_i + \mathbf{R}_r + \mathbf{R}_t + \mathbf{R}_a$	$\mathbf{R}_i + \mathbf{R}_r + \mathbf{R}_t + \mathbf{R}_a$
H	$\mathbf{H}_{samp}^{coloc}\mathbf{H}_{transp}^{LMDZ}\mathbf{H}_{dist}^{PKU}$	$\mathbf{H}_{samp}^{coloc}\mathbf{H}_{transp}^{LMDZ}\mathbf{H}_{dist}^{PKU}$
performance indicator	UR (Eq. 3)	UR (Eq. 3)
$\mathbf{x}^t$	–	$\mathbf{x}^{EDG\text{-}IER}$
$\mathbf{x}^b$	–	$\mathbf{x}^{PKU}$
$\mathbf{y}_o$	–	$\mathbf{H}_{samp}^{coloc}\mathbf{H}_{transp}^{LMDZ}\mathbf{H}_{distr}^{EDG\text{-}IER}\mathbf{x}^{EDG\text{-}IER} + \boldsymbol{\varepsilon}_i + \boldsymbol{\varepsilon}_r + \boldsymbol{\varepsilon}_t$
performance indicator	–	MR (Eq. 4)

a) theoretical inversions

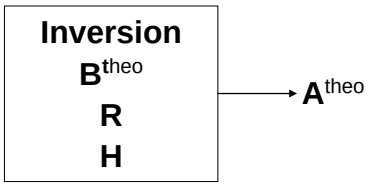

b) practical inversions

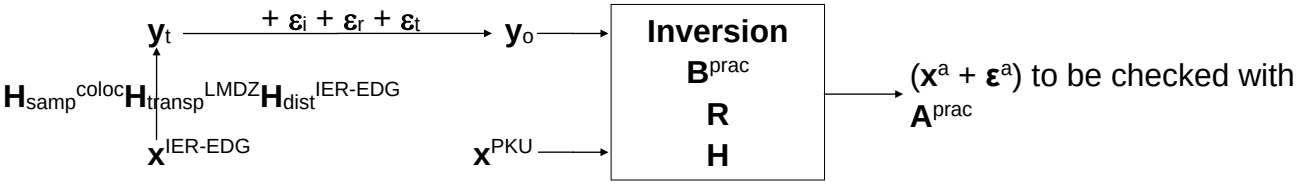

Figure 3 Illustration of the two types of OSSEs: a) theoretical inversions; b) practical inversions.

In this study, each type of OSSEs is conducted for each assumed observation networks and temporal sampling. The notations of the resulting eight OSSEs are listed in Table 4.

Table 4 The notations for the eight OSSE experiments. Numbers of observations of $FFCO_2$ gradients per year are given in parentheses

	theoretical inversions	practical inversions
NET17, 2-week sampling (416)	T-17W	P-17W
NET43, 2-week sampling (1092)	T-43W	P-43W
NET43, daily sampling (15288)	T-43D	P-43D
NET233, 2-week sampling (6032)	T-233W	P-233W

3.3 Results

3.3.1 Assessment of the performance of inversions when using the NET17/NET43 and 2-week integrated sampling

3.3.1.1. Analysis of the results at the regional and monthly scale

Figure 4 shows the UR for monthly emissions from inversions when using the NET17 and NET43 networks and 2-week mean sampling (OSSEs T-17W, P-17W, T-43W and P-43W according to Table 4). With NET17, the theoretical and practical inversions show very close patterns of URs. The largest UR occurs in the region of western Germany (34% and 38% for theoretical and practical inversions, respectively). This stems from the fact that several stations are located around this region and that the emission in this region is higher than the other area of Europe. Slight URs are also found for Benelux (12%) and Eastern France (15%) in practical inversions. The URs elsewhere are marginal. Adding new sites from NET17 to NET43 yields a significant increase of the UR for southern UK (from 3% to 23%), northern Italy (from 3% to 18%) and eastern Europe (from 2% to 15%) in theoretical inversions, while the increase of the URs due to the increase of the network in practical inversions mainly occurs in eastern France (from 16% to 33%) and Balkans (from 3% to 13%). Despite the divergence in their results for specific regions, both types of inversions highlight the overall increase of the URs in western European regions due to the fact that most of the new sites from NET17 to NET43 are located in this area. However, the increase of the URs (from 38% to 39% for theoretical inversion and from 33% to 35% for practical inversion) resulting from the expansion of the network from NET17 to NET43 does not impact much the URs for eastern Germany, around which the $FFCO_2$ mixing ratios are

already well sampled by the NET17 configuration.

The discrepancies between the maps of uncertainty reductions in the theoretical and practical inversions are shown in Fig. 4. They reveal the high sensitivity of the URs to the configuration of the prior uncertainties. Fig. 5a and 5b show the theoretical and practical configurations of **B.** They give a significantly different view of the regions for which the prior uncertainty in the emissions is the highest and thus where the potential to assimilate the atmospheric signal given this this uncertainty and to reduce this uncertainty. For example, the $\mathbf{B}^{prac}$ built from the statistics of the difference between the EDG-IER and PKU-CO_2 emission maps has a much larger uncertainty than $\mathbf{B}^{theo}$ over eastern France (43% in $\mathbf{B}^{prac}$ vs 16% in $\mathbf{B}^{theo}$) while this is the opposite for southern UK (4% in $\mathbf{B}^{prac}$ vs 14% in $\mathbf{B}^{theo}$).

The scores of prior and posterior uncertainties in Fig. 5 complement those of URs in Fig. 4 by giving insights on the precision of the estimates of monthly fossil fuel emissions that should be achievable with NET17 and NET43 and 2-week sampling. With NET17, the uncertainties of monthly fossil fuel emissions are reduced from 29% (or 17%) in the prior estimates to 17% (or 9%) in the posterior estimates for western Germany in theoretical (or practical) inversions. Using additional sites in NET43 further reduces the uncertainties in monthly fossil fuel emissions in Southern UK from 25% in the prior estimates to 19% in the posterior estimates in theoretical inversions, and reduces the uncertainties in monthly fossil fuel emissions in eastern France from 44% in the prior estimates to 29% in the posterior estimates in practical inversions.

The scores of the misfits and MRs for regional monthly fossil fuel emissions from the practical inversions using the NET17 and NET43 networks and 2-week sampling are also shown in Fig. 5 and Fig. 4. The prior uncertainties and misfits are similar since it was the purpose of building $\mathbf{B}^{prac}$ on the statistics of the differences between $\mathbf{x}^{PKU}$ and $\mathbf{x}^{EDG\text{-}IER}$. The spatial patterns of the posterior misfits in Fig. 5 are very close to those of the posterior uncertainties, which is a positive indication of the robustness of the theoretical computations of uncertainty reduction. However, there are slight differences between the MRs and URs. For example, in P-43W, the MR (21%) for Iberian Peninsula is larger than the UR (5%), while the MR (40%) for western Germany is slightly smaller than the UR (47%). The discrepancies in the posterior misfit and posterior uncertainty, and thus discrepancies between MRs and URs, are attributed to: 1) the prior uncertainty covariance matrix and the unbiased and Gaussian assumptions cannot perfectly reflect the differences between the prior

estimate of the monthly emissions and the synthetic true monthly emissions; and 2) the spatial and temporal distribution of emissions within each region and during each month that we used in the inversion system ($\mathbf{H}_{dist}^{PKU}$) is different from that we used in the synthetic truth observation operator ($\mathbf{H}_{dist}^{EDG\text{-}IER}$), but the set-up of the aggregation errors by the exponential functions is too simplified to capture the actual errors due to this mismatch.

Figure 6 shows the correlations in the prior and posterior uncertainties in monthly emissions over different regions, and their differences for the OSSEs T-43W and P-43W. The patterns of the correlations in the prior or posterior uncertainties from T-17W and P-17W are very similar but not shown here. After assimilating the observations, the change of correlations mainly occurs among regions with large URs (see Fig. S2 for the full correlation matrix). In both OSSEs, there are negative correlations between the posterior uncertainties in monthly emissions from neighboring regions (Fig. 6), for instance, between western Germany and eastern Germany (from -0.27 to -0.18 between different months). The negative correlations between the posterior uncertainties in monthly emissions of different regions indicate that the measurements from NET43 bring a large constraint on the budgets over a large area but not on the individual regions. The temporal correlations in the posterior uncertainties between different months for a specific region also change after assimilating the measurements. In theoretical inversion, the correlations between posterior uncertainties in monthly emissions is smaller than those between prior uncertainties in monthly emissions at time scale smaller than 3 months (negative change when time lag smaller than 3 months, Fig. 6e). But assimilating the observations from NET43 introduces positive long-term correlations into the posterior uncertainties (positive change when time lag exceed 3 months, Fig. 6e). Because our set-up of $\mathbf{B}^{theo}$ only considers an exponential temporal correlation where the correlation length is 2 months, the temporal correlations in observation errors, which contain a long-term component, are projected into the posterior uncertainties of monthly emissions. On the contrary, in the practical inversion, where the set-up of $\mathbf{B}^{prac}$ includes a component in the temporal correlations at annual scale, after assimilating the observations, the temporal correlations between posterior uncertainties in the monthly emissions are smaller than those between prior uncertainties. Differences in temporal correlations between posterior uncertainties and prior uncertainties (Fig. 6e and 6f) shows the potential of atmospheric observations at filtering the signature of the prior uncertainties at short-time scale. But the potential of filtering the signature of the prior uncertainties at

long-time scale varies with the prior knowledge about the emissions.

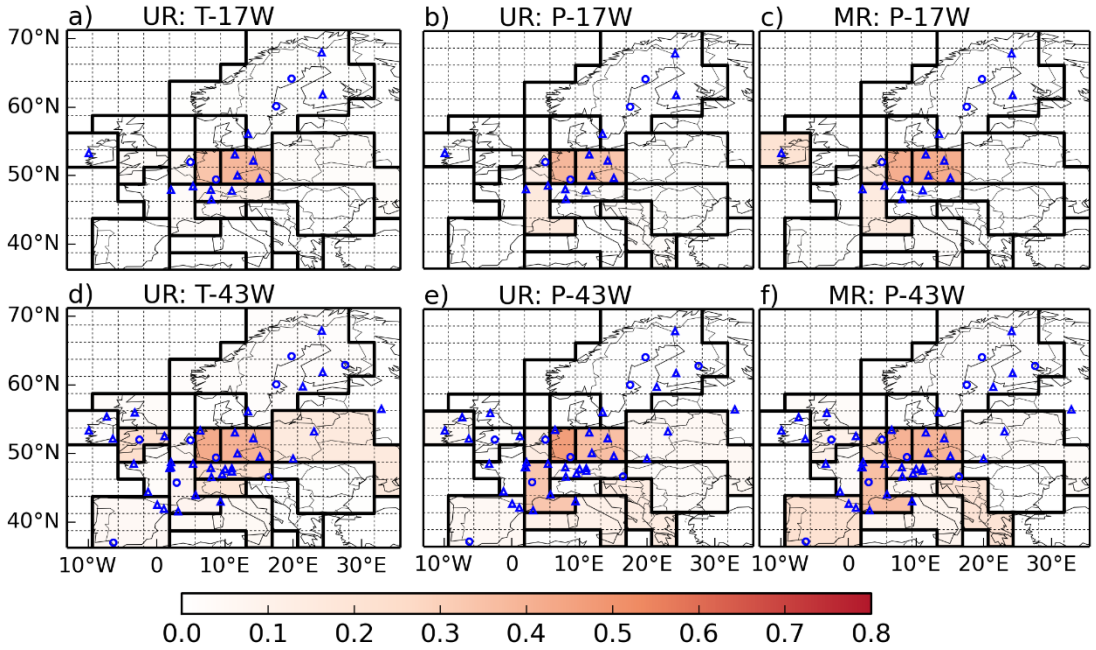

Figure 4 Uncertainty reduction (UR) and misfit reduction (MR) in monthly fossil fuel emissions over regions delineated by black lines using the NET17 and NET43 networks and 2-week sampling of $FFCO_2$. First column are the results of theoretical inversions. The second and third columns are the results of the practical inversions. The dots and triangles are the locations of the observation sites. Dots (triangles) correspond to "urban" (or "rural") stations defined in section 3.2.1. A value of UR and MR closer to unity means a better performance of an inversion to constrain fossil fuel emissions in a region.

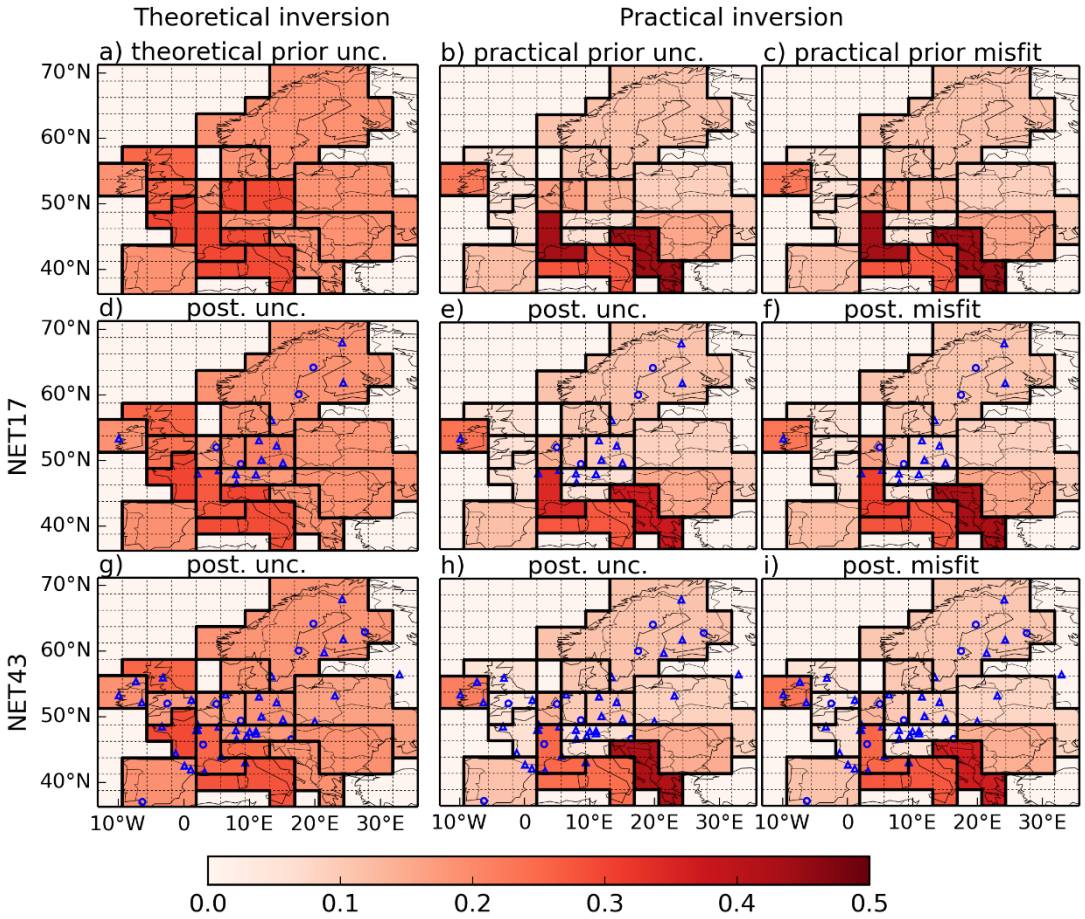

Figure 5 Relative prior and posterior uncertainties and misfits of monthly fossil fuel emissions over regions delineated by black lines using the NET17 and NET43 networks and 2-week sampling for the theoretical (first column) and practical (second and third columns) inversions. First row shows the prior uncertainties and misfits. The second row shows the posterior uncertainties and misfits after assimilating 2-week mean afternoon $FFCO_2$ observations from network NET17. The third row shows the posterior uncertainties and misfits after assimilating 2-week mean afternoon observations from network NET43. The dots and triangles are the locations of the observation sites. Dots (triangles) correspond to "urban" (or "rural") stations defined in section 3.2.1.

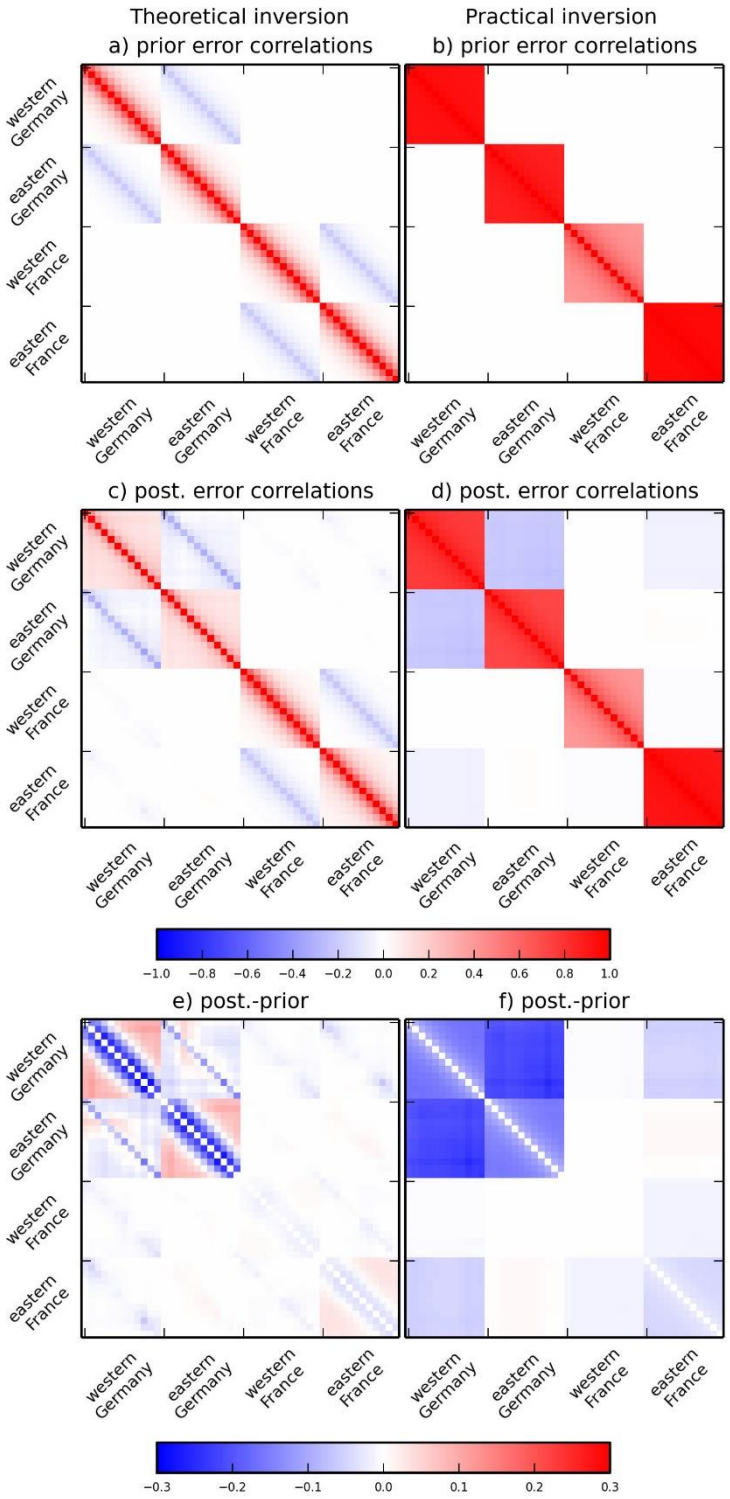

Figure 6 The correlation structure in the prior (a and b) and posterior (c and d) uncertainties in monthly fossil fuel emissions for the four Germany and France regions using the NET43 network and 2-week sampling for the theoretical (first column) and practical (second column) inversions, as well as their differences (e and f). The *x* and *y* axes cover the control region-months iterating through region first and the months in second. For clarity, we group these correlations into four regions and organize them for each region according to month indices. The full correlation matrix are shown in the Fig. S2.

3.3.1.2. Analysis for annual emissions

Now, we compare the performance of different types of inversions and networks for annual emissions. The URs, MRs, as well as the prior and posterior uncertainties/misfits at annual scale are shown in Fig. 7 and 8. The patterns and values of URs of annual emissions are in general similar to those at monthly scale (Fig. 4). High URs and MRs occur mostly in the regions where the observation networks are dense. Up to 47% UR is achieved for western Germany. Accordingly, the posterior uncertainties of annual fossil fuel emissions (Fig. 8), when using the NET43 network and 2-week sampling, are 10% (or 4%) for southern UK, 8% (or 8%) for western Germany and 15% (or 28%) for eastern France in theoretical (or practical) inversions.

The scores of the MRs of annual emissions in practical inversions (Fig. 7 c and f) is larger than that of the URs. The cause of the discrepancy between the scores of MR and UR was discussed in section 3.3.1.1 at the monthly scale. However, the distances between the MRs and URs are much larger at annual scale than at monthly scale. This is because the use of our simple models and Gaussian assumptions to fit actual errors in the prior estimate of emissions is less adapted for the emission budgets at annual scale than for the emission budgets at monthly scale.

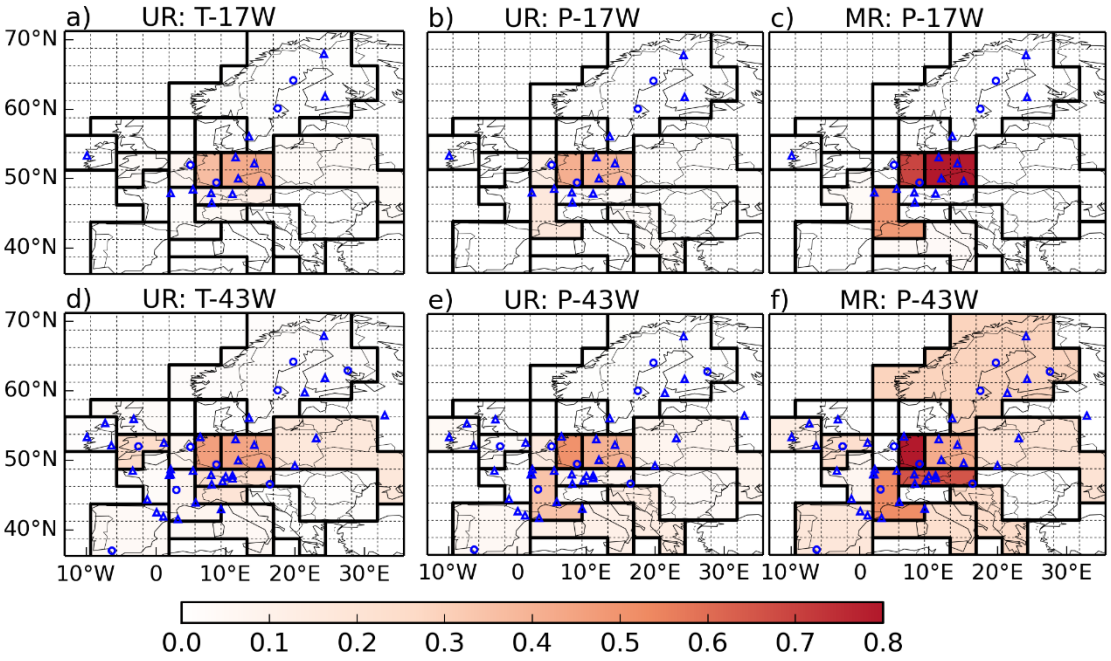

Figure 7 Uncertainty and misfit reductions in the annual fossil fuel emissions at the control resolution using the NET17 and NET43 networks and 2-week sampling. First column are the results of theoretical inversions. The second and third columns are the results of the practical inversions. The dots and triangles are the locations of the observation sites where the gradients are extracted with respect to the JFJ reference site. Dots (triangles) correspond to “urban” (or “rural”) stations defined in section 3.2.1.

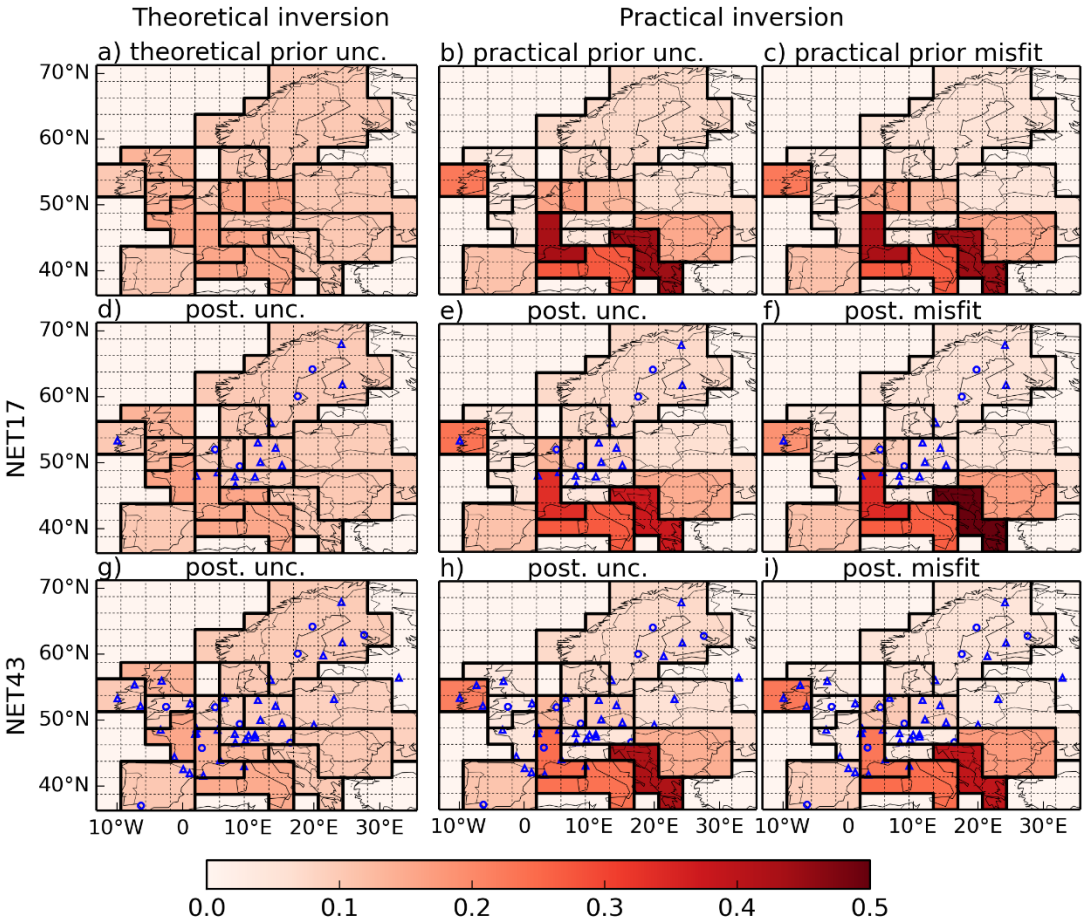

Figure 8 Relative prior and posterior uncertainties and misfits of annual fossil fuel emissions at the control resolution using the NET17 and NET43 networks and 2-week sampling for the theoretical (first column) and practical (second and third columns) inversions. First row shows the prior uncertainties and misfits. The second row shows the posterior uncertainties and misfits associated with the observation network NET17. The third row shows the posterior uncertainties and misfits corresponding to the observation network NET43. The dots and triangles are the locations of the observation sites where the gradients are extracted with respect to the JFJ reference site. Dots (triangles) correspond to "urban" (or "rural") stations defined in section 3.2.1.

3.3.2 Impact of using daily measurements and using a dense observation network

Figure 9 shows the URs in monthly emissions from inversions using the NET43 network and daily sampling and from inversions using NET233 network and 2 week sampling (results from OSSEs T-43D, P-43D, T-233W and P-233W in Table 4). When using the NET43 network and daily sampling, the URs of monthly emissions are (not surprisingly) generally larger than using NET43 network and 2-week sampling for all regions. The differences

between the URs of monthly emissions when using daily sampling and when using 2-week sampling are larger over the well-sampled regions, in particular, the URs of monthly emissions for western Germany reach as high as 62% (or 67%) in theoretical (or practical) inversions. When using the NET233 network and 2-week sampling (Fig. 9 d-f), the URs of monthly emissions for some regions that are poorly sampled by the NET17 or NET43 network, in particular in the eastern Europe (36%) in theoretical inversion and in Balkan (73%) in practical inversion, are much larger than those when using NET17 or NET43 networks and 2-week sampling.

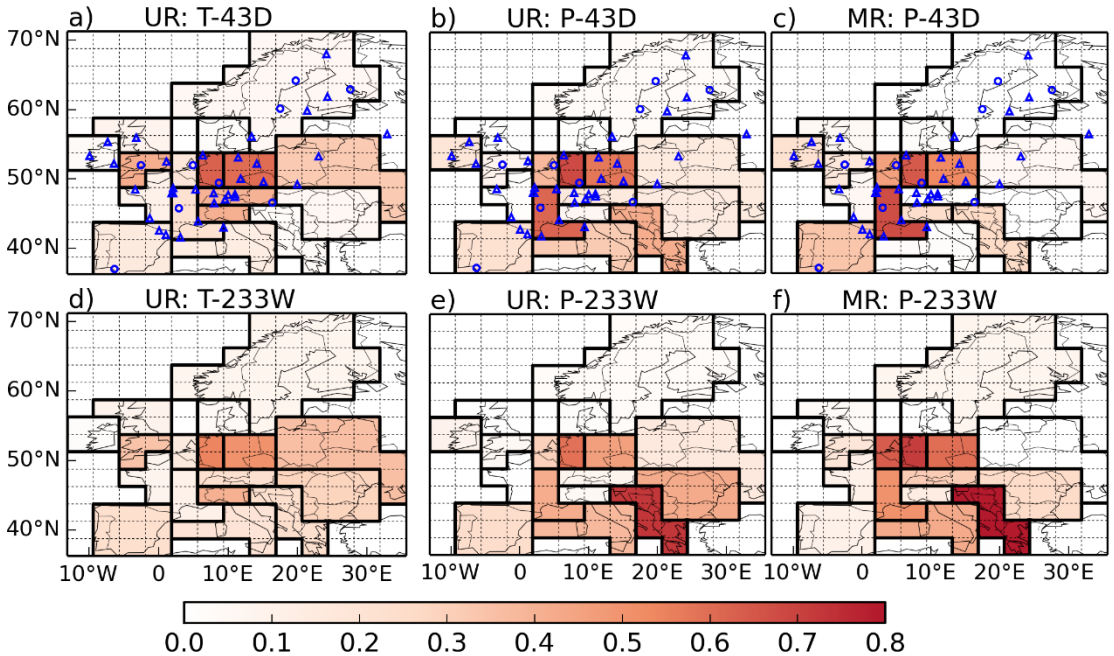

Figure 9 Uncertainty and misfit reductions in the monthly fossil fuel emissions at the control resolution using the NET43 network with daily sampling and NET233 network with 2-week sampling. First column are the results of theoretical inversions. The second and third columns are the results of the practical inversions. The dots and triangles are the locations of the observation sites where the gradients are extracted with respect to the JFJ reference site. Dots (triangles) correspond to "urban" (or "rural") stations defined in section 3.2.1. The locations of the sites in the OSSEs T-233W and P-233W are not plotted to avoid blurring the maps.

3.4 Discussion

3.4.1 Implication for long-term trend detection of fossil fuel emissions

In 2010, the European commission (2010) proposed a transition pathway to reduce its emissions by 80% by 2050 compared to a 1990 baseline. This pathway means annual reductions compared to 1990 of roughly 1% in the 2020s, 1.5% in the decade from 2020 until 2030, and 2 % in the two decades until 2050 (European commission, 2010). Levin and Rödenbeck (2007) showed that, taking into account the inter-annual variations of the atmospheric transport, changes of 7-26% in fossil fuel emissions in respective catchment areas when comparing two consecutive 5-year averages could be detected at the 95% confidence level with monthly mean atmospheric $^{14}CO_2$ observations sampled at two sites in southwestern Germany. However, the detectability of changes in the range 7-26% between 5-year averages is far from sufficient to support the detection of 1-2% annual change (which means 5-10% changes in two consecutive 5-year averages) corresponding to the European objective. When the trend of fossil fuel emissions is calculated from a series of estimates for multiple years, the uncertainty in the calculated trend is independent of the trend itself (see Appendix A3 for equations). Assuming that the posterior uncertainties in annual emissions of different years are fully independent, which can be supported by the independence of the observations used to constrain the estimates from year to year, we calculated the uncertainty in regressed trends for different time lengths (Table 5) given annual emission uncertainties from our OSSEs. The result shows that in order to get robust estimate of the emission trends, it favors the option of monitoring emissions for a long period over decreasing the uncertainties of emissions for a single year. In our OSSEs when using the ICOS-like network (NET17 or NET43) and 2-week sampling, the posterior uncertainty in annual emissions of the well-sampled regions, e.g. western Germany, is within 10% (section 3.3.1.2). In this case, it only supports the detection of the emission trend for at least 20 years, given the target of 1-2% annual reduction. For other regions where the URs are very small, the monitoring of the trend cannot be supported by assimilating observations within such an inversion system.

Table 5 Uncertainties in the regressed linear trends given different assumptions on the posterior uncertainty in annual emissions. The uncertainties are defined as the uncertainty budgets in percentage of the budget in the base year.

Assumed posterior uncertainty in annual emissions	10-year trend	20-year trend
10%	1.2% yr^{-1}	0.43% yr^{-1}
5%	0.78% yr^{-1}	0.27% yr^{-1}
1%	0.56% yr^{-1}	0.20% yr^{-1}

3.4.2 Adequacy of large-scale atmospheric inversion of fossil fuel emissions and potential of improvement of the inversion skills

In this study, we showed that given the 17 $^{14}CO_2$ measurement stations available in 2016, the potential of our atmospheric inversion of fossil fuel emissions at large scale using a coarse-resolution model is quite limited (see Fig. 4 and Fig. 5). When using the denser NET43 network and 2-week sampling and assimilating ~1000 measurements per year, the potential of the inversion system is improved, mainly over high emitting regions.

The results obtained in this study should not be over-interpreted. In our calculation, we assumed that atmospheric $FFCO_2$ gradients can be derived from the $^{14}CO_2$ measurements with a precision of 1 ppm. This 1 ppm error only corresponds to the errors in the atmospheric measurements and to uncertainties in the conversion of $^{14}CO_2$ and CO_2 measurements into $FFCO_2$. However, various fluxes that influence the atmospheric $^{14}CO_2$, such as cosmogenic production, ocean, biosphere and nuclear facilities, bring systematic errors to the conversion of ^{14}C into $FFCO_2$ (Lehman et al., 2013; Vogel et al., 2013). For example, over land regions, heterotrophic respiration, with its potentially large ^{14}C isotopic disequilibrium, is expected to be one of the main contributors to the large-scale signals of atmospheric $^{14}CO_2$ (Turnbull et al., 2009). Over large regions such as Europe, nuclear plant emissions of $^{14}CO_2$ may have even larger influences than plant and heterotrophic respiration in some areas (Graven and Gruber, 2011). The influences from these fluxes will introduce biases rather than a random error in the $FFCO_2$ mole fractions if they are not accounted for. So our results for the URs of fossil fuel emissions under the set-up of our inversion is optimistic in that respect.

In section 3.3.3, we explored the concept of having more observations assimilated in the inversion system by increasing the sampling frequency. In Wang et al. (2016), they have

shown that because the representation error, aggregation error and the projection of the prior uncertainty in the observation space (called "prior $FFCO_2$ errors") have very similar error structures in time, it is not encouraged to use daily sampling to filter the uncertainties in the prior estimate of the emissions. However, we showed that when using the NET43 network and daily sampling, the URs of monthly emissions are much larger than using the same network and 2-week sampling, stemming from the fact that having daily sampling decreases the weight of some other sources of observation errors which have a different structure, e.g. the measurement error which is temporally independent.

We also tested the concept of having a dense network with wide coverage across Europe by using the NET233 network and 2-week sampling. We confirmed a significant increase in the URs of monthly emissions all across Europe, especially over eastern Europe, that was expected in Wang et al. (2016). However, northern Europe, for example, still cannot be well constrained by the inversion, even using the NET233 network. This leads us to question the concept of using a coarse resolution transport model and a global inversion system to quantify the fossil fuel emissions over rather small European regions.

To answer this question, we assess the relevance of assimilating atmospheric observations in such an inversion system by investigating the number of degrees of freedom for signal (DFSs; Wu, 2016) in the inversions. The DFS characterizes the relative weight of the signal from the observations against the noise from the observations, having a value between zero and the number of observations d (Wu et al., 2011). If the uncertainty in the observations is very high or if the observations bring redundant information, the DFS will be small. In practice, the DFS is the trace of matrix $(\mathbf{B}\text{-}\mathbf{A})\mathbf{B}^{-1}$. In our OSSEs using different networks and sampling methods, the DFSs per observation (i.e. the ratio DFS/d) are all below 5%, implying that only a small percentage of observations are effectively assimilated. This means that the observation data contain a large variability that cannot be captured by the inversion system. Table 2 shows that representation error contributes most to the observation errors. Thus the small DFSs mainly result from the uncertainty in atmospheric modelling in capturing the variability within the coarse grid cells of LMDZv4 transport model.

The representation and the transport errors are highly dependent on the transport model resolution. Increasing the transport model resolution, which will reduce the representation errors and reduce the transport error through better modelling of the topography and the

variations at synoptic scales, are recommended as the most efficient way forward for improving the results from atmospheric inversion of fossil fuel emissions at regional scale. This would require using a high resolution transport model in the inversion system (Kadygrov et al., 2015; Broquet et al., 2013; Gourdji et al., 2012; Lauvaux et al., 2008). We conduct additional inversions that only solve for the fossil emissions of European regions without attempting to correct or account for the uncertainties from other continents. The results show that the influences of the signals of emissions from other continents on the posterior uncertainties, URs, posterior misfits and MRs over Europe regions are negligible (the differences are within 1%, not shown here). So we can consider a high-resolution regional model, in which the uncertainties in the signals of emissions from other continents can be accounted for by applying a boundary condition in a regional inversion framework.

By using a high-resolution regional inversion framework, we expect that better results (higher URs, lower posterior uncertainties), even over the regions that have been proven to have large URs when using a coarse-resolution inversion modelling, e.g. Germany. More importantly, by using a regional high resolution model, the fine scale patterns of the emissions and their trajectories can be better solved. The simulations using high-resolution regional transport model would give insights on the design of the observational network. For example, the ICOS network is more dedicated designed for monitoring the natural fluxes at current stage (Kadygrov et al., 2015). To improve the potential of the atmospheric inversions to quantify fossil fuel emissions, it is required that stations should be located carefully to capture the signals of large-scale $FFCO_2$, which would be a complement to the existing CO_2 network. This could only be evaluated using high-resolution transport models rather than using global transport models, whose horizontal resolution hardly exceeds 3°, such as LMDZv4.

3.5 Conclusion

In this study, we present the application of the global atmospheric inversion method of Wang et al. (2016) to quantify the fossil fuel emissions over Europe at regional scale using continental networks of $^{14}CO_2$ measurement sites. This method combines a prior emission estimate from an inventory with the information from atmospheric observations of $FFCO_2$ gradients to provide updated emission estimates with reduced uncertainty. A set of inversions

are performed to test the potential of such a global atmospheric inversion system and the relevance of the large-scale inverse modeling to monitor fossil fuel emissions. The results show that given the 17 $^{14}CO_2$ measurement stations available in 2016 and the typical 2-week sampling frequency, the inversion considerably reduces the uncertainties in monthly emission estimates for western Germany by 34% to 38%, according to the set-up of the prior uncertainty. By using a plausible network containing 43 measurement stations which is planned for the future and using 2-week sampling, one could expect higher URs of the emissions over the high emitters in Europe, e.g. eastern France (16% to 33%), southern UK (3% to 23%). Given the posterior uncertainty of the emissions that could be achieved in such an inversion system, the verifying of the trends in fossil fuel emissions favors the method of monitoring of $FFCO_2$ over the high emitting regions during a long period.

Increasing the number of observations assimilated in the inversion system by using daily sampling or a very dense observational network could potentially increase the URs over Europe regions. However, the concept of using a coarse-resolution transport model in a global inversion system to solve for fossil fuel emissions of the regions whose emissions are not as high as those of Germany/France is challenged by the fact that coarse-resolution transport model can hardly capture the variability within their coarse grid cells. Using a high-resolution transport models in a regional inversion framework could thus be a requirement for the monitoring of $FFCO_2$ and need further investigations.

Appendix

A1. Setup of $\mathbf{B}^{theo}$

The $\mathbf{B}^{theo}$ is a block diagonal matrix. The *i*th main diagonal block $\mathbf{B}_i$ corresponds to the 12 months for a given region *i*. Assuming the percent error δ_i for $\mathbf{x}^b_i$ are the same for 12 months and $\mathbf{x}^b_{i,j}$ is the emission for region *i* in month *m* (*m*=1 means January, *m*=12 means December), so that the diagonal entries of the $\mathbf{B}^{theo}$ are:

$$\mathbf{B}_{i,(m,m)}=(\delta_i \mathbf{x}^b_{i,m})^2 \qquad \text{(A1-1)}$$

The assumed 2-month temporal autocorrelation (section 3.2.2.2), expressed as an exponential decaying function, leads to the non-diagonal entries, which correspond to the covariance between the uncertainties in the emissions of 2 months (month *m* and *n*, for instance) to be:

$$\mathbf{B}_{i,(m,n)} = e^{-\frac{|n-m|}{2}} \times (\delta_i \mathbf{x}^b_{i,m}) \times (\delta_i \mathbf{x}^b_{i,n}) \quad \text{(A1-2)}$$

If region *i* and region *j* are within the same country, the off-diagonal block $\mathbf{B}_{i,j}$ is built to account for the spatial correlation between these two regions. We assume that $\delta_i=\delta_j=\delta_{ij}$ and the spatial correlation between this two regions for a same month *m* is -0.2 to account for fact that present emission estimates at such scales are generally disaggregated from national inventories, that is:

$$\mathbf{B}_{i,j,(m,m)} = -0.2 \times (\delta_{ij} \mathbf{x}^b_{i,m}) \times (\delta_{ij} \mathbf{x}^b_{j,m}) \quad \text{(A1-3)}$$

We assume the correlation between the emissions for region *i* in month *m* and the emission for region *j* in month *n* follows a Markov chain, so that the corresponding covariance is:

$$\mathbf{B}_{i,j,(m,n)} = -0.2 \times e^{-\frac{|n-m|}{2}} \times (\delta_{ij} \mathbf{x}^b_{i,m}) \times (\delta_{ij} \mathbf{x}^b_{j,n}) \quad \text{(A1-4)}$$

The δ for each region are determined so that the prior annual emission uncertainty is satisfied, i.e. 2% for US, 5% for European countries and 10% for China and other large regions.

A2. Setup of $\mathbf{B}^{prac}$

The $\mathbf{B}^{prac}$ is also a block diagonal matrix. For a given region *i* and a specific month *m*, assuming the prior control parameter corresponding to PKU-CO_2 emission is $\mathbf{x}^b_{i,m}$, the "true" value $\mathbf{x}$, corresponding to EDG-IER writes $\mathbf{x}^t_{i,m}$, so that the errors of the prior monthly emissions are:

$$\Delta \mathbf{x}_{i,m} = \mathbf{x}^t_{i,m} - \mathbf{x}^b_{i,m} \quad \text{(A2-1)}$$

The annual bias ε_{ann} equals:

$$\varepsilon_{ann} = \frac{1}{12} \sum_{m=1}^{12} \Delta \mathbf{x}_{i,m} \quad \text{(A2-2)}$$

The residues are:

$$\mathbf{r}^{ann}_{i,m} = \Delta \mathbf{x}_{i,m} - \varepsilon_{ann} \quad \text{(A2-3)}$$

Then the 6-month variation ε_{6m} equals to the standard deviation of the 6-month mean residues:

$$\varepsilon_{6m} = \text{SD of } (\frac{1}{6} \sum_{m=1}^{6} \mathbf{r}^{ann}_{i,m}, \frac{1}{6} \sum_{m=7}^{12} \mathbf{r}^{ann}_{i,m}) \quad \text{(A2-4)}$$

Again, the residues then becomes:

$$\mathbf{r}_{i,m}^{6m} = \Delta\mathbf{x}_{i,m} - \varepsilon_{ann} - \frac{1}{6}\sum_{m=1}^{6}\mathbf{r}_{i,m}^{ann} \qquad (\text{if } m <= 6)$$
$$\mathbf{r}_{i,m}^{6m} = \Delta\mathbf{x}_{i,m} - \varepsilon_{ann} - \frac{1}{6}\sum_{m=7}^{12}\mathbf{r}_{i,m}^{ann} \qquad (\text{if } m >= 7) \qquad \text{(A2-5)}$$

In the same way, the 3-month variation ε_{3m} equals to the standard deviation of the 3-month mean residues:

$$\varepsilon_{3m} = \text{SD of } (\frac{1}{3}\sum_{m=1}^{3}\mathbf{r}_{i,m}^{6m}, \frac{1}{3}\sum_{m=4}^{6}\mathbf{r}_{i,m}^{6m}, \frac{1}{3}\sum_{m=7}^{9}\mathbf{r}_{i,m}^{6m}, \frac{1}{3}\sum_{m=10}^{12}\mathbf{r}_{i,m}^{6m}) \qquad \text{(A2-6)}$$

The corresponding residues:

$$\mathbf{r}_{i,m}^{3m} = \Delta\mathbf{x}_{i,m} - \varepsilon_{ann} - \frac{1}{6}\sum_{m=1}^{6}\mathbf{r}_{i,m}^{ann} - \frac{1}{3}\sum_{m=1}^{3}\mathbf{r}_{i,m}^{6m} \qquad (\text{if } m \le 3)$$
$$\mathbf{r}_{i,m}^{3m} = \Delta\mathbf{x}_{i,m} - \varepsilon_{ann} - \frac{1}{6}\sum_{m=1}^{6}\mathbf{r}_{i,m}^{ann} - \frac{1}{3}\sum_{m=4}^{6}\mathbf{r}_{i,m}^{6m} \qquad (\text{if } 4 \le m \le 6)$$
$$\mathbf{r}_{i,m}^{3m} = \Delta\mathbf{x}_{i,m} - \varepsilon_{ann} - \frac{1}{6}\sum_{m=7}^{12}\mathbf{r}_{i,m}^{ann} - \frac{1}{3}\sum_{m=7}^{9}\mathbf{r}_{i,m}^{6m} \qquad (\text{if } 7 \le m \le 9) \qquad \text{(A2-5)}$$
$$\mathbf{r}_{i,m}^{3m} = \Delta\mathbf{x}_{i,m} - \varepsilon_{ann} - \frac{1}{6}\sum_{m=7}^{12}\mathbf{r}_{i,m}^{ann} - \frac{1}{3}\sum_{m=10}^{12}\mathbf{r}_{i,m}^{6m} \qquad (\text{if } 10 \le m \le 12)$$

The 1-month variation ε_{1m} equals the standard deviation of these residues:

$$\varepsilon_{1m} = \text{SD}(\mathbf{r}_{i,m}^{3m}) \qquad \text{(A2-6)}$$

In this decomposition, the root mean square of the errors (RMSE) between the prior and the "true" values $\Delta\mathbf{x}_{i,j}$ satisfy the following equation:

$$\text{RMSE}_i = \frac{1}{12}\sum_{m=1}^{12}\Delta\mathbf{x}_{i,m}^2 = \varepsilon_{ann}^2 + \varepsilon_{6m}^2 + \varepsilon_{3m}^2 + \varepsilon_{1m}^2 \qquad \text{(A2-7)}$$

At last, for the diagonal entries of the **B** matrix corresponding to the monthly emissions of region *i*, they are equal to the RMSE_i, for the non-diagonal entries, the covariance between month *j* and month *k* is expressed as the sum of the products of the different variations multiplied by exponential decay functions:

$$\mathbf{B}_{i,(m,n)} = \varepsilon_{ann}^2 + \varepsilon_{6m}^2 + \varepsilon_{3m}^2 + \varepsilon_{1m}^2 \qquad (\text{if } m = n)$$
$$\mathbf{B}_{i,(m,n)} = \varepsilon_{ann}^2 + e^{-\frac{|n-m|}{6}}\varepsilon_{6m}^2 + e^{-\frac{|n-m|}{3}}\varepsilon_{3m}^2 + e^{-\frac{|n-m|}{1}}\varepsilon_{1m}^2 \qquad (\text{if } m \ne n) \qquad \text{(A2-8)}$$

A3. Calculation of trends and corresponding uncertainties

Assuming the linear trend of the fossil fuel emissions of in a 10-year period is to be

calculated, which satisfies the function:

$$\mathbf{y} \approx \tilde{\mathbf{y}} = a\mathbf{x}+b \tag{A3-1}$$

, where **y** is the vector of annual emissions for the 10 years, $\tilde{\mathbf{y}}$ is the predicted value by the regression and x is the corresponding years, the slope *a* is the linear trend we are going to calculate by linear regression. We can express Eq. (A3-1) by matrix:

$$\underbrace{\begin{bmatrix} y_1 \\ \vdots \\ y_{10} \end{bmatrix}}_{\mathbf{Y}} \approx \underbrace{\begin{bmatrix} y_1 \\ \vdots \\ y_{10} \end{bmatrix}}_{\mathbf{Y}} = \underbrace{\begin{bmatrix} x_1 & 1 \\ \vdots & \vdots \\ x_{10} & 1 \end{bmatrix}}_{\mathbf{X}} \underbrace{\begin{bmatrix} a \\ b \end{bmatrix}}_{\mathbf{P}} \tag{A3-2}$$

Thus the linear trend *a* and the interception *b* can be solved using linear algebra. With the notations used in Eq. (A3-2), the result of the linear regression is:

$$\mathbf{P} = (\mathbf{X}^{\mathrm{T}}\mathbf{X})^{-1}\mathbf{X}^{\mathrm{T}}\mathbf{Y} \tag{A3-3}$$

, the associated uncertainties in the regression parameters in vector **P** is given by the following covariance matrix:

$$\mathrm{cov}(\mathbf{P}) = (\mathbf{X}^{\mathrm{T}}\mathbf{X})^{-1}\mathbf{X}^{\mathrm{T}}\,\mathrm{cov}(\mathbf{Y})\mathbf{X}(\mathbf{X}^{\mathrm{T}}\mathbf{X})^{-1} \tag{A3-4}$$

, where cov(.) is the covariance matrix for a set of variables.

Since **X** is a fixed matrix filled by the numbers of years and 1's, the uncertainties in the linear trend (first item in main diagonal of cov(**P**)), is independent of the annual emissions themselves but is only dependent on the uncertainties and associated correlations of annual emissions. As sketched in Fig. A1, this error covariance of **Y** should include two independent parts: 1) the uncertainties associated with the estimation of the emissions for each year in **Y** and 2) the inter-annual variability (IAV) in the detrended **Y**.

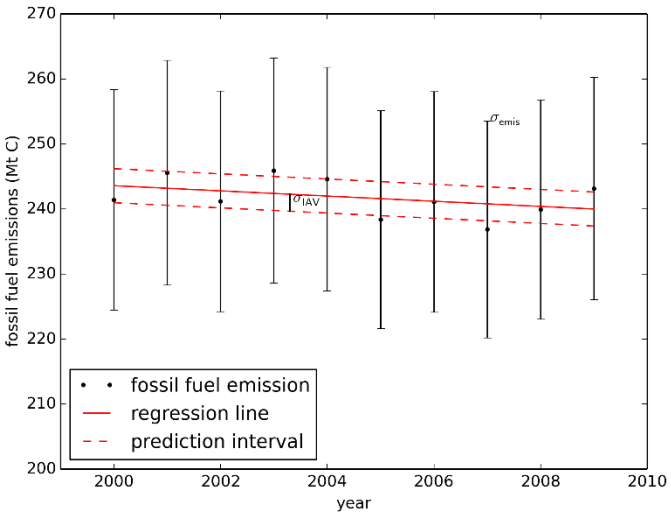

Figure A1 Annual fossil fuel emissions from Germany in the period 2000-2009 calculated from EDG-IER.

In this study, based on the time series of national annual emissions from EDG-IER, we assume a 5% IAV in the annual fossil fuel emissions for European countries. In general, this 5% IAV is the upper limit of the typical values for European countries (Levin and Rödenbeck, 2007). Ballantyne et al., 2015 assumed that in the self-reported fossil fuel emission inventories, the emission error in one year could be highly correlated with the error from the previous year by an autoregressive coefficient of 0.95, due to potential errors that are not corrected retroactively after about 20 years. However, we do not conduct a multi-year inversion to get a typical estimate of the correlations in the posterior uncertainties in annual emissions. The correlations between the posterior uncertainties in annual emissions are assumed to be zero. This assumption is fairly conservative, since Eq. (A3-4) implies that the larger the correlations between the estimation of fossil fuel emissions from different years, the smaller the uncertainties in the regressed trends.

References

Andres, R. J., Boden, T. A., and Higdon, D.: A new evaluation of the uncertainty associated with CDIAC estimates of fossil fuel carbon dioxide emission, Tellus B, 66, 2014.

Andres, R. J., Boden, T. A., Bréon, F. M., Ciais, P., Davis, S., Erickson, D., Gregg, J. S., Jacobson, A., Marland, G., Miller, J., Oda, T., Olivier, J. G. J., Raupach, M. R., Rayner, P., and Treanton, K.: A synthesis of carbon dioxide emissions from fossil-fuel combustion, Biogeosciences, 9, 1845-1871, 2012.

Ballantyne, A. P., Andres, R., Houghton, R., Stocker, B. D., Wanninkhof, R., Anderegg, W., Cooper, L. A., DeGrandpre, M., Tans, P. P., Miller, J. B., Alden, C. and White, J. W. C.: Audit of the global

carbon budget: estimate errors and their impact on uptake uncertainty, Biogeosciences, 12(8), 2565–2584, 2015.

Basu, S., Miller, J. B. and Lehman, S.: Separation of biospheric and fossil fuel fluxes of CO2 by atmospheric inversion of CO_2 and $^{14}CO_2$ measurements: Observation System Simulations, Atmospheric Chemistry and Physics, 16(9), 5665–5683, 2016.

Berrisford, P., Dee, D., Fielding, K., Fuentes, M., Kallberg, P., Kobayashi, S., and Uppala, S.: The ERA-Interim Archive, ERA report series, 1-16, 2009.

Bozhinova, D., van der Molen, M. K., van der Velde, I. R., Krol, M. C., van der Laan, S., Meijer, H. A. J. and Peters, W.: Simulating the integrated summertime $\Delta^{14}CO_2$ signature from anthropogenic emissions over Western Europe, Atmospheric Chemistry and Physics, 14(14), 7273–7290, 2014.

Br éon, F. M., Broquet, G., Puygrenier, V., Chevallier, F., Xueref-Remy, I., Ramonet, M., Dieudonn é, E., Lopez, M., Schmidt, M., Perrussel, O., and Ciais, P.: An attempt at estimating Paris area CO₂ emissions from atmospheric concentration measurements, Atmospheric Chemistry and Physics, 15, 1707-1724, 2015.

Broquet, G., Chevallier, F., Br éon, F. M., Kadygrov, N., Alemanno, M., Apadula, F., Hammer, S., Haszpra, L., Meinhardt, F., Morgu í, J. A., Necki, J., Piacentino, S., Ramonet, M., Schmidt, M., Thompson, R. L., Vermeulen, A. T., Yver, C., and Ciais, P.: Regional inversion of CO_2 ecosystem fluxes from atmospheric measurements: reliability of the uncertainty estimates, Atmospheric Chemistry and Physics, 13, 9039-9056, 2013.

Broquet, G., Chevallier, F., Rayner, P., Aulagnier, C., Pison, I., Ramonet, M., Schmidt, M., Vermeulen, A. T., and Ciais, P.: A European summertime CO_2 biogenic flux inversion at mesoscale from continuous in situ mixing ratio measurements, Journal of Geophysical Research, 116, 2011.

Cambaliza, M. O. L., Shepson, P. B., Caulton, D. R., Stirm, B., Samarov, D., Gurney, K. R., Turnbull, J., Davis, K. J., Possolo, A., Karion, A., Sweeney, C., Moser, B., Hendricks, A., Lauvaux, T., Mays, K., Whetstone, J., Huang, J., Razlivanov, I., Miles, N. L. and Richardson, S. J.: Assessment of uncertainties of an aircraft-based mass balance approach for quantifying urban greenhouse gas emissions, Atmospheric Chemistry and Physics, 14(17), 9029–9050, 2014.

Chen, H., Winderlich, J., Gerbig, C., Hoefer, A., Rella, C., Crosson, E., Van Pelt, A., Steinbach, J., Kolle, O., and Beck, V.: High-accuracy continuous airborne measurements of greenhouse gases (CO_2 and CH_4) using the cavity ring-down spectroscopy (CRDS) technique, Atmospheric Measurement Techniques, 3, 375-386, 2010.

Chevallier, F., and O'Dell, C. W.: Error statistics of Bayesian CO_2 flux inversion schemes as seen from GOSAT, Geophysical Research Letters, 40, 2013.

Chevallier, F., Ciais, P., Conway, T. J., Aalto, T., Anderson, B. E., Bousquet, P., Brunke, E. G., Ciattaglia, L., Esaki, Y., Fr öhlich, M., Gomez, A., Gomez-Pelaez, A. J., Haszpra, L., Krummel, P. B., Langenfelds, R. L., Leuenberger, M., Machida, T., Maignan, F., Matsueda, H., Morgu í, J. A., Mukai, H., Nakazawa, T., Peylin, P., Ramonet, M., Rivier, L., Sawa, Y., Schmidt, M., Steele, L. P., Vay, S. A., Vermeulen, A. T., Wofsy, S. and Worthy, D.: CO_2 surface fluxes at grid point scale estimated from a global 21 year reanalysis of atmospheric measurements, Journal of Geophysical Research, 115(D21), 2010.

Chevallier, F., Fisher, M., Peylin, P., Serrar, S., Bousquet, P., Br éon, F. M., Ch édin, A., and Ciais, P.: Inferring CO2 sources and sinks from satellite observations: Method and application to TOVS data, Journal of Geophysical Research, 110, 2005.

Chevallier, F., Viovy, N., Reichstein, M., and Ciais, P.: On the assignment of prior errors in Bayesian inversions of CO_2 surface fluxes, Geophysical Research Letters, 33, 2006.

Ciais, P., Paris, J. D., Marland, G., Peylin, P., Piao, S. L., Levin, I., Pregger, T., Scholz, Y., Friedrich, R., Rivier, L., Houwelling, S., and Schulze, E. D.: The European carbon balance. Part 1: fossil fuel emissions, Global Change Biology, 16, 1395-1408, 2010.

European Commission: Communication from the commission to the European Parliament, the council, the European economic and social committee and the committee of the regions: A Roadmap for moving to a competitive low carbon economy in 2050, 2010.

Graven, H. D., and Gruber, N.: Continental-scale enrichment of atmospheric $^{14}CO_2$ from the nuclear power industry: potential impact on the estimation of fossil fuel-derived CO_2, Atmospheric Chemistry and Physics, 11, 12339-12349, 2011.

Gregg, J. S., Andres, R. J., and Marland, G.: China: Emissions pattern of the world leader in CO_2 emissions from fossil fuel consumption and cement production, Geophysical Research Letters, 35, 2008.

Gourdji, S. M., Mueller, K. L., Yadav, V., Huntzinger, D. N., Andrews, A. E., Trudeau, M., Petron, G., Nehrkorn, T., Eluszkiewicz, J., Henderson, J., Wen, D., Lin, J., Fischer, M., Sweeney, C. and Michalak, A. M.: North American CO_2 exchange: inter-comparison of modeled estimates with results from a fine-scale atmospheric inversion, Biogeosciences, 9(1), 457–475, 2012.

Gurney, K. R., Law, R. M., Denning, A. S., Rayner, P. J., Baker, D., Bousquet, P., Bruhwiler, L., Chen, Y.-H., Ciais, P., and Fan, S.: Towards robust regional estimates of CO_2 sources and sinks using atmospheric transport models, Nature, 415, 626-630, 2002.

Gurney, K. R., Mendoza, D. L., Zhou, Y., Fischer, M. L., Miller, C. C., Geethakumar, S. and Can, S. de la R. du: High Resolution Fossil Fuel Combustion CO_2 Emission Fluxes for the United States, Environmental Science & Technology, 43(14), 5535–5541, 2009.

Hourdin, F., Musat, I., Bony, S., Braconnot, P., Codron, F., Dufresne, J.-L., Fairhead, L., Filiberti, M.-A., Friedlingstein, P., Grandpeix, J.-Y., Krinner, G., LeVan, P., Li, Z.-X., and Lott, F.: The LMDZ4 general circulation model: climate performance and sensitivity to parametrized physics with emphasis on tropical convection, Climate Dynamics, 27, 787-813, 2006.

Hsueh, D. Y., Krakauer, N. Y., Randerson, J. T., Xu, X., Trumbore, S. E., and Southon, J. R.: Regional patterns of radiocarbon and fossil fuel-derived CO_2 in surface air across North America, Geophysical Research Letters, 34, 2007.

Hungershoefer, K., Breon, F. M., Peylin, P., Chevallier, F., Rayner, P., Klonecki, A., Houweling, S., and Marshall, J.: Evaluation of various observing systems for the global monitoring of CO_2 surface fluxes, Atmospheric Chemistry and Physics, 10, 10503-10520, 2010.

Integrated Carbon Observing System (ICOS): A European research infrastructure dedicated to high precision observations of greenhouse gases fluxes, 2008.

Integrated Carbon Observing System (ICOS): A European research infrastructure dedicated to high precision observations of greenhouse gases fluxes, 2013.

Kadygrov, N., Broquet, G., Chevallier, F., Rivier, L., Gerbig, C. and Ciais, P.: On the potential of the ICOS atmospheric CO_2 measurement network for estimating the biogenic CO_2 budget of Europe, Atmospheric Chemistry and Physics, 15(22), 12765–12787, 2015.

Lauvaux, T., Uliasz, M., Sarrat, C., Chevallier, F., Bousquet, P., Lac, C., Davis, K. J., Ciais, P., Denning, A. S. and Rayner, P. J.: Mesoscale inversion: first results from the CERES campaign with synthetic data, Atmospheric Chemistry and Physics, 8, 3459–3471, 2008.

Le Quéré, C., Peters, G. P., Andres, R. J., Andrew, R. M., Boden, T. A., Ciais, P., Friedlingstein, P., Houghton, R. A., Marland, G., Moriarty, R., Sitch, S., Tans, P., Arneth, A., Arvanitis, A., Bakker, D. C. E., Bopp, L., Canadell, J. G., Chini, L. P., Doney, S. C., Harper, A., Harris, I., House, J. I., Jain, A. K., Jones, S. D., Kato, E., Keeling, R. F., Klein Goldewijk, K., Körtzinger, A., Koven, C., Lefèvre, N., Maignan, F., Omar, A., Ono, T., Park, G. H., Pfeil, B., Poulter, B., Raupach, M. R., Regnier, P., Rödenbeck, C., Saito, S., Schwinger, J., Segschneider, J., Stocker, B. D., Takahashi, T., Tilbrook, B., van Heuven, S., Viovy, N., Wanninkhof, R., Wiltshire, A., and Zaehle, S.: Global carbon budget 2013, Earth System Science Data, 6, 235-263, 2014.

Lehman, S. J., Miller, J. B., Wolak, C., Southon, J., Tans, P. P., Montzka, S. A., Sweeney, C., Andrews, A., LaFranchi, B., Guilderson, T. P. and Turnbull, J. C.: Allocation of Terrestrial Carbon Sources Using $^{14}CO_2$: Methods, Measurement, and Modeling, Radiocarbon, 55(2–3), 1484–1495, 2013.

Levin, I. and Rödenbeck, C.: Can the envisaged reductions of fossil fuel CO_2 emissions be detected by atmospheric observations?, Naturwissenschaften, 95(3), 203–208, 2008.

Levin, I., Hammer, S., Kromer, B., and Meinhardt, F.: Radiocarbon observations in atmospheric CO_2: determining fossil fuel CO_2 over Europe using Jungfraujoch observations as background, Science of The Total Environment, 391, 211-216, 2008.

Levin, I., Kromer, B., and Hammer, S.: Atmospheric $\Delta^{14}CO_2$ trend in Western European background air from 2000 to 2012, Tellus B, 65, 2013.

Levin, I., Kromer, B., Schmidt, M., and Sartorius, H.: A novel approach for independent budgeting of fossil fuel CO_2 over Europe by $^{14}CO_2$ observations, Geophysical Research Letters, 30, 2003.

Levin, I., Naegler, T., Kromer, B., Diehl, M., Francey, R. J., Gomez-Pelaez, A. J., Steele, L. P., Wagenbach,

D., Weller, R., and Worthy, D. E.: Observations and modelling of the global distribution and long-term trend of atmospheric $^{14}CO_2$, Tellus B, 62, 26-46, 2010.

Lindenmaier, R., Dubey, M. K., Henderson, B. G., Butterfield, Z. T., Herman, J. R., Rahn, T. and Lee, S.-H.: Multiscale observations of CO_2, $^{13}CO_2$, and pollutants at Four Corners for emission verification and attribution, Proceedings of the National Academy of Sciences, 111(23), 8386–8391, 2014.

Liu, Z., Guan, D., Wei, W., Davis, S. J., Ciais, P., Bai, J., Peng, S., Zhang, Q., Hubacek, K., Marland, G., Andres, R. J., Crawford-Brown, D., Lin, J., Zhao, H., Hong, C., Boden, T. A., Feng, K., Peters, G. P., Xi, F., Liu, J., Li, Y., Zhao, Y., Zeng, N. and He, K.: Reduced carbon emission estimates from fossil fuel combustion and cement production in China, Nature, 524(7565), 335–338, 2015.

Macknick, J.: Energy and carbon dioxide emission data uncertainties, IIASA Interim Report IR-09-32. Laxenburg: International Institute for Applied Systems Analysis, 2009.

Miller, S. M. and Michalak, A. M.: Constraining sector-specific CO_2 and CH_4 emissions in the United States, Atmospheric Chemistry and Physics Discussions, 1–33, doi:10.5194/acp-2016-643, 2016.

Oda, T. and Maksyutov, S.: A very high-resolution (1 km ×1 km) global fossil fuel CO_2 emission inventory derived using a point source database and satellite observations of nighttime lights, Atmospheric Chemistry and Physics, 11(2), 543–556, 2011.

Olivier, J. G. J., Van Aardenne, J. A., Dentener, F. J., Pagliari, V., Ganzeveld, L. N., and Peters, J. A. H. W.: Recent trends in global greenhouse gas emissions: regional trends 1970–2000 and spatial distribution of key sources in 2000, Environmental Sciences, 2, 81-99, 2005.

Pacala, S. W., Breidenich, C., Brewer, P. G., Fung, I., Gunson, M. R. and co-authors. 2010. Verifying Greenhouse Gas Emissions: Methods to Support International Climate Agreements. The National Academies Press, Washington, DC

Prather, M. J., Penner, J. E., Fuglestvedt, J. S., Kurosawa, A., Lowe, J. A., Höhne, N., Jain, A. K., Andronova, N., Pinguelli, L., and Pires de Campos, C.: Tracking uncertainties in the causal chain from human activities to climate, Geophysical Research Letters, 36, 2009.

Pregger, T., Scholz, Y., and Friedrich, R.: Documentation of the anthropogenic GHG emission data for Europe provided in the Frame of CarboEurope GHG and CarboEurope IP, Institut für Energiewirtschaft und Rationelle Energieanwendung, Universität Stuttgart, Stuttgart, Germany, 2007.

Ray, J., Yadav, V., Michalak, A., van Bloemen Waanders, B., and Mckenna, S. A.: A multiresolution spatial parameterization for the estimation of fossil-fuel carbon dioxide emissions via atmospheric inversions, Geoscientific Model Development, 7, 1901-1918, 2014.

Riley, W. J., Hsueh, D. Y., Randerson, J. T., Fischer, M. L., Hatch, J. G., Pataki, D. E., Wang, W., and Goulden, M. L.: Where do fossil fuel carbon dioxide emissions from California go? An analysis based on radiocarbon observations and an atmospheric transport model, Journal of Geophysical Research, 113, 2008.

Staufer, J., Broquet, G., Bréon, F.-M., Puygrenier, V., Chevallier, F., Xueref-Rémy, I., Dieudonné, E., Lopez, M., Schmidt, M., Ramonet, M., Perrussel, O., Lac, C., Wu, L. and Ciais, P.: A first year-long estimate of the Paris region fossil fuel CO_2 emissions based on atmospheric inversion, Atmospheric Chemistry and Physics Discussions, 1–34, 2016.

Tarantola, A.: Inverse problem theory and methods for model parameter estimation, siam, 2005.

Turnbull, J. C., Karion, A., Fischer, M. L., Faloona, I., Guilderson, T., Lehman, S. J., Miller, B. R., Miller, J. B., Montzka, S., Sherwood, T., Saripalli, S., Sweeney, C., and Tans, P. P.: Assessment of fossil fuel carbon dioxide and other anthropogenic trace gas emissions from airborne measurements over Sacramento, California in spring 2009, Atmospheric Chemistry and Physics, 11, 705-721, 2011.

Turnbull, J. C., Keller, E. D., Baisden, T., Brailsford, G., Bromley, T., Norris, M., and Zondervan, A.: Atmospheric measurement of point source fossil CO_2 emissions, Atmospheric Chemistry and Physics, 14, 5001-5014, 2014.

Turnbull, J. C., Keller, E. D., Norris, M. W. and Wiltshire, R. M.: Independent evaluation of point source fossil fuel CO2 emissions to better than 10%, Proceedings of the National Academy of Sciences, 113(37), 10287–10291, 2016.

Turnbull, J. C., Miller, J. B., Lehman, S. J., Tans, P. P., Sparks, R. J., and Southon, J.: Comparison of $^{14}CO_2$, CO, and SF_6 as tracers for recently added fossil fuel CO_2 in the atmosphere and implications for biological CO_2 exchange, Geophysical Research Letters, 33, 2006.

Turnbull, J., Rayner, P., Miller, J., Naegler, T., Ciais, P., and Cozic, A.: On the use of $^{14}CO_2$ as a tracer for fossil fuel CO_2: Quantifying uncertainties using an atmospheric transport model, Journal of Geophysical Research, 114, 2009.

US EPA, C. C. D.: U.S. Greenhouse Gas Inventory Report, [online] Available from: http://www3.epa.gov/climatechange/ghgemissions/usinventoryreport.html (Accessed 15 January 2016), 2015.

Vogel, F. R., Hammer, S., Steinhof, A., Kromer, B., and Levin, I.: Implication of weekly and diurnal ^{14}C calibration on hourly estimates of CO-based fossil fuel CO_2 at a moderately polluted site in southwestern Germany, Tellus B, 62, 512-520, 2010.

Vogel, F. R., Levin, I., and Worthy, D.: Implications for deriving regional fossil fuel CO2 estimates from atmospheric observations in a hot spot of nuclear power plant 14CO2 emissions, Radiocarbon, 55, 1556-1572, 2013.

Wang, Y., Broquet, G., Ciais, P., Chevallier, F., Vogel, F., Kadygrov, N., Wu, L., Yin, Y., Wang, R., Tao, S.: Estimation of observation errors for large scale atmospheric inversion of CO2 emissions from fossil fuel combustion, submitted to Tellus B (in review).

Wang, R., Tao, S., Ciais, P., Shen, H. Z., Huang, Y., Chen, H., Shen, G. F., Wang, B., Li, W., Zhang, Y. Y., Lu, Y., Zhu, D., Chen, Y. C., Liu, X. P., Wang, W. T., Wang, X. L., Liu, W. X., Li, B. G., and Piao, S. L.: High-resolution mapping of combustion processes and implications for CO_2 emissions, Atmospheric Chemistry and Physics, 13, 5189-5203, 2013.

Wu, L., Broquet, G., Ciais, P., Bellassen, V., Vogel, F., Chevallier, F., Xueref-Remy, I. and Wang, Y.: What would dense atmospheric observation networks bring to the quantification of city CO_2 emissions?, Atmospheric Chemistry and Physics, 16(12), 7743–7771, 2016.

Wu, L., Bocquet, M., Lauvaux, T., Chevallier, F., Rayner, P. and Davis, K.: Optimal representation of source-sink fluxes for mesoscale carbon dioxide inversion with synthetic data, Journal of Geophysical Research, 116(D21), 2011.

Supplementary

Table S1 Plausible locations of observation sites within ICOS network that measure $FFCO_2$ gradients to the JFJ reference site. The sites with a star is the existing stations measuring $^{14}CO_2$ and those used in the experiment T-17W and P-17W

Station ID	latitude (°N)	longitude (°E)
Jungfraujoch (JFJ)	46.55	7.99
Mace Head (MHD)*	53.33	-9.90
Heidelberg (HEI)*	49.42	8.67
Trainou (TRN)*	47.96	2.11
Schauinsland (SIL)*	47.92	7.92
Cabauw (CBW)*	51.97	4.93
Observatoire Pérenne de l'Environnement (OPE)*	48.48	5.36
Hohenpeißenberg (HPB)*	47.80	11.01
Lindenberg (LIN)*	52.21	14.12
Gartow (GRT)*	53.07	11.44
Hyltemossa (HYL)*	56.10	13.42
Ochsenkopf (OXK)*	50.02	11.80
Křešín u Pacova (KUP)*	49.58	15.08
Norunda (NRD)*	60.08	17.47
Hyytiälä (HYT)*	61.85	24.29
Pallas (PAL)*	67.97	24.12
Svartberget (SVB)*	64.17	19.77
Isny(ISN)	47.69	10.04
La muela (LMU)	41.95	1.10
Malin Head (MLH)	55.36	-7.33
Angus (TTA)	55.95	-3.22
Carnsore Point (CRP)	52.18	-6.37
Ridge Hill (RGL)	52.00	-2.53
Tacolneston (TAC)	52.52	1.14
Lutjewad (LUT)	53.40	6.35
Puijo (PUJ)	62.90	27.56
Bialystok (BIA)	53.23	23.03
Kasprowy Wierch (KAS)	49.23	19.98
Gif-sur-Yvette (GIF)	48.71	2.15
Puy de Dome (PUY)	45.77	2.97
Biscarrosse (BIS)	44.38	-1.23
Ersa (ERS)	42.97	9.38
Utö (UTO)	59.78	21.37
Observatoire de Haute Provence (OHP)	43.92	5.70
Pic du Midi (PDM)	42.56	0.08
Ile Grande (IGR)	48.48	-3.35
Orléans (ORL)	47.92	1.90
Tver (TVR)	56.47	32.93
Zugspitze (ZUG)	47.42	10.98
Hengelo (HGT)	46.57	16.38
Begur (BEG)	41.58	3.13
Vermunt(VER)	47.01	9.57

Doñana (DON)	37.02	-6.32

Table S2 Global configuration of the 56 regions

No.	Region	No.	Region	No.	Region
1	Ireland	20	US 3	39	China 4
2	northern UK	21	US 4	40	China 5
3	southern UK	22	US 5	41	China 6
4	Benelux	23	US 6	42	China 7
5	Switzerland/Swiss	24	US 7	43	China 8
6	northern Italy	25	US 8	44	China 9
7	southern Italy	26	US 9	45	China 10
8	Balkan	27	US 10	46	India
9	western Germany	28	US 11	47	Indochina
10	eastern Germany	29	south-eastern Canada	48	Malay Archipelago
11	Denmark	30	south-western Canada	49	South America
12	western France	31	Alaska	50	Africa
13	eastern France	32	northern Canada	51	Middle East
14	Iberia	33	Mexico	52	Australia
15	northern Europe	34	Cuba	53	Greenland
16	eastern Europe	35	Japan/Korea	54	Russia
17	south-eastern Europe	36	China 1	55	Ocean
18	US 1	37	China 2		
19	US 2	38	China 3		

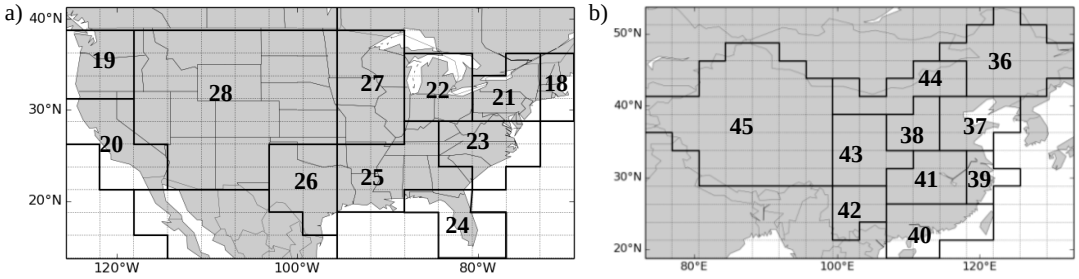

Figure S1 Maps of a) 11 regions in the United States and b) 10 control regions in China whose monthly emission budgets are controlled by the inversion

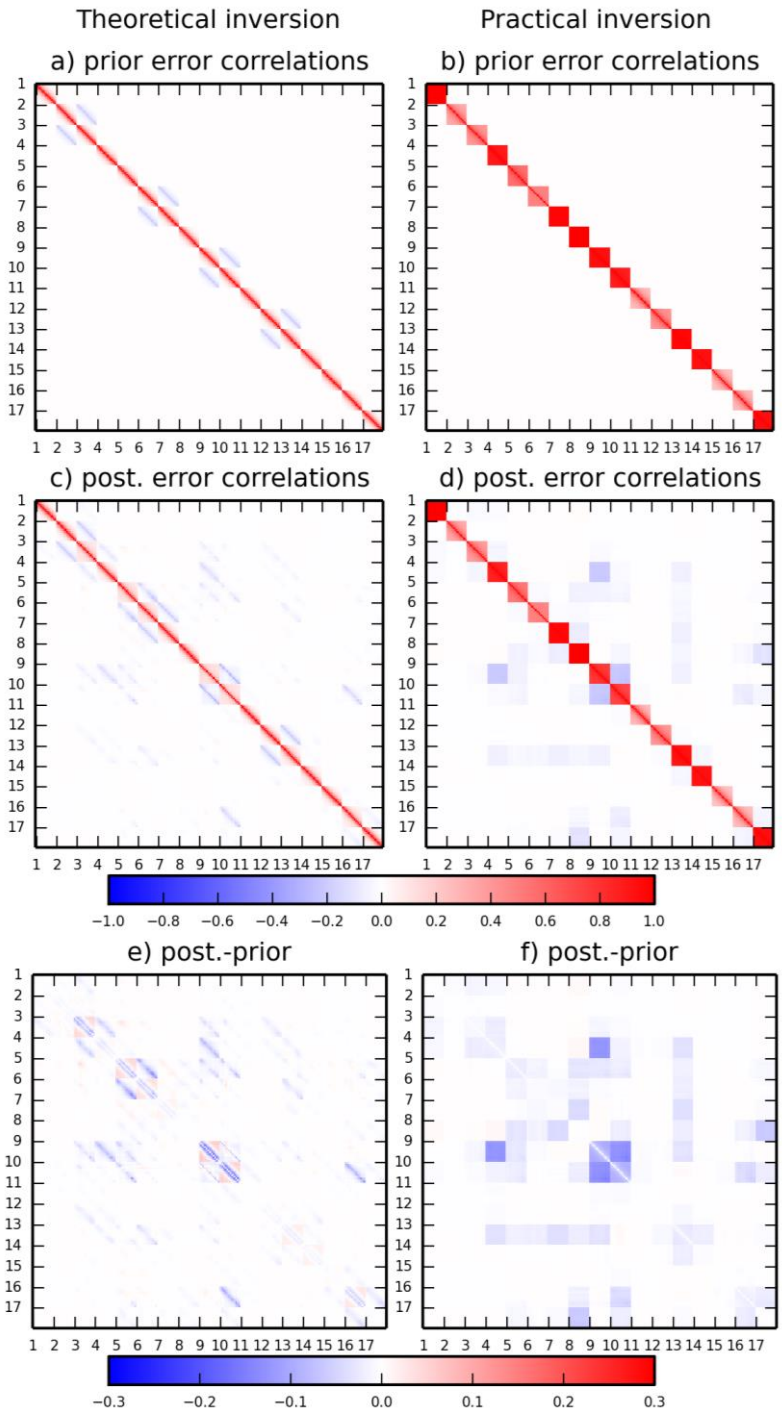

Figure S2 The correlation structure in the prior (a and b) and posterior (c and d) uncertainties in monthly regional $FFCO_2$ emissions at the control resolution using the NET43 network and 2-week sampling for the theoretical (first column) and practical (second column) inversions, as well as their differences (e and f). The *x* and *y* axes cover all the control region-months iterating through region first and the months in second. For clarity, we group these correlations into 17 regions and organize them for each region according to month indices. The numbers on the *x*-*y* axis are the indices of the control regions in Europe (see Fig. 2b).

Chapter 4 Potential of continental CO_2 and $^{14}CO_2$ observational networks to estimate fossil fuel CO_2 emissions via atmospheric inversions

Summary

The results obtained in the previous chapter showed optimistic potential of the inversion system to estimate fossil fuel emissions for western Europe. However, we ignored some other $^{14}CO_2$ fluxes that may influence the precision of ^{14}C-derived $FFCO_2$ observations and thus overestimate the skill of the inversion system.

In this chapter, I further developed an isotopic inversion system that can assimilate atmospheric CO_2 and $^{14}CO_2$ data simultaneously. Firstly, detailed estimate of different ^{14}C fluxes are made from the state-of-the-art methods and models. These estimates are evaluated against with actual observations from an extensive set of stations (Supplementary materials). The simulation captures the long-term trends and seasonal amplitude of atmospheric $^{14}CO_2$ and reproduces the north-south gradients of $^{14}CO_2$. The coarse resolution transport model, however, have difficulties in capturing the right seasonal amplitude at some sites that are influenced by strong local emissions.

In this chapter, I evaluate the potential of such an isotopic inversion system, in which the uncertainties from the other CO_2 and $^{14}CO_2$ fluxes are accounted for, to estimate the fossil fuel emissions over the Europe and China, by assimilating atmospheric CO_2 and $^{14}CO_2$ observations from continental networks of stations.

By applying the isotopic inversion and assimilating a massive amount of daily CO_2 measurements and ~1000 2-week integrated $^{14}CO_2$ measurements sampled from continental networks of ~40 sites in one year, the uncertainty in the inverted annual budgets of fossil fuel emissions is below 5% over western Europe and China. Although the results show that by assimilating a large number of daily atmospheric CO_2 data, the

inversions can reduce the uncertainties in fossil fuel emissions, the corrections of fossil fuel emissions by using CO_2 data are not reliable in such an inversion framework. Adding $^{14}CO_2$ data in the inversion system and solving for the non-linear relationship between CO_2 and $^{14}CO_2$ fluxes can help largely improve the estimate of fossil fuel emissions. The sensitivity tests showed that the biospheric $^{14}CO_2$ fluxes will influence the inversion of fossil fuel emissions. In addition, over Europe where there are a large number of nuclear facilities, the $^{14}CO_2$ fluxes from nuclear reactors will also significantly impact the inversion of fossil fuel emissions.

The analyses of the posterior uncertainties in the fossil fuel emissions, and of the correlations between the posterior uncertainties in fossil fuel emissions and biospheric fluxes, indicate that atmospheric $^{14}CO_2$ data can provide valuable information to separate the signals of fossil fuel emissions from those of biospheric fluxes. And given the ability of $^{14}CO_2$ data to separate the different CO_2 flux components, the isotopic inversion method allow for reducing errors in the annual budgets of regional NEE that would arise from a poor representation of the prescribed and fixed fossil fuel emissions in conventional CO_2 inversions.

Potential of continental CO_2 and $^{14}CO_2$ observational networks to estimate fossil fuel CO_2 emissions via atmospheric inversions

4.1 Introduction

Annual emission from combustion of fossil fuels is the primary driver of increasing atmospheric CO_2 (Ballantyne et al., 2015; Le Quéré et al., 2015). The self-reported national inventories of fossil fuel emissions have large uncertainties, ranging from 5% (2-σ) in OECD countries (Marland, 2008) to 50% (2-σ) or more for less-developed countries (Andres et al., 2014). Gridded emission maps exist, but subject to both the uncertainties in the national annual emissions and different downscaling assumptions or accounting methods (Andres et al., 2011; Oda and Maksyutov, 2010; Rayner et al., 2010; Ciais et al., 2010; Gregg et al., 2008). For any agreement to limit greenhouse gas emissions, monitoring and verification of emissions will be important to assess the effectiveness of emissions reductions, and in case of a binding agreement, the overall compliance. At the same time, in studies related to carbon budgets, the increasing errors of the global fossil fuel emissions, due to the larger share of global emissions from non-Annex I countries (emerging economies and developing countries) with less accurate inventories (Gregg et al., 2008; Marland et al., 2009), have made the errors in fossil fuel emissions to be one of the dominant factor contributing to the global natural (biospheric and oceanic) carbon uptake uncertainty (~38% in the year 2010, Ballantyne et al., 2015). Improved knowledge of fossil fuel emissions is thus essential to understand the drivers of their variations and to support policy-making and research on the carbon cycle.

An appealing method to independently assess fossil fuel emissions is to use an atmospheric inversion approach (Ray et al., 2014). The atmospheric inversion approach consists in adjusting the estimates of carbon fluxes to minimize the distance between simulated (using an atmospheric transport model and the flux estimates) and observed mixing ratios. It yields an optimized posterior estimate, accounting for the uncertainties in a prior estimate of the emissions and for all other sources of uncertainties in model-

measurement misfits. Atmospheric CO_2 inversions have been used so far for estimating natural CO_2 fluxes at the scale of large regions of the globe (Peters et al., 2010; Gurney et al., 2008; Maki et al., 2012; Rayner et al., 2008), or at sub-continental scales (Lauvaux et al., 2008; Broquet et al., 2011). But in conventional atmospheric inversions solving for natural biogenic and oceanic CO_2 fluxes (Peters et al., 2010; Piao et al., 2009; Chevallier et al., 2010; Broquet et al., 2011), fossil fuel emission is prescribed without attempting to correct it or account for its uncertainty. Under this condition, any deviation of the prescribed fossil fuel emissions from their true values can be expected to result in errors in the inverted natural fluxes. This error may reach up to 50% of the carbon sink during growing season in Europe (Gurney et al., 2005). Although some studies have raised high expectations regarding the use of new types of remote sensing data (Bovensmann et al., 2010; Kort et al., 2012; O'Brien et al., 2016) or pioneered the use of *in-situ* measurements (Bréon et al., 2015; Turnbull et al., 2016) to quantify fossil fuel emissions over large point sources or big cities, investigations on the potential to quantify the fossil fuel emissions at regional or national scales from the atmospheric measurements are less common. A recent Observing System Simulation Experiment (OSSE) study of Ray et al. (2014) demonstrated that if the atmospheric fossil fuel CO_2 (FFCO2) mixing ratios could be measured with an uncertainty of 0.1 ppm (which is very optimistic given the current precision of the measurement of $FFCO_2$ signals) at a network of 35 towers every 3 h across the U.S., an atmospheric inversion at 1 °×1 ° spatial resolution could reduce errors on 8 day-averaged country-level fossil-fuel emissions from about 15% (used as a prior knowledge in the Bayesian framework of the inversion, given by their reconstruction algorithm) down to 7%. However, because the biospheric CO_2 signal can overwhelm the $FFCO_2$, especially during the growing season at rural measurement sites, a difficulty for inversions to solve for fossil fuel emissions based on atmospheric observations on a continental scale network is to separate the $FFCO_2$ signals and that that from natural (biogenic and oceanic) fluxes in the atmospheric measurements (Shiga et al., 2014).

Several proxies, e.g. tracers more or less co-emitted with $FFCO_2$, namely CO, SF_6,

NO_x etc., have been proposed to circumvent this problem (Gamnitzer et al., 2006; Rivier et al., 2006; Silva et al., 2013), but none of them is as close to a pure tracer of $FFCO_2$ as radiocarbon in CO_2. Measurements of the depletion of the $^{14}C/C$ ratio in the ambient air can be used to quantify $FFCO_2$ based on the principle that $FFCO_2$ is radiocarbon-free (Levin et al., 2003). Currently, there are a large number of CO_2 sites and few radiocarbon observation sites across the world. A total of ~ 1000 $^{14}CO_2$ measurements and a large amount of actual CO_2 (>20 000) measurements (including flask, tall tower, aircraft and cruise) are made each year, most of which are located in North America (Basu et al., 2016). Most studies have used the atmospheric $^{14}CO_2$ gradients to interpret the surplus of $FFCO_2$ at local scale (Levin et al., 2008; Vogel et al., 2010; Turnbull et al., 2014), and few attempts have been made to integrate the atmospheric $^{14}CO_2$ observations for the monitoring of fossil fuel emissions at national to continental scales. Basu et al., (2016) is the first study documenting the setup of an atmospheric inversion system jointly assimilating (virtual) observations of CO_2 and $^{14}CO_2$ in order to simultaneously estimate fossil fuel emissions and biospheric exchange fluxes of CO_2 at the regional to national scales (focusing on the United States of America). They showed in their OSSEs that given the actual $^{14}CO_2$ measurements made in 2010 (1063 globally, among which 969 are over North America), the US national total fossil fuel emission can be recovered to better than 1% for the year 2010 and to within 5% for most months.

In this study, we conduct a similar study and OSSEs for European regions and China over one year, investigating the potential of jointly assimilating atmospheric CO_2 and $^{14}CO_2$ from continental networks of stations to separate $FFCO_2$ and the signal of the other CO_2 fluxes and to improve the monthly estimates of fossil fuel emissions at national/provincial scales. Similar to Wang et al. (2016) and Chapter 3, we do not solve for the spatio-temporal distribution of the fluxes within each control region/months.

In Wang et al. (2016) and Chapter 3, they setup a global inversion system that solves for the monthly budgets of fossil fuel emissions at sub-continental scale, assuming that $FFCO_2$ can be directly quantified by $^{14}CO_2$ measurements and pointed out the need to account for the spatial distribution of the emissions and $FFCO_2$ at sub-

grid scales of the transport model. They showed that the inversion would significantly reduce the uncertainties in monthly fossil fuel emissions of high emitting regions compared to the assumed uncertainty in the inventories used as a prior knowledge in the Bayesian framework. However, the assumption that variations in atmospheric $^{14}CO_2$ only relates to fossil fuel emissions is too optimistic. The influences on $^{14}CO_2$ gradients from fluxes other than that from fossil fuel combustion can be significant in some areas (Randerson et al., 2002; Graven and Grubber, 2011). Such influences include biospheric and oceanic disequilibrium fluxes, the nuclear power plant production, and intrusion of ^{14}C-enriched high tropospheric and stratospheric air. The biospheric disequilibrium fluxes are related to the fact that CO_2 respired by soils is enriched in ^{14}C compared to the current atmospheric signature because it contains carbon fixed during the nuclear bomb tests in the atmosphere. The oceanic disequilibrium fluxes relates to the isotopic fractionation (discrimination against the heavier isotopes in the exchange fluxes) in air-sea gas exchange and to the depletion of atmospheric $^{14}CO_2$. For example, the biosphere disequilibrium enriches the atmosphere in ^{14}C by an amount that can offset half of the fossil fuel dilution related decrease of $^{14}CO_2$ globally (Turnbull et al., 2009), and the largest biosphere disequilibrium is generated by ecosystems in the Northern Hemisphere, which is also the Hemisphere where most of the fossil fuel emission occur (Randerson et al., 2002). And Graven and Gruber (2011) showed that nuclear enrichment of the atmosphere in ^{14}C by nuclear power plants and facilities offset at least 20% the fossil fuel dilution in $^{14}CO_2$, which is a larger signal than the enrichment effect from the biosphere disequilibrium in some areas.

This chapter makes a further step on the base of Chapter 3. We adjust our inversion system to include other CO_2 and $^{14}CO_2$ fluxes to investigate the influence of these fluxes on the inversion of fossil fuel emissions. However, because the $^{14}CO_2$ fluxes are products of CO_2 fluxes and the signatures of $^{14}CO_2$ in these fluxes, the uncertainties in the CO_2 fluxes will also affect the uncertainties of $^{14}CO_2$ fluxes (see section 4.2.1). The close connections between the CO_2 and $^{14}CO_2$ fluxes make the inversion problem non-linear (detailed in section 4.2.1 and 4.2.2). In previous inversion studies that included

both CO_2 and carbon isotopes, the fluxes of carbon isotopes (called isoflux hereafter) were usually taken as independent variables from CO_2 fluxes (Rayner et al., 1999; Rayner et al., 2008; Basu et al., 2016). In this chapter, we propose new equations to solve for this non-linear relationship.

Conventionally, ^{14}C data are usually reported in $\Delta^{14}C$ notation (see definition in Stuiver and Polach, 1977). It contains a correction of the value of $\delta^{14}C$, by isotopic fractionation with respect to ^{13}C (Stuiver and Polach, 1977). Using $\Delta^{14}C$ in the equations for CO_2 and $^{14}CO_2$ will cause significant biases for heavy polluted areas (Supplementary materials S1). Following Vogel et al. (2013, supplement), we use $\delta^{14}C$ notation to build our inversion system. However, in some calculations in the following sections, we sometimes inevitably mention $\Delta^{14}C$ and made some assumptions and approximations on the value of $\delta^{13}C$ to convert $\Delta^{14}C$ values into $\delta^{14}C$ values, when the latter are not available. These assumptions and approximations will only slightly influence the estimate of $^{14}CO_2$ fluxes, as the variations in atmospheric $\delta^{13}C$ are relatively small (Vogel et al., 2013, supplement), but they will not impact our 1-year inversion.

Using synthetic data in an OSSE framework has been a common practice to assess the potential of atmospheric inversion for assessing CO_2 fluxes (Hungershoefer et al., 2010). A typical OSSE system includes the following components: 1) a synthetic truth about the variables of interest (CO_2 and $^{14}CO_2$ fluxes, for example), 2) a set of synthetic observations (atmospheric mole fractions, for example) generated from the truth with the observational characteristics of the proposed system including observation coverage, schedule, and associated errors, 3) an inversion system that assimilates these observations. In the inversion, a different estimation about the truth is used as the prior knowledge. After assimilating the synthetic observations, analysis of the difference between the errors in the inverted estimate of the variables (compared to the truth) and the errors in the prior estimate of the variables (compared to the truth) are evaluated to provide an objective measure of the value of the inversion system.

Of note is that the cost of the $^{14}CO_2$ analysis of one sample is presently so high that the common practice of monitoring of $^{14}CO_2$ favors the choice of integrated samples at

weekly to 2-week scale (Levin et al., 2011; Vogel et al., 2013; Turnbull et al., 2016). So in our OSSE, the synthetic $^{14}CO_2$ data are generated as 2-week mean data. On the contrary, the CO_2 measurements can be made at very high resolution (Kadygrov et al., 2015). Although hourly CO_2 observations are feasible in the actual measurements, but it is too computational expensive to assimilate hourly data through one year in the inversion system. In consequence, only synthetic daily CO_2 data are considered in this study.

In practice, the inversions and analysis are conducted for a 1-year period arbitrarily chosen to be a typical year 2007. This choice only impact the meteorological conditions and the level of emissions that are taken into account in our modeling framework. We assume that these conditions will not impact the conclusions from the analysis strongly.

The paper is organized as follows. Section 4.2 first builds the equations of the atmospheric transport that connects atmospheric CO_2 and $^{14}CO_2$ observations to all the involved fluxes. The inversion system is built on these equations and a set of OSSEs are described. Section 4.3 firstly evaluates the potential of different observations in the estimate of fossil fuel emissions in terms of uncertainty reduction (comparing the uncertainties in the inverted fossil fuel emissions, referred to as posterior uncertainties, to the typical uncertainties in the flux estimates used as prior information by the inversion, see section 4.2.6). The influences of other CO_2 and $^{14}CO_2$ fluxes on the inversion of fossil fuel emissions are analyzed. At last, the inversions assimilating only CO_2 data and the inversions jointly assimilating both CO_2 and $^{14}CO_2$ data are compared to evaluate the degree to which the inclusion of $^{14}CO_2$ observations allows us to separate the fossil fuel emissions from other CO_2 fluxes. Conclusions are drawn in section 4.4.

4.2 Methodology

4.2.1 The non-linear relationships between the atmospheric mole fractions and the fluxes of CO_2 and $^{14}CO_2$

The atmospheric mole fractions of CO_2 and $^{14}CO_2$ at a given point and a given time is expressed as the result of the atmospheric transport of the associated fluxes, shown by Eq. (1) and Eq. (2). Atmospheric transport of inert tracers like CO_2 and $^{14}CO_2$ (the decaying of ^{14}C is much longer than the time scale of the atmospheric transport and the time scale of inversion experiments in this study) is linear, and thus is expressed by a linear operator $\mathbf{H}_{transp}$.

$$C_a = H_{transp}(F_{FF} + F_{NPP} + F_{HR} + F_{ao} + F_{oa}) \quad (1)$$

$$R_a C_a = H_{transp}(R_{NPP}F_{NPP} + R_{HR}F_{HR} + R_{ao}F_{ao} + R_{oa}F_{oa} + F_{nuc} + F_{cosm}) \quad (2)$$

In Eq. (1) and (2), F_{FF} denotes the CO_2 emissions from fossil fuel combustion. The terrestrial ecosystem CO_2 fluxes are split into F_{NPP} and F_{HR}, corresponding respectively to the net uptake of CO_2 by the plants (net primary productivity, NPP) and to the net release from soil heterotrophic respiration (fluxes from disturbance such as ecosystem fires, which represent a far smaller component than the heterotrophic respiration in the regions of interests in this study, are grouped with F_{HR}). Note that we implicitly assume in Eq. (2) that autotrophic respiration takes place on short time scale respiring young carbon carrying the same ^{14}C signatures as photosynthesis. Consequently, the gross biospheric uptake in this study is NPP instead of gross primary productivity (GPP). F_{ao}, F_{oa} are the one-way gross exchange of CO_2 from atmosphere to ocean and vice versa. The isotopic ratios R_{NPP}, R_{HR}, R_{ao}, R_{oa} are the ^{14}C:^{12}C isotopic ratios in the corresponding CO_2 fluxes. F_{nuc} and F_{cosm} are pure $^{14}CO_2$ fluxes from nuclear facilities and cosmogenic production.

Defining the ^{14}C content in a CO_2 sample as the relative difference in isotopic ratios between this sample and a reference standard material and correcting for decay

between the times of sample collection and measurement (Stuiver and Polach, 1977), Eq. (2) can be reformulated in notations of $\delta^{14}C$:

$$\delta_a C_a = \mathbf{H}_{\text{transp}}(\delta_{FF}F_{FF} + \delta_{NPP}F_{NPP} + \delta_{HR}F_{HR} + \delta_{ao}F_{ao} + \delta_{oa}F_{oa} + \frac{1}{R_{std}}F_{nuc} + \frac{1}{R_{std}}F_{cosm})$$

(3)

Where $R_{std}=1.176\times10^{-12}$ is the ^{14}C:^{12}C standard ratio.

We consider two one-way gross fluxes between the atmosphere and the biosphere separately, due to the different processes that influence atmospheric radiocarbon during the photosynthesis uptake on one hand, and heterotrophic respiratory release on the other hand. The preferential fixation by plant photosynthesis of lighter carbon isotopes causes an enhancement of the atmospheric ^{14}C:^{12}C isotopic ratios, while the heterotrophic respiration releases carbon that was assimilated from years to decades before. Because atmospheric $\delta^{14}C$ has been decreasing in the post bomb era since the 1960s, the "recent" soil carbon formed from plant carbon fixed after the bomb tests is enriched in ^{14}C, while the "ancient" soil carbon formed before the bomb tests still has a lower ^{14}C:^{12}C ratio than current atmosphere (Braziunas et al., 1995). Therefore, CO_2 produced by heterotrophic respiration has an isotopic ratio being a mixture between "recent" enriched and "ancient" depleted values. In the heterotrophic respiration, we ignore the fractionation following Naegler et al., 2009, so that the ^{14}C:^{12}C ratio in F_{HR} equals to that in the soil carbon.

The effect of fractionation and release of old carbon applies to the CO_2 exchanges between the atmosphere and the ocean. Fractionations exist for both one-way gross fluxes between ocean and atmosphere. Accounting for these processes, we re-write Eq. (3) into:

$$C_a\delta_a = \mathbf{H}_{\text{transp}}\left[\delta_{FF}F_{FF} + (\delta_{a,surf} - \varepsilon_{NPP})F_{NPP} + \delta_{HR}F_{HR} + (\delta_{a,surf} - \varepsilon_{ao})F_{ao} + (\delta_o - \varepsilon_{oa})F_{oa} + \frac{1}{R_{std}}F_{nuc} + \frac{1}{R_{std}}F_{cosm}\right]$$

(4)

where ε_{NPP}, ε_{ao} and ε_{oa} are the fractionations (in permil) during corresponding one-way

gross fluxes, and δ_o is the radiocarbon content of total dissolved inorganic carbon in the surface layer of the ocean, while $\delta_{a,surf}$ is the atmospheric radiocarbon in the surface layer where the uptake/release of CO_2 by terrestrial ecosystems or oceans occur. Eq. (1) and (4) together connect the CO_2 and $^{14}CO_2$ fluxes and the atmospheric mole fractions of these two tracers and build the base of the inversion system. In this study, we use an average fractionation $\varepsilon_{NPP} = -36‰$ for C3 plants (which is two times $^{13}\varepsilon_{NPP}=-18‰$, where $^{13}\varepsilon_{NPP}$ is the fractionation of $^{13}CO_2$ during photosynthesis for C3 plants, Degens, 1969) and $\varepsilon_{NPP}=-8‰$ for C4 plants ($^{13}\varepsilon_{NPP}=-4‰$, Farquhar et al., 1989). We also use an average fractionation for $\varepsilon_{ao}=4$ ‰ ($^{13}\varepsilon_{ao}=2$ ‰, Siegenthaler and Oeschger, 1987) and an average fractionation for $\varepsilon_{oa}=20.6‰$ ($^{13}\varepsilon_{ao}=10.3$ ‰, Siegenthaler and Oeschger, 1987).

Of note is that in this study, the $^{14}CO_2$ data refers to the product of the CO_2 mole fractions and its $\delta^{14}C$ value as shown by Eq. (4).

4.2.2 The framework of the inversion system

In this section, we introduce the general principle of the inversion solving for the fluxes at monthly and sub-continental scales. We adjust Eq. (1) and (4), in particular to derive the expression of the observation operator (see below) in such an inversion system. The practical setup of the observation operator is detailed in section 4.2.4.3.

The atmospheric inversion follows a Bayesian statistical framework, which corrects a statistical prior estimate $\mathbf{x}^b$ of the actual value $\mathbf{x}^t$ for a set of the control variables $\mathbf{x}$. This correction is based on a set of atmospheric measurements, called hereafter the observations $\mathbf{y}_o$, accounting for uncertainties in the prior estimate and for all the other sources of uncertainties (which are called all together “observation errors”) when comparing the simulated and measured observations. Assuming that the uncertainties in $\mathbf{x}^b$ and $\mathbf{y}_o$ are unbiased and Gaussian, characterized by the uncertainty covariance matrix $\mathbf{B}$ and $\mathbf{R}$, the optimal estimate of $\mathbf{x}$ (denoted as $\mathbf{x}^a$), given $\mathbf{x}^b$ and $\mathbf{y}_o$, is obtained by minimizing the quadratic cost function $J(x)$ (Tarantola, 2005):

$$J(\mathbf{x}) = \frac{1}{2}\left(\mathbf{x} - \mathbf{x}^{\mathrm{b}}\right)^{T}\mathbf{B}^{-1}\left(\mathbf{x} - \mathbf{x}^{\mathrm{b}}\right) + \frac{1}{2}(H[\mathbf{x}] - \mathbf{y}_o)^{T}\mathbf{R}^{-1}(H[\mathbf{x}] - \mathbf{y}_o) \quad (5)$$

Where $^{\mathrm{T}}$ denotes the transpose, H is an observation operator, which maps the control variables to the observational space. The operator H: $\mathbf{x}\rightarrow H(\mathrm{x})$ can be rewritten as H: $\mathbf{x}\rightarrow H_{\mathrm{prac}}(\mathrm{x})+\mathbf{y}_{\mathrm{fixed}}$, where $\mathrm{y}_{\mathrm{fixed}}$ is the signature, through atmospheric transport, of the initial conditions (the CO_2 and $^{14}CO_2$ mole fractions on the initial date of the inversion) not controlled by the inversion. In order to simulate the full amount of CO_2 and $^{14}CO_2$ in the atmosphere, the inversion uses a fixed estimate of the initial condition without attempting to correct it or account for uncertainties in these fluxes. In this study, the operator H_{prac} is not linear (see below) unlike the observation operator used in Wang et al. (2016) and Chapter 3. This explains why we do not solve for the explicit formulation of $\mathbf{x}_{\mathrm{a}}$ and its covariance matrix $\mathbf{A}$ in the linear case as Wang et al. (2016) and Chapter 3.

Here, we use the quasi-Newton iterative approach as detailed by Tarantola (2005) to minimize the cost function given in Eq. (5): at each iteration *n+1*, the operator H is linearized against the best estimate of the control variables $\mathbf{x}_{\mathrm{n}}$ given by the previous iteration (or against $\mathbf{x}^{\mathrm{b}}$ for the first iteration):

$$\mathbf{H}_{\mathbf{x}_{\mathrm{n}}} = \left(\frac{\partial H}{\partial \mathbf{x}_{\mathrm{n}}}\right)_{\mathbf{x}_{\mathrm{n}}} \quad (6)$$

in this way, at each iteration, J is approximated by a quadratic function, whose minimum $\mathbf{x}_{\mathrm{n+1}}$ is given by:

$$\mathbf{A}_{\mathrm{n+1}} = \left(\mathbf{B}^{-1} + \mathbf{H}_{\mathbf{x}_{\mathrm{n}}}^{\mathrm{T}}\mathbf{R}^{-1}\mathbf{H}_{\mathbf{x}_{\mathrm{n}}}\right)^{-1} \quad (7)$$

$$\mathbf{x}_{\mathrm{n+1}} = \mathbf{x}^{\mathbf{b}} + \mathbf{A}_{\mathrm{n+1}}\mathbf{H}_{\mathbf{x}_{\mathrm{n}}}^{\mathrm{T}}\mathbf{R}^{-1}\left(\mathbf{y}^{\mathbf{0}} - H\left[\mathbf{x}_{\mathbf{n}}\right] - \mathbf{H}_{\mathbf{x}_{\mathrm{n}}}\left(\mathbf{x}^{\mathbf{b}} - \mathbf{x}_{\mathbf{n}}\right)\right) \quad (8)$$

The series of $\mathbf{x}_{\mathrm{n}}$ should converge towards $\mathbf{x}^{\mathrm{a}}$. In practice, we derive our approximation of $\mathbf{x}^{\mathrm{a}}$ as the value of $\mathbf{x}_{\mathrm{n}}$ when the relative difference between the values of the cost functions in two consecutive iterations is smaller than 0.1%. $\mathbf{A}_{\mathrm{n+1}}$, the uncertainty covariance matrix in the final iteration, is taken as an approximation of the uncertainties in the posterior estimates $\mathbf{x}^{\mathrm{a}}$ (Tarantola, 2005). Of note is that the uncertainty given in this study refers hereafter to the standard deviation of the

uncertainty in a specific flux, if not specified differently.

We define the control vector **x** as monthly budgets or scaling factors of different types of fluxes for sets of regions (see section 4.2.4.1 for the definition of regions). Specifically, **x** include: monthly budgets of FFCO_2 emissions $\mathbf{x}_{FF}$, monthly budgets of terrestrial CO_2 fluxes NPP ($\mathbf{x}_{NPP}$) and heterotrophic respiration ($\mathbf{x}_{HR}$), monthly budgets of gross one-way CO_2 fluxes between the ocean and atmosphere ($\mathbf{x}_{ao}$ and $\mathbf{x}_{oa}$), monthly budgets of cosmogenic production of $^{14}CO_2$ ($\mathbf{x}_{cosm}$) and monthly budgets of $^{14}CO_2$ fluxes from nuclear facilities ($\mathbf{x}_{nuc}$), monthly scaling factors for δ_{HR} and (δ_o–ε_{oa}) reflecting the mix of pre- and post-bomb radiocarbon now emitted by the terrestrial and oceanic reservoirs, denoted as $\mathbf{x}_{\delta HR}$ and $\mathbf{x}_{\delta o\text{-}\varepsilon oa}$ respectively. We define the observation vector $\mathbf{y}_o$ as a set of CO_2 and/or $^{14}CO_2$ observations (see section 4.2.4.2 for the practical configurations).

To connect the control vector and observation vector and to facilitate the linearization of Eq. (6), we decompose the operator $H_{prac}(\mathbf{x})$ into a chain of three sub-operators, $H_{prac}=\mathbf{H}_{samp}\mathbf{H}_{transp}H_{dist}(\mathbf{x})$, where $H_{distr}(\mathbf{x})$ maps the regional monthly budgets of fluxes and the scaling factors to a gridded flux map at the spatial and temporal resolution of the transport model, where $\mathbf{H}_{transp}$ is the linear atmospheric transport of CO_2 and $^{14}CO_2$ and where the linear operator $\mathbf{H}_{samp}$ is the sampling of CO_2 and $^{14}CO_2$ observations corresponding to the observation vector from the transport model outputs. H_{dist} contains a set of linear operators denoting the distribution of all the CO_2 fluxes, $^{14}CO_2$ fluxes from nuclear facilities and cosmogenic production within each region-month corresponding to the control vector. However, the operator $\mathbf{H}_{samp}\mathbf{H}_{transp}$ still represents an extremely large matrix, where its input is at the resolution of the transport model, and is too costly to compute. To decrease the size of the computation, we further decompose the non-linear operator $H_{dist}(\mathbf{x})$ into some fixed linear parts and other non-linear parts that are easy to linearize. We re-write the $H(\mathbf{x})$ operator into the following form:

$$
\begin{aligned}
\mathbf{x} \quad &\mapsto \quad \mathbf{y} \;=\; H(\mathbf{x}) \\
H{:}\begin{bmatrix} \mathbf{x}_{\mathrm{FF}} \\ \mathbf{x}_{\mathrm{NPP}} \\ \mathbf{x}_{\mathrm{HR}} \\ \mathbf{x}_{\mathrm{Foa}} \\ \mathbf{x}_{\mathrm{Fao}} \\ \mathbf{x}_{\mathrm{nuc}} \\ \mathbf{x}_{\mathrm{cos}} \\ \mathbf{x}_{\delta\mathrm{HR}} \\ \mathbf{x}_{\delta\mathrm{o}-\varepsilon\mathrm{oa}} \end{bmatrix} &\mapsto \begin{bmatrix} \boldsymbol{y}_{CO2} \\ \boldsymbol{y}_{CO2\cdot\delta} \end{bmatrix} = \begin{bmatrix} \mathbf{H}_{\mathrm{samp}}\mathbf{H}_{\mathrm{transp}}\left(\mathbf{H}_{\mathrm{dist}}^{\mathrm{FF}}\mathbf{x}_{\mathrm{FF}} + \mathbf{H}_{\mathrm{dist}}^{\mathrm{NPP}}\mathbf{x}_{\mathrm{NPP}} + \mathbf{H}_{\mathrm{dist}}^{\mathrm{HR}}\mathbf{x}_{\mathrm{HR}} + \mathbf{H}_{\mathrm{dist}}^{\mathrm{Fao}}\mathbf{x}_{\mathrm{Fao}} + \mathbf{H}_{\mathrm{dist}}^{\mathrm{Foa}}\mathbf{x}_{\mathrm{Foa}}\right) + \boldsymbol{y}_{fixed,CO2} \\ \mathbf{H}_{\mathrm{samp}}\mathbf{H}_{\mathrm{transp}}\left(\begin{array}{c} \delta_{\mathrm{FF}}\mathbf{H}_{\mathrm{dist}}^{\mathrm{FF}}\mathbf{x}_{\mathrm{FF}} + \left(H_{\mathrm{dist}}^{\delta_{\mathrm{a,surf}}} - \varepsilon_{\mathrm{NPP}}\right) \circ \mathbf{H}_{\mathrm{dist}}^{\mathrm{NPP}}\mathbf{x}_{\mathrm{NPP}} + \left(\mathbf{H}_{\mathrm{dist}}^{\delta\mathrm{HR}} \circ \mathbf{H}_{\mathrm{dist}}^{\mathrm{HR}}\right)\left(\mathbf{x}_{\delta\mathrm{HR}} \circ \mathbf{x}_{\mathrm{HR}}\right) \\ + \left(H_{\mathrm{dist}}^{\delta_{\mathrm{a,surf}}} - \varepsilon_{\mathrm{ao}}\right) \circ \mathbf{H}_{\mathrm{dist}}^{\mathrm{Fao}}\mathbf{x}_{\mathrm{Fao}} + \left(\mathbf{H}_{\mathrm{dist}}^{\delta\mathrm{o}-\varepsilon\mathrm{oa}} \circ \mathbf{H}_{\mathrm{dist}}^{\mathrm{Foa}}\right)\left(\mathbf{x}_{\delta\mathrm{o}-\varepsilon\mathrm{oa}} \circ \mathbf{x}_{\mathrm{Foa}}\right) + \frac{1}{\mathrm{R_{std}}}\mathbf{H}_{\mathrm{dist}}^{\mathrm{nuc}}\mathbf{x}_{\mathrm{nuc}} + \frac{1}{\mathrm{R_{std}}}\mathbf{H}_{\mathrm{dist}}^{\mathrm{cosm}}\mathbf{x}_{\mathrm{cosm}} \end{array}\right) + \boldsymbol{y}_{fixed,CO2\cdot\delta} \end{bmatrix}
\end{aligned}
\tag{9}
$$

where ○ represents the Hadamard (element-wise) product of two matrices, meaning that the $^{14}CO_2$ fluxes are calculated by the product of the CO_2 fluxes and the signatures of δ in these fluxes, and where the bold operator means it is linear, while an Italic operator means it is non-linear. Since δ_{FF}, $1/R_{std}$ are constant, it allows us to build $\mathbf{H}_{samp}\mathbf{H}_{transp}\mathbf{H}_{dist}^{FF}$, $\mathbf{H}_{samp}\mathbf{H}_{transp}\mathbf{H}_{dist}^{NPP}$, $\mathbf{H}_{samp}\mathbf{H}_{transp}\mathbf{H}_{dist}^{HR}$, $\mathbf{H}_{samp}\mathbf{H}_{transp}\mathbf{H}_{dist}^{Fao}$, $\mathbf{H}_{samp}\mathbf{H}_{transp}\mathbf{H}_{dist}^{Foa}$, $\mathbf{H}_{samp}\mathbf{H}_{transp}(\mathbf{H}_{dist}^{\delta HR}\circ\mathbf{H}_{dist}^{HR})$, $\mathbf{H}_{samp}\mathbf{H}_{transp}(\mathbf{H}_{dist}^{\delta o\text{-}\varepsilon oa}\circ\mathbf{H}_{dist}^{Foa})$, $\mathbf{H}_{samp}\mathbf{H}_{transp}\mathbf{H}_{dist}^{nuc}$ and $\mathbf{H}_{samp}\mathbf{H}_{transp}\mathbf{H}_{dist}^{cosm}$ separately, in which case the inputs of these matrices are at the resolution of the control vector and thus they are of much smaller size than $\mathbf{H}_{samp}\mathbf{H}_{transp}$. But, the distribution of $H_{dist}^{\delta a,surf}$ changes during each iteration and thus makes the computation of $\mathbf{H}_{samp}\mathbf{H}_{transp}H_{dist}^{a,surf}$ for each iteration not affordable. To avoid this, we make a simplification for $H_{dist}^{\delta a,surf}$, assuming it is homogenous within each region-month. In this way, $H_{dist}^{\delta a,surf}$ becomes a scalar for a given region-month. By doing this, Eq(9) can be re-ordered as:

$$
\begin{array}{ccc}
\mathbf{x} & \mapsto & \mathbf{y} = H(\mathbf{x}) \\
H: \begin{bmatrix} \mathbf{x}_{\mathrm{FF}} \\ \mathbf{x}_{\mathrm{NPP}} \\ \mathbf{x}_{\mathrm{HR}} \\ \mathbf{x}_{\mathrm{Foa}} \\ \mathbf{x}_{\mathrm{Fao}} \\ \mathbf{x}_{\mathrm{nuc}} \\ \mathbf{x}_{\mathrm{cos}} \\ \mathbf{x}_{\delta\mathrm{HR}} \\ \mathbf{x}_{\delta\mathrm{o}-\varepsilon\mathrm{oa}} \end{bmatrix} & \mapsto \begin{bmatrix} \boldsymbol{y}_{CO2} \\ \boldsymbol{y}_{CO2\cdot\delta} \end{bmatrix} = & \begin{bmatrix} \mathbf{H}_{\mathrm{samp}}\mathbf{H}_{\mathrm{transp}}\left(\mathbf{H}_{\mathrm{dist}}^{\mathrm{FF}}\mathbf{x}_{\mathrm{FF}} + \mathbf{H}_{\mathrm{dist}}^{\mathrm{NPP}}\mathbf{x}_{\mathrm{NPP}} + \mathbf{H}_{\mathrm{dist}}^{\mathrm{HR}}\mathbf{x}_{\mathrm{HR}} + \mathbf{H}_{\mathrm{dist}}^{\mathrm{Fao}}\mathbf{x}_{\mathrm{Fao}} + \mathbf{H}_{\mathrm{dist}}^{\mathrm{Foa}}\mathbf{x}_{\mathrm{Foa}}\right) + \boldsymbol{y}_{fixed,CO2} \\ \mathbf{H}_{\mathrm{samp}}\mathbf{H}_{\mathrm{transp}}\left(\begin{array}{c} \mathbf{H}_{\mathrm{dist}}^{\mathrm{FF}}\delta_{\mathrm{FF}}\mathbf{x}_{\mathrm{FF}} + \mathbf{H}_{\mathrm{dist}}^{\mathrm{NPP}}\left(H_{\mathrm{dist}}^{\delta_{\mathrm{a,surf}}} - \varepsilon_{\mathrm{NPP}}\right)\mathbf{x}_{\mathrm{NPP}} + \left(\mathbf{H}_{\mathrm{dist}}^{\delta\mathrm{HR}} \circ \mathbf{H}_{\mathrm{dist}}^{\mathrm{HR}}\right)\left(\mathbf{x}_{\delta\mathrm{HR}} \circ \mathbf{x}_{\mathrm{HR}}\right) \\ +\mathbf{H}_{\mathrm{dist}}^{\mathrm{Fao}}\left(H_{\mathrm{dist}}^{\delta_{\mathrm{a,surf}}} - \varepsilon_{\mathrm{ao}}\right)\mathbf{x}_{\mathrm{Fao}} + \left(\mathbf{H}_{\mathrm{dist}}^{\delta\mathrm{o}-\varepsilon\mathrm{oa}} \circ \mathbf{H}_{\mathrm{dist}}^{\mathrm{Foa}}\right)\left(\mathbf{x}_{\delta\mathrm{o}-\varepsilon\mathrm{oa}} \circ \mathbf{x}_{\mathrm{Foa}}\right) + \mathbf{H}_{\mathrm{dist}}^{\mathrm{nuc}}\frac{1}{\mathrm{R_{std}}}\mathbf{x}_{\mathrm{nuc}} + \mathbf{H}_{\mathrm{dist}}^{\mathrm{cosm}}\frac{1}{\mathrm{R_{std}}}\mathbf{x}_{\mathrm{cosm}} \end{array}\right) + \boldsymbol{y}_{fixed,CO2\cdot\delta} \end{bmatrix}
\end{array}
\tag{10}
$$

where the non-linear parts, e.g. $(H_{\mathrm{dist}}^{\delta\mathrm{a,surf}}\text{-}\varepsilon_{\mathrm{NPP}})\mathbf{x}_{\mathrm{NPP}}$, $\mathbf{x}_{\delta\mathrm{HR}} \circ \mathbf{x}_{\mathrm{HR}}$ are easy to linearize.

4.2.3 Bottom-up estimates of CO_2 and $^{14}CO_2$ fluxes

In order to build the inverse modeling framework and OSSEs, bottom-up knowledge about the fluxes of CO_2 and $^{14}CO_2$ will be needed for describing the variation of the fluxes at high temporal and spatial resolution (which will not be controlled by the inversion) and for defining the estimates of the large scale fluxes. For the OSSE, we derive two representation of the estimates of CO_2 and $^{14}CO_2$ fluxes. The first representation is used to build the synthetic true fluxes and true estimate of the large scale fluxes. In this study, we compare our simulation of the $^{14}CO_2$ fluxes with previous studies (see Supplementary material S2) and evaluate the reality of the true fluxes by running an 18-year simulation of the mole fractions of $^{14}CO_2$ in the atmosphere and by comparing these mole fractions to some actual observations (see Supplementary material S2) . We also derive a second representation of the fluxes that differed from thuth. This second representation of the fluxes is used to build the set of $\mathbf{H}_{dist}^{xx}$ (where "xx" applies to "FF", "NPP", "HR", "Foa", "Fao", "δHR", "δ_o-ε_{oa}", "nuc" and "cosm") in Eq. (10), as well as to build the prior estimates of the large scale fluxes. In order to avoid the costly simulations to derive the biospheric (see below) $^{14}CO_2$ fluxes, the second representation of the fluxes is mainly a perturbation of the true estimates (except fossil fuel emissions, see below) that reflects the typical uncertainties in the state-of-the-art estimates of carbon fluxes. This second representation are termed as the practical estimates afterwards. All the fluxes are built firstly at the horizontal resolution of the raw data, and then aggregated at the resolution of the transport model (see section 4.2.4.3).

4.2.3.1. Fossil fuel emissions

As in Wang et el. (2016) and Chapter 3, We use the product of the 0.1 °×0.1 ° EDGARv4.2 emission map (http://edgar.jrc.ec.europa.eu) convoluted with temporal profiles (at 1-hour resolution) from IER (available at http://carbones.ier.uni-stuttgart.de/wms/index.html) to model the true fossil fuel emissions (named EDG-IER

hereafter), and use the PKU-CO_2 product (Wang et al., 2013) to model the practical fossil fuel emissions.

4.2.3.2. Terrestrial gross fluxes

The terrestrial CO_2 fluxes of NPP and heterotrophic respiration are simulated with ORCHIDEE-MICT (Zhu et al., 2015) at the resolution of the transport model. ORCHIDEE-MICT is a process-based ecosystem model which accounts for half-hourly to muti-annual variability in photosynthesis and respiration of the biosphere (Krinner et al., 2005; Zhu et al., 2015). ORCHIDEE-MICT simulates the carbon fluxes of plants (13 plant functional types, one for bare soil, eight for forests, two for C3 and C4 grasslands, and two for C3 and C4 croplands, each with 8 different carbon pools, namely leaf, root, aboveground sapwood, below-ground sapwood, aboveground heartwood, below-ground heartwood, fruit, reserve pools), litter (4 different carbon pools) and soil (3 different carbon pools) for each grid cell and each time step.

To explicitly model the distribution of the ^{14}C in the biosphere and model the $^{14}CO_2$ fluxes, we run a simulation parallel to ORCHIDEE-MICT by using the CO_2 fluxes from ORCHIDEE-MICT and incorporating the signature of ^{14}C in each CO_2 flux, assuming that the $^{14}CO_2$ fluxes will not influence the CO_2 fluxes simulated by ORCHIDEE-MICT and that ^{14}C is well-mixed within each carbon pool. The signature of ^{14}C in each carbon pools (and thus in the CO_2 fluxes) is derived from impulse response function summarizing the ^{14}C signatuare in the input for that pool, the lifetime of radiocarbon in that pool, and λ the decay constant of ^{14}C. The simulation is first run for 100,000 years to get to equilibrium state of ^{14}C in the biosphere. Then the simulation is run at the daily time step from 1955 until 2007 to get the distribution of ^{14}C in the different carbon pools of the biosphere and the biospheric $^{14}CO_2$ fluxes during this period. The input of ^{14}C into the biosphere is the atmospheric $^{14}CO_2$. The $^{14}CO_2$ in the atmosphere before 1955 is assumed to have an average value of $\Delta^{14}C=-4.5‰$. Observed time series of atmospheric signature of ^{14}C for different latitudinal bands after 1955 are interpolated and smoothed at monthly resolution

using the method developed by Thoning et al. (1989) from observed atmospheric radiocarbon records (Manning and Melhuish, 1994; Levin et al., 1994; Meijer et al., 2006; Nydal and Lövseth, 1996; Levin and Kromer, 2004; Levin et al., 2008). According to our simulation, the contribution of the biospheric $^{14}CO_2$ fluxes to the mean global atmospheric $^{14}CO_2$ is 5.4‰ yr^{-1} in 2007.

The practical representation of the terrestrial biospheric CO_2 and $^{14}CO_2$ fluxes are perturbed for each grid cell and for each time step. In order to reflect the realistic uncertainties in the estimates of biospheric fluxes, this perturbation is based on the estimation of Chevallier et al. (2012) which compared the biospheric CO_2 fluxes derived by the ORCHIDEE model and eddy-covariance flux tower data. Specifically, the perturbations follow log-normal distributions (to keep the sign of NPP and heterotrophic respiration unchanged) and are conducted so that the standard deviations of the uncertainties in NPP and in heterotrophic respiration are proportional to the fluxes themselves from the ORCHIDEE-MICT simulation. A ceiling value is imposed so that the uncertainties in NPP or heterotrophic respiration for a given grid cell remains smaller than 3 g C m^{-2} day^{-1} (Chevallier et al., 2010; Kadygrov et al., 2015). Correlations in the perturbation are configured with values exponentially decreasing as a function of the lag between times and space locations. Correlation e-folding lengths for both NPP and heterotrophic respiration are set to 1 month and 500 km (about the east-west size of the transport model grid at the equator, Chevallier et al., 2007). The cross-correlations between the uncertainties in NPP and in heterotrophic respiration in the same grid cell and at the same time step are set to -0.15 (since NPP have negative values and heterotrophic respiration have positive values). This -0.15 negative correlation are derived from an evaluation of the statistics of the deviations of 11 dynamic global vegetation models (DGVMs) of the TRENDY v2 project (Trends in net land-atmosphere carbon exchange over the period 1980-2010, Sitch et al., 2015) from their mean. The full correlations between uncertainties in NPP (or heterotrophic respiration) in different grid cells and time steps are calculated by the Kronecker product of the spatial and temporal correlations of NPP (or heterotrophic respiration) and the cross-correlations. The

perturbation of the distribution of δ_{HR} follows a Gaussian distribution ~**N**(1,0.2) for each grid cell and time step. The e-folding length of the spatial correlation for the perturbation of δ_{HR} is 500 km, being the same with those assumed for CO_2 fluxes. The e-folding length of the temporal correlation for the perturbation of δ_{HR} is set to 30 years, close to the typical biospheric residence time of 20-40 years (Graven et al., 2015; Naegler and Levin, 2009).

4.2.3.3. Ocean gross fluxes

The one-way gross ocean CO_2 fluxes are derived from the estimates of Landschützer et al. (2015) at the horizontal resolution of 1 °×1 °, which is based on the pCO_2 (SOCATv2, Bakker et al., 2014) distribution. To derive the $^{14}CO_2$ fluxes from the ocean, the δ_o at the resolution of 1 °×1 °are estimated based on the observed data of surface ocean $\Delta^{14}C$ of dissolved inorganic carbon (DIC) measurements from the World Ocean Circulation Experiment (WOCE). Since the radiocarbon data of WOCE survey were primarily sampled during 1980s – 1990s, the current $^{14}CO_2$ content in the ocean is lower than this estimate. To account for this, we make a simple assumption that the δ_o linearly decreases at a rate of -3‰ yr^{-1} everywhere. According to the estimate used in this study, the resulting global contribution of the net ocean $^{14}CO_2$ fluxes on the atmospheric $^{14}CO_2$ is -4.4‰ yr^{-1} in 2007.

Similar to the perturbation of the biospheric fluxes, the practical ocean fluxes are perturbed for each grid cell and for each time step, with the following configurations: temporal correlation decays exponentially with a length of 1 month; spatial correlation follows an exponential decay function with e-folding length of 1000 km (Chevallier et al., 2007); standard deviations are set to 0.3 g C m^{-2} day^{-1} everywhere; and the cross-correlation between uncertainties in the two one-way gross fluxes is -0.15. The perturbation of the distribution of δ_O follows a Gaussian distribution ~**N**(1,0.2) for each grid cell and time step. The exponentially decaying spatial correlations for the perturbation of δ_O is 1000 km, and the e-folding length of the temporal correlations for the perturbation of δ_O is 10 years (Naegler and Levin, 2006; Key et al., 2004).

4.2.3.4. Cosmogenic radiocarbon production

Cosmogenic production of $^{14}CO_2$ occurs throughout the atmosphere. A total production of 365 mol yr^{-1} (Kanu et al., 2016) is distributed horizontally with maximum production rate at the magnetic poles and minimum production at the equator according to Masarik and Beer (2009). The production rates (atom m^{-2} s^{-1} air-atom^{-1}) are assumed to increase linearly with decreasing pressure from zero at 500 hPa to a maximum at the top of the atmosphere. Similar to Turnbull et al. (2009) and Basu et al. (2016), we distribute the $^{14}CO_2$ production to higher altitudes (from 500 hPa) as Masarik and Beer (1999) suggested, in order to build up a realistic vertical distribution of $^{14}CO_2$ compared to the few stratospheric $^{14}CO_2$ observations (Supplementary materials Fig. S8).

The practical fluxes of ^{14}C from cosmogenic production are derived by perturbing the true fluxes per latitudinal band and per month. The original fluxes of cosmogenic production are multiplied by scaling factors drawn from a Gaussian distribution ~$\mathbf{N}$(1,0.2). The e-folding length of the temporal error correlations for this perturbation are set to 3 months and no spatial correlations are assumed between latitudinal bands.

4.2.3.5. Radiocarbon emissions from nuclear facilities

$^{14}CO_2$ fluxes from nuclear facilities are estimated following Graven and Gruber (2011). We extend the estimation from Graven and Gruber (2011) to recent years, based on the annual electricity generation by nuclear power plants (International Atomic Energy Agency's Power Reactor Information System, IAEA PRIS, available at https://www.iaea.org/PRIS/CountryStatistics/CountryStatisticsLandingPage.aspx) and the emission factors of nuclear industry (UNSCEAR, 2008). Fluxes from four active fuel reprocessing sites, La Hague (France), Sellafield (UK), Karlsruhe (Germany) and Tokai (Japan), which have high $^{14}CO_2$ emissions, are also included based on the report of the European Commission (Stricht and Janssens, 2010) and Japan Atomic Energy Agency (Nakada, 2008).

The perturbation for ^{14}C emissions by nuclear facilities follows a log-normal distribution. As indicated by Graven and Gruber (2011), the ^{14}C emission factors of nuclear facilities bear substantial uncertainties as they vary, for example, due to episodic venting, replacement of resin columns and other maintenance. The standard deviation of the perturbation chosen in this study is 4 times the value of the true emissions at a given location and time. The temporal correlation of the perturbation in the same grid cell is set to exponentially decrease with an e-folding length assumed to be 5 days. No spatial correlation is specified between the perturbations of different nuclear facilities.

4.2.4 Practical setup of the inversion and OSSEs

4.2.4.1. Definition of the regions in the control vector

The definition of the regions of control depend of the type of fluxes or scaling factors. For the CO_2 fluxes between the land surface and atmosphere, namely fossil fuel emission, NPP and heterotrophic respiration, as well as the scaling factors of δ_{HR}, we divided the land surface into 54 regions (Fig. 1a) which roughly corresponds to administrative boundaries, following Wang et al. (2016). There is one additional region for fossil fuel emissions which corresponds to the emissions over the ocean.

For the CO_2 fluxes between the interface of the ocean and atmosphere, as well as the scaling factors of $(\delta_o - \varepsilon_{oa})$, we divid the ocean into 9 regions (Fig. 1b), namely North Pacific, Tropical Pacific, South Pacific, North Atlantic, Tropical Atlantic, South Atlantic, Tropical Indian Ocean, South Indian Ocean and Southern Ocean (south of 50 °S). We solve for the $^{14}CO_2$ flux from nuclear facilities for 10 continents (Fig. 1b), i.e. Europe, US, Canada, Tropical America, South America, Africa, Middle East, India, East Asia and Russia. For $^{14}CO_2$ cosmogenic production, we divide the globe into 13 latitudinal bands (90 °-60 ° and every 10 ° from 60 ° to 10 ° for both hemispheres and a tropical band 10 °S-10 °N) following Masarik and Beer (2009).

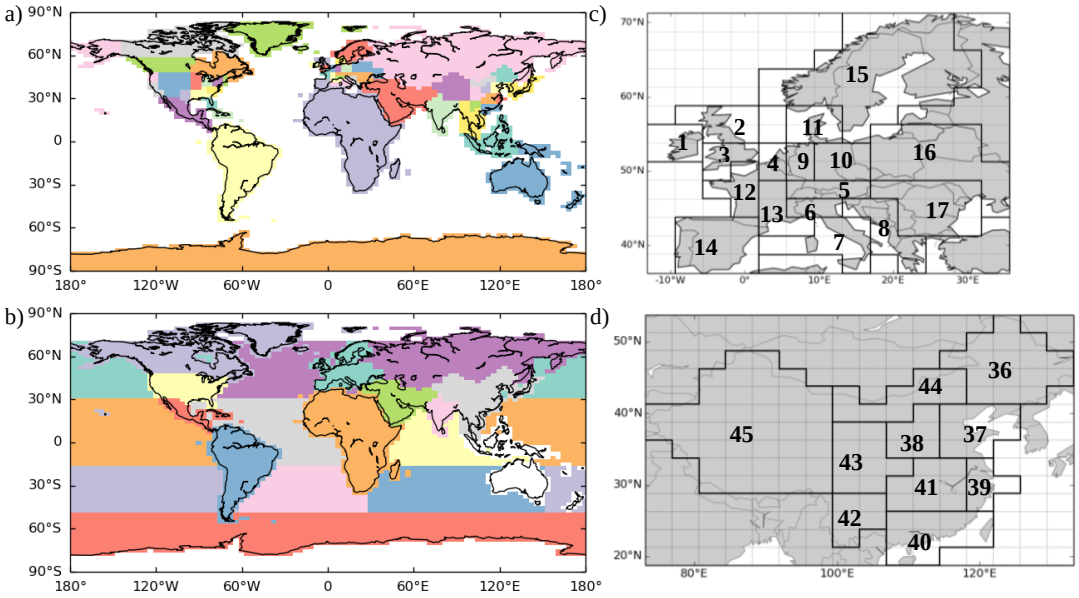

Figure 1 a) Map of the 55 regions whose monthly budgets of fossil fuel, NPP and heterotrophic respiration, as well as monthly scaling factors of δ_{HR} are controlled by the inversion. The ocean (white) is considered as one region for F_{FF}; b) Map of the 9 oceanic regions whose monthly budgets of F_{oa}, F_{ao}, as well as monthly scaling factors of (δ_o–ε_{oa}) are controlled by the inversion and of the 10 continental regions whose monthly budgets of $^{14}CO_2$ fluxes from nuclear facilities are solved. The regions filled with white color are not controlled due to the lack of estimates of CO_2/$^{14}CO_2$ fluxes in the Arctic Ocean (north of 71.25 °N) and due to the lack of nuclear facilities in Southeast Asia and Australia; c) zoom over the 17 control regions in Europe; d) zoom over the 10 control regions in China. Dotted lines in c) and d) show the grid of transport model.

4.2.4.2. Observation vector

In this study, the observation vector consists of atmospheric gradients of CO_2 and/or $^{14}CO_2$ between sites of the observation networks and a reference site representative of background free tropospheric air over a continent.

We consider a network of 43 sites in Europe like in Chapter 3. This network is a plausible near-term ICOS network, in which the High Alpine Research Station Jungfraujoch (JFJ), located at 3450 meter above sea level (masl) in Switzerland, is used as the reference station for the European sites. Similarly, we consider a virtual network of 39 sites spread all over China. The locations of the sites are arbitrarily and purposely selected so that the network is denser over the high emitting south-east coast of China (Fig. 2b). The reference site is located at 7500 masl, on top of the Tibet Plateau. The CO_2 and $^{14}CO_2$ measurements

made at any other sites are assumed to be sampled at 100 meters above ground level (magl), which is a typical height of tall towers (Kadygrov et al., 2015; Marquis and Tans, 2008).

The state-of-the-art inversion systems generally make use of data during afternoon only, due to the limitations of the transport models for simulating vertical mixing and thus mixing ratios during other periods of the day, even at 100 meters above ground. As we mentioned in the introduction, the sampling of $^{14}CO_2$ favors 2-week integrated samples. Of note is that in some OSSEs (see section 4.2.5), we only assimilate 2-week $^{14}CO_2$ data. In this case we assume that 2-week CO_2 mole fractions are also measured in these 2-week samples. Therefore, we define the observations to be selectively sampled daily or 2-week mean afternoon (12:00-18:00 local time) CO_2 and/or 2-week mean afternoon $^{14}CO_2$ gradients.

In consequence, the network in Europe will result in 15330 daily observations (of CO_2) per year (42 sites×365 days) and/or 1092 2-week observations (of CO_2 and/or $^{14}CO_2$) per year (42 sites×26 2-week periods). The network in China will have 13870 daily observations (of CO_2) per year (38 sites×365 days) and/or 988 2-week observations (of CO_2 and/or $^{14}CO_2$) per year (38 sites×26 2-week periods).

Wang et al., (2016) analyzed the distributions of the observation errors at potential sites across Europe and characterized two types of stations based on the population density of the grid cells (at the resolution of 0.5 °×0.5 °) within which the stations are located. Following their categorization, we define two types of sites: “urban” and “rural” sites (Fig. 2).

Due to the huge computational cost for matrix calculation, our inversions can only account for the observations from a network in either Europe or China separately. So our observation vectors are composed of daily afternoon mean total CO_2 and 2-week mean afternoon $^{14}CO_2$ gradients between the network of sites and the corresponding reference site over one continent.

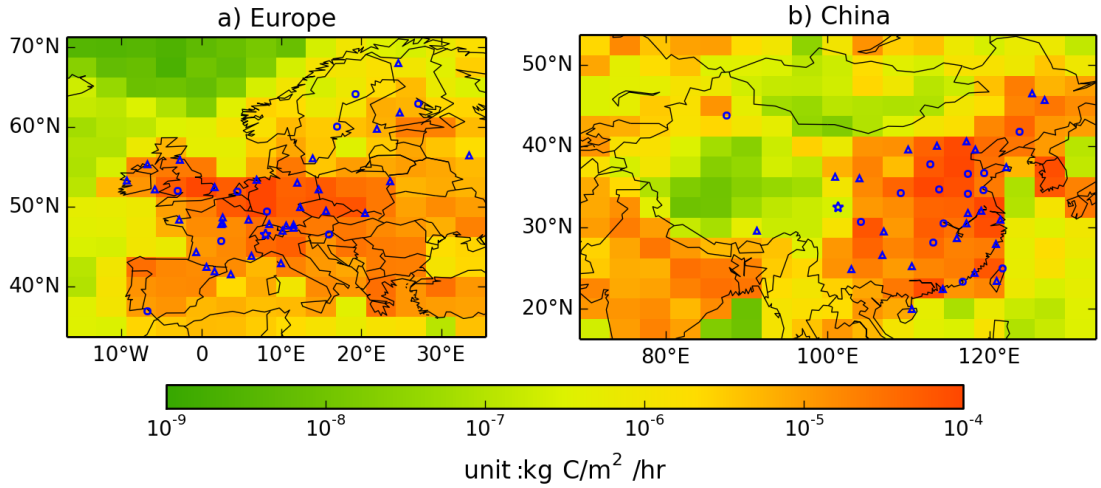

Figure 2 The continental networks of sites where atmospheric total CO_2 and $^{14}CO_2$ observations are sampled and assimilated in our OSSEs. Circles correspond to "urban" sites, triangles represent "rural" sites and stars are the reference sites. Urban and rural sites are categorized by the population density of the grid cells within which the stations are located, as described in Wang et al., (2016).

4.2.4.3. Observation operator

Transport model. Similar to Wang et al. (2016) and Chapter 3, the off-line version of the general circulation model of Laboratoire de Météorologie Dynamique LMDZv4 (Hourdin et al., 2006) is used as our atmospheric transport operator.

Sampling operator. The sampling of CO_2 and $^{14}CO_2$ gradients relies on the extraction of individual concentration at the measurement locations and then on the computation of differences between time series of the data to the concentration sampled at the reference site. The concentration data for a given site is sampled as the value in the transport model grid cell within which this site falls. All the measurements, except at the reference sites, sampled at 100 magl, is within the first level of LMDZv4. The measurements made at JFJ and the Chinese reference site are sampled at their actual heights, 3450 masl and 7500 masl, corresponding to the sixth and seventh level of LMDZv4, respectively. This operator is adapted according to the temporal averaging for daily afternoon mean and 2-week mean afternoon gradients of atmospheric total CO_2 and/or $^{14}CO_2$.

Flux distribution operator. As mentioned in section 4.2.3, the linear operators $\mathbf{H}_{dist}^{xx}$ are modelled and extracted by the practical representation of the fluxes.

Signatures from the initial conditions. By incorporating all the CO_2 fluxes and $^{14}CO_2$ fluxes in the atmospheric transport model, we run an 18-year simulation from 1990 to 2007 (see Supplementary material S2.5). We take the field of the mole fractions of CO_2 and $^{14}CO_2$ at Jan 1st, 2007 from the simulation as the initial condition for the 1-year inversion. A simulation is run with this initial condition and by removing all the CO_2 fluxes and $^{14}CO_2$ fluxes in 2007 to get the influence of the initial conditions on the distribution of atmospheric CO_2 and $^{14}CO_2$. $\mathbf{y}_{fixed}$ is thus sampled from the results of the simulation correspond to each observations.

4.2.4.4. Observation error covariance matrix

The observation error is a combination of the measurement errors, the model error (includes the transport error, i.e. the error in modelling of atmospheric transport, and the representation error, i.e. mismatch in temporal and spatial resolution between the transport model and the actual mole fractions/actual emissions), and errors from the model input that are not controlled by the inversion.

Our configuration of the measurement error keeps in line with the state-of-the-art measurement technology of CO_2 and $^{14}CO_2$ and with realistic estimates of the potential errors in the atmospheric transport and high temporal/spatial variability within grid cells of a coarse transport model like LMDZv4. A random measurement error of 0.1 ppm is assigned to the CO_2 data. The random measurement error of $\delta^{14}C$ in the atmospheric CO_2 is assigned to be 3‰, a typical precision of the analysis of air samples measured by accelerator mass spectrometry (AMS) (Vogel et al., 2010; Turnbull et al., 2014). The $^{14}CO_2$ measurement error is calculated by the error propagation rule, accounting for both the measurement error of atmospheric CO_2 and $\delta^{14}C$.

We make an estimation of the morel error by applying a similar estimate of Wang et al. (2016) and Chapter 3. The model error for daily data is computed as 0.8 times the standard

deviation of the 1-year long time series of the 3-hourly data for each site from a simulation which applies the transport model LMDZv4 to the true fluxes specified in section 4.2.2. The model error for 2-week data is computed as $0.8/\sqrt{14}$ times the standard deviation of the 1-year long time series of the 3-hourly data for each site. In such a configuration, the model error for the daily afternoon mean CO_2 data ranges from 2.6 to 11.2 ppm, which is on the same order of magnitude with the model errors estimated in other atmospheric inversions assimilating similar data (Piao et al., 2009; Chevallier et al., 2010; Peters et al., 2007; Peylin et al., 2013). The model error for the 2-week mean afternoon $^{14}CO_2$ data ranges from 1600 to 2400 ppm·‰. In addition, we also impose a representation error resulted from $FFCO_2$ which was not considered in the inversions mentioned before that do not solve for fossil fuel emissions. The implementation of the representation error of $FFCO_2$ follows the estimation of Wang et al. (2016). It depends on the locations and time of the sampled data, ranging from 0.9 ppm for "rural" sites in summer to 2.6 ppm for "urban" sites (Wang et al., 2016) in winter. This error has long-term temporal correlations (see Table 2 in Wang et al., 2016). In our inversion system, since the CO_2 and $^{14}CO_2$ data are collocated, we also account for the correlations between the errors in the synthetic CO_2 and $^{14}CO_2$ data at a given site through error propagation rules (supplementary materials S3). No spatial correlations between the data at different sites are assumed.

Our estimation of the aggregation errors follows the method proposed by Wang et al (2016). With the operators involved in the inversion, the aggregation error as: $\mathbf{H}_{\text{samp}}\mathbf{H}_{\text{transp}}H_{\text{distr}}{}^{\text{true}}\mathbf{x}^{\text{true}} - \mathbf{H}_{\text{samp}}\mathbf{H}_{\text{transp}}H_{\text{distr}}{}^{\text{prior}}\mathbf{x}^{\text{true}}$, where the superscript "true" means the operator is extracted from the synthetic true estimate of the fluxes and the superscript "prior" means the operator is extracted from the practical representation of the fluxes. We use a Gaussian distribution to approximate the statistics of the aggregation errors for different continents (e.g. Europe, Southeast Asia). The aggregation error is a function of the sampling semesters (spring/summer or autumn/winter) and of the integrated period of single samples, ranging from 2.2 ppm (for 2-week mean afternoon CO_2 observations over Europe in autumn/winter) to 3.8 ppm (for daily afternoon mean CO_2 observations over Europe in

autumn/winter), and ranging from 558 ppm·‰ (over Europe in spring/summer) to 732 ppm·‰ (over Europe in autumn/winter) for the 2-week mean afternoon $^{14}CO_2$ data. The temporal auto-correlations are also considered by fitting the statistics of the aggregation error using exponential decay functions, using the same method as Wang et al. (2016). No spatial correlations are considered (Wang et al., 2016).

In summary, the observation error covariance matrix is built as the sum of the covariances of the different components:

$$\mathbf{R} = \mathbf{R}_i + \mathbf{R}_m + \mathbf{R}_a \quad (11)$$

where $\mathbf{R}_i$, $\mathbf{R}_m$ and $\mathbf{R}_a$ are the covariance matrices of measurement error, model error and aggregation error, respectively.

4.2.4.5. Synthetic observation data

The synthetic observation data are generated by applying the transport model LMDZv4 to the true fluxes specified in section 4.2.2. The synthetic data are sampled and perturbed to mimic the actual variability that cannot be simulated by the sampling process and atmospheric transport model, in particular the measurement error and the model error.

4.2.4.6. Prior fluxes and error covariance matrix

The estimate of the prior error covariance for the fossil fuel emission follows the "practical" method of Chapter 3, by fitting the difference between the large scale fluxes from PKU-CO_2 and EDG-IER products.

For the other CO_2 and $^{14}CO_2$ fluxes, we derive them by perturbing the true fluxes in section 4.2.2. In principle, aggregating the uncertainties in each grid cell and at each time step used for the perturbation and accounting for the correlations between all pairs of the fluxes can give an estimate of the prior uncertainties for the control variables. But this calculation takes a huge computational cost, so we use a Monte Carlo ensemble approach to build the prior uncertainties. We perturb the true fluxes by using the same method in section 4.2.2 for 40 times, and derive the statistics of the 40 ensembles to approximate the

prior error covariance matrix. Quantitatively, the uncertainties for global net ecosystem change (NEE) and global net air-sea flux are 3.6 Pg C yr^{-1} and 2.5 Pg C yr^{-1}, while the uncertainties in the contributions from terrestrial and ocean $^{14}CO_2$ fluxes to the atmosphere in our setup are 828 Pg C ‰ and 591 Pg C ‰. The perturbation and resulting uncertainties in global budgets in our study are consistent with the typical uncertainties in the studies of global carbon budget (Chevallier et al., 2010; Le Quéré et al., 2015; Turnbull et al., 2009).

4.2.5 Experimental design of the OSSEs

We conduct four groups of OSSEs (Table 1), in which different sets of observations are assimilated. The first set, which is referred to as "CO2", assimilates the daily afternoon mean CO_2 gradients only. In the second set, which we refer to as "C14", 2-week mean afternoon CO_2 and 2-week mean afternoon $^{14}CO_2$ gradients are assimilated in the inversions. A third set, which we refer to as "COMB", jointly assimilates both daily afternoon mean CO_2 gradients and 2-week mean afternoon $^{14}CO_2$ gradients. The skill of constraining fossil fuel emissions at regional and monthly scales by different sets of observations will clarify the role of different observations in the inversion systems. In each group, we conduct a series of OSSEs, where in each one we remove one component (terrestrial biospheric, oceanic, nuclear facilities or cosmogenic production) from both the truth and the inversion configuration (see names of these sensitivity tests in Table 1). By doing this, the impact from other fluxes on the inversion of fossil fuel will be evaluated.

In addition, we also conduct an inversion, referred to as CO2-NAT, in which only CO_2 data are assimilated and only the natural fluxes are solved for as conventional atmospheric inversions do.

Table 1 Inversion configurations considered in this study. The "No" in the name of each sensitivity inversion stands for excluding, in the truth and optimization, the particular flux used as suffix of that name.

Inversions	Synthetic data	Short-name	Inverted fluxes/scaling factors
CO_2 inversions	daily afternoon mean CO_2 gradients	CO2-All	F_{FF}, F_{NPP}, F_{HR}, F_{oa}, F_{ao}
		CO2-NoBio	F_{FF}, F_{oa}, F_{ao}
		CO2-NoOce	F_{FF}, F_{NPP}, F_{HR}
$^{14}CO_2$ inversions	2-week mean afternoon total CO_2 gradients; 2-week mean afternoon $^{14}CO_2$ gradients	C14-All	F_{FF}, F_{NPP}, F_{HR}, F_{oa}, F_{ao}, F_{nuc}, F_{cosm}, δ_{HR}, δ_o-ε_{oa}
		C14-NoBio	all except F_{NPP}, F_{HR}, δ_{HR}
		C14-NoOce	all except F_{oa}, F_{ao},F_{FF}, δ_o-ε_{oa}
		C14-NoNuc	all except F_{nuc}
		C14-NoCos	all except F_{cosm}
Combined inversions	daily afternoon mean total CO_2 gradients; 2-week mean afternoon $^{14}CO_2$ gradients	COMB-All	F_{FF}, F_{NPP}, F_{HR}, F_{oa}, F_{ao}, F_{nuc}, F_{cosm}, δ_{HR}, δ_o-ε_{oa}
		COMB-NoBio	all except F_{NPP}, F_{HR}, δ_{HR}
		COMB-NoOce	all except F_{oa}, F_{ao},F_{FF}, δ_o-ε_{oa}
		COMB-NoNuc	all except F_{nuc}
		COMB-NoCos	all except F_{cosm}
"traditional" inversion	daily afternoon mean total CO_2 gradients	CO2-NAT	F_{NPP}, F_{HR}, F_{oa}, F_{ao}

4.2.6 OSSE evaluation

A common performance indicator is the theoretical uncertainty reduction (UR) for specific monthly budgets of the fossil fuel emissions, defined by:

$$\mathrm{UR} = 1 - \frac{\sigma^a}{\sigma^b} \tag{11}$$

where σ^a and σ^b are the posterior and prior uncertainties in the corresponding budget of emissions. Of note is that in the inversion, the estimate of the posterior uncertainty is only an approximation derived by Eq. (7). The actual error may depart from the posterior

uncertainty characterized by this approximated posterior error matrix **A**. In addition, as shown in Chapter 3, due to the limitation of the sampling of the prior and observation errors that may not purely unbiased and Gaussian, the extent to which fluxes estimated by the inversion match the true fluxes should also be evaluated as another metric for the assessment of the performance of the inversion.

In principle, a small uncertainty in the inverted fluxes means that the inversion can correctly allocate the fluxes into different parts. At the same time, because the sum of all the CO_2 and $^{14}CO_2$ fluxes is constrained by Eq. (1) and (4), an overestimation of one CO_2 (or $^{14}CO_2$) flux will lead to an underestimation of another CO_2 (or $^{14}CO_2$) flux, and thus it is likely to result in correlations between the uncertainties in the inverted fluxes. Given the same posterior uncertainty, a smaller magnitude in the correlations between the inverted fluxes means a better separation of different fluxes. Therefore, in our study, the posterior uncertainties, together with the magnitude of the correlations will be evaluated to give insights on the potential of $^{14}CO_2$ data in the separation of fossil fuel emissions and natural fluxes.

4.3 Results

Figure 3 shows the scores of UR of fossil fuel emissions for European regions and Chinese regions. In Europe, the most significant URs occur in western Europe, stemming from the dense observation network over this region. Since the URs and the differences between the prior and posterior fossil fuel emissions from other regions are rather small, in the following parts, our discussion will mainly focus on regions over Benelux (Fig. 1b, Region 4), Germany (Fig. 1b, Region 9+10), France (Fig. 1b, Region 12+13) and for western Europe (Fig. 1b, Region 1-14). In China, all regions except two have an UR larger than 20%. In the following, our discussion on Chinese regions focuses on three well sampled regions on the east coast: 1) the Bohai Economic Rim (No. 37 in Fig. 1, Beijing and its surroundings); 2) Yangtze River Delta Economic Zone (No. 39 in Fig. 1, Shanghai and its surroundings) and 3) Pearl River Delta Economic Zone (No. 40 in Fig. 1, Guangzhou and its surroundings).

4.3.1 Assessment of the performance of different observations on the estimation of fossil fuel emissions

4.3.1.1. Analysis of the uncertainty reductions

Fig. 3 and Table 2 compare the URs of monthly budgets of fossil fuel emissions for European and Chinese regions obtained by assimilating atmospheric CO_2 and/or $^{14}CO_2$ observations. When daily CO_2 and 2-week $^{14}CO_2$ data are assimilated (COMB-All, Fig. 4b and 4c), the URs of monthly budgets of fossil fuel emissions are much larger than those in the OSSEs that assimilating only daily CO_2 data (CO2-All, Fig. 3a and 4a). The number of 2-week CO_2 and $^{14}CO_2$ data (2184 in Europe and 1976 in China) in C14-All is much smaller than that in CO2-All (15330 in Europe and 13870 in China), but the URs of monthly budgets of fossil fuel emissions in C14-All are larger than those in CO2-All. At the same time, the differences between URs in COMB-All and C14-All are smaller than the differences between URs in C14-All and CO2-All (Table 2). The scores of uncertainty reductions indicate that the observational constraints brought by 2-week $^{14}CO_2$ data are much larger than those of the daily CO_2 data.

Fig. 3c shows the maps of URs for monthly fossil fuel emissions obtained by the "best case" (COMB-All) assimilating daily CO_2 and 2-week $^{14}CO_2$ observations. The UR on monthly emissions reaches 41% for Germany, 28% for France and 21% for western Europe. This inversion has much smaller URs of fossil fuel emissions for other regions of Europe that are not well sampled by the observation network, such as northern Europe and eastern Europe. In Chinese regions (Fig. 3f), the URs are larger than in European regions. The maximum UR is 65% for Yangtze River Delta Economic Zone (No. 39 in Fig. 1). Meanwhile, the eastern coast of China (No. 37 and 40 in Fig. 1), the most populated and developed area of China, as well as Shanxi province (No. 38 in Fig. 1), one of the leading coal-producing regions in China, also have large URs of fossil fuel emissions.

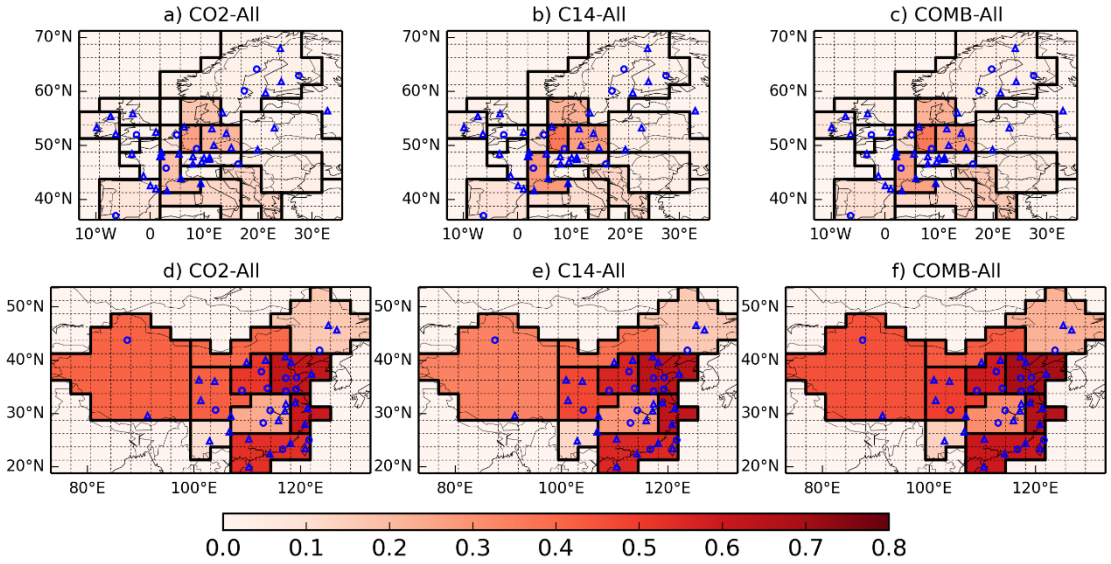

Figure 3 Comparison of URs in the monthly budgets of fossil fuel emissions of European regions (first row) and Chinese provinces (second row) between inversions assimilating daily CO_2 observations (first column), 2-week CO_2 + 2-week $^{14}CO_2$ observations (second column) and daily CO_2 + 2-week $^{14}CO_2$ observations (third columns). Circles (or triangles) dots correspond to "urban" (or "rural") stations (see section 4.2.4.2), where the gradients are extracted with respect to the reference sites.

Table 2 URs in the monthly budgets of fossil fuel emissions of Europe and Chinese regions between inversions assimilating daily CO_2 observations (CO2-All), 2-week CO_2 + 2-week $^{14}CO_2$ observations (C14-All) and daily CO_2 + 2-week $^{14}CO_2$ observations (COMB-All).

	CO2-All	C14-All	COMB-All
European regions			
Benelux	6%	10%	10%
Germany	27%	40%	41%
France	18%	26%	28%
Western EU	15%	19%	21%
Chinese regions			
Bohai Economic Rim	44%	59%	63%
Yangtze River Delta Economic Zone	47%	57%	65%
Pearl River Delta Economic Zone	39%	50%	56%
China	37%	47%	54%

4.3.1.2. Analysis of the posterior fossil fuel emissions and uncertainties

The time series of 12 monthly optimized fossil fuel emissions are shown in Fig. 4. Statistically, the distances between the posterior fossil fuel emissions (red lines) and the truth are largely reduced compared to the distance between prior emissions and the truth, when assimilating daily CO_2 and 2-week $^{14}CO_2$ simultaneously (COMB-All). The inversions also recover the seasonal cycle of the true emissions in China, while the posterior emissions of European regions are still almost flat.

On the other hand, although Fig. 3 shows that the URs of fossil fuel emissions when assimilating only CO_2 data are close to the results of inversions assimilating $^{14}CO_2$ data, the posterior emissions themselves (green lines in Fig. 4) are not well recovered compared to the true values. Although the posterior fossil fuel emissions from the inversion assimilating CO_2 get closer to the truth than the prior estimates for many region-months, corrections of the prior fossil fuel emissions are still in the wrong direction (resulting in larger misfit in the posterior estimates than in the prior emissions) for a significant number of region-months. For example, when assimilating only CO_2 data, the posterior emissions of Germany deviate more from the truth than the prior estimates, and the posterior emissions of Bohai Economic Rim in China have a seasonal cycle that are significantly different from the truth.

Fig. 5 shows the performance of the inversion on the posterior estimate of annual total fossil fuel emissions. For all the regions, the prior annual emission estimates have significant systematic errors compared to the true emission. Consistent with monthly results, the posterior annual emissions are recovered to within 5% for European regions only except France (within 13%, because the prior uncertainty in fossil fuel emissions over France is 22%, larger than Benelux and Germany) when assimilating daily CO_2 and 2-week $^{14}CO_2$ together. The misfits between the fossil fuel emissions of Chinese regions from the truth are recovered from more than 20% in the prior estimate to within 10% in the posterior estimate when daily CO_2 and 2-week $^{14}CO_2$ observations are jointly assimilated. Over large domains defined by groups of regions, the annual budget of emissions in western Europe lies 1%

away from the truth, while the distance between the posterior total national budget over China and the truth is below 3%. At the same time, Fig. 5 also shows that the posterior fossil fuel emissions from inversions CO2-All and C14-All are not constrained as well as those from COMB-All. The posterior fossil fuel emissions from inversion CO2-All deviate the most from the truth, indicating that $^{14}CO_2$ observations are essential for an accurate estimation of fossil fuel emissions.

Complementing the analysis of posterior estimates of fossil fuel emissions, Table 3 shows the prior and posterior uncertainties of the annual budgets of fossil fuel emissions over corresponding regions in inversion COMB-All. The uncertainties for western Europe is reduced from 6% in the prior estimate to 4% in the posterior estimate. For Chinese regions, although the prior uncertainties are larger than those for European regions, the posterior uncertainties are smaller, being below 10% at the scale of provinces, and the uncertainty in the annual emissions over China is reduced from 9% in the prior estimate to 3% in the posterior estimate.

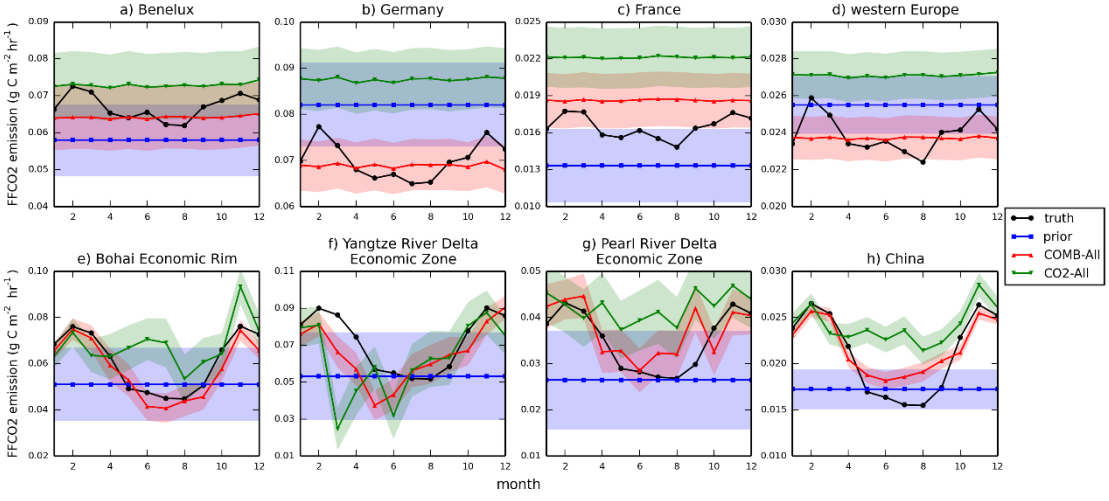

Figure 4 Prior (blue lines, calculated from PKU-CO_2) and posterior monthly budgets of fossil fuel emissions (colored lines) with associated uncertainties (1-σ, shaded area) from inversions assimilating daily CO_2 observations (green) and daily CO_2 + 2-week $^{14}CO_2$ observations (red), along with the true fluxes (black lines, calculated from EDG-IER).

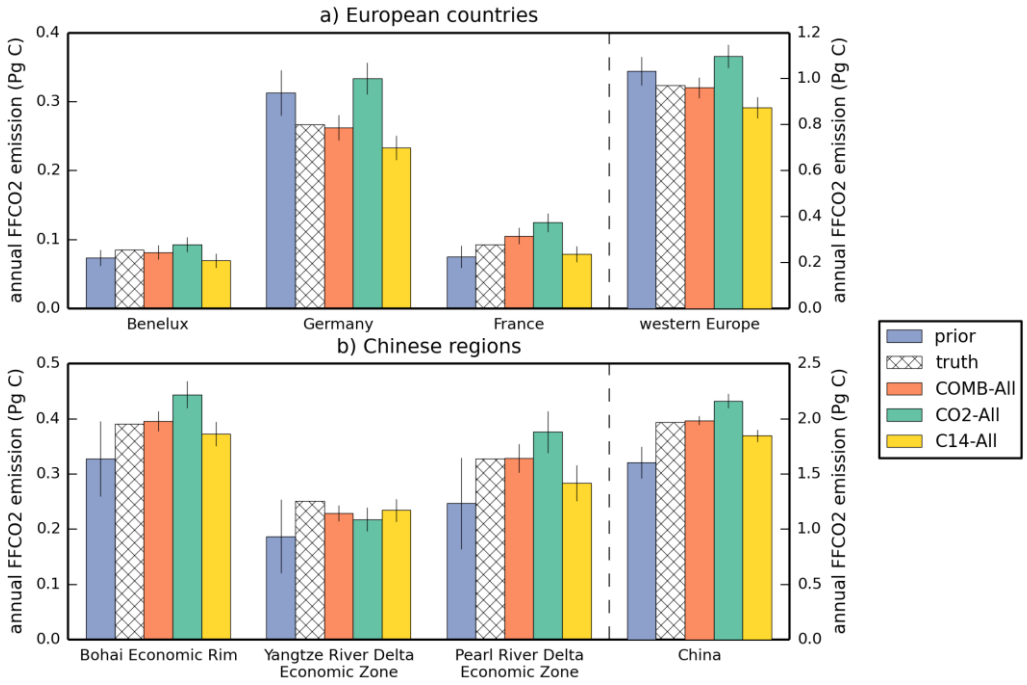

Figure 5 Prior (blue bars, calculated from PKU-CO_2) and posterior annual fossil fuel emissions (colored bars) with associated uncertainties (1-σ, whiskers) from inversions assimilating daily CO_2 observations (green), 2-week CO_2 + 2-week $^{14}CO_2$ observations (yellow) and daily CO_2 + 2-week $^{14}CO_2$ observations (red), along with the true fluxes (cross-hatched bars, calculated from EDG-IER).

Table 3 Prior and posterior uncertainty in annul fossil fuel emissions over European and Chinese regions from inversion COMB-All. The uncertainties is expressed as the percent of the prior emissions.

Europe			China		
Region	Prior unc.	Post. unc.	Region	Prior unc.	Post. unc.
Benelux	16%	14%	Bohai Rim	21%	5%
Germany	11%	6%	Yangzte River Delta	35%	8%
France	22%	16%	Pearl River Delta	34%	10%
western EU	6%	4%	China	9%	3%

4.3.2 Influences of uncertainties from other fluxes on the inversion of fossil fuel emissions

Fig. 6 and 7 show the differences between URs of monthly budgets of fossil fuel

emissions from the inversions which exclude a specific non-fossil flux and the inversion which solve for all the fluxes. When biospheric fluxes are removed from the truth and the inversion (CO2-NoBio, C14-NoBio, COMB-NoBio), the inversions show larger URs of fossil fuel emissions (Fig. 6 a-c and Fig. 7 a-c, positive difference). The differences are the largest between the inversions that only assimilate daily CO_2 data (CO2-NoBio and CO2-All), implying that the signal of $FFCO_2$ are easily mixed with the signal from biospheric CO_2 flux and thus prevent the use of CO_2 data to filter the signal of the uncertainties in fossil fuel emissions. When 2-week $^{14}CO_2$ data are assimilated (C14-NoBio vs C14-All and COMB-NoBio vs COMB-All), accounting for the uncertainties in biospheric fluxes only slightly impact the inversion of fossil fuel emissions (Fig. 6b, 6c and Fig. 7b, 7c). Of note is that in Europe, the differences between URs of the inversions COMB-NoBio and COMB-All are larger than the differences between those of C14-NoBio and C14-All, while it is on the opposite for China provinces. In China, as the URs in COMB-All are already quite large (~50%, see Table 2), removing the uncertainty in biospheric fluxes only slightly increase the URs of fossil fuel emissions.

The comparison between the URs of fossil fuel emissions from the inversions which exclude the $^{14}CO_2$ fluxes from nuclear facilities (C14-NoNuc and COMB-NoNuc) and those solving for all the fluxes (C14-All and COMB-All) are shown in Fig. 6d, 6e and Fig. 7d, 7e. In Europe, the uncertainties in nuclear facilities may also significantly impact the inversion of fossil fuel emissions. The influences of $^{14}CO_2$ fluxes of nuclear facilities are on the same order of magnitude, if not larger, as those of the biospheric fluxes, especially in the regions where the nuclear facilities are dense (e.g. regions near Germany and France). But in China, due to a limited number of nuclear facilities, the $^{14}CO_2$ fluxes from nuclear facilities seem not to impact the inversion of fossil fuel emissions.

Apart from two fluxes discussed above, we also investigate the URs from inversions that remove the other CO_2/$^{14}CO_2$ fluxes, e.g. oceanic fluxes and cosmogenic production (other OSSEs listed in Table 1). Since our stations are located inland and only sample ambient air near the surface (only except the reference sites), the influences from these fluxes

on URs of fossil fuel emissions are much smaller (<2%) than those from biosphere and nuclear facilities no matter which set of data are assimilated and thus are not further discussed here.

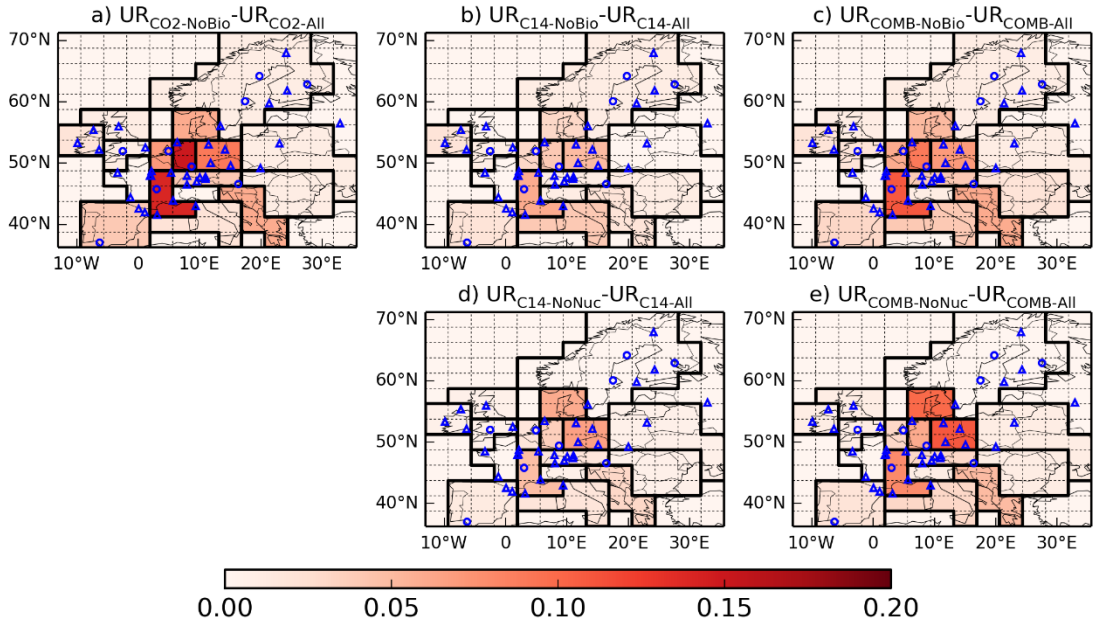

Figure 6 Differences between URs in the monthly budgets of fossil fuel emissions between inversions that exclude a specific flux and those solving for all the fluxes over European regions. Results are shown for inversions assimilating daily CO_2 observations (first column), 2-week CO_2 + 2-week $^{14}CO_2$ observations (second column) and daily CO_2 + 2-week $^{14}CO_2$ observations (third columns). Circles (or triangles) dots correspond to "urban" (or "rural") stations (see section 4.2.4.2), where the gradients are extracted with respect to the reference sites.

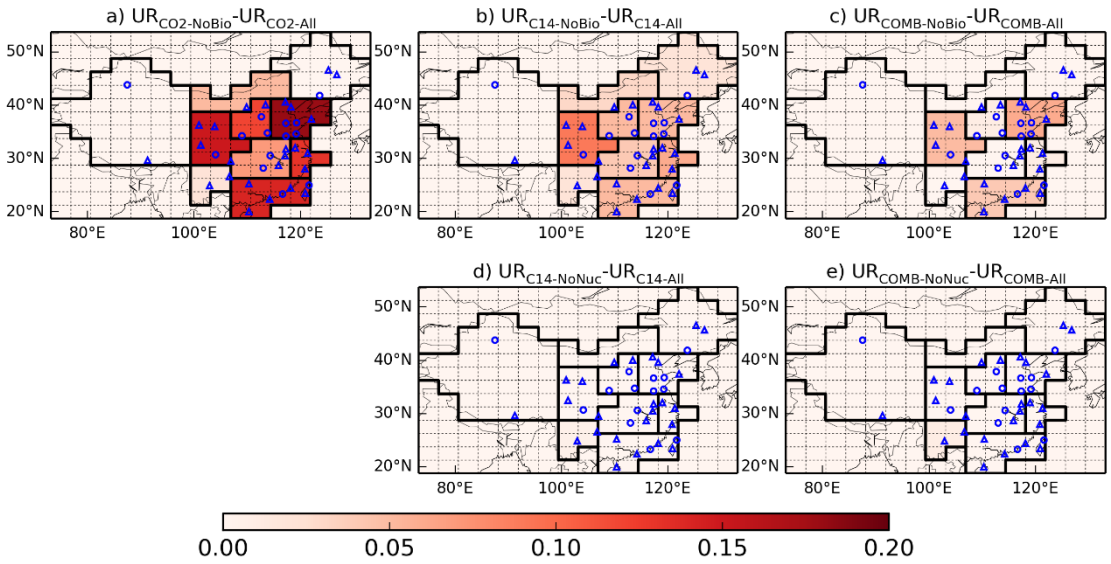

Figure 7 Differences between URs in the monthly budgets of fossil fuel emissions between inversions that exclude a specific flux and those solving for all the fluxes over Chinese provinces. Results are shown for inversions assimilating daily CO_2 observations (first column), 2-week CO_2 + 2-week $^{14}CO_2$ observations (second column) and daily CO_2 + 2-week $^{14}CO_2$ observations (third columns). Circles (or triangles) dots correspond to "urban" (or "rural") stations (see section 4.2.4.2), where the gradients are extracted with respect to the reference sites.

4.3.3 Separation of fossil fuel emissions and natural fluxes

In inversions that assimilate CO_2 data only and solve for both natural fluxes and fossil fuel emissions (CO2-All), the signals from both fossil fuel emissions and natural fluxes are mixed together in the atmospheric CO_2 data. Without additional observational constraints on the individual fluxes, it is difficult to dissociate the different carbon fluxes from each other. As a result, this can prevent a large decrease in the posterior uncertainties in each type of fluxes, and is characterized by large negative correlations between the posterior uncertainties in different CO_2 fluxes. This is seen in the inversion of CO2-All, for example (Fig. 7, green lines), over Germany and Chinese regions. In comparison, in the inversions C14-All and COMB-All, the negative correlations between the posterior uncertainties in fossil fuel emissions and biospheric CO_2 fluxes (Fig. 7, red lines) are smaller than those of CO2-All. Combined with the fact that the posterior uncertainties in fossil fuel emissions in C14-All and COMB-All are also smaller than those in CO2-All (Table 2), it proves that atmospheric

$^{14}CO_2$ data can better separate the fossil fuel and biospheric CO_2 fluxes than CO_2 data do. The comparison between C14-All and COMB-All is more complicated. On one hand, the magnitude of the negative correlations between the uncertainties in the biospheric CO_2 fluxes and fossil fuel emissions are larger in COMB-All than those in C14-All. But on the other hand, Fig. 3 and Table 2 show that the posterior uncertainty in fossil fuel emissions in COMB-All is slightly smaller than that in C14-All (given larger URs in COMB-All). This reflects the fact that the observational constraints of $^{14}CO_2$ data mainly contribute to the retrieval of fossil fuel emissions. But in COMB-All, because of a large number of daily CO_2 data, the sum of total CO_2 fluxes are well constrained so that only the remaining and smaller uncertainties in biospheric and fossil fuel fluxes are highly correlated. This demonstrates the different roles of CO_2 and $^{14}CO_2$ data in separating the signal of uncertainties in biospheric and fossil fuel CO_2 fluxes.

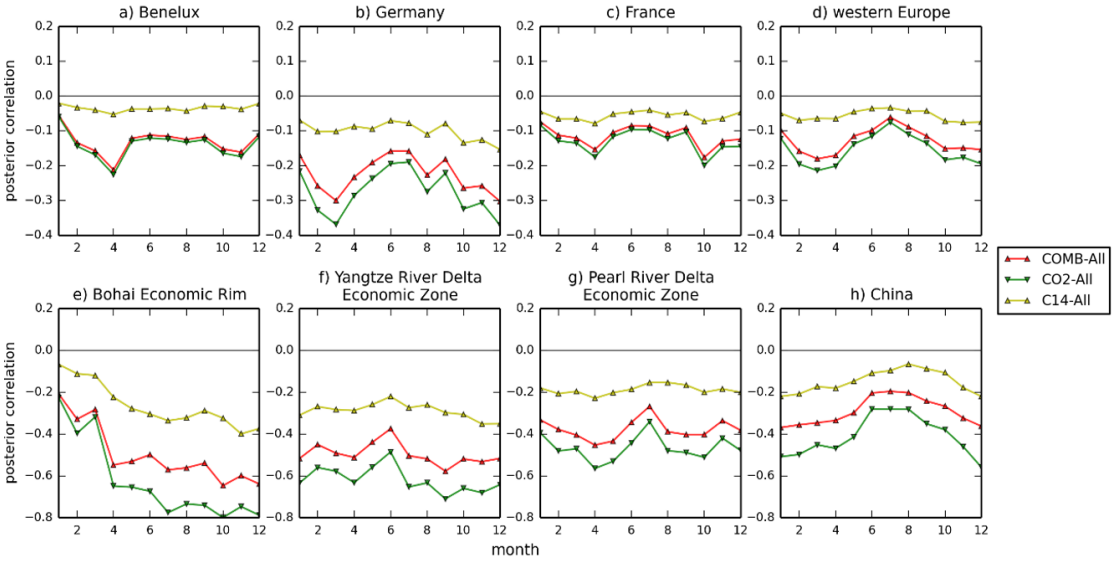

Figure 8 Correlations between posterior uncertainties in monthly budgets of fossil fuel emissions and biospheric fluxes obtained from inversions assimilating daily CO_2 observations (green), 2-week CO_2 + 2-week $^{14}CO_2$ observations (yellow) and daily CO_2 + 2-week $^{14}CO_2$ observations (red).

As indicated in the introduction, in conventional CO_2 inversion that only solves for NEE (Chevallier et al., 2010; Peters et al., 2010; Broquet et al., 2013; Peylin et al., 2013), the fossil fuel emissions are usually prescribed and not optimized. So the errors in the fossil fuel

emissions result in errors in the inverted biospheric fluxes. In principle, in the isotopoic inversion system, as the signal of $FFCO_2$ can be separated from the total CO_2, it can be expected that the signal of biospheric fluxes will be also better filtered and thus to improve the estimate of NEE. Fig. 9 shows the posterior monthly budgets of NEE from inversions COMB-All and CO2-NAT, along with the truth and prior estimates. It is obvious that the prior NEE significantly deviates from the truth. In both inversions, the posterior estimates of the budgets of NEE are corrected from the prior estimates and lie close to the true NEE fluxes (Fig. 9). This is due to the widespread network of observational stations and the large number of CO_2 data, as well as due to the fact that the errors in the prescribed fossil fuel emissions is usually one order of magnitude smaller than the differences between the prior and the true NEE. When aggregating at annual scale (Fig. 10), it is seen that the errors in the estimates of NEE due to unsolved fossil fuel emissions (CO2-NAT, green bars) are comparable with the errors in the prior estimate of fossil fuel emissions (compared to the truth). For example, the prior annual budget of fossil fuel emissions in Germany is higher than the truth by 0.05 Pg C, which results in a posterior annual budget of NEE 0.07 Pg C lower than the truth in the inversion CO2-NAT. And the prior fossil fuel emissions in Yangtze River Delta Economic Zone of China, is smaller than the truth by 0.06 Pg C, leading to a +0.07 Pg C offset in the posterior NEE in inversion CO2-NAT. In COMB-All, where $^{14}CO_2$ data are assimilated in addition to daily CO_2 data, the misfit between posterior annual budgets of NEE and the truth is only 0.001 Pg C for Germany and 0.03 Pg C for Yangtze River Delta Economic Zone of China. However, as shown in Fig. 10, adding constraints from atmospheric $^{14}CO_2$ observations, the posterior NEE from inversion COMB-All does not necessarily result in better NEE estimates over large domain like western Europe and China. This is because in other regions that are sparsely sampled (e.g. southern Europe and western China), the posterior fossil fuels emissions are not accurately recovered, and the NEE in different regions are either higher or lower than the truth. When aggregated, the errors from different regions may be cancelled out each other.

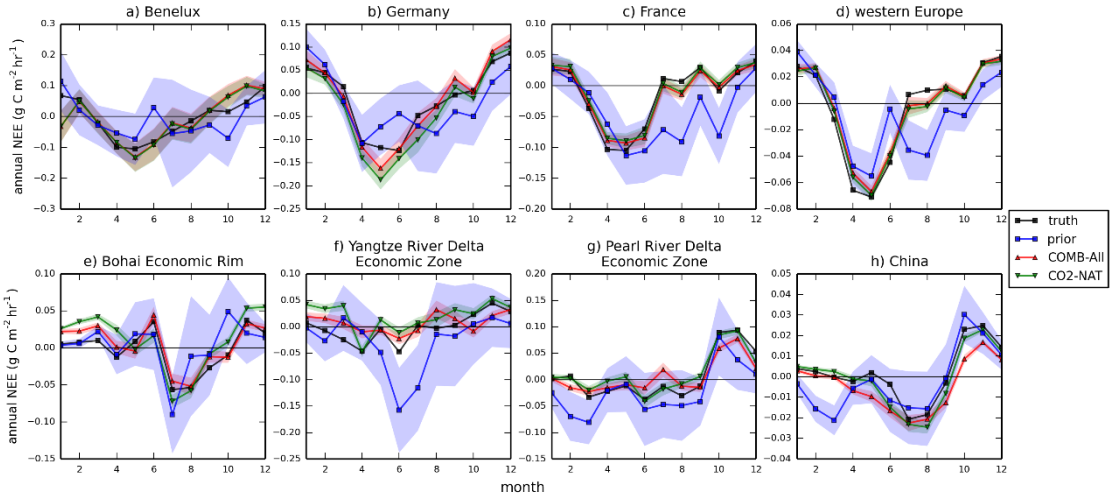

Figure 9 Prior (blue lines, a perturbation of the simulation by ORCHIDEE-MICT) and posterior monthly budgets of NEE (colored lines) with associated uncertainties (1-σ, shaded area) from inversions using daily CO_2 and 2-week $^{14}CO_2$ observations to solve for all the fluxes (CO2-All, red lines) and from inversion using daily CO_2 observations to solve for biospheric and oceanic CO_2 fluxes (CO2-NAT, green lines), along with the true fluxes (black lines, simulated by ORCHIDEE-MICT).

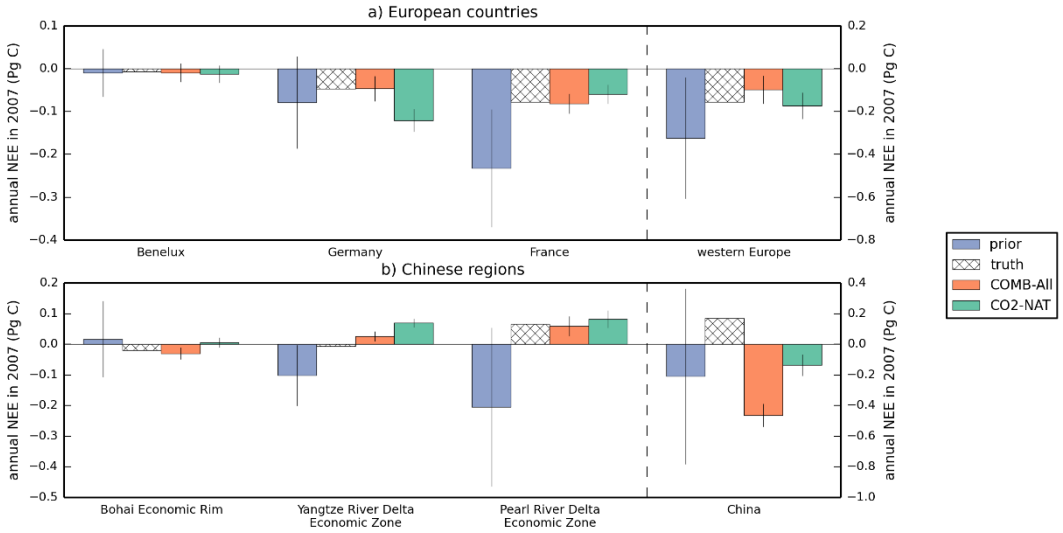

Figure 10 Prior (blue bars, perturbed from the simulation by ORCHIDEE-MICT) and posterior annual NEE (solid lines) with associated uncertainties (1-σ, shaded area) from inversions using daily CO_2 and 2-week $^{14}CO_2$ observations to solve for all the fluxes (CO2-All, red bars) and from inversion using daily CO_2 observations to solve for biospheric and oceanic CO_2 fluxes (CO2-NAT, green bars), along with the true fluxes (cross-hatched bars, simulated by ORCHIDEE-MICT).

4.4 Conclusion

In this work we develop a global inversion system that jointly assimilate atmospheric CO_2 and $^{14}CO_2$ data from continental networks to estimate CO_2 emitted from fossil fuel over

Europe and China, accounting for the influences of the uncertainties in other CO_2 and $^{14}CO_2$ fluxes. Atmospheric CO_2 data has a poor ability to reduce the errors in the monthly budgets of fossil fuel emissions at regional scale, while a large network of $^{14}CO_2$ measurements as the one evaluated in this study should bear a high potential to verify the fossil fuel emissions by using a joint isotopic inversion method. In our study, given the continental network of ~40 sites across Europe and China, the posterior uncertainties of the annual fossil fuel emissions are within 5% over these areas. A set of OSSEs are performed and show that the CO_2 signals from fossil fuel emissions are mixed with those of biospheric CO_2 fluxes and prevent the estimate of monthly budgets of regional fossil fuel emissions by using CO_2 data. Atmospheric $^{14}CO_2$ data can help to efficiently filter the signals of fossil fuel emissions from the total CO_2 and thus provide more constraints on the fossil fuel emissions, but is likely to be influenced by the $^{14}CO_2$ fluxes from nuclear facilities. As indicated by the uncertainties in the posterior estimate of fossil fuel emissions and the correlations between the posterior uncertainties in fossil fuel CO_2 emissions and biospheric CO_2 fluxes, atmospheric $^{14}CO_2$ data show a high potential to efficiently separate the signals of fossil fuel emissions from the total CO_2 and thus provide robust constraints on the fossil fuel emissions. In the context of national commitments, $^{14}CO_2$ data could provide useful information for independent verification of these commitments for emitters where a large observing network of $^{14}CO_2$ stations are established.

References

Andres, R. J., Boden, T. A. and Higdon, D.: A new evaluation of the uncertainty associated with CDIAC estimates of fossil fuel carbon dioxide emission, Tellus B, 66, 2014.

Andres, R. J., Gregg, J. S., Losey, L., Marland, G. and Boden, T. A.: Monthly, global emissions of carbon dioxide from fossil fuel consumption, Tellus B, 63(3), 309–327, 2011.

Bakker, D. C., Pfeil, B., Olsen, A., Chierici, M., Fransson, A., Johannessen, T., Lauvset, S. K., Skjelvan, I. and Tjiputra, J.: An update to the Surface Ocean CO_2 Atlas (SOCAT version 2), 2014.

Ballantyne, A. P., Andres, R., Houghton, R., Stocker, B. D., Wanninkhof, R., Anderegg, W., Cooper, L. A., DeGrandpre, M., Tans, P. P., Miller, J. B., Alden, C. and White, J. W. C.: Audit of the global carbon budget: estimate errors and their impact on uptake uncertainty, Biogeosciences, 12(8), 2565–2584, 2015.

Basu, S., Miller, J. B. and Lehman, S.: Separation of biospheric and fossil fuel fluxes of CO_2 by atmospheric inversion of CO_2 and $^{14}CO_2$ measurements: Observation System Simulations, Atmospheric Chemistry and Physics, 16(9), 5665–5683, 2016.

Berrisford, P., Dee, D., Fielding, K., Fuentes, M., Kallberg, P., Kobayashi, S. and Uppala, S.: The ERA-Interim Archive, ERA report series, (1), 1–16, 2009.

Bovensmann, H., Buchwitz, M., Burrows, J. P., Reuter, M., Krings, T., Gerilowski, K., Schneising, O., Heymann, J., Tretner, A. and Erzinger, J.: A remote sensing technique for global monitoring of power plant CO_2 emissions from space and related applications, Atmospheric Measurement Techniques, 3(4), 781–811, 2010.

Braziunas, T. F., Fung, I. Y. and Stuiver, M.: The preindustrial atmospheric $^{14}CO_2$ latitudinal gradient as related to exchanges among atmospheric, oceanic, and terrestrial reservoirs, Global Biogeochemical Cycles, 9(4), 565–584, 1995.

Br éon, F. M., Broquet, G., Puygrenier, V., Chevallier, F., Xueref-Remy, I., Ramonet, M., Dieudonn é, E., Lopez, M., Schmidt, M., Perrussel, O. and Ciais, P.: An attempt at estimating Paris area CO_2 emissions from atmospheric concentration measurements, Atmospheric Chemistry and Physics, 15(4), 1707–1724, 2015.

Broquet, G., Chevallier, F., Rayner, P., Aulagnier, C., Pison, I., Ramonet, M., Schmidt, M., Vermeulen, A. T. and Ciais, P.: A European summertime CO_2 biogenic flux inversion at mesoscale from continuous in situ mixing ratio measurements, Journal of Geophysical Research, 116(D23), 2011.

Chevallier, F., Br éon, F.-M. and Rayner, P. J.: Contribution of the Orbiting Carbon Observatory to the estimation of CO_2 sources and sinks: Theoretical study in a variational data assimilation framework, Journal of Geophysical Research, 112(D9), 2007.

Chevallier, F., Feng, L., B ösch, H., Palmer, P. I. and Rayner, P. J.: On the impact of transport model errors for the estimation of CO_2 surface fluxes from GOSAT observations, Geophysical Research Letters, 37(21), 2010.

Chevallier, F., Wang, T., Ciais, P., Maignan, F., Bocquet, M., Altaf Arain, M., Cescatti, A., Chen, J., Dolman, A. J., Law, B. E., Margolis, H. A., Montagnani, L. and Moors, E. J.: What eddy-covariance measurements tell us about prior land flux errors in CO_2-flux inversion schemes, Global Biogeochemical Cycles, 26(1), GB1021, 2012.

Ciais, P., Paris, J. D., Marland, G., Peylin, P., Piao, S. L., Levin, I., Pregger, T., Scholz, Y., Friedrich, R., Rivier, L., Houwelling, S. and Schulze, E. D.: The European carbon balance. Part 1: fossil fuel emissions, Global Change Biology, 16(5), 1395–1408, 2010.

Degens, E. T.: Biogeochemistry of stable carbon isotopes, in Organic geochemistry, pp. 304–329, Springer, 1969.

Engelen, R. J., Denning, A. S. and Gurney, K. R.: On error estimation in atmospheric CO_2 inversions, Journal of Geophysical Research: Atmospheres, 107(D22), 2002.

Farquhar, G. D., Ehleringer, J. R. and Hubick, K. T.: Carbon isotope discrimination and photosynthesis, Annual review of plant biology, 40(1), 503–537, 1989.

Gamnitzer, U., Karstens, U., Kromer, B., Neubert, R. E. M., Meijer, H. A. J., Schroeder, H. and Levin, I.: Carbon monoxide: A quantitative tracer for fossil fuel CO_2?, Journal of Geophysical Research, 111(D22), 2006.

Geels, C., Gloor, M., Ciais, P., Bousquet, P., Peylin, P., Vermeulen, A. T., Dargaville, R., Aalto, T., Brandt, J., Christensen, J. H., Frohn, L. M., Haszpra, L., Karstens, U., R ödenbeck, C., Ramonet, M., Carboni, G. and Santaguida, R.: Comparing atmospheric transport models for future regional inversions over Europe – Part 1: mapping the atmospheric CO_2 signals, Atmos. Chem. Phys., 7(13), 3461–3479, 2007.

Graven, H. D. and Gruber, N.: Continental-scale enrichment of atmospheric $^{14}CO_2$ from the nuclear power industry: potential impact on the estimation of fossil fuel-derived CO2, Atmospheric Chemistry and Physics, 11(23), 12339–12349, 2011.

Graven, H. D.: Impact of fossil fuel emissions on atmospheric radiocarbon and various applications of radiocarbon over this century, PNAS, 112(31), 9542–9545, 2015.

Gregg, J. S., Andres, R. J. and Marland, G.: China: Emissions pattern of the world leader in CO_2 emissions from fossil fuel consumption and cement production, Geophysical Research Letters, 35(8), 2008.

Guan, D., Liu, Z., Geng, Y., Lindner, S. and Hubacek, K.: The gigatonne gap in China's carbon dioxide inventories, Nature Climate Change, 2012.

Gurney, K. R., Baker, D., Rayner, P. and Denning, S.: Interannual variations in continental-scale net carbon exchange and sensitivity to observing networks estimated from atmospheric CO_2 inversions

for the period 1980 to 2005, Global Biogeochemical Cycles, 22(3), GB3025, 2008.

Gurney, K. R., Chen, Y.-H., Maki, T., Kawa, S. R., Andrews, A. and Zhu, Z.: Sensitivity of atmospheric CO_2 inversions to seasonal and interannual variations in fossil fuel emissions, Journal of Geophysical Research , 110(D10), 2005.

Gurney, K. R., Mendoza, D. L., Zhou, Y., Fischer, M. L., Miller, C. C., Geethakumar, S. and Can, S. de la R. du: High resolution fossil fuel combustion CO_2 emission fluxes for the United States, Environmental Science & Technology, 43(14), 5535–5541, 2009.

Hourdin, F., Musat, I., Bony, S., Braconnot, P., Codron, F., Dufresne, J.-L., Fairhead, L., Filiberti, M.-A., Friedlingstein, P., Grandpeix, J.-Y., Krinner, G., LeVan, P., Li, Z.-X. and Lott, F.: The LMDZ4 general circulation model: climate performance and sensitivity to parametrized physics with emphasis on tropical convection, Climate Dynamics, 27(7–8), 787–813, 2006.

Hungershoefer, K., Breon, F. M., Peylin, P., Chevallier, F., Rayner, P., Klonecki, A., Houweling, S. and Marshall, J.: Evaluation of various observing systems for the global monitoring of CO_2 surface fluxes, Atmospheric Chemistry and Physics, 10(21), 10503–10520, 2010.

Kadygrov, N., Broquet, G., Chevallier, F., Rivier, L., Gerbig, C. and Ciais, P.: On the potential of the ICOS atmospheric CO_2 measurement network for estimating the biogenic CO_2 budget of Europe, Atmospheric Chemistry and Physics, 15(22), 12765–12787, 2015.

Kaminski, T., Rayner, P. J., Heimann, M. and Enting, I. G.: On aggregation errors in atmospheric transport inversion, Journal of Geophysical Research, 106, 4703–4715, 2001.

Kanu, A. M., Comfort, L. L., Guilderson, T. P., Cameron-Smith, P. J., Bergmann, D. J., Atlas, E. L., Schauffler, S. and Boering, K. A.: Measurements and modeling of contemporary radiocarbon in the stratosphere, Geophysical Research Letters, 43(3), 2016.

Key, R. M., Kozyr, A., Sabine, C. L., Lee, K., Wanninkhof, R., Bullister, J. L., Feely, R. A., Millero, F. J., Mordy, C. and Peng, T.-H.: A global ocean carbon climatology: Results from Global Data Analysis Project (GLODAP), Global Biogeochemical Cycles, 18(4), 2004.

Kort, E. A., Frankenberg, C., Miller, C. E. and Oda, T.: Space-based observations of megacity carbon dioxide, Geophysical Research Letters, 39(17), L17806, 2012.

Krinner, G., Viovy, N., de Noblet-Ducoudré, N., Ogée, J., Polcher, J., Friedlingstein, P., Ciais, P., Sitch, S. and Prentice, I. C.: A dynamic global vegetation model for studies of the coupled atmosphere-biosphere system, Global Biogeochemical Cycles, 19(1), 2005.

Landschützer, P., Gruber, N., Haumann, F. A., Rödenbeck, C., Bakker, D. C. E., Heuven, S. van, Hoppema, M., Metzl, N., Sweeney, C., Takahashi, T., Tilbrook, B. and Wanninkhof, R.: The reinvigoration of the Southern Ocean carbon sink, Science, 349(6253), 1221–1224, 2015.

Lauvaux, T., Uliasz, M., Sarrat, C., Chevallier, F., Bousquet, P., Lac, C., Davis, K. J., Ciais, P., Denning, A. S. and Rayner, P. J.: Mesoscale inversion: first results from the CERES campaign with synthetic data, Atmospheric Chemistry and Physics, 8, 3459–3471, 2008.

Le Quéré, C., Moriarty, R., Andrew, R. M., Peters, G. P., Ciais, P., Friedlingstein, P., Jones, S. D., Sitch, S., Tans, P., Arneth, A. and others: Global carbon budget 2014, Earth System Science Data, 7(1), 47–85, 2015.

Levin, I. and Kromer, B.: The tropospheric $^{14}CO_2$ level in mid latitudes of the northern hemisphere (1959-2003), Radiocarbon, 46(3), 1261–1271, 2004.

Levin, I., B. Kromer, H. Schoch-Fischer, M. Bruns, M. Münnich, D. Berdau, J.C. Vogel, and K.O. Münnich: $\delta^{14}CO_2$ record from Vermunt. In Trends: A Compendium of Data on Global Change. Carbon Dioxide Information Analysis Center, Oak Ridge National Laboratory, U.S. Department of Energy, Oak Ridge, Tenn., U.S.A., 1994.

Levin, I., Hammer, S., Eichelmann, E. and Vogel, F. R.: Verification of greenhouse gas emission reductions: the prospect of atmospheric monitoring in polluted areas, Philosophical transactions. Series A, Mathematical, physical, and engineering sciences, 369(1943), 1906–24, 2011.

Levin, I., Hammer, S., Kromer, B. and Meinhardt, F.: Radiocarbon observations in atmospheric CO_2: determining fossil fuel CO_2 over Europe using Jungfraujoch observations as background, The Science of the total environment, 391(2–3), 211–6, 2008.

Levin, I., Kromer, B., Schmidt, M. and Sartorius, H.: A novel approach for independent budgeting of fossil fuel CO_2 over Europe by $^{14}CO_2$ observations, Geophysical Research Letters, 30(23), 2003.

Levin, I., Munnich, K. O., Weiss, W.: The effect of anthropogenic CO_2 and ^{14}C sources on the distribution

of 14C in the atmosphere, Radiocarbon, 22, 379–391, 1980.
Liu, Z., Guan, D., Wei, W., Davis, S. J., Ciais, P., Bai, J., Peng, S., Zhang, Q., Hubacek, K., Marland, G., Andres, R. J., Crawford-Brown, D., Lin, J., Zhao, H., Hong, C., Boden, T. A., Feng, K., Peters, G. P., Xi, F., Liu, J., Li, Y., Zhao, Y., Zeng, N. and He, K.: Reduced carbon emission estimates from fossil fuel combustion and cement production in China, Nature, 524(7565), 335–338, 2015.
Macknick, J.: Energy and carbon dioxide emission data uncertainties, IIASA Interim Report IR-09-32. Laxenburg: International Institute for Applied Systems Analysis, 2009.
Maki, T., Ikegami, M., Fujita, T., Hirahara, T., Yamada, K., Mori, K., Takeuchi, A., Tsutsumi, Y., Suda, K. and Conway, T. J.: New technique to analyse global distributions of CO_2 concentrations and fluxes from non-processed observational data, Tellus B, 62(5), 797–809, 2010.
Manning, M.R., and W.H. Melhuish. 1994. Atmospheric $\delta^{14}C$ record from Wellington. In Trends: A Compendium of Data on Global Change. Carbon Dioxide Information Analysis Center, Oak Ridge National Laboratory, U.S. Department of Energy, Oak Ridge, Tenn., U.S.A.
Marland, G., Hamal, K. and Jonas, M.: How Uncertain Are Estimates of CO_2 Emissions?, Journal of Industrial Ecology, 13(1), 4–7, 2009.
Marland, G.: Uncertainties in Accounting for CO_2 From Fossil Fuels, Journal of Industrial Ecology, 12(2), 136–139, 2008.
Marquis, M. and Tans, P.: Carbon Crucible, Science, 320(5875), 460–461, 2008.
Masarik, J. and Beer, J.: An updated simulation of particle fluxes and cosmogenic nuclide production in the Earth's atmosphere, Journal of Geophysical Research, 114(D11), D11103, 2009.
Masarik, J. and Beer, J.: Simulation of particle fluxes and cosmogenic nuclide production in the Earth's atmosphere, Journal of Geophysical Research, 104(D10), 12099, 1999.
Meijer, H.A.J, M.H. Pertuisot, and J. van der Plicht: High-accuracy ^{14}C measurements for atmospheric CO_2 samples from the South Pole and Point Barrow, Alaska, by Accelerator Mass Spectrometry [Radiocarbon 48(3)355-372]. Carbon Dioxide Information Analysis Center, Oak Ridge National Laboratory, U.S. Department of Energy, Oak Ridge, Tenn., U.S.A., 2006
Mook, W. and Rozanski, K.: Environmental isotopes in the hydrological cycle, 2000.
Mook, W. G., Bommerson, J. C. and Staverman, W. H.: Carbon isotope fractionation between dissolved bicarbonate and gaseous carbon dioxide, Earth and Planetary Science Letters, 22(2), 169–176, doi:10.1016/0012-821X(74)90078-8, 1974.
Naegler, T. and Levin, I.: Biosphere-atmosphere gross carbon exchange flux and the $\delta^{13}CO_2$ and $\Delta^{14}CO_2$ disequilibria constrained by the biospheric excess radiocarbon inventory, Journal of Geophysical Research, 114(D17), doi:10.1029/2008jd011116, 2009.
Naegler, T. and Levin, I.: Closing the global radiocarbon budget 1945–2005, Journal of Geophysical Research, 111(D12), 2006.
Nakada, A., Miyauchi, T., Akiyama, K., Momose, T., Kozawa, T., Yokota, T. and Ohtomo, H.: Radioactive airborne effluent discharged from Tokai reprocessing plant. 1998-2007, Japan Atomic Energy Agency, Tokai, Ibaraki (Japan), 2008.
Nakamura, T., Nakazawa, T., Honda, H., Kitagawa, H., Machida, T., Ikeda, A. and Matsumoto, E.: Seasonal variations in ^{14}C concentrations of stratospheric CO_2 measured with accelerator mass spectrometry, Nuclear Instruments and Methods in Physics Research Section B: Beam Interactions with Materials and Atoms, 92(1–4), 413–416, 1994.
Nakamura, T., Nakazawa, T., Nakai, N., Kitagawa, H., Honda, H., Itoh, T., Machida, T. and Matsumoto, E.: Measurement of ^{14}C Concentrations of Stratospheric CO_2 by Accelerator Mass Spectrometry, Radiocarbon, 34(3), 745–752, 1992.
Nydal, R. and Lövseth, K.: Corbon-14 Measurements in Atmospheric CO_2 from Northern and Southern Hemisphere Sites, 1962-1993. 1996
O'Brien, D. M., Polonsky, I. N., Utembe, S. R. and Rayner, P. J.: Remote sensing CO_2, CH_4 and CO emissions in a polluted urban environment, Atmospheric Measurement Techniques Discussions, 1–49, 2016.
Oda, T. and Maksyutov, S.: A very high-resolution (1 km ×1 km) global fossil fuel CO_2 emission inventory derived using a point source database and satellite observations of nighttime lights, Atmospheric Chemistry and Physics, 11(2), 543–556, 2011.
Peters, W., Jacobson, A. R., Sweeney, C., Andrews, A. E., Conway, T. J., Masarie, K., Miller, J. B.,

Bruhwiler, L. M., Petron, G., Hirsch, A. I., Worthy, D. E., van der Werf, G. R., Randerson, J. T., Wennberg, P. O., Krol, M. C. and Tans, P. P.: An atmospheric perspective on North American carbon dioxide exchange: CarbonTracker, Proceedings of the National Academy of Sciences of the United States of America, 104(48), 18925–30, 2007.

Peters, W., Krol, M. C., Van Der Werf, G. R., Houweling, S., Jones, C. D., Hughes, J., Schaefer, K., Masarie, K. A., Jacobson, A. R., Miller, J. B. and others: Seven years of recent European net terrestrial carbon dioxide exchange constrained by atmospheric observations, Global Change Biology, 16(4), 1317–1337, 2010.

Peylin, P., Law, R. M., Gurney, K. R., Chevallier, F., Jacobson, A. R., Maki, T., Niwa, Y., Patra, P. K., Peters, W., Rayner, P. J., Rödenbeck, C., van der Laan-Luijkx, I. T. and Zhang, X.: Global atmospheric carbon budget: results from an ensemble of atmospheric CO2 inversions, Biogeosciences, 10, 6699–6720, 2013.

Peylin, P., Rayner, P. J., Bousquet, P., Carouge, C., Hourdin, F., Heinrich, P., Ciais, P. and contributors, A.: Daily CO_2 flux estimates over Europe from continuous atmospheric measurements: 1, inverse methodology, Atmospheric Chemistry and Physics, 5, 3173–3186, 2005.

Piao, S., Fang, J., Ciais, P., Peylin, P., Huang, Y., Sitch, S. and Wang, T.: The carbon balance of terrestrial ecosystems in China, Nature, 458(7241), 1009–1013, 2009.

Pregger, T., Scholz, Y. and Friedrich, R.: Documentation of the anthropogenic GHG emission data for Europe provided in the Frame of CarboEurope GHG and CarboEurope IP, Institut für Energiewirtschaft und Rationelle Energieanwendung, Universität Stuttgart, Stuttgart, Germany, 2007.

Randerson, J. T., Enting, I. G., Schuur, E. A. G., Caldeira, K. and Fung, I. Y.: Seasonal and latitudinal variability of troposphere $\Delta^{14}CO_2$: Post bomb contributions from fossil fuels, oceans, the stratosphere, and the terrestrial biosphere, Global Biogeochemical Cycles, 16(4), 59-1-59–19, 2002.

Ray, J., Yadav, V., Michalak, A., van Bloemen Waanders, B. and Mckenna, S. A.: A multiresolution spatial parameterization for the estimation of fossil-fuel carbon dioxide emissions via atmospheric inversions, Geoscientific Model Development, 7(5), 1901–1918, 2014.

Rayner, P., Enting, I., Francey, R. and Langenfelds, R.: Reconstructing the recent carbon cycle from atmospheric CO_2, $\delta^{13}C$ and O_2/N_2 observations, Tellus B, 51(2), 213–232, 1999.

Rayner, P. J., Law, R. M., Allison, C. E., Francey, R. J., Trudinger, C. M. and Pickett-Heaps, C.: Interannual variability of the global carbon cycle (1992-2005) inferred by inversion of atmospheric CO_2 and $\delta^{13}CO_2$ measurements, Global Biogeochemical Cycles, 22(3), 2008.

Rayner, P. J., Raupach, M. R., Paget, M., Peylin, P. and Koffi, E.: A new global gridded data set of CO_2 emissions from fossil fuel combustion: Methodology and evaluation, Journal of Geophysical Research, 115, 2010.

Rivier, L., Ciais, P., Hauglustaine, D. A., Bakwin, P., Bousquet, P., Peylin, P. and Klonecki, A.: Evaluation of SF_6, C_2Cl_4, and CO to approximate fossil fuel CO_2 in the Northern Hemisphere using a chemistry transport model, Journal of Geophysical Research, 111(D16), 2006.

Rödenbeck, C., Houweling, S., Gloor, M. and Heimann, M.: CO 2 flux history 1982–2001 inferred from atmospheric data using a global inversion of atmospheric transport, Atmospheric Chemistry and Physics, 3(6), 1919–1964, 2003.

Shiga, Y. P., Michalak, A. M., Gourdji, S. M., Mueller, K. L. and Yadav, V.: Detecting fossil fuel emissions patterns from subcontinental regions using North American in situ CO_2 measurements, Geophysical Research Letters, 41(12), 4381–4388, 2014.

Siegenthaler, U. and Oeschger, H.: Biospheric CO_2 emissions during the past 200 years reconstructed by deconvolution of ice core data, Tellus B, 39(1–2), 1987.

Silva, S. J., Arellano, A. F. and Worden, H. M.: Toward anthropogenic combustion emission constraints from space-based analysis of urban CO_2/CO sensitivity, Geophysical Research Letters, 2013.

Sitch, S., Friedlingstein, P., Gruber, N., Jones, S. D., Murray-Tortarolo, G., Ahlström, A., Doney, S. C., Graven, H., Heinze, C., Huntingford, C. and others: Recent trends and drivers of regional sources and sinks of carbon dioxide, Biogeosciences, 12(3), 653–679, 2015.

Stricht, S. V. der and Janssens, A.: Radioactive effluents from nuclear power stations and nuclear fuel reprocessing sites in the European Union, 2004-08, Luxembourg, 2010.

Stuiver, M. and Polach, H. A.: Discussion: reporting of C-14 data, Radiocarbon, 19(3), 355–363, 1977.

Takahashi, T., Sutherland, S. C., Chipman, D. W., Goddard, J. G., Ho, C., Newberger, T., Sweeney, C. and

Munro, D. R.: Climatological distributions of pH, pCO_2, total CO_2, alkalinity, and $CaCO_3$ saturation in the global surface ocean, and temporal changes at selected locations, Marine Chemistry, 164, 95–125, 2014.

Tarantola, A.: Inverse problem theory and methods for model parameter estimation, siam., 2005.

Thoning, K. W., Tans, P. P., Komhyr, W. D. and others: Atmospheric carbon dioxide at Mauna Loa Observatory: 2. Analysis of the NOAA GMCC data, 1974–1985, Journal of Geophysical Research, 94(6), 8549–8565, 1989.

Turnbull, J. C., Keller, E. D., Baisden, T., Brailsford, G., Bromley, T., Norris, M. and Zondervan, A.: Atmospheric measurement of point source fossil CO_2 emissions, Atmospheric Chemistry and Physics, 14(10), 5001–5014, 2014.

Turnbull, J. C., Keller, E. D., Norris, M. W. and Wiltshire, R. M.: Independent evaluation of point source fossil fuel CO2 emissions to better than 10%, Proceedings of the National Academy of Sciences, 113(37), 10287–10291, 2016.

Turnbull, J., Rayner, P., Miller, J., Naegler, T., Ciais, P. and Cozic, A.: On the use of $^{14}CO_2$ as a tracer for fossil fuel CO2: Quantifying uncertainties using an atmospheric transport model, Journal of Geophysical Research, 114(D22), 2009.

United Nations Scientific Committee on the Effects of Atomic Radiation (UNSCEAR): Sources and effects of ionizing radiation: sources, United Nations Publications, 2000.

Vogel, F. R., Hammer, S., Steinhof, A., Kromer, B. and Levin, I.: Implication of weekly and diurnal 14C calibration on hourly estimates of CO-based fossil fuel CO_2 at a moderately polluted site in southwestern Germany, Tellus B, 62(5), 512–520, 2010.

Vogel, F. R., Levin, I. and Worthy, D.: Implications for deriving regional fossil fuel CO_2 estimates from atmospheric observations in a hot spot of nuclear power plant $^{14}CO_2$ emissions, Radiocarbon, 55(2), 1556–1572, 2013.

Wang, R., Tao, S., Ciais, P., Shen, H. Z., Huang, Y., Chen, H., Shen, G. F., Wang, B., Li, W., Zhang, Y. Y., Lu, Y., Zhu, D., Chen, Y. C., Liu, X. P., Wang, W. T., Wang, X. L., Liu, W. X., Li, B. G. and Piao, S. L.: High-resolution mapping of combustion processes and implications for CO_2 emissions, Atmospheric Chemistry and Physics, 13(10), 5189–5203, 2013.

Wang, Y., Broquet, G., Ciais, P., Chevallier, F., Vogel, F., Kadygrov, N., Wu, L., Yin, Y., Wang, R., Tao, S.: Estimation of observation errors for large scale atmospheric inversion of CO2 emissions from fossil fuel combustion, submitted to Tellus B (in review).

Zhang, X., Gurney, K. R., Rayner, P., Liu, Y. and Asefi-Najafabady, S.: Sensitivity of simulated CO_2 concentration to regridding of global fossil fuel CO_2 emissions, Geoscientific Model Development, 7(6), 2867–2874, 2014.

Zhu, D., Peng, S. S., Ciais, P., Viovy, N., Druel, A., Kageyama, M., Krinner, G., Peylin, P., Ottlé, C., Piao, S. L., Poulter, B., Schepaschenko, D. and Shvidenko, A.: Improving the dynamics of Northern Hemisphere high-latitude vegetation in the ORCHIDEE ecosystem model, Geoscientific Model Development, 8(7), 2263–2283, 2015.

Supplementary

Supplement S1

Here, we use the values assumed in Vogel et al. (2013, supplement) for the background air and terrestrial biosphere: C_{bg}=380 ppm, δ^{13}_{bg}=−8‰, Δ^{14}_{bg}=50‰, δ^{13}_{bio}=δ^{13}_{FF}=−25‰, δ^{14}_{bio}=Δ^{14}_{bio}=95‰.

We follow the calculation of Vogel et al. (2013, supplement) and the bias due to the mass balance in terms of Δ^{14} is only about 0.3 ppm for a typical C_{FF}=10 ppm. However, when C_{FF} reaches 30 ppm in a non-diffusive synoptic event (exemplified by Heidelberg in Germany during winter, Peylin et al, 2011), this bias amounts to 1 ppm (Fig. S1). This 1 ppm bias in $FFCO_2$ is close to the error caused by the uncertainties (~3‰) in the chemical analysis of air samples and the uncertainties in the conversion of $^{14}CO_2$ and CO_2 measurements into $FFCO_2$ (Levin et al., 2003; Vogel et al., 2010; Turnbull et al., 2014). Meanwhile, assuming C_{FF}=30 ppm and a 10% uncertainty in the emission inventories, the projected uncertainties in the concentration field is 30×10%=3 ppm. Thus the 1 ppm bias due to the use of Δ^{14} is comparable to the uncertainty in the fossil fuel emission inventories and is not negligible for heavy polluted areas.

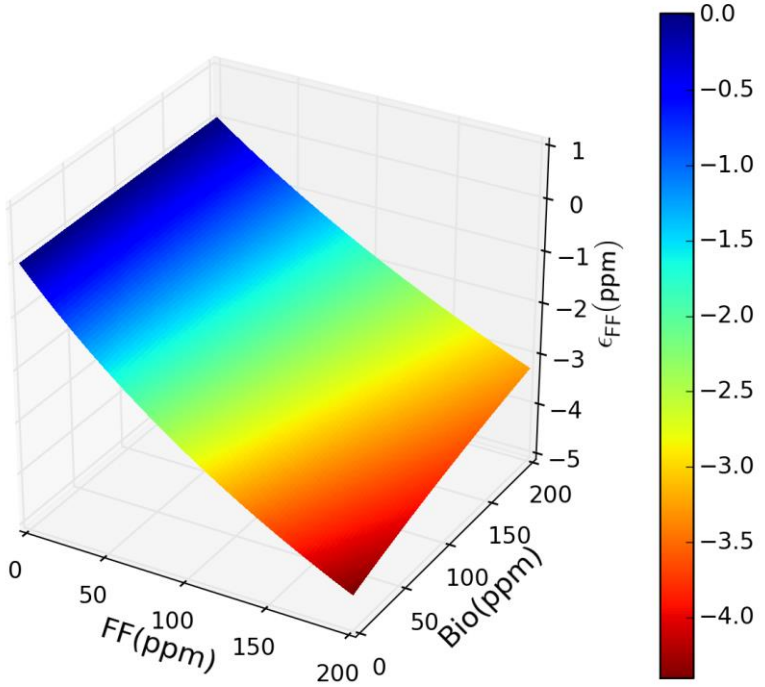

Figure S1 The bias of calculated $FFCO_2$ using $\Delta^{14}CO_2$ as a function of actual CO_2 contribution from fossil fuel (FF) emissions and terrestrial biosphere (Bio); unit: ppm

Supplement S2 Contribution of the different fluxes on the atmospheric $^{14}CO_2$ mixing ratios and gradients

To verify our estimation of the $^{14}CO_2$ fluxes are realistic enough, we first present model results for the individual processes. We then compare our combined model time series with other studies and with the actual observations from radiocarbon stations.

S2.1 Fossil fuels

Atmospheric fossil fuel CO_2 plumes through the transport created significantly depleted annual mean and large seasonal amplitudes (trough-to-peak) of $\delta^{14}C$ values in the atmospheric CO_2 over the east coast of Asia, Europe and the east coast of North America (Fig. S2 a). Globally, the minimum of annual mean $\delta^{14}C$ (-43‰ relative to the South Pole) contributed by the combustion of fossil fuel occurred over China, the largest emitter of $FFCO_2$. However, despite relatively large fossil fuel emissions from the west coast of North

America, there is not evidently large plume over western North America in our simulation. In addition, the hemispheric distribution of the fossil fuel emissions caused the large negative north-south gradients of the $\delta^{14}C$ depletion. The $\delta^{14}C$ seasonal amplitude due to $FFCO_2$ have a very close pattern with the annual mean. The large seasonal amplitudes are generated over the east coast of Asia, Europe and the east coast of North America (Fig. S2 b), reaching a maximum over China at 46‰. And the seasonal cycle also show a north-south differences of ~10‰.

In general, our results are similar to those simulated by Goddard Institute for Space Studies (GISS) atmospheric transport model and the fossil fuel emission estimates in the year 2000 (Randerson et al., 2002). The signals in our simulations are much larger than those of Randerson et al., 2002. The discrepancies are mainly due to the fact that the spatial resolution of LMDZv4 (3.75°×2.5°, longitude×latitude; vertically, the lowest model level extends from the surface to ~150m) are much higher than the GISS model (10°×8°, longitude×latitude; vertically, the lowest model level extends from the surface to ~400m), and due to the fast increase of fossil fuel emissions from 2000 to 2007, especially in China.

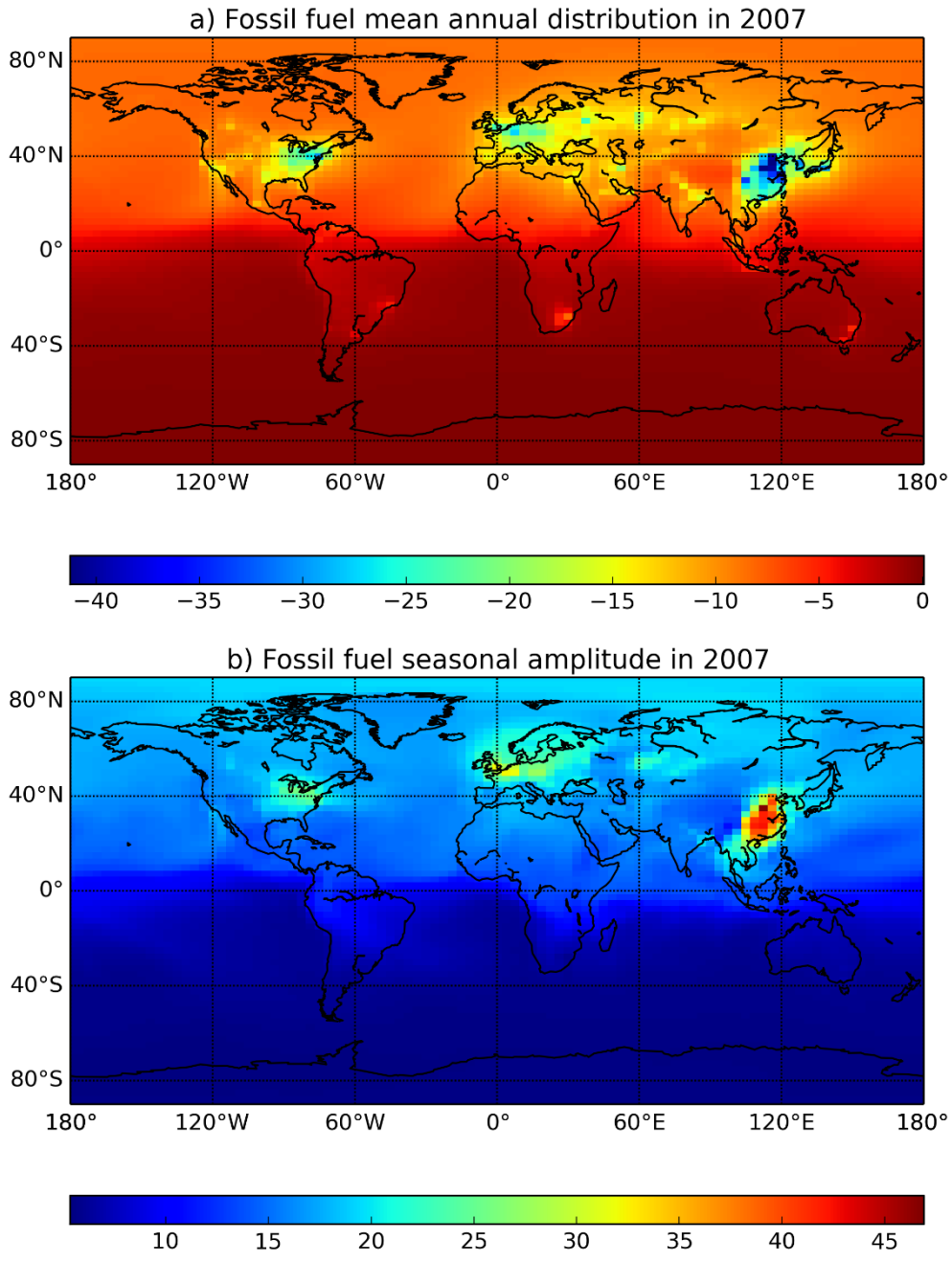

Figure S2 The contribution of fossil fuel emission in 2007 to a) the annual mean atmospheric $\delta^{14}C$ (relative to the South Pole) and b) the seasonal amplitude of atmospheric $\delta^{14}C$ at the surface level of LMDZv4; unit: ‰

S2.2 Terrestrial Biosphere

The modeled effect of terrestrial ecosystem fluxes on the annual mean $\delta^{14}C$ is greatest over Siberia, North America, East Asia and the tropics (Fig. S3). In the year 2007, terrestrial

biosphere fluxes caused a north-south atmospheric gradient of ~7‰, primarily due to the respiration from northern ecosystems was enriched of ^{14}C compared to the atmosphere and the fractionation of ^{14}C during photosynthesis. The seasonal amplitude of the atmospheric $\delta^{14}C$ value from the terrestrial biosphere fluxes is the largest over Siberia (~11‰), while it is intermediate over North America, East Asia and the tropical region (~7‰).

Compared with the results of Randerson et al. (2002), our simulation shows a larger domain of significant positive effect on annual mean $\delta^{14}C$ over the tropical region. However, the results of the simulations are largely model-dependent. Due to the fact that the vegetation models and the transport models used in the study of Randerson et al. (2002) and in our study are different in many aspects, e.g. the residence time of carbon in the terrestrial ecosystem, the discrepancies between Randerson et al. (2002) and our study indicate a large uncertainty in the estimate of the effect of terrestrial biosphere fluxes on the annual mean atmospheric $\delta^{14}C$ value. Nevertheless, the two simulations show comparable results over Europe, Siberia, North America and East Asia, which are the main target region of our study, and thus will not impair the conclusion of our study over these regions.

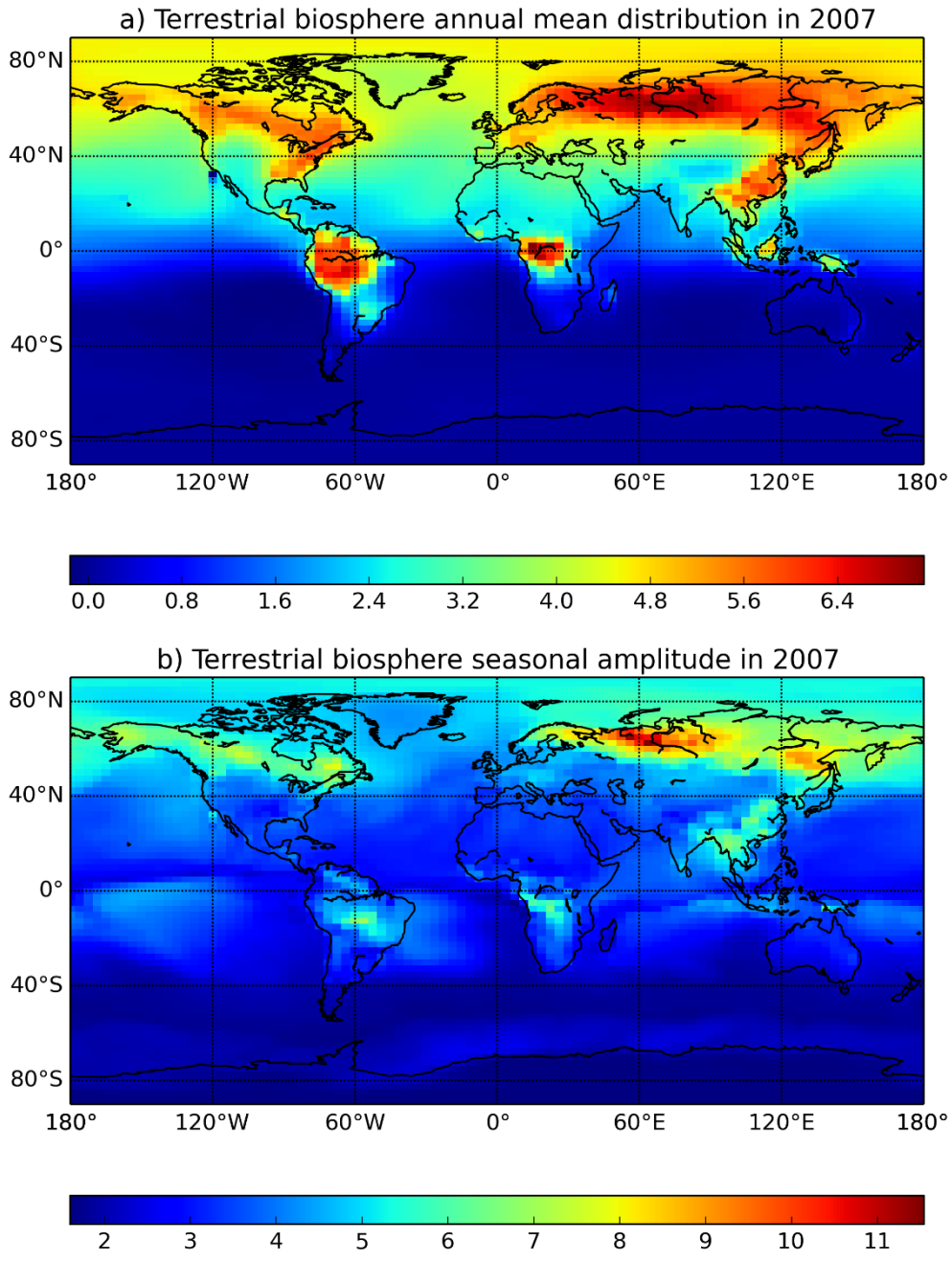

Figure S3 The contribution of terrestrial biosphere fluxes in 2007 to a) the annual mean atmospheric $\delta^{14}C$ (relative to the South Pole) and b) the seasonal amplitude of atmospheric $\delta^{14}C$ at the surface level of LMDZv4; unit: ‰

S2.3 Ocean

The annual mean pattern of atmospheric $\delta^{14}C$ arising from exchange fluxes between ocean and the atmosphere were relatively uniform over equatorial regions and the Northern

Hemisphere (Fig. S4). The effect of the ocean fluxes on the annual mean atmospheric $\delta^{14}C$ is about 4‰ relative to the South Pole. In contrast, due to the short residence time and thus low $\delta^{14}C$ in the surface water of the Southern Ocean (Key et al., 2004), a negative $\delta^{14}C$ contribution to the atmosphere are simulated in this region. The seasonal amplitude of the atmospheric $\delta^{14}C$ from ocean fluxes show a minimum of 1‰ north of the equator. In the southern Hemisphere, the seasonal cycle are rather smooth, while in the high latitude of northern Hemisphere, there is evident land/sea contrast driven by the wind directions in different seasons.

Our simulation of the effect of ocean fluxes on the annual mean and seasonal amplitudes of atmospheric $\delta^{14}C$ are consistent with those of Randerson et al. (2002) in the large scale north-south gradients. Discrepancies exist between the regional patterns, mainly due to the different transport models used.

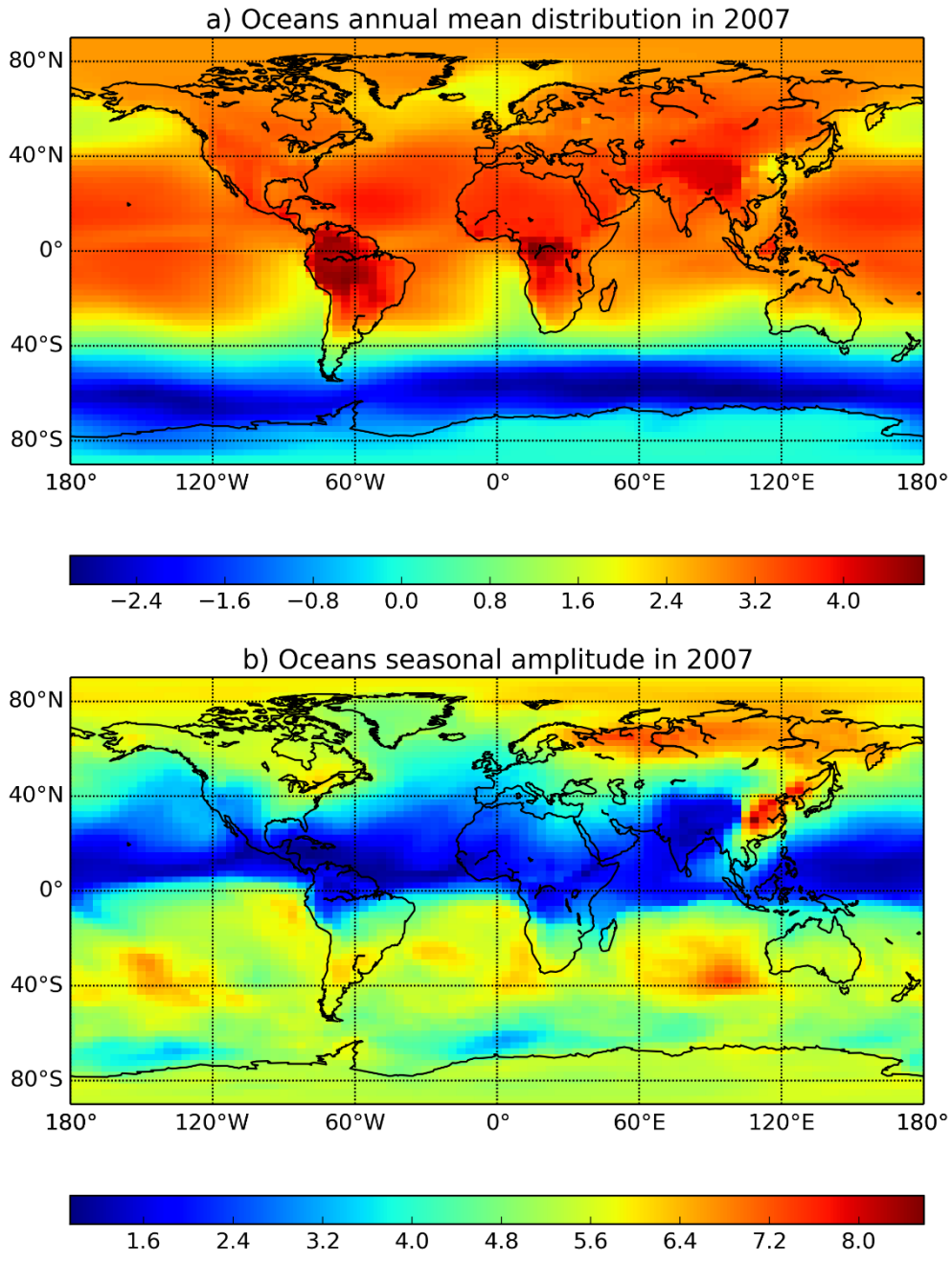

Figure S4 The contribution of ocean fluxes in 2007 to a) the annual mean atmospheric $\delta^{14}C$ (relative to the South Pole) and b) the seasonal amplitude of atmospheric $\delta^{14}C$ at the surface level of LMDZv4; unit: ‰

S2.4 Cosmogenic production

The effect of cosmogenic production of radiocarbon on the surface atmospheric ^{14}C value have clear latitudinal distribution, both for the annual mean and for the seasonal

amplitude (Fig. S5). The largest annual mean atmospheric ^{14}C arising from cosmogenic production is over the mid-latitude regions in both hemispheres, while the effect along the equator is rather small. This feature is a result of the large scale atmospheric circulation, i.e. the Hadley cell. On the other hand, with symmetric cosmogenic production across both hemispheres, our model generated no north-south gradient in the production of radiocarbon. However, smaller troposphere-stratosphere exchange in the southern Hemisphere generated a lower annual mean contribution of the stratospheric radiocarbon to the surface $\delta^{14}C$ than in the northern Hemisphere (Randerson et al., 2002). On the contrary, the seasonal amplitude of surface atmospheric ^{14}C due to cosmogenic production in the southern Hemisphere is slightly larger than in the northern Hemisphere.

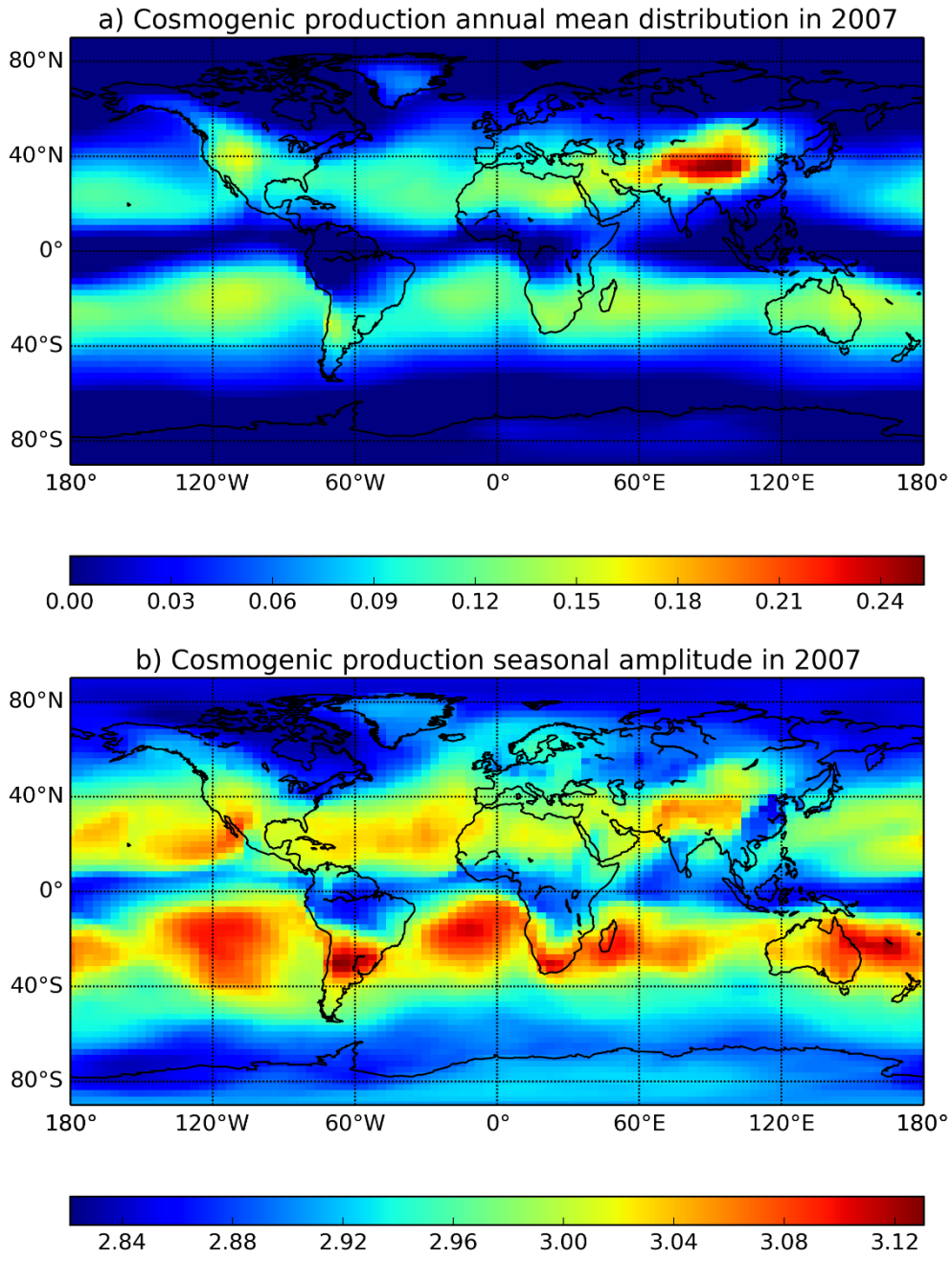

Figure S5 The contribution of cosmogenic production in 2007 to a) the annual mean atmospheric $\delta^{14}C$ (relative to the South Pole) and b) the seasonal amplitude of atmospheric $\delta^{14}C$ at the surface level of LMDZv4; unit: ‰

S2.5 Nuclear facilities

The nuclear facilities caused increased atmospheric $\delta^{14}C$ values, but their influences are usually restricted to the vicinity of the sources (Fig. S6). For example, the spent fuel

reprocessing plant in La Hague (France), Sellafield and gas-cooled nuclear reactors in the UK generate pronounced enrichment (>5‰) of atmospheric $\delta^{14}C$ over only northwest France and UK. Over other parts of European continents, the influence from nuclear facilities are very small. Over North America, substantial influence of nuclear facilities on the atmospheric $\delta^{14}C$ occurred around the Great Lakes region, while the influence over East Asia are much smaller and are mainly centered over central Japan and South Korea. However, our modelled influence (2.0‰) is half as large as the estimate of local influence from the nuclear power plant in Philippsburg at Heidelberg (4.8±2.0‰, Levin et al., 2003). Similar to the simulation of TM3 atmospheric transport model (Graven and Gruber, 2011), this is mainly due to coarse resolution of the transport model LMDZv4 that underestimate the influence from the local sources.

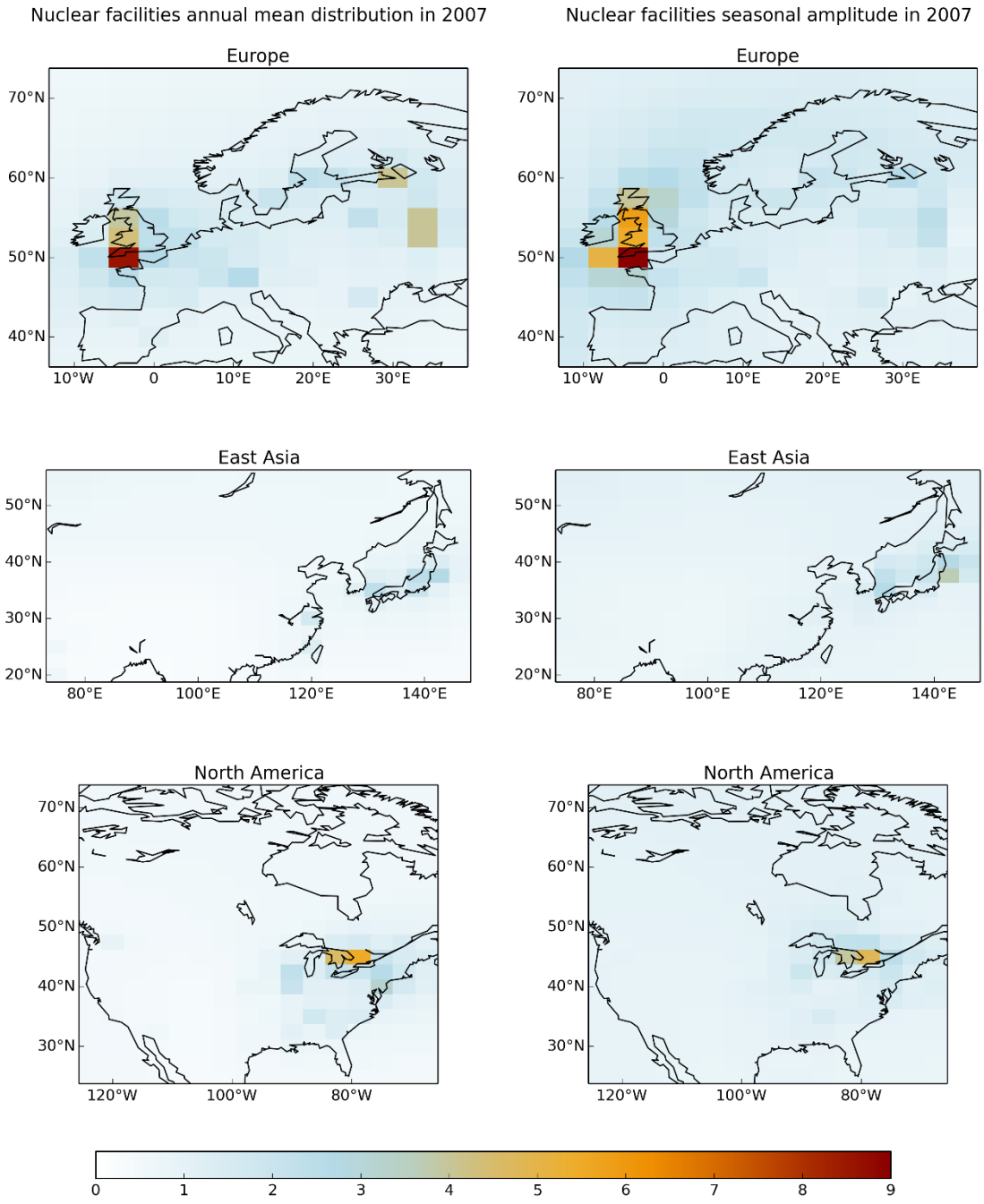

Figure S6 The contribution of nuclear facilities in 2007 to the annual mean atmospheric $\delta^{14}C$ (left panel) and the seasonal amplitude of atmospheric $\delta^{14}C$ (right panel) at the surface level of LMDZv4 over Europe, East Asia and North America; unit: ‰

S2.5 Combined effects and comparison with actual observations

To evaluate the reality of our model in simulating the evolution of the atmospheric $\delta^{14}C$, in this section, we combine all the fluxes mentioned above and run an 18 year simulation from 1990 to 2007. After an 8 year "spin-up" period to build up enough ^{14}C and to reach equilibrium conditions in the stratosphere, we obtained model results for 1998-2007 and we compare our modelled time series of monthly mean atmospheric $\delta^{14}C$ with actual observations during this period from an extensive set of stations. The set of observational sites (summarized in Table S1) includes a global network (Scripps CO_2 Program) span from high latitude in the northern Hemisphere to the South Pole (Graven, 2008), which enable the evaluation of the modelled north-south gradients of atmospheric $\delta^{14}C$. Observations from two high-altitude sites representative of the free troposphere at continental scale, Niwot Ridge (North America) and Jungfraujoch (Europe), are also included in the comparison. In addition, several European regional surface stations with medium or strong local influences are considered as well. So this comparison has a comprehensive coverage of stations in different latitudinal bands and in different pollution levels.

The results are shown in Fig. S7. Our simulations capture reasonably well the seasonal cycle and the globally decreasing trends of atmospheric $\delta^{14}C$ for most sites. More specific, our simulation shows a good agreement between the modelled atmospheric $\delta^{14}C$ and the actual observations at stations far away from the local effects , e.g. Scripps CO_2 stations and the two free troposphere stations. At stations with medium influences from local emissions, e.g. Schauinsland and Košetice, the modelled atmospheric $\delta^{14}C$ values are also close to the observations in both annual trends and seasonal amplitude. However, at stations in the vicinity of heavy anthropogenic emissions, our simulation tend to underestimate the seasonal amplitude of the atmospheric $\delta^{14}C$ values in winter, but the decreasing trends are well captured. Due to the coarse resolution of the transport model, our simulation is likely unable to adequately resolve the strong local influences on the atmospheric $\delta^{14}C$.

The spatial distribution of the effect of our model fluxes shown in previous sections and the modelled time series of atmospheric $\delta^{14}C$ at the comprehensive network of stations

suggest that our model fluxes are realistic, allowing us to use the model to further explore the potential of the atmospheric inversion to constrain the corresponding carbon fluxes by using atmospheric $\delta^{14}C$ data.

Table S1 The observational sites used in this study and the sources of the data

Sites	Latitude	Longitude	Time period	Reference	Source
La Jolla	32.87 °N	117.25 °W	1998-2006	Graven, 2008	fitted monthly value[a]
Barrow	71.38 °N	156.47 °W	1999-2006		
Mauna Loa	19.53 °N	155.58 °W	2001-2006		
Samoa	14.25 °S	170.57 °W	2001-2006		
Palmer	64.92 °S	64.00 °W	2005-2006		
South Pole	89.98 °S	24.80 °W	1999-2006		
Niwot Ridge	40.05 °N	105.59 °W	2003-2007	Turnbull et al., 2008[e]	published data
Baring Head	41.41 °S	174.87 °E	1998-2007	Currie et al., 2011	fitted monthly mean value[b]
Jungfraujoch	46°33′N	7°59′E	1998-2007	Levin and Kromer, 2004	published data
Schauinsland	47°55′N	7°54′E	1998-2007	Levin et al., 2013	
Heidelberg	49°25′N	8°41′N	1998-2007	Levin et al., 2011	digitalized[c]
Prague-Bulovka	50°07′N	14°27′E	2001-2007	Svetlik et al., 2010	digitalized[d]
Košetice	49°35′N	15°05′E	2004-2007		
Slovakia	48°09′N	17°07′E	2000-2007		
Hungary	46°47′N	18°57′E	2000-2007		

[a] Monthly values of $\Delta^{14}C$ were determined by fitting the event observations to the function: $y = a + bt + c\cos(2\pi t) + d\sin(2\pi t) + s(t)$. The fitted function was evaluated at the middle of each month to produce the monthly values. This evaluation has been done in Graven, 2008.

[b] Daily values of $\Delta^{14}C$ are fitted and interpolated using the method of Thoning et al. (1989). Daily values within each month are averaged to produce the monthly values.

[c] Digitalized from Fig. 3a in Levin et al., 2011

[d] Digitalized from Fig. 2 in Svetlik et al., 2010

[e] available at http://www.esrl.noaa.gov/gmd/

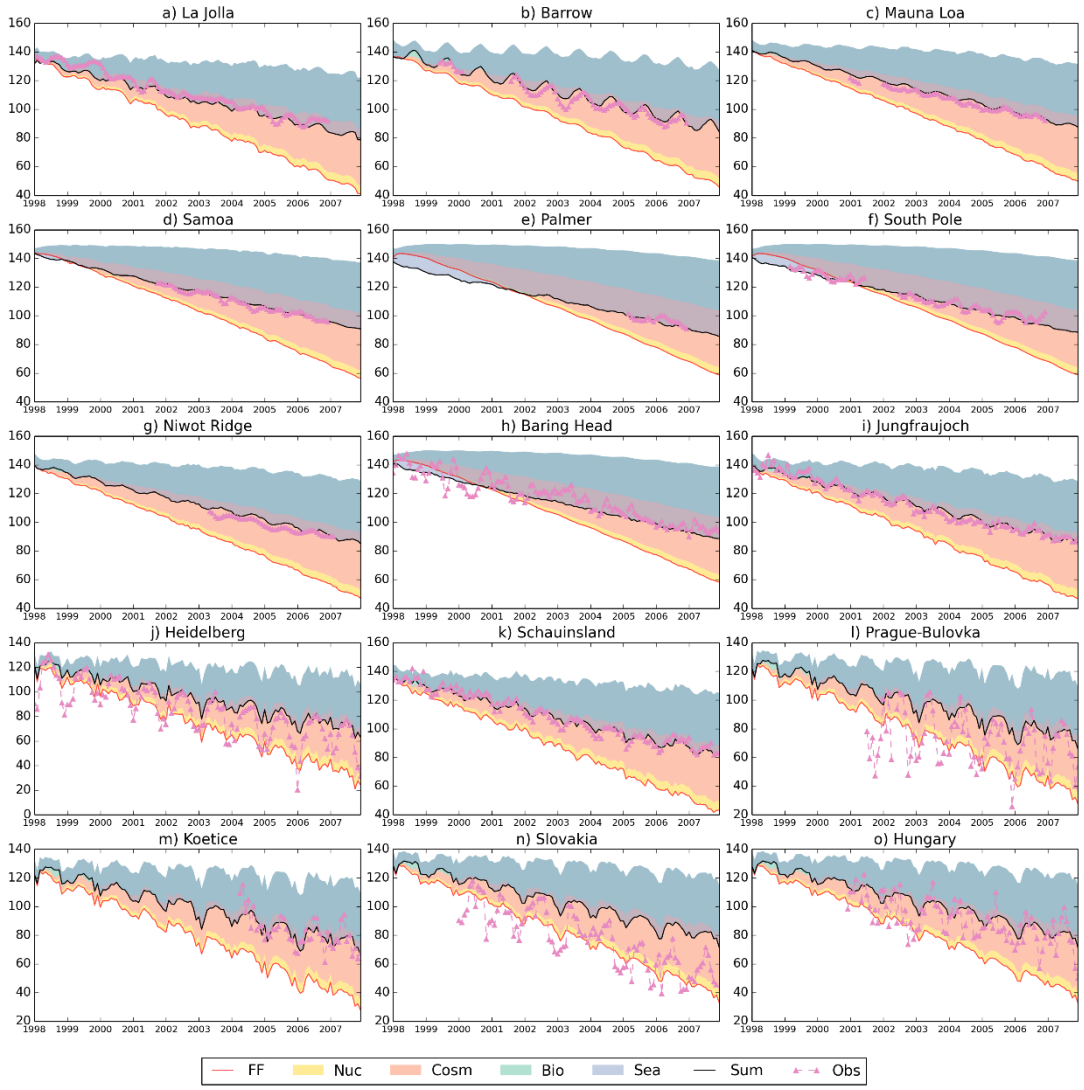

Figure S7 The contribution of different components to the monthly mean atmospheric $\delta^{14}C$ and comparison between observed and modelled monthly mean atmospheric $\delta^{14}C$ at fifteen observational sites. unit: ‰. A -8‰ for atmospheric $\delta^{13}C$ is assumed for sites where no $\delta^{13}C$ value is reported to convert the $\Delta^{14}C$ value into $\delta^{14}C$ value.

In Fig. S7, the contribution of different CO_2 components to the atmospheric $\delta^{14}C$ values at the observational stations are also displayed. In most stations, the largest signals due to the fossil fuel emissions are partly offset by fluxes from nuclear facilities, cosmogenic productions and terrestrial biosphere. The ocean fluxes also caused a depletion of the atmospheric $\delta^{14}C$ globally, through the fractionation in the exchange between ocean surface water and the atmosphere (Mook and Rozanski, 2000). For stations in the northern Hemisphere, the depletion of atmospheric $\delta^{14}C$ from the ocean flux and the enrichment of

atmospheric $\delta^{14}C$ from the disequilibrium flux from biosphere are close to each other, while in the southern Hemisphere, the depletion of atmospheric $\delta^{14}C$ from the ocean flux is more significant, especially at high-latitude stations, e.g. Palmer and South Pole. This phenomenon is consistent with the global pattern of the effect due to ocean flux shown in Fig. S4.

The ^{14}C from cosmogenic production is a large contributor of the low-altitude atmospheric $\delta^{14}C$, as shown in Fig. S5 and S7. In addition, the estimates of the cosmogenic production of ^{14}C are highly uncertain, ranging from 1.8×10^{26} atoms yr^{-1} (Kanu et al., 2016) to 4.0×10^{26} atoms yr^{-1} (Lingenfelter et al., 1963). To evaluate the reality of our simulation of the cosmogenic production of ^{14}C and the troposphere-stratosphere exchange, we compare our modelled $\delta^{14}C$ values with the measurements collected by high-altitude balloon flights over Japan in early 1990s (Nakamura et al., 1992, 1994) and over North America (Kanu et al., 2016) in early 2000s. Fig. S8 shows that our modelled vertical profile of atmospheric $\delta^{14}C$ agrees fairly well with the very few stratospheric $\delta^{14}CO_2$ observations and adequate ^{14}C has been built up in the atmosphere.

Our simulations shows that the $\delta^{14}C$ values increase with increasing altitude, as expected for a long-lived tracer with a stratospheric source and a tropospheric sink. This general pattern agrees with the simulation by another global chemical-transport model IMPACT (Integrated Massively Parallel Atmospheric Chemical Transport, Kanu et al., 2016). However, some small patterns of the vertical distribution during single flight, for example, the higher $\delta^{14}C$ values near 50 mbar over Fort Sumner in 2003 (Fig. S8 a), cannot be captured by our simulations.

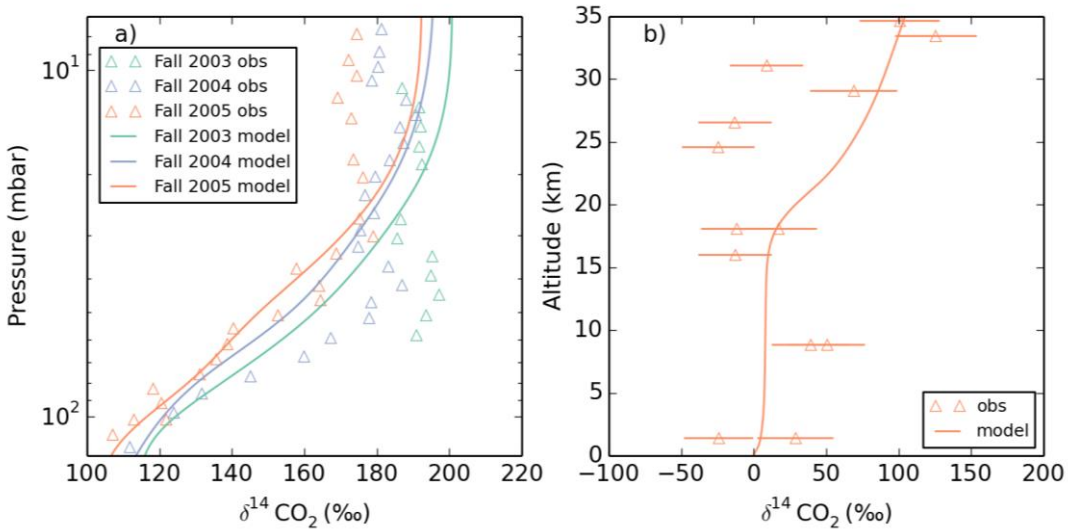

Figure S8 a) $\delta^{14}C$ values versus pressure (mbar) for the model results (solid lines) and samples collected from the 34 ℃N over Fort Sumner, NM (triangles) for single flights in 2003–2005. b) $\delta^{14}C$ gradients between the high altitude and the surface for the model results (solid line) and samples collected over Sanriku (39.2 ℃N, 141.8 ℃E), Japan.

Supplement S3 Covariance between uncertainties in CO_2 data and $^{14}CO_2$ data

In OSSE COMB-All, for example, we assimilate daily CO_2 data and 2-week $^{14}CO_2$ data simultaneously. In this OSSE, the 2-week $^{14}CO_2$ data also depend on the daily CO_2 measurements, i.e. C_a is calculated as the mean of 14 daily sampling. So any uncertainties in CO_2 data will transferred to $^{14}CO_2$ data and result in significant correlations between these two observational data.

Taking the calculation of the variance between daily CO_2 and 2-week $^{14}CO_2$ data as an example, assuming that during a 2-week period, the observation error in one daily CO_2 data *i* is ε_i, the error in 2-week C_a is:

$$\varepsilon_{a,2w} = \frac{\sum_{i=1}^{14} \varepsilon_i}{14} \quad \text{(S1)}$$

The error in $C_a\delta_a$ is:

$$\varepsilon_{Ca\delta a} = \varepsilon_{a,2w}\delta_a + C_a\varepsilon_{\delta a} = \frac{\sum_{i=1}^{14} \varepsilon_i\delta_a}{14} + C_a\varepsilon_{\delta a} \quad \text{(S2)}$$

At last, assuming that the error in C_a (ε_i) and δ_a ($\varepsilon_{\delta a}$) is independent, the covariance between the uncertainties in daily CO_2 data (*i*) and 2-week $^{14}CO_2$ data is:

$$cov(\varepsilon_i, \varepsilon_{Ca\delta a}) = E\left(\varepsilon_i^T \varepsilon_{Ca\delta a}\right) = \frac{E\left(\sum_{j=1}^{14} \varepsilon_i^T \varepsilon_j\right)}{14} \delta_a$$

$$= \frac{\sum_{j=1}^{14} cov(i,j)}{14} \delta_a \quad \text{(S3)}$$

where E(.) is the expectation of a variable, and T means the transpose of a vector, and *j* denote the any daily CO_2 data in the 2-week period.

References

Currie, K. I., Brailsford, G., Nichol, S., Gomez, A., Sparks, R., Lassey, K. R. and Riedel, K.: Tropospheric $^{14}CO_2$ at Wellington, New Zealand: the world's longest record, Biogeochemistry, 104(1–3), 5–22, 2011.

Graven, H. D.: Advancing the use of radiocarbon in studies of global and regional carbon cycling with high precision measurements of ^{14}C in CO_2 from the Scripps CO_2 Program, PhD Thesis, 2008.

Kanu, A. M., Comfort, L. L., Guilderson, T. P., Cameron-Smith, P. J., Bergmann, D. J., Atlas, E. L., Schauffler, S. and Boering, K. A.: Measurements and modeling of contemporary radiocarbon in the stratosphere, Geophys. Res. Lett., 43(3), 2016.

Levin, I. and Kromer, B.: The tropospheric $^{14}CO_2$ level in mid latitudes of the northern hemisphere (1959-2003), Radiocarbon, 46(3), 1261–1271, 2004.

Levin, I., Hammer, S., Eichelmann, E. and Vogel, F. R.: Verification of greenhouse gas emission reductions: the prospect of atmospheric monitoring in polluted areas, Philosophical transactions. Series A, Mathematical, physical, and engineering sciences, 369(1943), 1906–24, 2011.

Levin, I., Kromer, B. and Hammer, S.: Atmospheric $\Delta^{14}CO_2$ trend in Western European background air from 2000 to 2012, Tellus B, 65(0), 2013.

Levin, I., Kromer, B., Schmidt, M. and Sartorius, H.: A novel approach for independent budgeting of fossil fuel CO2 over Europe by $^{14}CO_2$ observations, Geophysical Research Letters, 30(23), 2003.

Lingenfelter, R. E.: Production of carbon-14 by cosmic-ray neutrons, Rev. Geophys., 1(1), 35–55, 1963.

Mook, W. and Rozanski, K.: Environmental isotopes in the hydrological cycle., 2000.

Nakamura, T., Nakazawa, T., Honda, H., Kitagawa, H., Machida, T., Ikeda, A. and Matsumoto, E.: Seasonal variations in ^{14}C concentrations of stratospheric CO_2 measured with accelerator mass spectrometry, Nuclear Instruments and Methods in Physics Research Section B: Beam Interactions with Materials and Atoms, 92(1–4), 413–416, 1994.

Nakamura, T., Nakazawa, T., Nakai, N., Kitagawa, H., Honda, H., Itoh, T., Machida, T. and Matsumoto, E.: Measurement of ^{14}C Concentrations of Stratospheric CO_2 by Accelerator Mass Spectrometry, Radiocarbon, 34(3), 745–752, 1992.

Peylin, P., Houweling, S., Krol, M. C., Karstens, U., Rödenbeck, C., Geels, C., Vermeulen, A., Badawy, B., Aulagnier, C., Pregger, T., Delage, F., Pieterse, G., Ciais, P. and Heimann, M.: Importance of fossil fuel emission uncertainties over Europe for CO_2 modeling: model intercomparison, Atmospheric Chemistry and Physics, 11(13), 6607–6622, 2011.

Randerson, J. T., Enting, I. G., Schuur, E. A. G., Caldeira, K. and Fung, I. Y.: Seasonal and latitudinal variability of troposphere $\Delta^{14}CO_2$: Post bomb contributions from fossil fuels, oceans, the stratosphere, and the terrestrial biosphere, Global Biogeochemical Cycles, 16(4), 59-1-59–19, 2002.

Svetlik, I., Povinec, P. P., Molnár, M., Váňa, M. and Sivo, A.: Radiocarbon in the Air of Central Europe: Long-Term Investigations, Radiocarbon, 52(2), 823–834, 2010.

Thoning, K. W., Tans, P. P., Komhyr, W. D. and others: Atmospheric carbon dioxide at Mauna Loa Observatory: 2. Analysis of the NOAA GMCC data, 1974–1985, J. Geophys. Res, 94(6), 8549–

8565, 1989.
Turnbull, J. C., Keller, E. D., Baisden, T., Brailsford, G., Bromley, T., Norris, M. and Zondervan, A.: Atmospheric measurement of point source fossil CO_2 emissions, Atmospheric Chemistry and Physics, 14(10), 5001–5014, 2014.
Vogel, F. R., Hammer, S., Steinhof, A., Kromer, B. and Levin, I.: Implication of weekly and diurnal ^{14}C calibration on hourly estimates of CO-based fossil fuel CO_2 at a moderately polluted site in southwestern Germany, Tellus B, 62(5), 512–520, 2010.
Vogel, F. R., Levin, I. and Worthy, D.: Implications for deriving regional fossil fuel CO_2 estimates from atmospheric observations in a hot spot of nuclear power plant $^{14}CO_2$ emissions, Radiocarbon, 55(2), 1556–1572, 2013.

Chapter 5 Conclusions and perspectives

This thesis presented a series of studies that aim to understand the potential of atmospheric $^{14}CO_2$ measurements to independently verify and reduce uncertainties in the estimate of fossil fuel emissions from inventories based on energy statistics. This approach is based on the atmospheric inversion modelling framework, which synthesize atmospheric measurements with a model for atmospheric transport and prior knowledge of the emissions, accounting for uncertainties in each component. The atmospheric inverse methods has been widely used to infer natural CO_2 fluxes, but rarely applied to the estimate of fossil fuel emissions. In this thesis, a series inversion systems aiming at solving for the fossil fuel emissions at sub-continental scale are presented.

Firstly, the critical sources of errors that may affect the inversion of fossil fuel emissions was investigated. It was found in Chapter 2 that such errors have large temporal auto-correlation scales. While the correlations of the observation errors are generally ignored in traditional atmospheric inversion solving for natural CO_2 fluxes, this analysis demonstrates how critical it should be to account for them when solving for fossil fuel emissions. It also shows that these errors have small spatial correlation scales, highlighting the need for dense networks to improve the estimate of FFCO2 emissions at large scale.

The second part in Chapter 3 builds upon the error characterization of the previous chapter and focuses on the evaluation of the skill of the large-scale inversion system which aims at estimating the monthly to annual budgets of fossil fuel emissions in European regions. Based on a series of Observing System Simulation Experiments (OSSEs), it is shown that in the framework of large scale inverse modelling, using virtual atmospheric observations of $FFCO_2$ from a continental network of $^{14}CO_2$ stations can reduce the uncertainties in the fossil fuel emissions of traditional inventories used as the prior knowledge in the inversion system over high emitting regions.

The third part presents the implementation of an inversion framework that jointly assimilates atmospheric CO_2 and $^{14}CO_2$ data, which avoids the assumption that ^{14}C is a perfect tracer of $FFCO_2$ and accounts for other $^{14}CO_2$ sources. This inversion system further examines the influences of natural fluxes on the estimate of fossil fuel emissions. The results show that $^{14}CO_2$ data provide useful information to separate fossil fuel and natural CO_2

fluxes. The filtering of the signatures of the uncertainties in the traditional inventories used as a prior knowledge in the inversion system is not significantly affected by the uncertainties in the estimate of natural fluxes when the atmospheric $^{14}CO_2$ data is assimilated. Furthermore, assimilating $^{14}CO_2$ data in the inversion frameworks allows for detection and reduction in the transferred biases to NEE that would arise from the erroneous representation of prescribed fossil fuel emissions in conventional atmospheric inversions.

In conclusion, the results from this study confirm previous work (Levin et al., 2013; Turnbull et al., 2009) that accurate $^{14}CO_2$ measurements have a high potential to independently verify the fossil fuel emissions and improve inventories (here "improve" means reducing the random error but also correcting a biased inventory to better match the true emissions). However, beyond the results presented in this thesis, new opportunities are opened up for a wide range of applications of the inversion approach on the estimate of fossil fuel emissions.

As mentioned in chapter 2, there are already 17 radiocarbon measurement stations operating all across European continent. Meanwhile, about 1000 radiocarbon measurements are made at eleven surface sites and two aircraft sites per year in America (Basu et al., 2016). However, no real atmospheric $^{14}CO_2$ data have been assimilated in the inversion systems, even if optimistic results have been shown by OSSEs in this thesis and other studies (Pacala et al., 2010; Basu et al., 2016). The networks of observational sites are expanding in some regions (Pacala et al., 2010; Ciais et al., 2015), but we do not know when / if a large number of continuous and high-precision radiocarbon measurements will be available in the coming decade. In this context, assimilating the first real observations of $^{14}CO_2$ in addition to CO_2 from the ICOS network or other sources in the inversion system is a priority to move away from OSSEs to the use of real data.

This thesis has shown the potential of $^{14}CO_2$ observations as a "proxy" tracer in the estimate of fossil fuel emissions. However, although $^{14}CO_2$ could provide the most accurate and direct information on fossil fuel emissions (Gamnitzer et al., 2006; Turnbull et al., 2006), the analysis of $^{14}CO_2$ samples is labor intensive and expensive. Even denser network than current is expected in the future, the temporal/spatial coverage of $^{14}CO_2$ observations will still be quite limited compared to the large number of continuous CO_2 observations achievable today. In addition, the growth of fossil fuel emissions over the coming decades will change the sensitivity of atmospheric $^{14}CO_2$ to fossil fuel emissions and thus reduce the

effectiveness of using $^{14}CO_2$ as a tracer for $FFCO_2$ (Graven et al., 2015). In this context, other tracers, such as CO, NOx, which are less costly and can be measured continuously or can be measured by satellites with large spatial coverage and high resolution, will complement the observational constraints by $^{14}CO_2$ and be used as additional proxies of $FFCO_2$ (Palmer et al., 2006; Gamnitzer et al., 2006; Turnbull et al., 2006; Super et al., 2016). The CO (or NOx) emitted from different sectors have different CO/CO_2 (or NOx/CO_2) ratios (Lopez et al., 2013; Konovalov et al., 2016), so that the atmospheric CO (or NOx) mixing ratios in the atmosphere may bear information about sectoral fossil fuel CO_2 sources. In many cases, CO and NOx are reasonable tracers of fossil fuel emissions, but subject to the large uncertainties in emission ratios of the different trace gases caused by differences in fuel type and combustion efficiency. The combination of hybrid fossil fuel emission estimates derived from $^{14}CO_2$, CO, NOx and other tracers can compensate the limitations of single tracer and provide a comprehensive constraints on the estimate of fossil fuel emissions.

In addition, observations from pilot urban CO_2 networks have been used to estimate fossil CO_2 emissions at the scale of large cities (Bréon et al., 2015; Staufer et al., 2016; Turnbull et al., 2015). Experience from a pilot network of four stations deployed around the Paris area showed that total CO_2 emissions inventories for this city could be constrained and their uncertainty reduced (Bréon et al., 2015). A hypothetical dense urban network of sensors of moderate precision (1 ppm) could separate (to some extent) emissions from different main sectors in the case of the Paris urban area, reducing the uncertainty of total CO_2 emissions of this city down to 5%, which is comparable to the accuracy achieved now at national scale by the best inventories (Wu et al., 2016). In recent years, some additional urban CO_2 stations are being installed in other megacities (Boon et al., 2016; Super et al., 2016). In-situ urban networks and regional in-situ observing networks are complementary to each other. While continental-scale networks give a verification of emissions budgets aggregated over larger spatial scales, urban networks allow to measure some hotspots of emissions.

To improve the spatial and temporal coverage and resolution of the sampling of $FFCO_2$, precise and global spatially-resolved images of these tracers from space-based platforms constitute a crucial component. Remote sensing offers spatial coverage superior to any in-situ network. Ground footprints, sampled by observations of column-averaged dry air mole fractions of CO_2, CO and NOx (XCO_2, XCO and XNOx) from satellites in low Earth orbit (LEO), such as GOAST, OMI, GOME, should capture large hotspot emissions and achieve

a complete global coverage with as frequent as possible repeat passes for resolving short-term changes of emissions (e.g., from strong local sources such as large cities or power plants, Kort et al., 2012; Janardanan et al., 2016). High resolution imagery of tracers sampled from some planned sensors in Geostationary Orbit (GEO) would be complementary to the LEO observations by providing high frequency measurements throughout the sunlit part of the diurnal cycle (O'Brien et al., 2016). For example, in a theoretical study about the proposed geostationary geoCARB satellite that I am involved in, some preliminary results show that with the high imagery capacity, the patterns of the variations in atmospheric CO_2 at fine spatial and temporal scales can be measured efficiently over China. In consequence, the geoCARB or other geostationary satellites show a high potential to separate and estimate the fossil fuel emissions and biogenic fluxes.

The above-mentioned complementary observations of in-situ fossil fuel emission tracer data and a set of space-borne sensors provide dense sampling of the fossil fuel CO_2 signal in the atmosphere, in space and time, will enable the tracking of fossil fuel emissions at a level of accuracy compliant with policy and scientific needs. Such sampling should not only give insights on the high-resolution spatio-temporal distribution of the emissions, but also bear more information about the emitting processes (e.g. emission factors, intensity of the activities, etc.). However, challenges also exist. Because of differences in measurement techniques and standards, different observations can have distinct information and error characteristics. Using more than one data in a single assimilation/inversion system requires large efforts to reconcile the systematic differences between different data products.

Apart from the observing technology, this thesis highlights that using the coarse-resolution transport model suffers from the large representation error and is hard to capture the sub-grid variations of the emissions. Because the fossil fuel emissions are at small scales, a robust fossil fuel emission observing system will require higher resolution transport models to better solve the fine patterns of the emissions. The use of the high-resolution transport model should, in principle, increase the potential of the inversion to constrain the fossil fuel emissions, even targeting the large scale budgets. At the same time, as the satellite will measure the column-integrated mole fractions at the horizontal scale of few km, the increase of the spatial resolution of the transport model to ideally the same scale as the satellite data, will facilitate the assimilation of these data.

In the Bayesian framework of the inversion/data assimilation systems, emission

inventories data (or an emission model) are the essential input as the prior information. More accurate inventory can improve the prior emissions data input, and thereby greatly reduce the posterior uncertainties leading to much higher accuracy in final emission estimates. However, the present inventories or emission maps is likely insufficient at the spatial and temporal scales. To improve estimates of fossil fuel emissions and use them within inverse modelling, emission estimates and associated uncertainties at a resolution of few km and of 1-hour is urgently needed. Such information is presently not available for CO_2 emissions but air quality studies have shown the possibilities to derive the estimates at high spatial and temporal resolution.

Last but not the least, recent development of atmospheric inversion approach would benefit from all the improvements in the measurement technology, transport models and inventory modelling. This approach is called Fossil Fuel Data Assimilation System (FFDAS). The principle of FFDAS is to assimilate diverse atmospheric measurements as well as other data-streams such as national statistics on fossil fuel consumption and other census data, into an emission model to improve its parameters and to provide optimized emission estimates with their uncertainties. Future efforts to combine the multiple datasets will make such a FFDAS system an international and independent information system for determining the distribution of anthropogenic emissions, and the ways in which they are consistent or not with efforts to reduce the emissions at policy-relevant temporal and spatial scales.

Reference

Basu, S., Miller, J. B. and Lehman, S.: Separation of biospheric and fossil fuel fluxes of CO_2 by atmospheric inversion of CO_2 and $^{14}CO_2$ measurements: Observation System Simulations, Atmospheric Chemistry and Physics, 16(9), 5665–5683, 2016.

Boon, A., Broquet, G., Clifford, D. J., Chevallier, F., Butterfield, D. M., Pison, I., Ramonet, M., Paris, J.-D. and Ciais, P.: Analysis of the potential of near-ground measurements of CO_2 and CH_4 in London, UK, for the monitoring of city-scale emissions using an atmospheric transport model, Atmospheric Chemistry and Physics, 16(11), 6735–6756, 2016.

Br éon, F. M., Broquet, G., Puygrenier, V., Chevallier, F., Xueref-Remy, I., Ramonet, M., Dieudonn é, E., Lopez, M., Schmidt, M., Perrussel, O. and Ciais, P.: An attempt at estimating Paris area CO_2 emissions from atmospheric concentration measurements, Atmospheric Chemistry and Physics, 15(4), 1707–1724, 2015.

Ciais, P., Crisp, D., Denier van der Gon, H. A. C., Engelen, R., Heimann, M., Janssens-Maenhout, G., Rayner, P. and Scholze, M.: Towards a European Operational Observing System to Monitor Fossil CO2 emissions, European Commission Directorate-General for Internal Market, Industry, Entrepreneurship and SMEs Directorate I — Space Policy, Copernicus and Defence., 2015.

Gamnitzer, U., Karstens, U., Kromer, B., Neubert, R. E. M., Meijer, H. A. J., Schroeder, H. and Levin, I.: Carbon monoxide: A quantitative tracer for fossil fuel CO_2?, Journal of Geophysical Research, 111(D22), 2006.

Janardanan, R., Maksyutov, S., Oda, T., Saito, M., Kaiser, J. W., Ganshin, A., Stohl, A., Matsunaga, T., Yoshida, Y. and Yokota, T.: Comparing GOSAT observations of localized CO_2 enhancements by large emitters with inventory-based estimates, Geophysical Research Letters, 43(7), 2016.

Konovalov, I. B., Berezin, E. V., Ciais, P., Broquet, G., Zhuravlev, R. B. and Janssens-Maenhout, G.: Estimation of fossil-fuel CO_2 emissions using satellite measurements of "proxy" species, Atmospheric Chemistry and Physics Discussions, 1–55, 2016.

Kort, E. A., Frankenberg, C., Miller, C. E. and Oda, T.: Space-based observations of megacity carbon dioxide, Geophysical Research Letters, 39(17), L17806, 2012.

Lopez, M., Schmidt, M., Delmotte, M., Colomb, A., Gros, V., Janssen, C., Lehman, S. J., Mondelain, D., Perrussel, O., Ramonet, M., Xueref-Remy, I. and Bousquet, P.: CO, NOx and $^{13}CO_2$ as tracers for fossil fuel CO_2: results from a pilot study in Paris during winter 2010, Atmospheric Chemistry and Physics, 13(15), 7343–7358, 2013.

O'Brien, D. M., Polonsky, I. N., Utembe, S. R. and Rayner, P. J.: Potential of a geostationary geoCARB mission to estimate surface emissions of CO_2, CH_4 and CO in a polluted urban environment: case study Shanghai, Atmospheric Measurement Techniques, 9(9), 4633–4654, 2016.

Pacala, S. W., Breidenich, C., Brewer, P. G., Fung, I. Y., Gunson, M. R., Heddle, G., Law, B. E., Marland, G., Paustian, K., Prather, M. and others: Verifying greenhouse gas emissions: methods to support international climate agreements., 2010.

Palmer, P. I., Suntharalingam, P., Jones, D. B. A., Jacob, D. J., Streets, D. G., Fu, Q., Vay, S. A. and Sachse, G. W.: Using CO_2:CO correlations to improve inverse analyses of carbon fluxes, Journal of Geophysical Research, 111(D12), 2006.

Ray, J., Yadav, V., Michalak, A., van Bloemen Waanders, B. and Mckenna, S. A.: A multiresolution spatial parameterization for the estimation of fossil-fuel carbon dioxide emissions via atmospheric inversions, Geoscientific Model Development, 7(5), 1901–1918, 2014.

Rayner, P. J., Raupach, M. R., Paget, M., Peylin, P. and Koffi, E.: A new global gridded data set of CO_2 emissions from fossil fuel combustion: Methodology and evaluation, J Geophys Res-Atmos, 115, 2010.

Staufer, J., Broquet, G., Bréon, F.-M., Puygrenier, V., Chevallier, F., Xueref-Rémy, I., Dieudonné, E., Lopez, M., Schmidt, M., Ramonet, M., Perrussel, O., Lac, C., Wu, L. and Ciais, P.: A first year-long estimate of the Paris region fossil fuel CO_2 emissions based on atmospheric inversion, Atmospheric Chemistry and Physics Discussions, 1–34, 2016.

Super, I., Denier van der Gon, H. A. C., Visschedijk, A. J. H., Moerman, M. M., Chen, H., van der Molen, M. K. and Peters, W.: Interpreting continuous in-situ observations of carbon dioxide and carbon monoxide in the urban port area of Rotterdam, Atmospheric Pollution Research, 2016.

Turnbull, J. C., Miller, J. B., Lehman, S. J., Tans, P. P., Sparks, R. J. and Southon, J.: Comparison of $^{14}CO_2$, CO, and SF_6 as tracers for recently added fossil fuel CO_2 in the atmosphere and implications for biological CO_2 exchange, Geophysical Research Letters, 33(1), 2006.

Wu, L., Broquet, G., Ciais, P., Bellassen, V., Vogel, F., Chevallier, F., Xueref-Remy, I. and Wang, Y.: What would dense atmospheric observation networks bring to the quantification of city CO_2 emissions?, Atmospheric Chemistry and Physics, 16(12), 7743–7771, 2016.